EFFECTS OF SURFACE ROUGHNESS ON BLOODSTAIN SPREADING AND SPINE FORMATION

by

Raquel Murray

This thesis is submitted in partial fulfilment of the requirements for the Degree of Doctor of Philosophy

Cranfield Defence and Security (Defence Engineering)
Cranfield University

Supervisor: Dr. Clare Knock

Abstract

Expert witnesses employ bloodstain pattern analysis (BPA), to provide objective analysis of bloodstain evidence in criminal cases. This thesis added to the scientific understanding of BPA by generating and analysing a large data set of 785 horse blood experiments. The experiments produced impact velocities, u_0, of $2.89\,\mathrm{m\,s^{-1}}$ to $6.54\,\mathrm{m\,s^{-1}}$, with impact angles, θ_f, 90°, 72°, 54°, 36°, and 18°. Different surface roughnesses were investigated: conditioned and unconditioned paper, smooth steel, and three roughened steel substrates with roughness values, R_a, 1.6×10^{-6} m, 3.2×10^{-6} m, and 6.3×10^{-6} m. To analyse the data, two computational tools were developed. The first tool extracted the diameter and velocity of a droplet from high-speed videos. The second tool measured stain properties and counted spines of stains resulting from 90° and 72°.

The results of these experiments are investigated, extracting relationships between impact properties of droplets to stain properties. Each of the stain properties were related to some combination of a non-dimensional number (Bond number, Bo, Froude number, Fr, or Reynolds number, Re) and impact angle. It was found that the stain area and stain perimeter are proportional to $\mathrm{Bo}\,(\sin\theta_f)^{-1}$. The number of spines and/or tails on a stain is dependent on $\mathrm{Fr}\,(\sin\theta_f)^2$. The major diameter is proportional to $\mathrm{Re}\,(\sin\theta_f)^{-2}$ and conversely the minor diameter is proportional to $\mathrm{Re}\,(\sin\theta_f)^2$. The full length of the stain is proportional to $\mathrm{Bo}\,(\sin\theta_f)^{-2}$. The results showed that increased surface roughness, promotes increased variability in the bloodstains, up to a limit of $R_a = 6.3\times10^{-6}\,\mathrm{m}$. The roughest steel is statistically the same as paper in almost all stain properties.

The results proved a need to account for surface roughness in modelling the spreading of a droplet on a substrate. Starting from the laws of conservation of energy, a new model for predicting spread factor was derived which accounts for the impact angle and substrate roughness. This model uses a coefficient based on properties from the stain and is able to predict the experimental spread factors in this thesis more accurately than the spread factor models in literature. Two new equations were derived that calculate the impact velocity and droplet diameter using only stain properties, not experimental fitting constants, making the expressions more robust.

Dedication

I would like to dedicate this thesis to my parents, Wayne and Pauline Murray, who have always believed in me and supported me in all of my life endeavours. Thank you for making me the person I am today.

Acknowledgements

To my supervisor, Dr. Clare Knock: Thank you for working with me and encouraging me every step of this journey. You are the best supervisor any student can ask for.

To Dr. Debra Carr: Thank you for being a mentor and great friend. You are a fount of knowledge, not only academically, but in life.

To my landlady, Jane Hollick (and puppy, Alfie): Thank you for giving me a home away from home for the entirety of this PhD and for stepping in as my mum when I was 5000 km away from home.

To my friends and family, civilian or military, here in the UK or home in Canada, thank you for your faith and support.

Contents

1 Introduction **1**

1.1 Introduction 1

1.2 Motivation 4

1.3 Contributions 4

1.4 Aim and objectives 5

1.5 Thesis structure 5

2 Literature review **7**

2.1 Physics parameters and relevant numbers 8

2.1.1 Dimensionless numbers 9

2.2 Properties of non-Newtonian fluids 16

2.3 Phases of impact and stain properties 17

2.3.1 Assumptions concerning droplet impacts on surfaces 23

2.4 Surface roughness 24

2.5 Contact angle 28

2.6 Energy conservation 34

2.6.1 Kinetic energy before impact 35

2.6.2 Surface energy before impact 36

2.6.3 Surface energy after impact 36

2.6.4 Deformation of the droplet 40

2.7 Investigating spread factor 43

2.7.1 Spread factor according to Engel [1955] 44

2.7.2 Spread factor according to Cheng [1977] 46

2.7.3 Spread factor according to Chandra and Avedisian [1991] and others . . 48

2.7.4 Spread factor according to Hulse-Smith et al. [2005] 50

2.7.5 Comparison of spread factors 51

2.8 Investigating the evolution of spines . . . 53
2.9 Terminal velocity of a droplet . . . 58
2.10 Calculating u_0 and d_0 of a blood droplet . . . 64
2.11 Current methods used in BPA . . . 68
2.12 Predicting the position of the source of bloodletting . . . 76
2.12.1 Errors in calculating the source of bloodletting . . . 80
2.13 Blood substitute . . . 82

3 Computational tools developed **89**
3.1 Automation of counting spines on vertical impact drip stains . . . 89
3.1.1 Motivation . . . 89
3.1.2 Strategy . . . 91
3.1.3 Survey . . . 92
3.1.4 Experimental technique . . . 93
3.1.5 Computational determination of stain properties . . . 93
3.1.6 Conclusion . . . 97
3.2 Automation of estimating the droplet properties at impact . . . 98
3.2.1 Motivation . . . 98
3.2.2 Retrieving droplet diameter . . . 98
3.2.3 Retrieving the impact velocity . . . 100
3.2.4 Testing the accuracy of the DVVP . . . 103
3.2.5 Conclusion . . . 104

4 Experimental methodology **105**
4.1 Motivation . . . 105
4.2 Experimental method . . . 106
4.3 Recommendations to improve experimental methods . . . 114
4.4 Experimental results . . . 115

4.4.1 Circular bloodstains . . . 115
4.4.2 Elliptical bloodstains . . . 118
4.4.3 Miscellaneous stains . . . 123
4.5 Error Analysis . . . 125
4.6 Summary . . . 126
4.6.1 New definitions of stain properties . . . 127

5 Results of the horse blood experiments 129

5.1 Context . . . 129
5.2 Fluid Flow . . . 129
5.3 General view of the data . . . 131
5.3.1 Droplets impacting at 90° . . . 133
5.3.2 Droplets impacting at 72° . . . 135
5.3.3 Droplets impacting at 54° . . . 136
5.3.4 Droplets impacting at 36° . . . 136
5.3.5 Droplets impacting at 18° . . . 139
5.4 Effect of u_0 and θ_f on various stain properties . . . 141
5.4.1 Effect of u_0 and θ_f on stain area . . . 141
5.4.2 Effect of u_0 and θ_f on stain perimeter . . . 146
5.4.3 Effect of u_0 and θ_f on the number of spines and tails . . . 148
5.4.4 Effect of u_0 and θ_f on the major diameter of stains . . . 152
5.4.5 Effect of u_0 and θ_f on the minor diameter of stains . . . 155
5.4.6 Effect of u_0 and θ_f on the length of stains . . . 158
5.5 Statistical results . . . 160
5.6 Summary . . . 162

6 Mathematical expressions developed for BPA 165

6.1 Motivation for new spread factor . . . 165

6.2 Derivation of a new spread factor . . . 166
6.3 Test spread factors against experimental data . . . 172
6.4 Motivation for new impact velocity and droplet diameter equations . . . 181
6.5 Calculating the impact velocity and droplet diameter . . . 181
6.6 Testing new equations for u_0 and d_0 . . . 182

7 Conclusions **185**
7.1 Summary . . . 185
7.2 Contributions . . . 186
7.2.1 Large experimental data set . . . 186
7.2.2 Classification of stain properties . . . 186
7.2.3 Irrelevance of conditioning paper and the direction of milling . . . 187
7.2.4 The Diameter and Velocity Video Processor (DVVP) . . . 187
7.2.5 The Automated Spine Counter (ASC) . . . 188
7.2.6 Relationships discovered between impact properties and stain properties 188
7.2.7 Novel spread factor . . . 190
7.2.8 Two novel equations to calculate u_0 and d_0 . . . 190
7.3 Future Work . . . 190

References **192**

Bibliography **200**

Appendices **203**

Appendix A British Standards **203**

Appendix B Calculating percent error and percent difference **205**

Appendix C Definitions of statistical tests **207**
C.1 Interpretation of the p-value . . . 207

C.2 Levene's Test . . . 208
C.3 One-sample Kolmogorov-Smirnov test . . . 208
C.4 Analysis of variance Test (ANOVA) . . . 209
C.5 Tukey Test . . . 209

Appendix D Testing the effect of grain direction: Results of the one-way ANOVA 211

Appendix E Raw statistics from experimental data used in Chapter 5 215

Appendix F ASC and manual counting 229

F.1 Motivation . . . 229
F.2 Using horse blood . . . 229
F.3 Using pig blood . . . 234
F.4 Conclusions . . . 239

Appendix G Paper conditioning 241

G.1 Introduction and motivation . . . 241
G.2 Strategy . . . 241
G.3 Experimental technique . . . 242
G.4 Statistical tests . . . 242
G.4.1 Comparing number of spines . . . 242
G.4.2 Comparing inner diameter . . . 244
G.4.3 Comparing outer diameters . . . 245
G.4.4 Comparing stain area . . . 246
G.4.5 Comparing stain perimeter . . . 247
G.5 Conclusion . . . 248

Appendix H Pig versus horse blood 251

H.1 Introduction and motivation . . . 251
H.1.1 Strategy . . . 251

H.1.2 Survey . . . 252
H.2 Experimental technique . . . 255
H.3 Statistical tests . . . 255
H.3.1 Comparing the number of spines . . . 255
H.3.2 Comparing the inner diameter . . . 256
H.3.3 Comparing the outer diameter . . . 256
H.3.4 Comparing the stain area . . . 257
H.3.5 Comparing the stain perimeter . . . 257
H.4 Conclusion . . . 264

Appendix I ASC versus *ImageJ* 265
I.1 Introduction and motivation . . . 265
I.1.1 Strategy . . . 265
I.2 Experimental technique . . . 266
I.3 Statistical tests . . . 266
I.3.1 Comparing the stain areas . . . 266
I.3.2 Comparing the stain perimeters . . . 268
I.4 Conclusion . . . 269

Appendix J Derivation of the dissipation function 273

Appendix K Kinetic energy before impact 275

Appendix L Kinetic energy before impact by Engel [1955] 277

Appendix M Surface energy before impact 283

Appendix N Deformation energy by Engel [1955] 285

Appendix O Deformation energy by Chandra and Avedisian [1991] 289

Appendix P Deformation energy by Pasandideh-Fard et al. [1996] 293

Appendix Q Spread factor by Chandra and Avedisian [1991] 299

Appendix R Spread factor by Pasandideh-Fard et al. [1996] 303

Appendix S The Del Operator 307

Appendix T Unit Analysis 309

Appendix U Derivation of d_0 and u_0 based on Knock and Davison [2007]'s work 311

Appendix V Testing other non-dimensional numbers for better correlations to stain properties 315

List of Tables

2.1 Equilibrium contact angle (θ_e) of a droplet indicating the wettability of a liquid (Carey [1992]). 28

2.2 Characteristics of free falling human blood by MacDonell [1993] (units have been converted to SI units) 58

2.3 List of fitting constants in the work by Wobus et al. [1971] 61

2.4 Comparisons of the physical properties of blood, water, and Kollidon VA64 . . 87

3.1 Comparing the estimated of droplet diameter, d_0, by *Phantom Camera Control* software (PCC) and the Diameter and Velocity Video Processor (DVVP). . . . 103

3.2 Comparing the estimated of impact velocity, u_0, by *Phantom Camera Control* software (PCC) and the Diameter and Velocity Video Processor (DVVP). . . . 104

5.1 Number of repeats (reps) and mean impact velocities ($\bar{u_0}$) of droplets impacting substrates at 90°. The range of droplet diameters in this data set is 3.2×10^{-3} m to 4.3×10^{-3} m. 134

5.2 Number of repeats (reps) and mean impact velocities ($\bar{u_0}$) of droplets impacting substrates at 72°. The range of droplet diameters in this data set is 3.1×10^{-3} m to 4.5×10^{-3} m. 135

5.3 Number of repeats (reps) and mean impact velocities ($\bar{u_0}$) of droplets impacting substrates at 54°. The range of droplet diameters in this data set is 3.3×10^{-3} m to 4.4×10^{-3} m. 137

5.4 Number of repeats (reps) and mean impact velocities ($\bar{u_0}$) of droplets impacting substrates at 36°. The range of droplet diameters in this data set is 3.6×10^{-3} m to 4.3×10^{-3} m. 138

5.5 Number of repeats (reps) and mean impact velocities ($\bar{u_0}$) of droplets impacting substrates at 18°. The range of droplet diameters in this data set is 3.1×10^{-3} m to 4.3×10^{-3} m. 140

6.1 The average percent error of calculating d_0 and u_0 using Equations 6.25 and 6.26 with different methods of counting spines. 183

C.1 Guidelines on how to interpret the p-value from statistical tests. 207

D.1 Results of a one-way ANOVA test regarding grain direction for an impact angle of 72°. 211

D.2 Results of a one-way ANOVA test regarding grain direction for an impact angle of 54°. 212

D.3 Results of a one-way ANOVA test regarding grain direction for an impact angle of 36°. 213

D.4 Results of a one-way ANOVA test regarding grain direction for an impact angle of 18°. 214

E.1 Resolution of high-speed videos and digital photographs and the circularity of stains 215

E.2 Statistical properties of the experimental data from droplets impacting paper at 90°. 216

E.3 Statistical properties of the experimental data from droplets impacting smooth steel at 90°. 217

E.4 Statistical properties of the experimental data from droplets impacting roughened steel ($R_a = 1.6 \times 10^{-6}$ m) at 90°. 217

E.5 Statistical properties of the experimental data from droplets impacting roughened steel ($R_a = 3.2 \times 10^{-6}$ m) at 90°. 218

E.6 Statistical properties of the experimental data from droplets impacting roughened steel ($R_a = 6.3 \times 10^{-6}$ m) at 90°. 218

E.7 Statistical properties of the experimental data from droplets impacting paper at 72°. 219

E.8 Statistical properties of the experimental data from droplets impacting smooth steel at 72°. 219

E.9 Statistical properties of the experimental data from droplets impacting roughened steel ($R_a = 1.6 \times 10^{-6}$ m) at 72°. 220

E.10 Statistical properties of the experimental data from droplets impacting roughened steel ($R_a = 3.2 \times 10^{-6}$ m) at 72°. 220

E.11 Statistical properties of the experimental data from droplets impacting roughened steel ($R_a = 6.3 \times 10^{-6}$ m) at 72°. 221

E.12 Statistical properties of the experimental data from droplets impacting paper at 54°. 221

E.13 Statistical properties of the experimental data from droplets impacting smooth steel at 54°. 222

E.14 Statistical properties of the experimental data from droplets impacting roughened steel ($R_a = 1.6 \times 10^{-6}$ m) at 54°. 222

E.15 Statistical properties of the experimental data from droplets impacting roughened steel ($R_a = 3.2 \times 10^{-6}$ m) at 54°. 223

E.16 Statistical properties of the experimental data from droplets impacting roughened steel ($R_a = 6.3 \times 10^{-6}$ m) at 54°. 223

E.17 Statistical properties of the experimental data from droplets impacting paper at 36°. 224

E.18 Statistical properties of the experimental data from droplets impacting smooth steel at 36°. 224

E.19 Statistical properties of the experimental data from droplets impacting roughened steel ($R_a = 1.6 \times 10^{-6}$ m) at 36°. 225

E.20 Statistical properties of the experimental data from droplets impacting roughened steel ($R_a = 3.2 \times 10^{-6}$ m) at 36°. 225

E.21 Statistical properties of the experimental data from droplets impacting roughened steel ($R_a = 6.3 \times 10^{-6}$ m) at 36°. 226
E.22 Statistical properties of the experimental data from droplets impacting paper at 18°. 226
E.23 Statistical properties of the experimental data from droplets impacting smooth steel at 18°. 227
E.24 Statistical properties of the experimental data from droplets impacting roughened steel ($R_a = 1.6 \times 10^{-6}$ m) at 18°. 227
E.25 Statistical properties of the experimental data from droplets impacting roughened steel ($R_a = 3.2 \times 10^{-6}$ m) at 18°. 228
E.26 Statistical properties of the experimental data from droplets impacting roughened steel ($R_a = 6.3 \times 10^{-6}$ m) at 18°. 228

F.1 Number of spines on horse bloodstains as counted by participants, calculated by the ASC, and predicted by various models. 233
F.2 Number of spines on horse bloodstains as counted by participants, calculated by the ASC, and predicted by various models. Heights of 0.2 m, 0.4 m, 0.6 m, and 0.8 m. 235
F.3 Number of spines on horse bloodstains as counted by participants, calculated by the ASC, and predicted by various models. Heights of 1.0 m and 1.5 m. . . . 236
F.4 Number of spines on horse bloodstains as counted by participants, calculated by the ASC, and predicted by various models. Heights of 2.0 m. 237

G.1 Number of spines on horse bloodstains as counted by the ASC. 243
G.2 Inner diameter (in m) of horse bloodstains as measured by the ASC. 244
G.3 Outer diameter (in m) of horse bloodstains as measured by the ASC. 245
G.4 Stain area (in 10^{-4} m^2) of horse bloodstains as measured by the ASC. 246
G.5 Stain perimeter (in m) of horse bloodstains as measured by the ASC. 248

H.1 Physical properties of water at different temperatures from literature 252
H.2 Physical properties of human blood at different temperatures from literature . . 253
H.3 Physical properties of pig blood at different temperatures from literature 253
H.4 Physical properties of horse blood at different temperatures from literature . . . 254
H.5 Impact velocity and diameter of horse blood and pig blood droplets. 258
H.6 Number of spines on pig and horse bloodstains as counted by the ASC. 259
H.7 Inner diameter (in 10^{-2} m) of pig and horse bloodstains as measured by the ASC. 260
H.8 Outer diameter (in 10^{-2} m) of pig and horse bloodstains as measured by the ASC. 261
H.9 Stain area (in 10^{-4} m^2) of pig and horse bloodstains as measured by the ASC. . 262
H.10 Stain perimeter (in 10^{-2} m) of pig and horse bloodstains as counted by the ASC. 263

V.1 R^2 values for alternative correlations of impact properties to stain properties . . 315

List of Figures

2.1 Illustration of a droplet's diameter, d_0, before impact (in part a) and droplet's impact velocity (in part b), u_0, as well as the height from which the droplet has fallen from, H. The droplet is falling vertically down in the negative y direction, heading for impact onto a surface on the x plane. 11

2.2 An edited depiction of the four phases of impact as they occur in varying angles of impact (Bevel and Gardner [2001]). In each box, the drawing on the left shows a side view of the droplet impact. The drawing on the right depicts an over head view. 18

2.3 An edited depiction (tail of bloodstain is labelled) of classical measuring of bloodstains, where the direction of travel is indicated by the position of the tail of the bloodstain (Maloney and Maloney [2009]). The width of the bloodstain is denoted by d_i and the length of the bloodstain is denoted by d_j. 20

2.4 The range of stain shapes that result from the varying impact angles (Bevel and Gardner [2001]). More acute angles of impact result in elliptical stains, while more perpendicular angles of impact result in round stains. This figure has been edited to indicate the direction of travel of the droplets. 21

2.5 Illustration of vertical distances (ξ_i) measured along a rough surface. The measurements are made to the mean line which is indicated in red. In this example $n = 6$, *i.e.*, six measurements are made. 25

2.6 Published work by Adam [2013]. Human bloodstains formed from droplets falling from a height of 0.5 m onto (a) gloss paint, (b) vinyl silk paint, and (c) matt paint. The stains have a diameter of approximately 1.5×10^{-2} m. The diameter of the droplets were 4.21×10^{-3} m. 27

2.7 Illustration of the advancing contact angle, θ_a, when a droplet of radius r_0, falling in the negative y direction, first impacts a surface along the x plane. The droplet's height, h_0, has not yet begun to compress from impact. 30

2.8 Illustration of a droplet during its impact with a surface along the x plane. The droplet is compressing in the y direction, thus its height $h_s(t)$ is decreasing over time. The droplet's diameter is increasing over time during impact and is denoted by $d_s(t)$. The spherical cap changing over time is denoted by $d_{\text{cap}}(t)$. . 30

2.9 Illustration of a droplet impacting a solid surface by Rein [1993]. Figure has been edited here to label secondary droplets. 43

2.10 Illustration of the maximum extension, d_{max}, of a droplet during impact with a surface on the x plane before settling into the surface. 47

2.11 Illustration of the final diameter of the bloodstain, d_f, once a droplet has completed impacting the surface on the x plane and has settled. 47

2.12 The effect of contact angle on the maximum spread factor as proposed by Pasandideh-Fard et al. [1996]. The droplet diameter used is $d_0 = 3.76 \times 10^{-3}$ m. 50

2.13 A comparison of spread factors for a droplet $d_0 = 3.76 \times 10^{-3}$ m: Cheng [1977] (Equation 2.62), Chandra and Avedisian [1991] (Equation 2.63), Hulse-Smith et al. [2005] without fitting coefficient (Equation 2.65), and Pasandideh-Fard et al. [1996] (Equation 2.64). 52

2.14 Different models for predicting the number of spines on a bloodstain using the Weber number. Data in this figure are from Mehdizadeh et al. [2004], Hulse-Smith et al. [2005], and Knock and Davison [2007]. For reference, the line $C = 1$ is included which would represent the relationship between number of spines and the Weber number without any experimental coefficient. 57

2.15 The terminal velocity calculated using Equation 2.76 (labelled Koenig), Equation 2.77 (labelled Wobus), and Equation 2.75 (labelled Kessler) with a range of radii from 1×10^{-4} m to 5×10^{-3} m with their respective corrections using Equation 2.81. The absolute value of the terminal velocity is used. All three models can be found in the work by Wobus et al. [1971]. 63

2.16 An overhead view of the intersection of blood droplet paths by Maloney and Maloney [2009]. The region in the blue square is considered the region of intersection. The arrows show the direction of motion of the droplet. The bloodstain is created on the *y* plane. 69

2.17 A screen capture from Illes et al. [2005] of the trajectory reconstruction produced by *BACKTRACK*™. A view from the side where droplets are moving from right to left. The virtual flight paths of the downward moving droplets are shown to be originating from the ceiling. The three virtual flight paths show to be originating from the floor are upward moving droplets. The intersection of all these virtual flight paths are used to approximate the *z* coordinate. 70

2.18 Illustration of a droplet's initial position using (1) a straight line geometric reconstruction and (2) a ballistic estimation. 71

2.19 A screen capture from Maloney et al. [2011a] of cast-off analysis in *HEMOSPAT*™. Two-dimensional views of the complex cast-off pattern generated by a swinging hammer. Blue lines may indicate the backward-cast off, pink lines for forward cast-off, and red lines for impact trajectories. 72

2.20 Experimental set up by Maloney et al. [2011b] where a pool of blood sitting on a hockey puck is struck with a hammer. 73

2.21 A comparison between *BACKTRACK*™ and *HEMOSPAT*™ by de Bruin et al. [2011]. 14 bloodstains were analysed using *HEMOSPAT*™ (dark grey) or *BACKTRACK*™ (light grey). The deviation of the estimated source of bloodletting from the known solution was measured and the mean deviations are shown in this figure. The difference between *BACKTRACK*™ and *HEMOSPAT*™ is enlarged in the small graphs on the bottom. 74

2.22 Illustration of a droplet before and after it impacts a surface where x_i and y_i are the coordinates of the droplet's initial position and the droplet is given an initial velocity of u_i. The droplet's impact velocity is denoted as u_0 and the droplet's final position (or coordinates of the resulting bloodstain) are denoted by x_f and y_f. 77

2.23 An edited depiction (tail of bloodstain is labelled) of classical measuring of bloodstains, where the direction of travel is indicated by the position of the tail of the bloodstain (Maloney and Maloney [2009]). The width of the stain (d_i) and length of the stain (d_j) are also labelled. 78

2.24 Measurements of the average viscosity (over five samples of each species) of human, pig, and sheep blood as a function of shear rate by Laurent et al. [1999] 83

3.1 Porcine bloodstains produced by Hulse-Smith et al. [2005]. Blood droplets impacted a paper surface vertically, and exhibited spines. Droplet radii, r, and height h are as follows: a) $r = 1.85 \times 10^{-3}$ m, $h = 0.305$ m, b) $r = 1.5 \times 10^{-3}$ m, $h = 1.219$ m, c) $r = 2.15 \times 10^{-3}$ m, $h = 0.61$ m, d) $r = 1.85 \times 10^{-3}$ m, $h = 1.219$ m. Examples of spines are highlighted by the circles. 90

3.2 Photograph of the resulting bloodstain from a horse blood droplet, of radius 2.3×10^{-3} m, falling from a height of 0.5 m. 94

3.3 Bloodstain cropped from digital photograph 94

3.4 Bloodstain converted to binary image. 94

3.5 Edge and region of bloodstain visualised in MATLAB. 95

3.6 Identified spines, inner (black circle) and outer diameter (red circle) overlaid on the bloodstain. The green and orange squares identifies spines on the bloodstain that corresponds with the peaks in the green and orange squares in Figure 3.7. There are 20 spines identified on this stain. 96

3.7 Distances from the centre of the bloodstain to the edge of the bloodstain with a Savitsky-Golay filter and identified peaks. The green and orange squares identifies peaks that corresponds with spines on the edge of the bloodstain in the green and orange squares in Figure 3.6. There are 20 spines identified in this example. 97
3.8 Screenshot from the DVVP showing the user measuring, in pixels, a known distance on the physical ruler in the high-speed video. 99
3.9 Screenshots from the DVVP showing the program successfully finding the droplet within the high-speed video and preparing to track the droplet. 100
3.10 x and y position of a horse blood droplet, with diameter 4.00×10^{-3} m, falling from a height of 2.0 m to impact a roughened steel substrate. 102
3.11 Plot of the velocity of the droplet tracked in every frame of the high-speed video, with a linear fit. The impact velocity is calculated using Equation 3.9. 102

4.1 Pipette mounted onto retort stand, used to drip single droplets onto a known substrate from a known height. 106
4.2 Laboratory setup for dripping single droplets onto different substrates. 107
4.3 Phantom V12, black and white, high-speed camera, mounted onto a lab jack. . 108
4.4 Canon camera fitted with a 58 mm lens used to photograph the resulting stains. 108
4.5 Illustration of a droplet impacting a ramp at impact angle θ_f. 109
4.6 Ramps upon which substrates are placed to achieve angled impacts. 110
4.7 Steel substrate placed onto $\theta_f = 18°$ ramp. 110
4.8 Apparatus set up in the white box. 111
4.9 Temperature and humidity in the lab setup as measured by a protimeter during a day of experiments. 111
4.10 Illustration of assumed triangular grooves on the roughened surfaces used in this work. 112
4.11 Illustration of a theoretical roughened surface. 113

4.12 Resulting drip stains from droplets (with diameter, d_0, and impact velocity, u_0) falling from different heights, H, onto unconditioned paper. The number of spines, N, reported was counted by the Automated Spine Counter (ASC, Chapter 3). 116

4.13 Resulting bloodstain from a droplet of diameter 4.4×10^{-3} m, falling from 1.5 m onto conditioned paper, impacting at a velocity of $5.43\,\mathrm{m\,s^{-1}}$. The ASC found 31 spines on this stain. The inner diameter and outer diameter was also measured by the ASC. Note: there is a spine that may appear to extend outside the measured outer diameter (in Subfigure 4.13b). The spine has a satellite stain right outside the outer diameter, the satellite stain is not apart of the spine. . . . 116

4.14 Bloodstain from a droplet of diameter 3.64×10^{-3} m, impacting a smooth steel surface with velocity $5.10\,\mathrm{m\,s^{-1}}$. This bloodstain has no spines. 118

4.15 Analysis (by the ASC) of the bloodstain shown in Figure 4.14. 118

4.16 Bloodstain from a droplet impacting a steel substrate of roughness $R_a = 6.3 \times 10^{-6}$ m. The droplet's diameter before impact was 3.84×10^{-3} m and its impact velocity was $5.56\,\mathrm{m\,s^{-1}}$. 119

4.17 Drip stain from a droplet of diameter 3.46×10^{-3} m, impact velocity of $3.15\,\mathrm{m\,s^{-1}}$, impacting unconditioned paper at an angle of impact, 18°. 120

4.18 Resulting drip stain from a droplet of diameter 3.26×10^{-3} m, impacting a smooth steel surface with velocity $3.11\,\mathrm{m\,s^{-1}}$. The angle of impact is 18°. . . . 121

4.19 Resulting drip stain from a droplet of diameter 3.9×10^{-3} m, impacting a steel substrate of roughness $R_a = 6.3 \times 10^{-6}$ m (with the grain) with velocity $5.44\,\mathrm{m\,s^{-1}}$ at 18°. This bloodstain has two tails. 122

4.20 Resulting drip stain from a droplet of diameter 3.14×10^{-3} m, impacting a steel substrate of roughness 1.6×10^{-6} m (against the grain) with velocity $3.13\,\mathrm{m\,s^{-1}}$ at 18°. The total length of this drip stain is 9.753×10^{-2} m. 123

4.21 Bloodstain from a droplet of diameter 3.26×10^{-3} m, impacting a smooth steel surface with velocity $3.12\,\mathrm{m\,s^{-1}}$ at an angle of 18°. 124

4.22 Bloodstain from a droplet of diameter 3.96×10^{-3} m, impacting a steel surface of roughness 6.3×10^{-6} m with velocity $5.46\,\mathrm{m\,s^{-1}}$ at 18°. 125

5.1 Resulting stain from a droplet with a bubble formed inside. $H = 1.0\,\mathrm{m}$, $d_0 = 3.76 \times 10^{-3}\,\mathrm{m}$, $u_0 = 4.26\,\mathrm{m\,s^{-1}}$, $d_{\mathrm{out}} = 2.73 \times 10^{-2}\,\mathrm{m}$. 134

5.2 Resulting bloodstains from droplets falling from a height of $H = 1.5\,\mathrm{m}$ impacting unconditioned paper at 72°. 136

5.3 Resulting bloodstains from droplets falling from a height of $H = 1.0\,\mathrm{m}$ impacting smooth steel at 36°. Subfigure 5.3a is described as a "stream" (Chapter 4). . 139

5.4 The effect of impact velocity and impact angle on the mean area of the stains from droplets impacting different surfaces at different angles. The data has been averaged at each height and the error bars represent the standard error. 143

5.5 Four droplets impacting smooth steel from four different heights. 144

5.6 The effect of impact velocity and impact angle on the mean area of the stains from droplets impacting paper at different angles. The data has been averaged at each height and the error bars represent the standard error. 145

5.7 The effect of Bond number (Equation 5.4) and impact angle on the mean area of the stains from droplets impacting different surfaces at different angles. The data has been averaged at each height and the error bars represent the standard error. 146

5.8 The effect of impact velocity and impact angle on the mean perimeter of the stains from droplets impacting different surfaces at different angles. The data has been averaged at each height and the error bars represent the standard error. 147

5.9 The effect of impact velocity on the mean perimeter of the stains from droplets impacting different surfaces at different angles. The data has been averaged at each height and the error bars represent the standard error. 149

5.10 The effect of Bond number (Equation 5.4) and impact angle on the mean perimeter of the stains from droplets impacting different surfaces at different angles. The data has been averaged at each height and the error bars represent the standard error. 150

5.11 The effect of impact velocity and impact angle on the mean number of spines and tails of the stains from droplets impacting different surfaces at different angles. The data has been averaged at each height and the error bars represent the standard error. 151

5.12 The effect of impact velocity and impact angle on the mean number of spines and tails of the stains from droplets impacting paper at different angles. The data has been averaged at each height and the error bars represent the standard error. 152

5.13 The effect of Froude number (Equation 5.5) and impact angle on the mean number of spines and tails on stains from droplets impacting different surfaces at different angles. The data has been averaged at each height and the error bars represent the standard error. 153

5.14 The effect of impact velocity and impact angle on the mean major diameter of the stains from droplets impacting different surfaces at different angles. The data has been averaged at each height and the error bars represent the standard error. 154

5.15 The effect of the Reynolds number and impact angle on the mean major diameter of the stains from droplets impacting different surfaces at different angles. The data has been averaged at each height and the error bars represent the standard error. 155

5.16 The effect of the Bond number and impact angle on the mean major diameter of the stains from droplets impacting different surfaces at different angles. The data has been averaged at each height and the error bars represent the standard error. 156

5.17 The effect of impact velocity and impact angle on the mean minor diameter of the stains from droplets impacting different surfaces at different angles. The data has been averaged at each height and the error bars represent the standard error. 157

5.18 The effect of Reynolds number and impact angle on the mean minor diameter of stains from droplets impacting different surfaces at different angles. The data has been averaged at each height and the error bars represent the standard error. 158

5.19 The effect of impact velocity and impact angle on the mean length of the stains from droplets impacting different surfaces at different angles. The data has been averaged at each height and the error bars represent standard error. 159

5.20 The effect of the Bond number and impact angle on the mean length of the stains from droplets impacting different surfaces at different angles. The data has been averaged at each height and the error bars represent standard error. . . 160

6.1 A comparison of spread factors against experimental data using the Reynolds number: Cheng [1977] (Equation 6.15), Chandra and Avedisian [1991] (Equation 2.63), Hulse-Smith et al. [2005] (Equation 6.18), Pasandideh-Fard et al. [1996] (Equation 2.64), and Murray (Equation 6.13). 174

6.2 A comparison of spread factors against experimental data using the Weber number: Cheng [1977] (Equation 6.15), Chandra and Avedisian [1991] (Equation 2.63), Hulse-Smith et al. [2005] (Equation 6.18), Pasandideh-Fard et al. [1996] (Equation 2.64), and Murray (Equation 6.13). 175

6.3 A comparison of spread factors against experimental data using the Reynolds number: Cheng [1977] (Equation 6.15), Hulse-Smith et al. [2005] (Equation 6.18), Pasandideh-Fard et al. [1996] (Equation 2.64), and Murray (Equation 6.13). 176

6.4 A comparison of spread factors against experimental data using the Weber number: Cheng [1977] (Equation 6.15), Hulse-Smith et al. [2005] (Equation 6.18), Pasandideh-Fard et al. [1996] (Equation 2.64), and Murray (Equation 6.13). . . 176

6.5 Comparing Equation 6.13 (Murray) to the experimental spread factors over impact velocity. 177

6.6 Comparing Equation 6.13 (Murray) to the experimental spread factors over impact angle. 177

6.7 Comparing Equation 6.19 (Murray) to the experimental spread factors over impact velocity. This spread factor model includes the adjustment coefficient. . 178

6.8 Comparing Equation 6.19 (Murray) to the experimental spread factors over impact angle. This spread factor model includes the adjustment coefficient. . . 178

6.9 A comparison of spread factors against experimental data using the Reynolds number: Cheng [1977] (Equation 6.15), Hulse-Smith et al. [2005] (Equation 6.18), Pasandideh-Fard et al. [1996] (Equation 2.64), and Murray (Equation 6.19) with the adjustment coefficient added. 179

6.10 A comparison of spread factors against experimental data using the Weber number: Cheng [1977] (Equation 6.15), Hulse-Smith et al. [2005] (Equation 6.18), Pasandideh-Fard et al. [1996] (Equation 2.64), and Murray (Equation 6.19) with the adjustment coefficient added. 179

6.11 A comparison of all spread factor models against the experimental spread factor. 180

6.12 The lines of best fit for each model, and their R^2 values, compared against the experimental factor. 180

F.1 A comparison of the means of the number of spines on horse bloodstains as counted manually by five participants and counted automatically by the ASC. The circles are the means of each group and the lines are the comparison intervals around each mean. 231

F.2 A comparison of the means of the number of spines on horse bloodstains as counted manually by five participants, counted automatically by the ASC, and as predicted by the models: Knock and Davison [2007], Hulse-Smith et al. [2005], and Mehdizadeh et al. [2004]. The circles are the means of each group and the lines are the comparison intervals around each mean. 232

F.3 A comparison of the means of the number of spines on pig bloodstains as counted manually by Davison [2005], counted automatically by the ASC, and predicted by the model by Knock and Davison [2007]. The circles are the means of each group and the lines are the comparison intervals around each mean. . . 237

F.4 A comparison of the means of the number of spines on pig bloodstains as counted manually by Davison [2005], counted automatically by the ASC, and as predicted by the models: Knock and Davison [2007], Hulse-Smith et al. [2005], and Mehdizadeh et al. [2004]. The circles are the means of each group and the lines are the comparison intervals around each mean. 238

I.1 Bloodstain from a droplet impacting a steel substrate of roughness $R_a = 1.6 \times 10^{-6}$ m at 18°. The droplet's diameter before impact was 4.11×10^{-3} m and its impact velocity was $5.62\,\mathrm{m\,s^{-1}}$. 270

L.1 Edited illustrations (from Engel [1955]) of the cross-sectional area of a droplet spreading along a solid surface after impact, the cross sectional area of a droplet spreading as observed by Worthington [1876]. 277

L.2 Edited illustrations (from Engel [1955]) of the cross-sectional area of a droplet spreading along a solid surface after impact, an assumed shape of the cross section of the spreading of a droplet during impact stated by Engel [1955]. . . . 277

P.1 Droplet spreading with dimensions labeled. 295

Nomenclature

Abbreviations

ASC Automated Spine Counter

BPA Bloodstain Pattern Analysis

CSI Crime Scene Investigator

DVVP Diameter and Velocity Video Processor

HVIS High Velocity Impact Spatters

LVIS Low Velocity Impact Spatters

MVIS Medium Velocity Impact Spatters

SI International System of Units (abbreviated from French "Le Système international d'unités")

SLGR Straight Line Geometric Reconstruction

SWGSTAIN Scientific Working Group on Bloodstain Pattern Analysis

Definitions

p-value: Most statistical tests output a *p*-value which indicates if the null hypothesis should be accepted or not. It's a measurement of how significant results are. Small *p*-values (≤ 0.05) indicate there is strong evidence against the null hypothesis. Large *p*-values (> 0.05) indicate there is weak evidence against the null hypothesis. Other *p*-values ($0.01 \leq p \leq 0.05$) suggests the null hypothesis could be accepted or rejected.

bloodstain pattern: a grouping or distribution of bloodstains that indicates through regular or repetitive form, order, or arrangement the manner in which the pattern was deposited (Scientific Working Group on Bloodstain Pattern Analysis [2013])

bloodstain: a deposit of blood on a surface (Scientific Working Group on Bloodstain Pattern Analysis [2013])

cast-off pattern: a bloodstain pattern resulting from blood drops released from an object due to its motion (Scientific Working Group on Bloodstain Pattern Analysis [2013])

coefficient of variation: shown as CV; the measurement of the variation of data points in a sample.

drip stain: a bloodstain resulting from a falling drop that formed due to gravity (Scientific Working Group on Bloodstain Pattern Analysis [2013], called passive stain or gravitational drop by Wonder [2007])

drip trail: a bloodstain pattern resulting from the movement of a source of drip stains between two points (Scientific Working Group on Bloodstain Pattern Analysis [2013])

edge characteristics: a physical feature of the periphery of a bloodstain (Scientific Working Group on Bloodstain Pattern Analysis [2013])

erythrocyte disaggregation: the spreading out or thinning of red blood cells

hysteresis: phenomenon in which the value of a physical property lags behind changes in the effect causing it

inertial force: a fluid's resistance to motion

Kolmogorov-Smirnov test: The null hypothesis for this test is that the data set comes from a standard normal distribution. In MATLAB, *kstest*, will return a h value (see definition, h) of 1 if the results rejects the null hypothesis, and 0 otherwise.

parent stain: a bloodstain from which a satellite stain originated (Bevel and Gardner [2001], Scientific Working Group on Bloodstain Pattern Analysis [2013]).

satellite stain: a smaller bloodstain that originated during the formation of the parent stain as a result of blood impacting a surface (Bevel and Gardner [2001], Scientific Working Group on Bloodstain Pattern Analysis [2013]).

shear rate: the gradient of velocity in a flowing material

shear stress: a ratio of the force applied onto a material by the cross-sectional area parallel to the applied force

spines: thin ligament structures that emerges from the raised rim of a droplet spreading, also known as fingers (Kieser et al. [2013])

standard deviation: shown as SD; the measurement of how much variation exists in a set of given values

strain tensor: a tensor describing the deformation of a material or the displacement between particles in a material

stress tensor: a tensor describing the internal forces that particles exert on one another in a continuous material

substrate: a surface upon which a droplet impacts

tensor: a multidimensional array used to describe the relationship between scalars, vectors, or other tensors

viscous force: the rate of change of a fluid's viscosity over time

Variables and Constants

$\tilde{A}$ adhesion tension; $\mathrm{N\,m^{-1}}$

A surface area; $\mathrm{m^2}$

a speed of sound in a fluid; $\mathrm{m\,s^{-1}}$

A_{ac} actual surface area of a substrate; $\mathrm{m^2}$

A_{ASC} full area of a bloodstain as measured by the Automated Spine Counter (Chapter 3); $\mathrm{m^2}$

A_{geo} geometrical surface area of a substrate; $\mathrm{m^2}$

A_{IJ} full area of a bloodstain as measured by *ImageJ*; $\mathrm{m^2}$

$\beta = \frac{d_{\max}}{d_0}$ spread factor; dimensionless

$\beta_{\max}$ maximum spread factor of a droplet; dimensionless

$\mathrm{Bo} = \frac{\rho_l g d_0^2}{\sigma_{lg}}$ Bond number; dimensionless

$\mathrm{Ca} = \frac{\mu_l u_0}{\sigma_{lg}}$ Capillary number; dimensionless

c speed of sound; $\mathrm{m\,s^{-1}}$

CV coefficient of variation; same units as the given data set

$\bar{d} = (d_i + d_j)/2$ average diameter of spread; m

δ boundary layer thickness; m

d diameter; m

$d_0 = \frac{r_0}{2}$ initial diameter of the droplet before impact; m

d_{cap} the spherical cap at the base of a droplet at impact (Pasandideh-Fard et al. [1996]); m

d_{in} inner diameter of final stain as measured by the Automated Spine Counter (not including spines); m

d_{max} maximum extension of the droplet on the surface during impact; m

d_{out} outer diameter of final stain as measured by the Automated Spine Counter (including spines); m

d_f final diameter of the stain; m

d_i minor diameter of the stain or width of a stain; m

d_j major diameter of the stain or length of a stain; m

d_s diameter of the flattened droplet or the diameter of the cylindrical shape the droplet forms during impact; m

$\text{Fr} = \frac{u_0}{\sqrt{g d_0}}$ Froude number; dimensionless

F_d force of drag (or air resistance); N

F_g force of gravity; N

$\dot{\gamma}$ shear rate; s^{-1}

H initial height the droplet has fallen from; m

h hypothesis test result in statistical tests, $h = 1$ indicates a rejection of the null hypothesis, $h = 0$ indicates a failure to reject the null hypothesis.

κ drag coefficient; dimensionless

L length; m

L_{IJ} full length of an elliptical bloodstain as measured by *ImageJ*; m

$\hat{\mu}$ mean of data; same units as the data

$\text{M} = \frac{u_0}{a}$ Mach number; dimensionless

μ dynamic viscosity; Pa s

m mass of a droplet; kg

ν kinematic viscosity; $\text{m}^2\,\text{s}^{-1}$

N number of spines (or fingers) on a bloodstain

$\text{Oh} = \frac{\mu_l}{\sqrt{\rho_l \sigma_{lg} d_0}}$ Ohnesorge number; dimensionless

Ω volume of the boundary layer around a droplet; m^3

P perimeter; m

P_{ASC} perimeter of a stain as measured by the Automated Spine Counter (Chapter 3); m

P_{IJ} perimeter of a stain; m

$Q = \frac{4\pi A}{P^2}$ Isoperimetric Quotient (or circularity); dimensionless

$\mathbb{R}$ ratio of the actual surface area to the geometrical surface area; dimensionless

$\text{Re} = \frac{\rho_l u_0 d_0}{\mu_l}$ Reynolds number; dimensionless

ρ	density; $\mathrm{kg\,m^{-3}}$
r	radius; m
r_0	radius of a droplet before impact; m
R_a	roughness parameter for surfaces; m
r_s	observed radius of the droplet's spread; m
$\hat{\sigma}$	standard deviation; same units as the data
σ_{lg}	surface tension of a fluid or interfacial tension between a liquid and a gas; $\mathrm{N\,m^{-1}}$
σ_{sg}	interfacial tension between a solid and a gas; $\mathrm{N\,m^{-1}}$
σ_{sl}	interfacial tension between a solid and a liquid; $\mathrm{N\,m^{-1}}$
SD	Standard deviation; same units as sample set
τ	shear stress; $\mathrm{N\,m^{-2}}$
θ_{a}	advancing contact angle; rad
θ_f	droplet impact angle on the surface; rad
t	time; s
$t_{\max}$	time it takes for a fluid to reach maximum spread after impact; s
$T_{IJ} = L_{IJ} - d_j$	tail length of an elliptical bloodstain; m
$\tilde{u}_t$	corrected terminal velocity of a droplet according to Wobus et al. [1971]; $\mathrm{m\,s^{-1}}$
u	velocity; $\mathrm{m\,s^{-1}}$
u_0	impact velocity; $\mathrm{m\,s^{-1}}$
u_{edge}	velocity of the fluid at the edge of spreading; $\mathrm{m\,s^{-1}}$
u_f	impact velocity of the droplet on the surface; $\mathrm{m\,s^{-1}}$
u_t	terminal velocity of a droplet; $\mathrm{m\,s^{-1}}$
V	volume of a droplet; $\mathrm{m^3}$
$\mathrm{We} = \frac{\rho_l u_0^2 d_0}{\sigma_{lg}}$	Weber number; dimensionless
x_0	initial x-coordinate of a droplet
x_f	final y-coordinate of a droplet
y_0	initial y-coordinate of a droplet
y_f	final y-coordinate of a droplet
z	splat thickness; m

Chapter 1

Introduction

1.1 Introduction

Bloodstain pattern analysis (BPA) is one of many forensic tools used by crime scene investigators to gather knowledge about what has occurred during a crime. To ensure the correct delivery of justice and to avoid miscarriages of justice, it is imperative that the methodology for analysing bloodstains is accurate. Therefore, the methods must include the relevant scientific laws on the creation of a bloodstain pattern. The forces of gravity and drag on a droplet's trajectory are examples of scientific laws that should be considered in the analysis of a bloodstain. For example, the source of bloodletting can be estimated 2 m higher than the correct source if the forces of gravity and drag are neglected (Buck et al. [2010]). An example of this error, in determining the of the origin of bloodletting, would be BPA leading to the assumption that a victim (from whom the blood is emerging), is standing rather than sitting. Details such as these could be crucial to a conviction in a court of law and is a major reason why scientific laws should be incorporated in BPA methodologies.

An example of a criminal case where BPA was utilised, without accounting for fundamental scientific laws, is the death of Bonnie Horinek, 14 March 1995 (Warren R. Horinek v. The State of Texas [1998]). During this investigation, a qualified bloodstain pattern analyst testified on

the creation of a specific type of stain, without any scientific backing as proof. The events of Bonnie Horinek's death are as follows. After a night of eating and drinking, Bonnie Horinek and her husband Warren Horinek returned to their homes. Warren Horinek claimed that he was in another room when he heard a gunshot and arrived in their bedroom to find Bonnie with a single gunshot wound to her chest. Warren Horinek called 911 and began performing CPR until paramedics arrived and pronounced Bonnie dead. During the investigation there was a large weight of evidence suggesting this was a case of suicide (including gunshot residue on Bonnie's chest from a contact wound, and there were no signs of a struggle). Warren Horinek was found innocent, but Bonnie's parents could not accept this verdict; they proceeded to hire a private investigator and attorney. The case was reopened and the trial, again, showed overwhelming evidence for suicide, until the final expert testimony was delivered. Tom Bevel, well-known in the field of BPA, and author of *Bloodstain Pattern Analysis: With an introduction to crime scene reconstruction* (Bevel and Gardner [2001]), was recruited to the prosecution. He testified to the court that the atomised backspatter pattern (Scientific Working Group on Bloodstain Pattern Analysis [2013]) on Warren Horinek's shirt resulted from a gunshot, and not from administering CPR. Bevel reported that these backspatter patterns indicated, with little doubt, that Warren Horinek shot someone at close range. The jury accepted Bevel's testimony over the other evidence presented in the case, and Warren Horinek was convicted of the murder of Bonnie Horinek. However, there was debate between bloodstain pattern analysts whether the bloodstains on Warren Horinek's shirt were caused by Bonnie exhaling blood during the CPR attempts, or backspatter from the gunshot. Ambiguity in the analysis of these stains could be removed if it accounted for physical forces. How much force is needed to push blood out of an airway during CPR? With what velocities would exhaled blood droplets leave the airways? Could the velocities of those droplets be calculated using sound mathematical expressions dependent on stain properties? At what distance would the shooter need to stand from the victim, in order to receive backspatter patterns? What effect would the material of Warren Horinek's shirt have on the shape and size of the bloodstains?

Another example of scientific laws being ignored in BPA methodologies is seen in the case of the murder of Kersten Kischnick on 25 October 1987 (State of Florida v. Dieter Riechmann [2000]). Her partner, Dieter Riechmann, was indicted with her murder. Riechmann and Kischnick were on holiday in Florida in a rental car. Upon getting lost they stopped to ask directions from a stranger. Riechmann (who was driving) claims that when Kischnick was reaching for money to tip the stranger for his assistance, the stranger shot Kischnick in the right side of her head. In the investigation, a serologist concluded that because there were small bloodstains on the driver's side door, it was impossible that Riechmann could have been sat in the driver's seat at the time. However, the serologist admitted they could not explain why those stains were on the car door. Those stains were not photographed for evidence, and thus no analysis was carried out on their shape or size. Further, the type of surface (of the car door) was not considered. The serologist concluded that Riechmann must have been outside of the car at the time of Kischnick's murder which opposed Riechmann's testimony, implying he was the murderer with insurance money as the motive. Riechmann was convicted of murder and given a death sentence. In 1994, after the conviction, Stuart H. James' report on the case showed the serologist's analysis of the bloodstains to be largely erroneous. James presented a detailed report on his interpretation of the evidence (James et al. [2005]), with the six bloodstains on the driver's side door being the most troubling part of the analysis. The serologist claimed that those bloodstains would not be there if Riechmann was in the driver's seat. Further, the serologist theorised that those bloodstains could have been created by Kischnick exhaling blood over from the passenger side, reaching the driver's side door, because Riechmann was not sat there. James reported that this theory is highly unlikely. The distance of Kischnick's head to the door, the force needed on those droplets to reach the door, the angle of her head required for the droplets (affected by gravity and drag) to exit her airways and strike the door, were all physically implausible. James demonstrated using a simple test, flicking blood, that the six stains could have been produced from any movement of the driver, any object in the vehicle, or even the police or paramedics arriving at the scene. Those six stains, wrongly interpreted

because of BPA methodologies lacking basic physics principles, cost Riechmann at least 25 years on death row.

These are just a few examples of the need for BPA methodologies to be carried out correctly and scientifically. This thesis endeavours to contribute scientifically sound methodologies to the field of BPA.

This thesis will be investigating:

- how the roughness of a surface alters the shape and size of a bloodstain;
- how the impact angle alters the shape and size of a bloodstain;
- a quicker and more accurate method for measuring stain properties; and
- the physics behind the spreading of a droplet on a surface.

1.2 Motivation

In BPA, the purpose of the analysis is to locate the source of bloodletting and if possible, identify the method, or weapon used to cause the bloodletting. This information is extracted from the bloodstains on surfaces; the distribution of the stains, their shapes and sizes, and how large or small the overall bloodstain pattern is. If the information extracted from individual bloodstains is incorrect, the error can be amplified in the analysis of where or how the bloodletting occurred. These errors can be detrimental to the overall view of a case, and ultimately a conviction in court. This research is needed to ensure that the information extracted from bloodstains on certain surfaces is as accurate as possible, in order to avoid unnecessary errors in BPA.

1.3 Contributions

This thesis will contribute to the following areas of:

- automated systems for BPA;
- effect of surface roughness on stain shape and size;
- effect of impact angles of droplets on stain shape and size;

- experimental data sets, using single horse blood droplets, for the purposes of comparing and analysing the shape and size of the stains; and
- fluid dynamics of droplet impacts on different surfaces.

1.4 Aim and objectives

In order to achieve the contributions listed in Section 1.3, experimental work needs to be performed and a model of the droplet impacts needs to be constructed and validated by the experiments.

The aim of this work is to investigate the effect of surface roughness of non-yielding, non-absorbent surfaces, and impact angle, on the shape and size of bloodstains. The objectives of this thesis are:

- to create experiments with single droplet impacts onto different surfaces, at different angles;
- to investigate how surface roughness influences the properties of bloodstains;
- to present a correlation between stain shape or size to surface roughness; and
- to validate the computational models, which are based on the laws of physics, of droplet impacts using the experiments.

1.5 Thesis structure

The structure of this thesis begins with a literature review of properties of: fluid flow for droplets impacts, the roughness of surfaces, the conservation of energy equations for droplets impacting surfaces, and the current methods to find the source of bloodletting, with and without the force of gravity. Following the literature review (Chapter 2), two computational tools developed in this thesis were shown (Chapter 3). These tools were created to expedite the analysis of the bloodstains outputted from the experiments. Next, a description of the experiments performed in this thesis was presented (Chapter 4). Then, the results from the single droplet experiments

were presented, with discussions included (Chapter 5). Following these results, a derivation of a new spread factor equation was shown alongside some other new expressions for calculating impact velocity and droplet diameter (Chapter 6). Finally, a conclusion of the work carried out in this thesis and a list of possible future research questions was outlined (Chapter 7).

Chapter 2

Literature review

The reviewed literature on bloodstain pattern analysis will be presented in this chapter. These topics are: the physical properties of blood; the non-Newtonian properties of blood; the behaviour of blood droplets impacting a substrate; the shape and size of a bloodstain; and the effect of surface roughness on a stain. The terminology used in this literature review will be in accordance with the recommended terminology offered by the Scientific Working Group on Bloodstain Pattern Analysis [2013] (SWGSTAIN).

The literature review has thirteen sections. First, the physical parameters that govern the fluid in these droplets (Section 2.1) and their Newtonian or non-Newtonian nature (Section 2.2). The next section of the literature review deals with how droplets create stains. There, the phases of a droplet impacting a surface will be covered (Section 2.3). Next, the non-yielding, non-absorbent surfaces that the droplets interact with are described, and the roughnesses of these surfaces are investigated: this is discussed in Sections 2.4 and 2.5. Following this, the conservation of energy of a droplet impacting a surface is reviewed. The purpose of this section is to ascertain how far a droplet spreads, which is given by the spread factor. The spread factor is a ratio of the final stain diameter, to the droplet diameter before impact. This is discussed in Sections 2.6 and 2.7. Section 2.8 investigates the evolution of spines during the spreading of a droplet on a substrate. Sections 2.9 and 2.10 then present the maths behind calculating the terminal velocity

of a droplet, and using stain properties to find the impact velocity of a droplet, and initial droplet diameter. After, the current methods used in BPA to find the source of bloodletting and the errors associated to those methods are introduced (Section 2.11). Since the current methods in BPA neglect the forces of gravity and drag, there are large errors (specifically in estimating the height of bloodletting). These shortcomings of current BPA methods are outlined in Section 2.12. This inclusion of gravity and drag results in the need to know a droplets initial velocity and initial diameter (Section 2.12). Lastly, possible fluid substitutes that can be used in lieu of blood are reviewed in Section 2.13.

2.1 Physics parameters and relevant numbers

The density, ρ, the dynamic viscosity, μ, the kinematic viscosity, ν, and the surface tension, σ, of a fluid, are important properties to consider when looking at the dynamics of a fluid (White [1999]). These quantities are used often in the calculations of dimensionless numbers (describing fluid behaviour) and the forces acting upon the fluid. This is expanded further throughout this section.

The density of a fluid (measured in $\mathrm{kg\,m^{-3}}$), ρ, is (Acheson [1990]):

$$\rho = \frac{m}{V}, \tag{2.1}$$

where m (measured in kg) is the mass of a droplet and V is the volume (measured in $\mathrm{m^3}$). A droplet is assumed to be a sphere, therefore its volume is:

$$V = \frac{\pi}{6} d_0^3, \tag{2.2}$$

where d_0 is the diameter of the droplet (measured in m). Measuring the mass of a droplet is not trivial but it can be estimated by using the density of the fluid (which is either known or can be measured) and the volume of a sphere (Equation 2.2). Rearranging Equation 2.1 for mass gives:

$$m = \frac{\pi}{6}\rho d_0^3 . \tag{2.3}$$

There are two types of viscosity: dynamic, μ, and kinematic, ν. Dynamic viscosity (measured in $\mathrm{N\,s\,m^{-2}}$), is the fluid's resistance to flow under an applied force and is also known as the coefficient of viscosity or absolute viscosity. Dynamic viscosity is described by the ratio of the shear stress, τ, to the shear rate, $\dot{\gamma}$ (Acheson [1990]):

$$\mu = \frac{\tau}{\dot{\gamma}}, \tag{2.4}$$

where shear stress (measured in $\mathrm{N\,m^{-2}}$) is the force applied to a fluid compared to the cross-sectional area upon which the force is being applied, and the shear rate (measured in $\mathrm{s^{-1}}$) is the gradient of velocity of the fluid.

Kinematic viscosity (measured in $\mathrm{m^2\,s^{-1}}$), is described as the diffusivity of momentum of the fluid and is mathematically represented as the ratio of the dynamic viscosity, to the fluid's density, as shown by the following expression (Acheson [1990]):

$$\nu = \frac{\mu}{\rho} . \tag{2.5}$$

In this thesis, the dynamic viscosity is principally used. The surface tension, σ, (measured in $\mathrm{N\,m^{-1}}$) is the force along a droplet's boundary which encourages the droplet to stay spherical in shape (Sherman [1990]).

2.1.1 Dimensionless numbers

Capillary number

The capillary number (Ca) is a ratio of viscous and surface tension forces, acting between a liquid and a gas (Li [2008]). In the case of this thesis, this is between the droplet and the air. The capillary number is expressed mathematically as (Saylor and Bounds [2012]) :

$$\mathrm{Ca} = \frac{\mu_l u_0}{\sigma_{lg}}, \tag{2.6}$$

where μ_l is the dynamic viscosity of the droplet, u_0 is the impact velocity of the droplet, and σ_{lg} is the surface tension (measured in $\mathrm{N\,m^{-1}}$) of the droplet. A small capillary number indicates high surface tension forces, whereas a large capillary number indicates high viscous forces. In general, a low capillary number is less than 10^{-5} (Ding and Kantzas [2007]).

Reynolds number

The Reynolds number (Re) is a dimensionless number. It is the ratio of inertia forces to viscous forces in a fluid and is used to characterise a fluid's flow behaviour (Acheson [1990]; Batchelor [2000]). When the viscous force is dominant, the flow is laminar or smooth, and the Reynolds number is low. When the inertia force is dominant, the flow is turbulent, and the Reynolds number is high.

The expression for the Reynolds number is (Li [2008]):

$$\mathrm{Re} = \frac{\rho U L}{\mu}, \tag{2.7}$$

where ρ is density, U is a characteristic velocity, L is a characteristic length, and μ is the dynamic viscosity. It should be stated clearly what the Reynolds number is being used to describe. For example, in literature regarding the flight of a droplet through the air, where the droplet is assumed to be a solid system, the Reynolds number has been used to describe the flow around a solid sphere moving through the air. There, the Reynolds number uses the following variables (Murray [2012]):

$$\mathrm{Re}_1 = \frac{\rho_g d_0 u}{\mu_g}, \tag{2.8}$$

where d_0 is the droplet diameter before impact, u is the flight velocity of the droplet, ρ_g is the density of the gas the droplet is moving through (the air), and μ_g is the dynamic viscosity of the

gas the droplet is moving through (the air). The droplet diameter before impact and the velocity of the droplet falling from an initial height H are shown in Figure 2.1, which depicts a vertical impact onto a surface. The Reynolds number in Equation 2.8 was used to describe the droplet before impact.

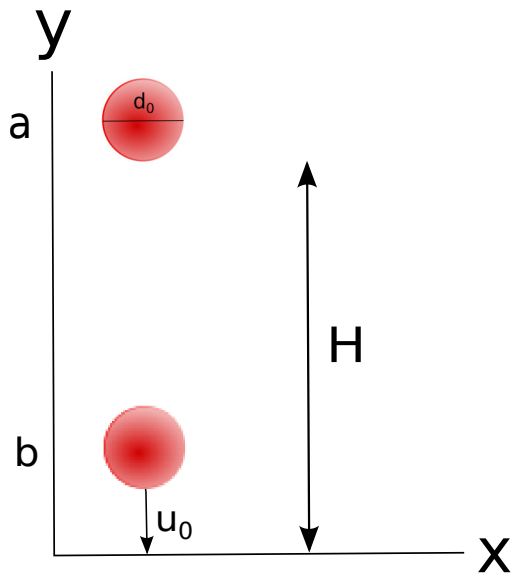

Figure 2.1: Illustration of a droplet's diameter, d_0, before impact (in part a) and droplet's impact velocity (in part b), u_0, as well as the height from which the droplet has fallen from, H. The droplet is falling vertically down in the negative y direction, heading for impact onto a surface on the x plane.

Another Reynolds number is used to describe the flow of the droplet during impact. This resembles the flow in an open channel because of the free surface nature of the droplets impact (*i.e.*, the droplet is not confined to a closed pipe). The droplet has two boundaries, one interacting with the substrate and the other interacting with the air which is the free surface.

In this case the Reynolds number is defined as:

$$\mathrm{Re}_2 = \frac{\rho_l d_0 u_0}{\mu_l}, \tag{2.9}$$

where d_0 is the droplet diameter, u_0 is the velocity of the droplet, ρ_l is the density of the droplet, and μ_l is the dynamic viscosity of the droplet. The droplet's diameter and velocity changes during impact but at the very first instant of impact, the Reynolds number uses d_0 and u_0. The

flow of the spreading of a droplet across a surface is similar to the flow of a free stream fluid along a plate. This type of flow will reach a critical Reynolds number at 5×10^5 (Holman [2010]; Bergman et al. [2011]). In the range $5 \times 10^5 < \mathrm{Re}_2 < 5 \times 10^6$ the flow transitions from laminar to turbulent. This thesis does not focus on the droplet during flight, but rather the interaction of the droplet with the substrate. Therefore, the only Reynolds number used in this thesis will be Equation 2.9 and it will be written as Re for the rest of this thesis.

Weber number

The Weber number (We) is a dimensionless number used to analyse fluid flows where there are two different fluids interacting. Physically, the Weber number is a measure of the fluid's inertia compared to its surface tension. The Weber number is (Li [2008]):

$$\mathrm{We} = \frac{\rho U^2 L}{\sigma}, \tag{2.10}$$

where ρ is density, U is a characteristic velocity, L is a characteristic length, and σ is the surface tension of the fluid which is defined as the propensity a fluid has to resist an external force. The Weber number can be derived by multiplying the Reynolds number (Equation 2.9) by the capillary number (Equation 2.6):

$$\begin{aligned} \mathrm{We} &= \mathrm{Re} \times \mathrm{Ca} \\ &= \frac{\rho_l d_0 u_0}{\mu_l} \left(\frac{\mu_l u_0}{\sigma_{lg}} \right) \\ &= \frac{\rho_l u_0^2 d_0}{\sigma_{lg}}, \end{aligned} \tag{2.11}$$

where d_0 is the droplet diameter, u_0 is velocity of the droplet, ρ_l is the density of the droplet, and σ_{lg} is the surface tension of the droplet. Surface tension attempts to minimise a droplet's surface area and retain a droplet's shape, which results in a spherical shape for small droplets (Sirignano

[1999]). The Weber number can be used to describe when a droplet will become prone to breaking apart. Sirignano [1999] states that at We = 5, the droplet will begin experiencing aerodynamic forces, then at a critical range of Weber numbers ($10 < \text{We} < 20$) the droplet will begin to deform. Weber numbers above this critical range will cause the droplet to rip away from the surface it is spreading along, causing satellite drops or spines (Sirignano [1999]). Both the Reynolds number and the Weber number are often used to calculate properties of bloodstains (*e.g.* the total energy and spreading of an impacting droplet) which will be discussed in Section 2.6.

Bond number

The Bond number, Bo, (also known as the Eötvös number) is a measure of body forces versus surface tension forces (Sirignano [1999]). In this thesis, the body forces are gravitational forces and hence (Sirignano [1999]):

$$\text{Bo} = \frac{\rho_l g d_0^2}{\sigma_{lg}}, \tag{2.12}$$

where d_0 is the droplet diameter, ρ_l is the density of the droplet, and σ_{lg} is the surface tension of the droplet. When the surface tension dominates, it yields a low Bond number which is typically less than 1. There is a critical Bond number at Bo = 11.22 (Harper et al. [1972], Sirignano [1999]). Above this critical Bond number, surface waves in the fluid begin to cause disturbances in the flow. The Bond number is used alongside the Weber number to describe droplet breakup and both are used together to derive the Froude number.

Froude number

The Froude number (Fr), another dimensionless number, is the ratio between the characteristic velocity of a fluid and the gravitational wave velocity (*i.e.*, inertia and gravitational forces on a droplet). Gravity waves occur when:

- two layers or interfaces of a single gas or fluid interact with each other; or

- when two different media, interact with each other;

and the restoring force of this interaction is gravity. For blood droplets spreading along a surface, the liquid is interacting with the air. Later in this literature review (Section 2.8), this interaction between a liquid and the air will be described using the Rayleigh-Taylor instability, which in theory causes spines on stains.

The Froude number is a ratio of the Weber number (Equation 2.11) and the Bond number (Equation 2.12) (White [1999]; Li [2008]):

$$\begin{aligned} \mathrm{Fr} &= \frac{\mathrm{We}}{\mathrm{Bo}} \\ &= \frac{\rho_l u_0^2 d_0}{\sigma_{lg}} \left(\frac{\sigma_{lg}}{\rho_l g d_0^2} \right) \\ &= \frac{u_0^2}{g d_0} \end{aligned} \tag{2.13}$$

where g is the acceleration due to gravity. The Froude number describes the performance of a hydraulic jump in a fluid. A hydraulic jump is the phenomenon where a flow of high velocity spills into a flow of low velocity (White [1999]). The Froude number can also be written as:

$$\hat{\mathrm{Fr}} = \frac{u_0}{\sqrt{g d_0}}, \tag{2.14}$$

which is the square root of Equation 2.13 and it is in this form that the following classifications are made. In general, according to White [1999], a fluid flow with $\hat{\mathrm{Fr}} < 1$ is considered subcritical (and a hydraulic jump is impossible) and a flow with $\hat{\mathrm{Fr}} > 1$ is deemed supercritical (Acheson [1990]). Finally, $\hat{\mathrm{Fr}} = 1$ is critical flow. This Froude number is only relevant to free-surface flows, like blood droplets impacting a surface. It is unclear why some fields of study use Equation 2.13 or Equation 2.14. This thesis will use Equation 2.14 in order to describe the droplet's flow using the classifications listed above.

Mach number

The Mach number (M) is (White [1999]):

$$\mathrm{M} = \frac{u_0}{a}, \tag{2.15}$$

and is the ratio of the speed of an object to the speed of sound in the fluid, a. It is accepted that flows are incompressible if they have a velocity lower than $100\,\mathrm{m\,s^{-1}}$ and thus a small Mach number of $\mathrm{M} \leq 0.3$ (White [1999]). Similar to the Froude number, the Mach number has ranges describing flow regimes: $\mathrm{M} > 1$ is supersonic, $\mathrm{M} = 1$ is sonic, $\mathrm{M} < 1$ is subsonic (White [1999]).

Ohnesorge number

The Ohnesorge number is the ratio of the viscous forces in a fluid to the inertia and surface tension forces *i.e.* the relationship between the Weber number (Equation 2.11) and the Reynolds number (Equation 2.9) (Li [2008]):

$$\begin{aligned} \mathrm{Oh} &= \frac{\sqrt{\mathrm{We}}}{\mathrm{Re}} \\ &= \sqrt{\frac{\rho_l u_0^2 d_0}{\sigma_{lg}}} \left(\frac{\mu_l}{\rho_l d_0 u_0} \right) \\ &= \frac{\mu_l}{\sqrt{\rho_l \sigma_{lg} d_0}}, \end{aligned} \tag{2.16}$$

where μ_l, ρ_l, σ_{lg}, are the dynamic viscosity, density, and surface tension of the droplet, respectively, and d_0 is the diameter of the droplet before impact. The Ohnesorge number is an indication of a fluid's ability to form a droplet. Lower Ohnesorge numbers indicate higher surface tension forces, which promotes the formation of a droplet. Higher Ohnesorge numbers indicate higher viscous forces, which promotes dissipation rather than droplet formation.

Isoperimetric Quotient

Lastly, in order to describe how circular the stains are, the dimensionless isoperimetric quotient (also known as the circularity) is used (Croft et al. [1991]):

$$Q = \frac{4\pi A}{P^2}, \tag{2.17}$$

where A is the area of the stain and P is the perimeter of the stain. For a perfect circle, Equation 2.17 is one therefore less circular objects will yield a Q less than one.

2.2 Properties of non-Newtonian fluids

The distinction between Newtonian and non-Newtonian fluids is made mathematically in the relationship between the dynamic viscosity and the shear rate or deformation of the fluids (Kabaliuk et al. [2014]). In both cases, either Newtonian or non-Newtonian fluid, the viscosity can be a function of pressure and temperature. Newtonian fluids, such as water, have a linear relationship with shear rate (Ahmed et al. [2013]) whereas non-Newtonian fluids, such as blood have a shear-thinning behaviour which leads to a non-linear relationship between dynamic viscosity and shear rate. The motion of a fluid is given by the Navier-Stokes equations (Batchelor [2000]). The standard form is:

$$\rho_l \left(\frac{\partial \mathbf{u}}{\partial t} + \mathbf{u} \cdot \nabla \mathbf{u} \right) = -\nabla p + \nabla \cdot \tau + \mathbf{q}, \tag{2.18}$$

where ρ_l is the density of the fluid, $\mathbf{u}$ is the velocity of the fluid, ∇ is the del operator (see Equation S.1), p is the pressure, and $\mathbf{q}$ represents any external forces acting upon the fluid (*e.g.*, gravity).

The divergence of the stress tensor, $\nabla \cdot \tau$ in Equation 2.18 is commonly known as the viscous term because of its relationship to the viscosity of the fluid (Appendix S, Equation 2.4). Similarly, $\rho \mathbf{u} \cdot \nabla \mathbf{u}$ in Equation 2.18 is commonly referred to as the inertia term because it

emerges from the conservation of momentum, when deriving the Navier-Stokes equations. The Reynolds number, Re, described by Equation 2.9, is the ratio of these inertia and viscous terms. The inertia term is also seen in the Weber number (Equation 2.11).

2.3 Phases of an impacting droplet and resulting properties of the stain

At a crime scene, different bloodstains will have different properties. These properties are relevant in the analysis of that bloodstain as they give an indication as to how the stain was formed. A bloodstain is defined to be a single instance of blood on a substrate and a bloodstain pattern is an accumulation of bloodstains in a form that gives an indication of how the blood droplets impacted that surface (Scientific Working Group on Bloodstain Pattern Analysis [2013]). Therefore, as few as two stains would form a bloodstain pattern.

Bevel and Gardner [2001] described the dynamics of a droplet impacting a surface in four stages (as shown in Figure 2.2):

1. contact/collapse: the first moment a droplet touches a substrate, the substrate will cause the droplet to begin deforming from an assumed sphere into a spherical cap;
2. displacement: the phase where the droplet first begins spreading along the surface, and is normally in a cylindrical shape at this point (where the base of the cylinder is parallel to the surface);
3. dispersion: the moment were any part of the droplet with enough energy will begin to lift off from the surface; and
4. retraction: the last phase, where satellite droplets will disconnect from the parent stain to form satellite stains and the parent stain (responding to the separation of the satellite drops) will cave inwards.

The stain shape and overall size is affected by the angle of impact, as shown in the columns of Figure 2.2. A decrease in impact angle changes the bloodstain from a circular shape to a

more elliptical shape.

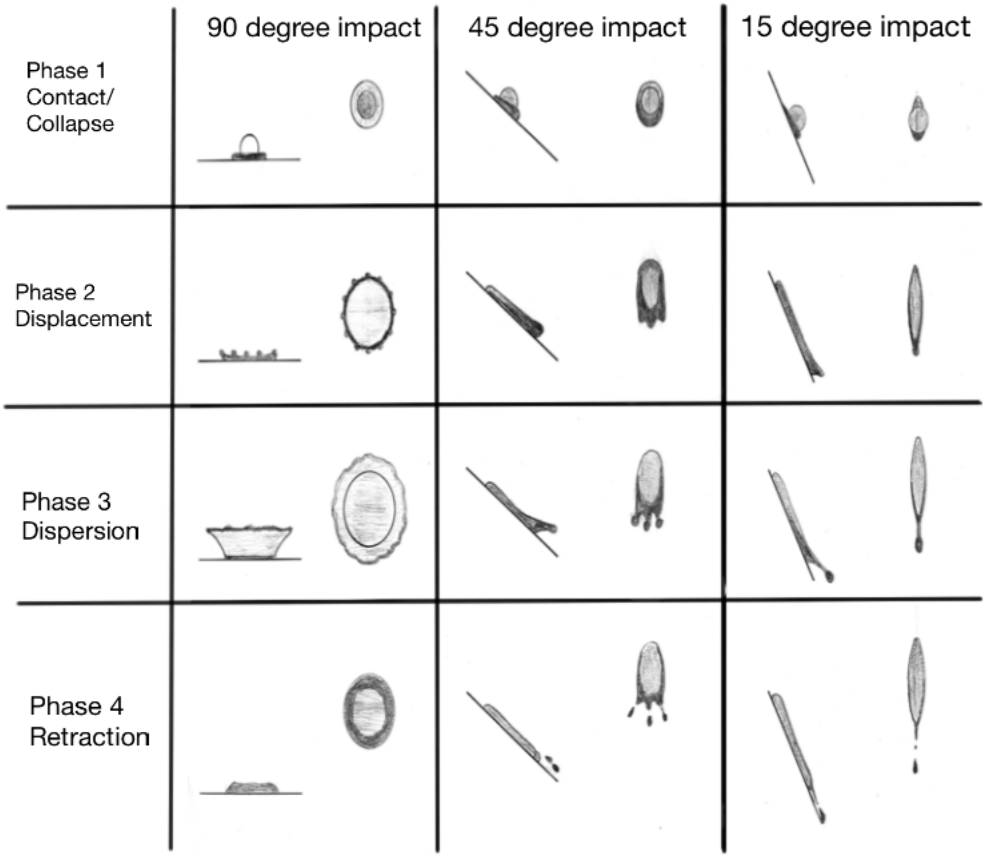

Figure 2.2: An edited depiction of the four phases of impact as they occur in varying angles of impact (Bevel and Gardner [2001]). In each box, the drawing on the left shows a side view of the droplet impact. The drawing on the right depicts an over head view.

A droplet approaching a substrate will be spherical because of the surface tension forces (Sirignano [1999]). Therefore most computational models assume the droplet to be a sphere before impact (Engel [1955]; Stow and Hadfield [1981]; Rein [1993]; Murray [2012]).

The droplet will make contact with the surface and begin to collapse, starting with the portion of the droplet that is touching the surface. This is the first phase: contact/collapse.

During the collapse, some of the droplet's mass will be forced outward to form a ring (see phase 1 of Figure 2.2). Depending on the angle of impact and the amount of energy with which the droplet is impacting the surface, the mass of the droplet will either be forced outward in all directions equally (for perpendicular impacts), or in favour of the direction of travel (for more

acute angled impacts).

In the displacement phase (phase 2), the mass of the droplet that is pushing outward along the surface is nearly at its maximum extension (see the second row in Figure 2.2). The droplet has not begun forming spines at this point (if there is indeed enough energy in the impact). A spine is defined to be a thin ligament that extends off the main body of a bloodstain (Scientific Working Group on Bloodstain Pattern Analysis [2013]). However, the droplet has completely collapsed, and the rim of the droplet is ending its lateral movement and is preparing to move in an upward direction.

The third phase of impact is the dispersion phase which is also known as the crown or blossom effect (see the third row in Figure 2.2). The droplet becomes unstable at this point as the rim is moving upwards (opposing the direction of original momentum). This instability is caused by the initial impact to a surface. Since the droplet is not 'cushioned' into the surface and is simply 'crashing' into the surface, the droplet will move abruptly from its spherical shape, to a crown, then to a shape that is not necessarily constant. In this phase the surface tension is trying to retain the shape of the droplet, while the mass of the droplet in the rim is trying to disconnect from the main body. If the force of inertia overcomes the surface tension, that mass of the extending droplet will break off the main droplet and create satellite drops. Satellite drops are droplets that form smaller bloodstains outside the main body of the parent bloodstain. They are not connected to the main bloodstain. If there is not enough energy for the small masses to disconnect from the main parent stain, they will form either spines (for perpendicular impacts) or a tail (acute angle impacts). A tail on a bloodstain is a single long extension that normally occurs on elliptical bloodstains (see Figure 2.3).

The final phase of impact is called the retraction phase (see the fourth row in Figure 2.2). In this phase, any mass of the droplet that has had enough energy to disconnect from the main part of the stain, has done so. The droplet has settled onto the surface and will often retract inwards because of surface tension forces.

Figure 2.4 from Bevel and Gardner [2001] shows droplets (it is not mentioned if they are

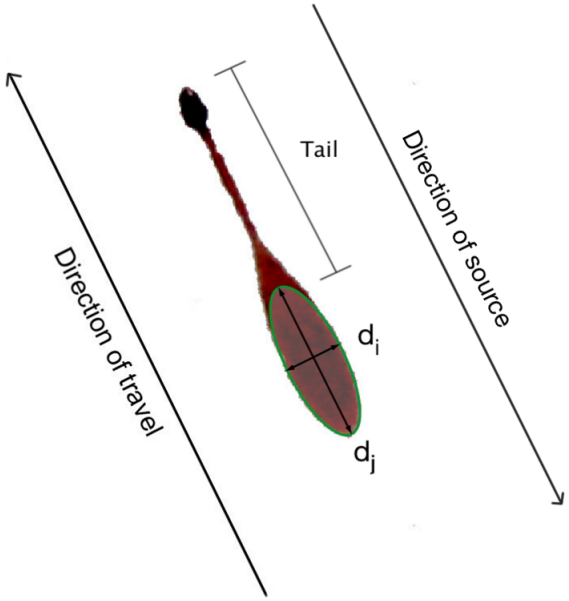

Figure 2.3: An edited depiction (tail of bloodstain is labelled) of classical measuring of bloodstains, where the direction of travel is indicated by the position of the tail of the bloodstain (Maloney and Maloney [2009]). The width of the bloodstain is denoted by d_i and the length of the bloodstain is denoted by d_j.

blood droplets) impacting a surface at different angles and their resulting stains. Acute angles tend to produce elliptical stains with a tail (Figure 2.3) whereas less acute angles, closer to 90°, produce more circular stains with spines. Figure 2.4 also shows a notable change in the shape of the stains when the angle of impact is increased from 40° to 50°. The change from stains exhibiting tails to exhibiting spines occurs in this range of impact angles. This change is also seen in the experiments carried out in this thesis and will be discussed further in Chapter 4. The bloodstain in Figure 2.3 is an illustration of a hypothetical droplet that has impacted the surface at an angle, hence its elliptical shape. The tail of the bloodstain indicates the direction of travel.

All of the bloodstains in this thesis are classified as drip stains which are defined by the Scientific Working Group on Bloodstain Pattern Analysis [2013] as bloodstains " . . . resulting from a falling drop that formed due to gravity". These stains are not to be confused with drip patterns, which are defined as a pattern formed when blood drips into another liquid (Bevel and Gardner [2001]) or more generally, a pattern formed when a liquid drips into another liquid, one of which being blood (Scientific Working Group on Bloodstain Pattern Analysis [2013]).

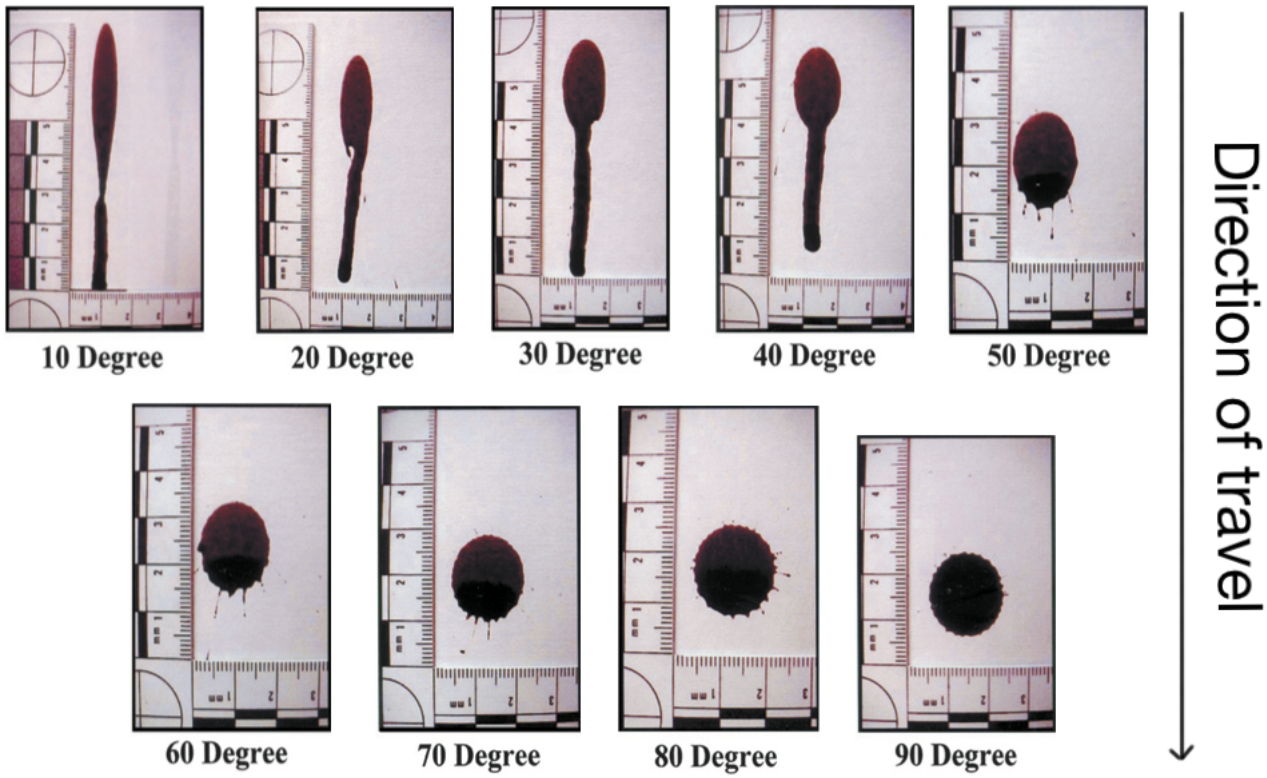

Figure 2.4: The range of stain shapes that result from the varying impact angles (Bevel and Gardner [2001]). More acute angles of impact result in elliptical stains, while more perpendicular angles of impact result in round stains. This figure has been edited to indicate the direction of travel of the droplets.

MacDonell [1993] defined a drip pattern more specifically as being a resulting stain from blood dripping into blood.

Spines are in general not very well defined. Definitions of spines in the literature include:

- "The pointed edge characteristics that radiate away from the centre of a bloodstain. Their formation depends upon impact velocity and surface texture." – MacDonell [1993]
- "Linear characteristics evident in both single-drop stains and volume stains " – Bevel and Gardner [2001]
- "Spines are the pointed-edge characteristics of a bloodstain that radiate away from the central area of the stain." – James et al. [2005]
- "When a droplet impacts a surface, thin ligament structures that are formed after a raised rim or crown has settled." – Kieser et al. [2013]

The Scientific Working Group on Bloodstain Pattern Analysis [2013] does not have a definition for spines.

Most elliptical stains will have a main body of the stain which can be approximated by an ellipse, followed by a tail which indicates directionality (Scientific Working Group on Bloodstain Pattern Analysis [2013]), *i.e.* the direction the droplet was traveling before impact (much like an arrow).

The width, d_i, and length, d_j, of a bloodstain (see Figure 2.3) is measured to calculate the angle of impact. Research by Balthazard et al. [1939] has shown that the angle of impact is approximately given by:

$$\sin\theta_f = \frac{d_i}{d_j}, \tag{2.19}$$

where θ_f is the impact angle.

In the literature there are three recognised types of impact spatters: low velocity impact spatter (LVIS), medium velocity impact spatter (MVIS), and high velocity impact spatter (HVIS). The velocities that characterise these impact spatters are the velocities of the wounding agent, not the blood droplets in flight (Bevel and Gardner [2001]). The velocities of the wounding agents resulting in a LVIS, MVIS, and HVIS, are approximately $1.5\,\mathrm{m\,s^{-1}}$ or less, from $1.5\,\mathrm{m\,s^{-1}}$ to $7.6\,\mathrm{m\,s^{-1}}$, and over $30.5\,\mathrm{m\,s^{-1}}$, respectively (Bevel and Gardner [2001]; Wonder [2001]; Maloney and Maloney [2009]; James et al. [2005]). It should be noted that these ranges are very approximate and missing a definition for the range $7.6\,\mathrm{m\,s^{-1}}$ to $30.5\,\mathrm{m\,s^{-1}}$. The diameter of droplets creating a LVIS are 4×10^{-3} m or larger, MVIS is from 1×10^{-3} m to 4×10^{-3} m, and finally a HVIS is smaller than 1×10^{-3} m (James et al. [2005]). LVIS patterns tend to be passive drops pulled under the force of gravity, for example, the blood dripping off the tip of a weapon. MVIS patterns tend to be identified with beating or bludgeoning bloodstain patterns, while HVIS patterns are associated with bloodletting events caused by gunshots (Wonder [2007]). These classifications are no longer used in BPA as they do not help clarify the type of bloodstain.

2.3.1 Assumptions concerning droplet impacts on surfaces

Physical analysis of any kind of droplet impacting any kind of surface can be applicable to BPA because of the diversity of surfaces found in a crime scene. Work on understanding the behaviour of droplets will be helpful to this field, regardless if the droplets are Newtonian, or non-Newtonian, homogenous, or non-homogenous. For example, Thoroddsen and Sakakibara [1998] looked at water droplets impacting a glass plate and were reportedly successful in creating a visualisation of the spines of a water stain. Thoroddsen and Sakakibara [1998] compared their results to the work done with drops of mercury (Worthington [1876], Worthington [1908]). Mercury was used in these studies because of its higher surface tension and lower kinematic viscosity, resulting in its droplets keeping its spherical shape during the fall toward the surface, while still replicating the Reynolds number of water (Thoroddsen and Sakakibara [1998]). Consequently, the stains will look as ideal as possible because the droplet is not undergoing oscillations or radial contractions (Raymond et al. [1996a]). This is beneficial and easier for modelling the impacts, but is a less realistic depiction of how blood behaves. The purpose of Thoroddsen and Sakakibara [1998]'s research was to observe and visualise the evolution of the spines of a droplet during its impact with the surface. This is will discussed further in Section 2.8. Rein [1993] investigated the use of droplet impacts and recognised its application in the following areas:

- spray coating or painting;
- ink-jet printing;
- erosion of a solid surface from high speed impacts of droplets;
- droplets impacting superheated liquids or heated solid surfaces;
- raindrops; and
- agriculture.

The main purpose of Rein [1993]'s review was to investigate the fluid mechanics of drop impacts, different cases of droplet impacts, and the conditions under which they occur. Some

assumptions that are noted by Rein [1993] are:

- the drops are spherical;
- the liquid is homogenous;
- it is argued that oscillations in the droplet before impact are damped off at the moment of impact (thus not changing the characteristics of impacts on shallow liquids or solid walls); and
- often the impact velocity of a droplet is assumed to be equal to the terminal velocity of that droplet.

However, blood is neither homogenous, nor Newtonian (Section 2.2). Furthermore, the droplets are not spherical when moving through the air because they are being acted upon by the force of gravity and drag which causes radial deviations (Raymond et al. [1996a]). The assumption about the terminal velocity is addressed in Section 2.9. If the droplet is accelerating, more than likely it is falling under the influence of gravity and if the drop height is small it is unlikely that the droplet will reach terminal velocity (Section 2.9). It is possible that air resistance can cause internal circulation and oscillations in a droplet (Rein [1993]). These assumptions may not be detrimental to the study of bloodstain pattern analysis but that is yet to be proven.

2.4 Surface roughness

The investigation of how droplets impact surfaces can be split into two areas of interest. First, how the droplet behaves when it goes from a state of flight to impacting a surface (oscillations and deformations). Second, the type of surface the droplet is impacting, *i.e.*, how the droplet interacts with a surface and how the roughness and absorbency of the surface affects the droplet and the resulting stain. Before looking into literature using rough surfaces in experiments, how surface roughness is measured must be defined.

One way of determining the surface roughness parameter (R_a) is by using an arithmetic

average of the vertical distances (ξ_i) of any point on the surface to the average peak height. The average of the vertical distances is divided by the number of data points measured (n):

$$R_a = \frac{1}{n}\sum_{i=1}^{n} |\xi_i| \,. \tag{2.20}$$

To visualise the vertical distances along a rough surface and the meanline, Figure 2.5 shows an example of six measurements taken on a rough surface.

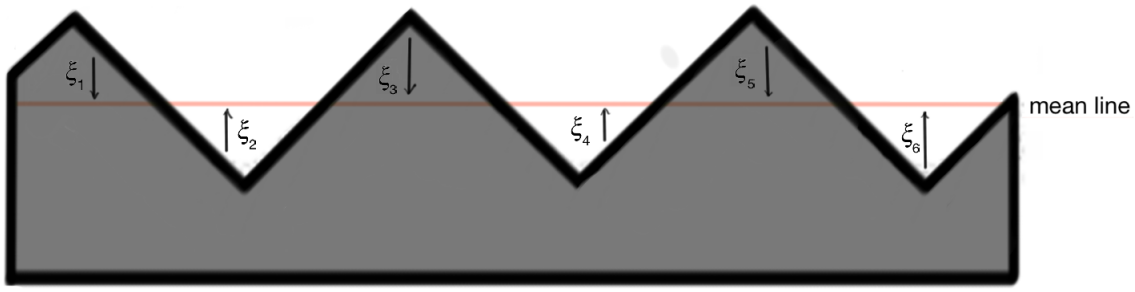

Figure 2.5: Illustration of vertical distances (ξ_i) measured along a rough surface. The measurements are made to the mean line which is indicated in red. In this example $n = 6$, *i.e.*, six measurements are made.

Another way to determine a surface roughness parameter is to use the root mean squared measurement (R_{RMS}):

$$R_{RMS} = \sqrt{\frac{1}{n}\sum_{i=1}^{n} \xi_i^2} \,. \tag{2.21}$$

An unofficial way to measure a surface roughness parameter is to use the ratio of actual surface area (A_{ac}) to geometric surface area (A_{geo}):

$$\mathbb{R} = \frac{A_{ac}}{A_{geo}} \,, \tag{2.22}$$

where the actual surface area (A_{ac}) is best described as a surface's real surface area (accounting for peaks and troughs due to surface roughness). Geometric surface area (A_{geo}) is measured using known formulae for surface area of shapes, but does not account for surface roughness. For example, in this thesis, the surface area of a rectangle is used because the substrates are

rectangular prisms. If a surface is assumed to be completely smooth, the actual surface area and geometric surface area of the interaction are identical. However, with increased surface roughness, the actual surface area will be greater than the geometric surface area. This ratio will be seen again in Equation 2.30.

In work by Stow and Hadfield [1981], the roughness of non-absorbent steel and aluminium surfaces was measured using a Talysurf. This device magnifies the profile of the metal surface and provides a roughness parameter R_a. The radii of the droplets being dripped onto the different surfaces were from 1.1×10^{-3} m to 2.2×10^{-3} m. In some instances a droplet was blown off a fine needle using a pulsed jet of air (producing what is assumed to be a curved trajectory for the droplet) and those droplets had radii from 5×10^{-4} m to 1.1×10^{-3} m. It was noted that the droplets do have oscillations at the time of impact but there seems to be an assumption that the drops can be described as spheres (Stow and Hadfield [1981]). Impacts of droplets traveling faster than the terminal velocity were obtained by moving the target surface up towards the droplet as it fell down toward the surface. The target could move from $1\,\mathrm{m\,s^{-1}}$ to $9\,\mathrm{m\,s^{-1}}$. The resulting impact velocity of the droplet is not noted, but an example of a typical experiment by Stow and Hadfield [1981] include a droplet of radius 1.7×10^{-3} m falling at a velocity of $3.9\,\mathrm{m\,s^{-1}}$ and impacting a target moving upwards at the moment of impact at a velocity of $8.1\,\mathrm{m\,s^{-1}}$. The purpose of the experiments done by Stow and Hadfield [1981] were to provide experimental data for further numerical and analytical models of droplet impacts. However, Stow and Hadfield [1981] noted that the surface tension and viscous drag (in the air) cannot be neglected when looking at this fluid flow. Further, the surface tension and viscous drag are represented by the Weber number and the Reynolds number. The effects of gravity and compressibility are described by the Froude number and the Mach number, all which are defined in Section 2.1. The primary finding of the experiments and analysis by Stow and Hadfield [1981] was that surface roughness promotes the ejection of secondary droplets during impact.

The effect of surface roughness on the size and shape of a bloodstain was also studied by Adam [2013]. The experiments used droplets of human blood from heights of 0.05 m to 2.1 m,

where for each height, five repeats were performed. The experiments using angled impacts were from $\theta_f = 90°$ down to $\theta_f = 20°$ using 10° intervals (angle of impact measured from the y-axis, parallel to the droplet's fall down), again with five repeats. The substrates included matt emulsion paint, vinyl silk emulsion paint, and gloss paint. Adam [2013] found that lower drop heights seemed to not form spines on the bloodstains (for perpendicular impacts) but splash seemed to occur on the matt painted surfaces. The actual value of surface roughness of these substrates are not stated in the work by Adam [2013] but it seems the matt emulsion paint has the higher surface roughness and the gloss paint has the lower surface roughness. Adam [2013] concludes that there is not a lot of difference in stain dimensions when hitting vinyl or gloss painted surfaces but the matt painted surfaces showed a 5 % reduction in stain dimensions (see Figure 2.6). The reduction in relative stain dimensions decreases as the impact velocity decreases.

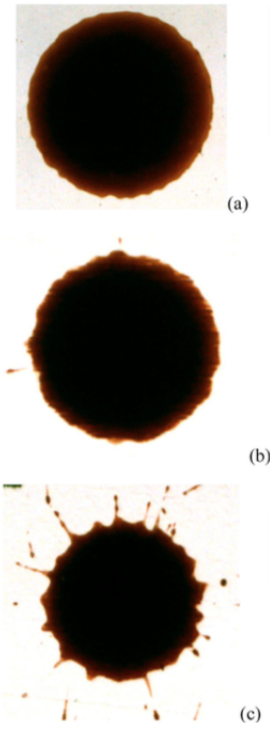

Figure 2.6: Published work by Adam [2013]. Human bloodstains formed from droplets falling from a height of 0.5 m onto (a) gloss paint, (b) vinyl silk paint, and (c) matt paint. The stains have a diameter of approximately 1.5×10^{-2} m. The diameter of the droplets were 4.21×10^{-3} m.

It is important to recognise the effect of surface roughness on the shape of the droplet as it is being forced outward, because surface roughness (and absorbency) will affect the shape and size of a bloodstain. The substrate with a higher roughness will impede the spreading of a droplet (due to friction) more than a substrate with lower roughness. This will change the shape of the bloodstain, and the shape of a bloodstain is used to predict the source of bloodletting. If a crime scene investigator analyses a bloodstain without accounting for the change in shape (due to surface roughness) then the analysis may be incorrect.

2.5 Contact angle

Contact angles are the angles made between the droplet and the surface as it impacts the surface. During the impact the contact angle will change as the droplet interacts with the surface. Figure 2.7 shows the equilibrium contact angle θ_e as the droplet of diameter $d_0 = 2r_0$ begins to interact with the surface.

The equilibrium contact angle is normally only observed when a droplet is placed onto a surface or has settled on a surface (for example, in sessile droplets). This angle (measured from the horizontal axis) is constant (if the droplet is not moving) and is a description of the wettability of a liquid. Wettability is defined as the propensity of a droplet to spread and 'wet' a surface, *i.e.* hydrophobic surfaces will be less wettable than hydrophilic surfaces. Table 2.1 shows a comparison of the wettability of a liquid and the contact angle of a droplet.

Table 2.1: Equilibrium contact angle (θ_e) of a droplet indicating the wettability of a liquid (Carey [1992]).

θ_e	Wettability
0	completely wetting
$0 < \theta_e < 90$	wetting
$90 \leq \theta_e < 180$	non-wetting
180	completely non-wetting

When a fluid is completely wetting it will spread as far as it possibly can, covering as much

surface area as possible. When a liquid is completely non-wetting, the droplet will retain its spherical shape as much as possible. Equilibrium contact angles can be measured by taking still photographs of a droplet, and measuring the angle directly from the photograph (Carey [1992]).

The advancing and receding contact angles occur when a liquid is moving along a surface, or when a surface is moving in a liquid. The advancing contact angle will be formed (in the case of a droplet impacting a surface) as the droplet is compressing and spreading out onto the surface. The receding contact angle is formed when the droplet is retracting (after the maximum extension is reached) and the lamella of the droplet is settling. The receding contact angle is formed in areas where the liquid has already been in contact with the surface. In the case of a droplet impacting a surface at an angle, the advancing contact angle will be at the front edge of the droplet and the receding contact angle at the rear of the droplet, with respect to the direction the droplet is moving. The difference between the advancing contact angle and the receding contact angle is called contact angle hysteresis (Carey [1992], Gao and McCarthy [2006]). A good literature survey of contact angle hysteresis is presented by Eral et al. [2013]. Some theoretical models of contact angle hysteresis are discussed. Establishing the difference between the advancing and receding contact angles is predominately to ascertain the direction the droplet is moving. If the droplet is evaporating then the volume of the droplet is decreasing and the droplet has a receding contact angle. If the droplet is compressing against a surface then the volume of the droplet is pushing outwards on the surface and therefore has an advancing contact angle. If the droplet is sliding down a substrate then it will lead with the advancing contact angle and trail with a receding contact angle.

When the droplet is spherical on impact, its height h_0 will equal its diameter d_0 as shown in Figure 2.7. However, once the droplet begins compressing along the surface, the diameter of the droplet (d_s) will increase as the height of the droplet (h_s) decreases (shown in Figure 2.8). During this phase of the impact, while the droplet is compressing, the diameter of the droplet is larger than the height of the droplet, *i.e.*, $d_s(t) > h_s(t)$. Figure 2.8 also illustrates the spherical cap, $d_{\text{cap}}(t)$, that forms during impact.

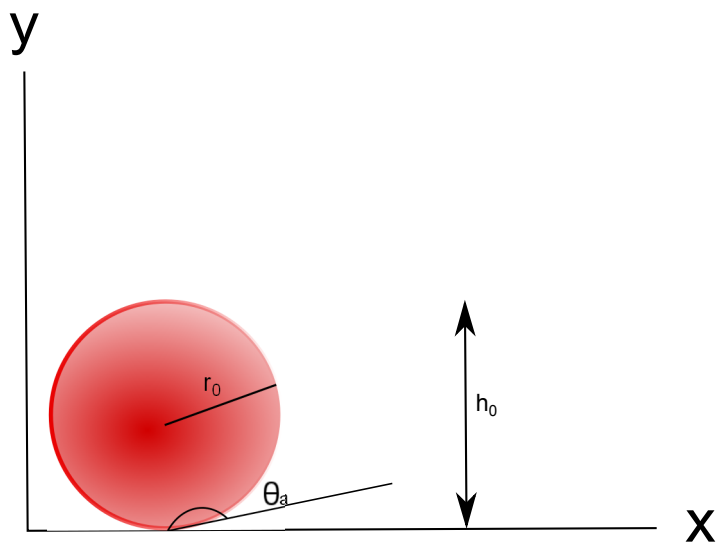

Figure 2.7: Illustration of the advancing contact angle, θ_a, when a droplet of radius r_0, falling in the negative y direction, first impacts a surface along the x plane. The droplet's height, h_0, has not yet begun to compress from impact.

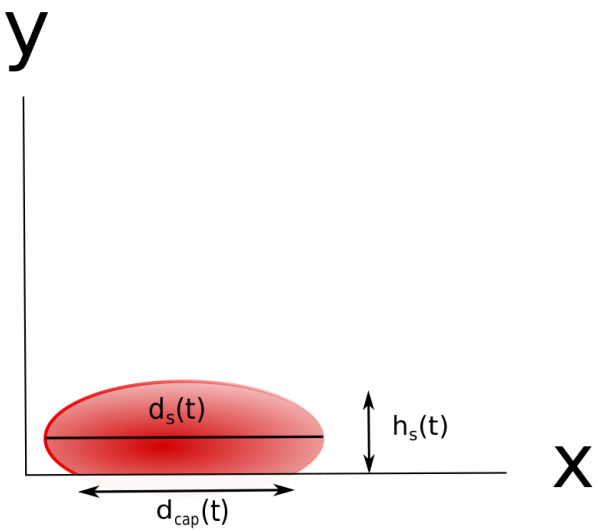

Figure 2.8: Illustration of a droplet during its impact with a surface along the x plane. The droplet is compressing in the y direction, thus its height $h_s(t)$ is decreasing over time. The droplet's diameter is increasing over time during impact and is denoted by $d_s(t)$. The spherical cap changing over time is denoted by $d_{\text{cap}}(t)$.

The contact angle between a liquid and a surface was investigated by Wågberg and Westerlind [2000]. They stated the contact angle should be measured when the droplet has reached equilibrium, but this measurement is only valid if there is negligible to no absorption of the liquid into the surface. The literature does not state how much absorption is negligible. Measuring the

contact angle on paper is difficult because because paper is rough, porous, and non-homogenous. The experimental work in this thesis does not investigate the change of contact angle during impact because the contact angle is difficult to measure. Wågberg and Westerlind [2000] first investigated droplets (water, ethylene glycol, and glycerol) impacting either two-layered sheets or homogenous sheets of pulp (*i.e.*, the same type of fibre was used for the whole sheet). The surface roughness was altered by beating the pulp to different degrees (19° SR being the roughest and 70° SR being the smoothest). In textiles, the units SR refer to the Schopper Riegler test, which is used to indicate how quickly or slowly water can be drained from a pulp, it is a function of the degree of beating of the pulp (Gharenhkhani et al. [2015]). However, there is no indication in the paper as to when a degree of beating is considered to move from 'large scale roughness' to 'small scale roughness'.

In both cases (droplets impacting two-layered sheets or homogenous sheets) there was a large change of contact angle over time. In the case of water impacting the two ply paper, the water droplets always penetrated both papers. From the experiments, Wågberg and Westerlind [2000] found that the change of contact angle over time is different depending on the liquid. To test if the spreading and absorption of a liquid into a surface is controlled by the properties of the liquid, the time of the impact was non-dimensionalised using the surface tension and viscosity of the liquid, and the radius of the droplet. Wågberg and Westerlind [2000] found that plotting the contact angle against the non-dimensionalised time forced the contact angle of different liquids to collapse onto one curve.

Two equations were proposed for calculating the apparent contact angle, the first for "large scale roughness" as described by Wågberg and Westerlind [2000]:

$$\theta_a = \theta_e + \phi_m \,, \tag{2.23}$$

where θ_a is the apparent contact angle, θ_e is the equilibrium contact angle, and ϕ_m is the maximum slope of the roughness on the surface in the advancing direction (Oliver et al. [1980]). Since roughness on a surface is made up of grooves of a certain depth and width, the slopes

are referring to the steepness at which the groove dives downward into the substrate. There is further explanation on surface roughness in Section 2.4. Wågberg and Westerlind [2000] attribute this equation to Shuttleworth and Bailey [1948] who originally wrote Equation 2.23 in two parts, the first part being identical to Equation 2.23:

$$\theta_a = \theta_e + \phi_m \,, \tag{2.24}$$

for when the droplet is spreading on the surface and then the second part:

$$\theta_a = \theta_e - \phi'_m \,, \tag{2.25}$$

for when the droplet is receding and ϕ'_m is the maximum slope of the roughness on the surface in the receding direction (Oliver et al. [1980]). Shuttleworth and Bailey [1948] admit that Equation 2.24 and Equation 2.25 are not applicable when the surface is rough.

The second equation written by Wågberg and Westerlind [2000] (and by Oliver et al. [1980]) was for "small scale roughness" and is called the Wenzel equation:

$$\cos\theta_a = \mathbb{R}\cos\theta_e \,. \tag{2.26}$$

However, the original equation stated by Wenzel [1936] is:

$$\mathbb{R}\tilde{A} = \sigma_{lg}\cos\theta_a \tag{2.27}$$

where $\tilde{A}$ is the adhesion tension, σ_{lg} is the surface tension of the liquid, θ_a is the contact angle, and $\mathbb{R}$ (in Equation 2.26 and Equation 2.27), is the roughness factor which is the ratio of actual surface area (A_{ac}) and geometric surface area (A_{geo}) which are described in Section 2.4. Wenzel [1936] defines the adhesion tension as the product of surface tension and contact angle. This would cause Equation 2.27 to reduce down to $\mathbb{R} = 1$, and it is unclear as to how Equation 2.27 was derived. It is unclear how Wågberg and Westerlind [2000] get from Equation 2.27 to

Equation 2.26.

Marmur [1994] developed a theoretical model, Equation 2.28, for the apparent contact angle which assumes constant interfacial tensions and neglects external fields such as gravity:

$$\cos\theta_a = \frac{\mathbb{R}}{1 - y_s' \tan\theta_a} \cos\theta_Y \tag{2.28}$$

where y_s' is the rate of change of the profile of the solid surface, and $\cos\theta_Y$ is from the Young equation:

$$\cos\theta_Y = \frac{\sigma_{sg} - \sigma_{sl}}{\sigma_{lg}}\,. \tag{2.29}$$

θ_Y is the value of the equilibrium contact angle in the ideal situation where a substrate is smooth, rigid, homogenous, and insoluble, with constant interfacial tensions. In Equation 2.29, σ_{sg} is the interfacial tension between the solid surface and the surrounding fluid (the air), σ_{sl} is the interfacial tension between the solid surface and the liquid (the droplet), and σ_{lg} is the interfacial tension between the droplet and the air. Interfacial tensions hold a phase (solid, liquid, or gas) together. Surface tension is an example of an interfacial tension between a liquid and a gas. Equation 2.28 is a very simple model for the contact angle that would work with surfaces with zero roughness.

Wolansky and Marmur [1999] showed that the Wenzel Equation (as written in Equation 2.26) deviates from the apparent contact angle developed by Marmur [1994] in Equation 2.28 at high values of roughness, but when the roughness decreases as compared to the droplet size, Equation 2.27 and Equation 2.28 come into agreement. It is unclear in their publication how large the droplet needs to be for Equation 2.27 to work. It is also unclear how high the roughness factor needs to be in order for Equation 2.28 to agree with Equation 2.27.

An alternate method of accounting for the surface roughness is given by Carey [1992]:

$$\cos\theta_{rough} = \frac{A_{ac}}{A_{geo}} \cos\theta_Y\,, \tag{2.30}$$

where θ_{rough} is the contact angle on a rough surface, A_{ac} is the actual surface area of a surface, A_{geo} is the geometric surface area. This ratio of the actual surface area to the geometric surface area is just one of a few ways to measure surface roughness. For more details on actual and geometric surface roughness of a substrate see Section 2.4. Later, a version of Equation 2.30 will be used in a derivation of the spread factor (in Chapter 6).

2.6 Energy conservation

When a droplet impacts a substrate, the droplet will obey the laws of conservation of energy. Knowing the amount of energy a droplet has before impact, during impact, and after impact, can help to understand how far a droplet will spread along the surface when forming a stain. The conservation of energy of a droplet impacting a surface, in general, is:

$$E_P + E_K + E_S = E'_P + E'_K + E'_S + E_D\,, \tag{2.31}$$

where E_P, E_K, and E_S are the potential, kinetic, and surface energy of the droplet before impact (respectively). E'_P, E'_K, E'_S are the potential, kinetic, and surface energy of the droplet after impact (respectively). E_D is the energy lost due to the droplet deforming upon impact.

According to Rein [1993], the potential energy (before and after impact) can be neglected because it does not contribute very much to the total energy. The potential energy before impact does not contribute very much to the overall energy because the height before impact of the droplet is taken to be an infinitesimal distance from the surface. The reason for using an infinitesimal distance from the surface rather than the height from which the droplet has fallen, is because the energy studied in this thesis is not the energy of the droplet's flight but rather the energy of the droplet's impact. Also the potential energy after impact will be negligible because the droplet has settled onto the surface at this point and has no height to fall from. Further, there is no kinetic energy once the droplet settles on the surface (and stops moving) thus the kinetic energy after impact vanishes.

The conservation of energy then reduces to:

$$E_K + E_S = E'_S + E_D \,. \tag{2.32}$$

Each energy has its own equation which will be derived in the following sections (supplemented by appropriate appendices). The conservation of energy written by Roisman et al. [2002] includes energy along the contact line E_θ:

$$E_K + E_S = E'_S - E_\theta + E_D \,, \tag{2.33}$$

which is an advancement from the previous models. E_θ is negative in Equation 2.33 because the work along the contact line is impeding the spread of the droplet and so it is energy lost to the surface. The following subsections will present different expressions for each of the energies in Equation 2.33. The energies are sometimes used by the authors to calculate spread factors (Section 2.7) but in some cases the expressions for energy are used for other purposes. The relative magnitude of each energy equation will be discussed when they are compiled together in the spread factors in Section 2.7.

2.6.1 Kinetic energy before impact

The kinetic energy (starting with $E_K = \frac{1}{2}mu^2$) of a droplet before impact, E_K, is (Chandra and Avedisian [1991]; Pasandideh-Fard et al. [1996]; Roisman et al. [2002]; Adam [2012]):

$$E_K = \frac{\pi}{12}\rho_l d_0^3 u_0^2 \,, \tag{2.34}$$

where ρ_l is the density of the droplet, d_0 is the diameter of the droplet before impact and u_0 is the impact speed of the droplet. See Appendix K for the derivation of Equation 2.34.

Alternatively, Engel [1955] has written the kinetic energy of an impacting droplet as:

$$E_K \approx \frac{m}{16}\left(\frac{d_{\max}}{t}\right)^2 \tag{2.35}$$

where m is the mass of the droplet, t is time and $d_{\max}$ is the diameter of the droplet spread (see Appendix L for derivation of Equation 2.35). It is curious that Engel [1955]'s equation for kinetic energy before the droplet impacts the substrate includes a term related to the droplet impacting the surface ($d_{\max}$). The reason for this is because the time t that Engel [1955] used starts with $t = 0$ to be the first point of impact. It is unclear however how the mass of the droplet would be measured, either using the volume of a sphere or the volume of a short cylinder.

2.6.2 Surface energy before impact

The surface energy of a droplet before it impacts a substrate is obtained by taking the surface tension of the droplet against the air (σ_{lg}) and multiplying it by the surface area of the droplet (which is assumed to be spherical). Therefore, the surface energy is (Engel [1955]; Chandra and Avedisian [1991]; Pasandideh-Fard et al. [1996]; Roisman et al. [2002]; Adam [2012]):

$$E_S = \sigma_{lg}\pi d_0^2\,, \tag{2.36}$$

where d_0 is the diameter of the droplet before impact and σ_{lg} is the surface tension of the fluid against the air. See Appendix M for derivation of Equation 2.36.

2.6.3 Surface energy after impact

In the literature, derivations and explanations of the surface energy of the droplet after impact are scarce. The surface energy as written by Engel [1955] is:

$$E_S' = \left(\sigma_{lg} + \sigma_{sl}\right)\frac{\pi}{4}d_{\max}^2\,, \tag{2.37}$$

where σ_{lg} is the surface tension of the fluid and σ_{sl} is the interfacial tension between the fluid and the substrate. In the case of Equation 2.37, σ_{sl} is the interfacial tension between water and the substrate. Engel [1955] performed experiments using water droplets impacting glass substrates. There is no derivation shown for Equation 2.37 by Engel [1955]. The surface tension is broken into two components, one component to account for the fluid interacting with the substrate and the second component to account for the fluid interacting with the air. It is multiplied by the area of a circle which is assumed to be the bottom of a thin cylinder (which is the assumed shape of the droplet when at maximum extension). This assumption, however, is ignoring any edge effects of the surface energy *i.e.* the lateral area of the thin cylinder is ignored. This version of the surface energy after impact does not account for the contact angle (see Section 2.5).

Ford and Furmidge [1967c] write the surface energy after impact as:

$$E'_S = \frac{\pi}{4} d_{\max}^2 \sigma_{lg} \left(1 - \cos\theta_a\right) + \frac{2\pi}{3} \frac{d_0^3}{d_{\max}} \sigma_{lg}\,, \tag{2.38}$$

where θ_a is the advancing contact angle which is the angle made between the substrate and the droplet's edge, as the droplet is spreading outwards onto the substrate (Section 2.5). Ford and Furmidge [1967c] do not show a derivation for Equation 2.38. This expression for surface energy was developed for work in agricultural research (Ford and Furmidge [1967b,a]). This equation is cited by Rein [1993] (in a review of properties of liquid droplet impacts) but is not explained in the review. Equation 2.38 is also cited by Chandra and Avedisian [1991] (investigating n-heptane, *i.e.* fuel, drops of diameter 1.5×10^{-3} m impacting polished stainless steel) and Pasandideh-Fard et al. [1996] (study of water droplets impacting a polished stainless steel surface), but they do not write Equation 2.38 in full, nor do they show a derivation for the expression. Chandra and Avedisian [1991] and Pasandideh-Fard et al. [1996] instead write the surface energy as:

$$E'_S = \frac{\pi}{4} \sigma_{lg} \left(1 - \cos\theta_a\right) d_{\max}^2\,. \tag{2.39}$$

It is possible that the $1-\cos\theta_a$ term can be broken down into the liquid-gas energy (which is similar to the surface energy described in the previous subsection, Equation 2.36) and the liquid-surface energy (which would be similar to the energy along the contact line that is described later in this subsection, Equation 2.44). Further, Stow and Hadfield [1981] write Equation 2.39 as the total final energy of the flattened drop, not just the surface energy after impact. Hence, Stow and Hadfield [1981] have neglected the energy loss due to deformation in their final energy expression. The experiments by Stow and Hadfield [1981] used water droplets impacting stainless steel of known roughness parameters but do not show the use of Equation 2.39.

Roisman et al. [2002] (focused on the development of a theoretical model for the evolution of droplet diameter, compared to experimental data using water and glycerine droplets) write the surface energy after impact using the area of the top of a cylinder ($\frac{\pi}{4}d_{\max}^2$) and the lateral surface area of a cylinder ($\pi d_{\max} h_{\min}$) multiplied by the constant surface tension of the fluid (σ_{lg}):

$$E_S' = \sigma_{lg}\left(\frac{\pi}{4}d_{\max}^2 + \pi d_{\max} h_{\min}\right), \tag{2.40}$$

where $d_{\max}$ is the maximum extension of the droplet on the surface during impact (in this case the width of the assumed cylinder) and $h_{\min}$ is the height of the spread (again, the height of the assumed cylinder). Since the height of the cylinder is very difficult to measure there is an expression that can be used for h_{min} which involves equating the volume of the cylinder (during impact) to the volume of a sphere (droplet before impact). The minimum height of the spread can then be described as (Pasandideh-Fard et al. [1996]):

$$h_{min} = \frac{2d_0^3}{3d_{\max}^2}, \tag{2.41}$$

therefore Equation 2.40 becomes:

$$\begin{aligned} E'_S &= \sigma_{lg}\left(\frac{\pi}{4}d_{\max}^2 + \pi d_{\max} h_{\min}\right) \\ &= \sigma_{lg}\left(\frac{\pi}{4}d_{\max}^2 + \pi d_{\max}\frac{2d_0^3}{3d_{\max}^2}\right) \\ &= \pi\sigma_{lg}\left(\frac{d_{\max}^2}{4} + \frac{2d_0^3}{3d_{\max}}\right). \end{aligned} \tag{2.42}$$

It would be reasonable to use the interfacial forces between the fluid and the air, σ_{lg} for Equation 2.42 because that is the part of the fluid's assumed cylinder shape that is interacting with the air. This assumption is not written by Roisman et al. [2002], nor is there a derivation for Equation 2.42.

Roisman et al. [2002] continue by writing the work done along the contact line of the droplet as the integral taken from the centre of the bottom of the cylinder to the edge of the cylinder ($r_{\max}$). Roisman et al. [2002] included the advancing contact angle, θ_a, as well since it is relevant to work done along the contact line. Roisman et al. [2002] writes the work along the contact line as:

$$\begin{aligned} E_\theta &= \int_0^{r_{\max}} 2\pi r\sigma\cos\theta_a dr \\ &= 2\pi\sigma_{lg}\cos\theta_a\left(\frac{r_{\max}^2}{2}\right) \end{aligned} \tag{2.43}$$

where $r_{\max}$ is the radius of the bottom of the assumed cylinder, which is in contact with the surface and σ_{lg} is the surface tension of the fluid. The final expression for work done along the contact line is:

$$E_\theta = \frac{\pi}{4}d_{\max}^2\sigma_{lg}\cos\theta_a. \tag{2.44}$$

The expressions by Roisman et al. [2002] are not only simple and physically sensible but

this is the most recent publication noting the surface energy of the droplet after impact.

All of these expressions (Equations 2.38, 2.39, and 2.42) are based on a surface tension multiplied by the area of a circle. The assumption here is that the droplet spreading on the surface does so as a perfect circle. In cases where the droplet is spherical and impacting a surface vertically, this is reasonable, however, for angled impacts or impacts that produce spines, this assumption may fail. Another similarity that all these derivations have (all except the equation by Engel [1955], Equation 2.37) is that they all include a dependency on the contact angle. Conversely, Engel [1955]'s model of the surface energy after impact is the only model to include the interfacial tension of the substrate.

2.6.4 Deformation of the droplet

When a droplet impacts a non-yielding surface, it deviates from its spherical shape to a flattened cylinder on the surface. When this occurs, there is a loss of energy due to deformation, E_D. This is also referred to as work done against the droplet due to viscosity. The deformation of a droplet during impact is described by Engel [1955] to be the dissipation of energy integrated over the volume of the droplet, over time. The expression Engel [1955] uses for the energy dissipated, E_D, is (see Appendix N for derivation):

$$E_D = \varpi \int_0^{t_{max}} \frac{d_{\max}^4}{t^3} dt \,, \tag{2.45}$$

where ϖ is a constant with the units $\mathrm{N\,s\,m^{-2}}$ (the same as dynamic viscosity), $d_{\max}$ is the observed diameter of the droplet's spread and t_{max} is the time it takes for the droplet to reach its maximum extension. Unit analysis shows that Equation 2.45 does not yield the units for energy (which are $\mathrm{N\,m}$) it has the units $\mathrm{N\,m^2\,s^{-1}}$ instead.

Chandra and Avedisian [1991] took a different approach in mathematically describing the energy lost due to deformation. They wrote the work done against the droplet due to viscosity, E_D as (see Appendix O for derivation):

$$E_D = \frac{\pi \mu_l u_0 d_0 d_{\max}^2}{4 h_{\min}}, \tag{2.46}$$

where μ_l is the dynamic viscosity of the droplet, u_0 is the impact velocity of the droplet, d_0 is the initial droplet diameter, $d_{\max}$ is the maximum spread of the droplet on the substrate, and $h_{\min}$ is the thickness of the droplet when it is at its maximum extension. Unit analysis shows that Equation 2.46 does yield the units for energy.

Pasandideh-Fard et al. [1996] later stated that the results by Chandra and Avedisian [1991] (using Equation 2.45) overestimated the maximum spread of a droplet by 40%. Therefore, instead of assuming the characteristic length of the spreading droplet is equal to its thickness ($h_{\min}$), Pasandideh-Fard et al. [1996] uses the boundary layer thickness of the liquid on the solid surface. Pasandideh-Fard et al. [1996] writes the deformation as (see Appendix P):

$$E_D = \frac{\pi \rho_l u_0^2 d_0 d_{\max}^2}{3\sqrt{\mathrm{Re}}}. \tag{2.47}$$

Equation 2.47, describing the deformation of a droplet, does yield the units for energy.

Roisman et al. [2002] also had a theory for the dissipation of energy due to viscosity. They made the assumption that most of the dissipation occurs at the bottom of the droplet, when the sphere is compressing into a flat shape upon contact with the substrate (see d_{cap} in Figure P.1). Roisman et al. [2002] write the dissipation (without showing a derivation) as:

$$E_D = \pi \rho_l d_0^3 u_0^2 \bar{e}_D, \tag{2.48}$$

where

$$\bar{e}_D = \frac{1}{\mathrm{Re}} \left(\frac{1}{20 \bar{h}_{min}^3} + \frac{3}{5 \bar{h}_{min}} \right). \tag{2.49}$$

According to Roisman et al. [2002], $\bar{h}_{min}$ is the dimensionless thickness of the spread and can be written as $\frac{h_{min}}{d_0}$. Using that ratio and substituting Equation 2.49 into Equation 2.48:

$$E_D = \pi \rho_l d_0^3 u_0^2 \bar{e}_D \tag{2.50}$$

$$E_D = \pi \rho_l d_0^3 u_0^2 \left[\frac{1}{\mathrm{Re}} \left(\frac{1}{20 \bar{h}_{min}^3} + \frac{3}{5 \bar{h}_{min}} \right) \right] \tag{2.51}$$

$$E_D = \pi \rho_l d_0^3 u_0^2 \frac{\sigma_{lg}}{\sigma_{lg}} \left[\frac{1}{\mathrm{Re}} \left(\frac{1}{20} \frac{h_{min}^3}{d_0^3} + \frac{3}{5} \frac{h_{min}}{d_0} \right) \right] \tag{2.52}$$

$$E_D = \pi \sigma_{lg} d_0^2 \left(\frac{\mathrm{We}}{\mathrm{Re}} \right) \left[\left(\frac{1}{20} \frac{h_{min}^3}{d_0^3} + \frac{3}{5} \frac{h_{min}}{d_0} \right) \right] \tag{2.53}$$

$$E_D = \frac{\pi \sigma_{lg}}{5} \left(\frac{\mathrm{We}}{\mathrm{Re}} \right) \left[\left(\frac{1}{4} \frac{h_{min}^3}{d_0} + 3 h_{min} d_0 \right) \right]. \tag{2.54}$$

This does yield the units for energy, but it is very difficult to measure h_{min} experimentally (as it would require high resolution video) and would be impractical to measure h_{min} at a crime scene. As shown previously (Equation 2.41), the minimum height of the spread can be described as (Pasandideh-Fard et al. [1996]):

$$h_{min} = \frac{2 d_0^3}{3 d_{\max}^2} \tag{2.55}$$

Substitute this into the energy of deformation, and:

$$E_D = \frac{\pi \sigma_{lg}}{5} \left(\frac{\mathrm{We}}{\mathrm{Re}} \right) \left[\frac{1}{4} \frac{1}{d_0} \left(\frac{2 d_0^3}{3 d_{\max}^2} \right)^3 + 3 \left(\frac{2 d_0^3}{3 d_{\max}^2} \right) d_0 \right] \tag{2.56}$$

$$E_D = \frac{2 \pi \sigma_{lg}}{5} \left(\frac{\mathrm{We}}{\mathrm{Re}} \right) \left[\frac{1}{27} \left(\frac{d_0^8}{d_{\max}^6} \right) + \frac{d_0^4}{d_{\max}^2} \right]. \tag{2.57}$$

This expression for deformation of the droplet satisfies unit analysis.

2.7 Investigating spread factor

In general, the spread factor (β) is used to find how much a droplet would spread on a surface ($d_{\max}$) as a ratio to the initial droplet diameter (d_0). Non-absorbent, non-yielding surfaces tend to produce secondary droplets. The maximum spread does not include secondary droplets (see Figure 2.9) because it is a description of the parent stain only. Secondary droplets will form satellite stains.

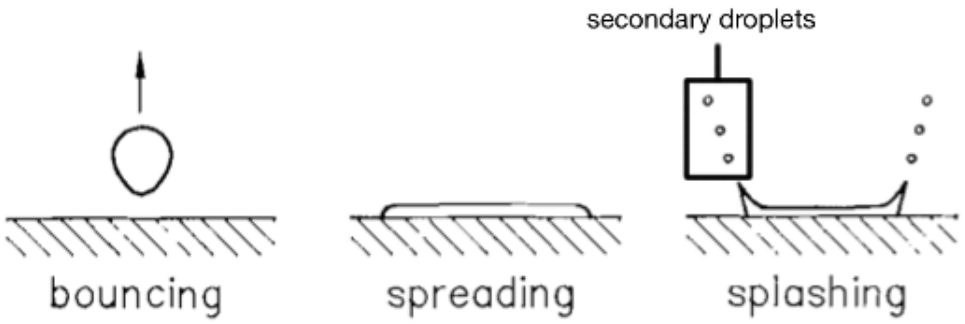

Figure 2.9: Illustration of a droplet impacting a solid surface by Rein [1993]. Figure has been edited here to label secondary droplets.

The spread factor is a dimensionless number that is dependent on the properties of the fluid (density, viscosity, and surface tension), the droplet size, the droplet's impact velocity, the surface roughness, and surface absorbance. The ratio is:

$$\beta = \frac{d_{\max}}{d_0}. \tag{2.58}$$

There are some spread factors read in the literature that compare the maximum spread ($d_{\max}$) to the diameter of the spread during impact (d_s), as seen by Liu and Megaw [1986]. Liu and Megaw [1986] used yielding substrates where the droplet would make an impression on the substrate. This is not the case in the work presented here, where the substrates are unyielding. Furthermore, this thesis does not utilise d_s in the spread factor because it is difficult to measure the diameter of the spread over time accurately, and in BPA, this information would not be available at a crime scene.

However, there are some spread factors (Hulse-Smith et al. [2005]) that compare the spread during impact (d_s), to initial drop diameter (d_0), because the assumption is made that the maximum spread diameter is equal to d_s. This assumption may be incorrect if the droplet recedes before settling into the final stain.

2.7.1 Spread factor according to Engel [1955]

The first attempt to find the maximum spread of a droplet after impact was derived by Engel [1955]. Engel [1955] approached the problem of a spherical water droplet impacting a solid surface because of the issue of high-speed aircraft being damaged when flying through rain. The aim was to produce an expression for the maximum impact pressure of the droplet and the rate of spread of the water after collision. The pressure was calculated theoretically and measured experimentally (by recording water droplet impacts using a high-speed camera) by Engel [1955]. In the experiments, the water droplets were accelerated to their terminal velocity by shielding their fall (from air circulation in the building) to the surface using a tube. This experiment was done under the assumption that a droplet falling vertically onto a surface will simulate an aircraft wing (or any surface) moving toward the droplet at some speed. Engel [1955] states that the droplets have high impact velocities but in the experiments the droplets (of radii from 4.1×10^{-3} m to 2.3×10^{-2} m) were falling from a height of approximately 12.2 m and had terminal velocities of approximately $8.2\,\mathrm{m\,s^{-1}}$ which is not particularly high. Not only are the water droplets assumed to be spheres in this specific problem, but because of the high velocity impact, they are assumed to be hard spheres. A crystal also was inserted into the droplets, this was done to view the contours of the radial flow more clearly. However it is unknown if adding this crystal changes the fluid enough to alter its impacting behaviour. In addition, it was noted that the droplets do oscillate between vertical and horizontal elongation before impact.

The characteristics of the flow of a water droplet impacting a surface, depends on the type of surface the droplet is impacting and the droplet's impact velocity (Engel [1955]). The surfaces tested by Engel [1955] were natural rubber, GR-I synthetic rubber, dry clean glass, buffed iron,

as-received iron, and fine sand in a petri dish. The surface roughness was not measured but the elasticity differences between natural rubber and GR-I synthetic rubber were stated as 30 and 20 Shore 'A' hardness, respectively. A durometer is used to measure the hardness of a material and an 'A' scale is used for softer plastics. Higher values on the scale indicate a harder material, therefore natural rubber is harder than GR-I synthetic rubber. In the semi-empirical analysis, Engel [1955] also assumed that the surfaces are non-yielding, non-absorbent, and do not absorb any energy.

There are four assumptions Engel [1955] makes when considering the impact of a water droplet onto a solid surface:

1. At the moment of impact a compressional wave is initiated in the droplet. This compressional wave pushes all particles within the droplet in the same direction as the compressional wave, with the same velocity as the compressional wave.
2. Maximum pressure is reached once the compressional wave has finished traversing the droplet.
3. The first portion of liquid to impact the surface will form a thin cylinder under the droplet and will flow radially.
4. As collision continues, compressional waves are initiated (as described in the first two assumptions) at new points of contact in the rest of the droplet.

Engel [1955] developed the following equation for observed spread, d_s (this equation has been arranged to show the observed diameter instead of the observed radial spread):

$$d_s^2 = \frac{t^2\left(m-\frac{k}{2}d_s^2\right)}{m+\chi t^2}\left[\frac{d_{\max}^2\left(m+\chi t_{\max}^2\right)}{t_{\max}^2\left(m-\frac{k}{2}d_{\max}^2\right)}\right], \tag{2.59}$$

where

$$\chi = 4\pi\left(\sigma_{lg}+\sigma_{sl}\right). \tag{2.60}$$

This expression for observed spread is theoretical. The derivation by Engel [1955] can be

found in the publication. $d_{\max}$ is the maximum spread of the droplet, $t_{\max}$ is the time at which maximum spread is reached, m is the mass of the droplet, k is a constant, σ_{lg} is the surface tension of water droplet against the air, and σ_{sl} is the interfacial tension between the water droplet and the glass. It is unclear why this equation is implicit but it is valid from when the droplet is in a flat cylinder form, until the maximum spread is reached (Engel [1955]). It was thought, by Engel [1955], that this equation would be used for finding the spread of a droplet during the impact (before the droplet has settled). This would not be useful for bloodstain pattern analysis as at a crime scene the bloodstains would be settled and probably dry already. However, the derivation to find this equation uses the concept of energy conservation and the following derivations for other spread factors use the same starting point. An attempt was made to put Equation 2.59 into a form that isolates the spread factor but this was not possible.

2.7.2 Spread factor according to Cheng [1977]

It is expected that bigger droplets and droplets moving at a higher velocity will yield a larger spread factor, because conceptually bigger droplets will have more fluid to spread, and higher velocity droplets will have more kinetic energy. The terminal velocity of a droplet will also affect the spread of a droplet as noted by Wonder [2001]. A simple theory was presented by Cheng [1977], where a liquid droplet impacts a non-absorbing surface perpendicularly, and the assumption is that the droplet will flatten into a symmetrical thin disk.

The height of the flattened droplet is (from equating the volume of the sphere to the volume of a disk):

$$h_{\min} = \frac{2d_0^3}{3d_{\max}^2}, \tag{2.61}$$

where d_0 is the diameter of the spherical droplet ($d_0 = 2r_0$), and $d_{\max}$ is the diameter of the base of the flattened drop. The final diameter of a stain (d_f) is its maximum extension ($d_{\max}$), because even when the droplet retracts and the lamella settles, the area on the surface that has

been covered by the primary extension will remain (Laan et al. [2014]). Figures 2.10 and 2.11 show illustrations of the maximum extension of the droplet and final stain diameter, respectively.

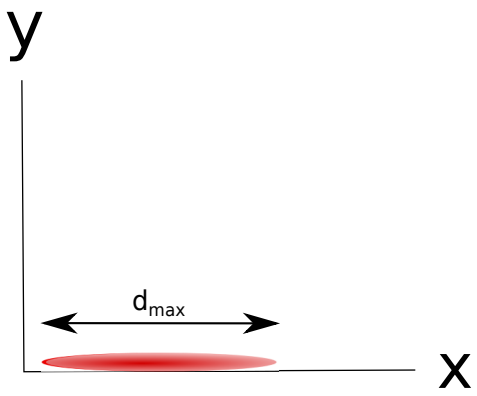

Figure 2.10: Illustration of the maximum extension, $d_{\max}$, of a droplet during impact with a surface on the x plane before settling into the surface.

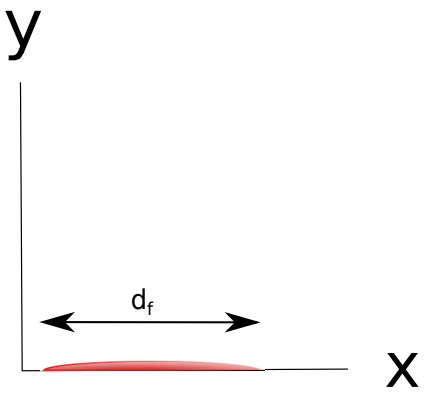

Figure 2.11: Illustration of the final diameter of the bloodstain, d_f, once a droplet has completed impacting the surface on the x plane and has settled.

In the experiments by Cheng [1977], the impact velocities ranged from $5.78 \times 10^{-2}\,\mathrm{m\,s^{-1}}$ to $1.5\,\mathrm{m\,s^{-1}}$ and the drop diameters (before impact) ranged from 2.43×10^{-3} m to 4.2×10^{-4} m. The larger drops had lower impact velocities and the smaller drops had higher impact velocities in these experiments (Cheng [1977]). A model for spread factor (comparing maximum spread to the initial droplet diameter) was proposed by Cheng [1977]:

$$\beta = 0.816\mathrm{We}^{\frac{1}{4}}\left(1+\frac{1}{2\mathrm{Fr}}\right)^{\frac{1}{4}} \tag{2.62}$$

The Froude number (Fr) is defined in Equation 2.13. The expectation that bigger droplets

or faster moving droplets will have a higher β is confirmed, because it can been seen that as the diameter, d_0 increases, the Weber number also increases and similarly for the speed of the droplet, u_0. The assumption is made by Cheng [1977] that $d_{\max}$ is much greater than the height of the droplet and that the ratio $d_{\max}/d_0 > 1$.

Cheng [1977] states that the assumptions result in β being 1 % less than its exact value for $\beta = 4$, and 3 % less for $\beta = 2$, but for practical purposes, these errors are negligible. Cheng [1977] also states "water drops in sprays from high-pressure nozzles typically have a small diameter and a high velocity"; therefore in Equation 2.62, the second parenthetical factor is virtually equal to one.

2.7.3 Spread factor according to Chandra and Avedisian [1991] and others

Starting from the conservation of energy, Chandra and Avedisian [1991] show the maximum spread factor of a droplet (β), when $\mathrm{Re} \to \infty$ (which implies a high impact velocity and/or large droplet diameter) as:

$$\beta \approx \sqrt{\frac{\frac{\mathrm{We}}{3} + 4}{1 - \cos\theta_a}}. \tag{2.63}$$

See Appendix Q for the derivation. It can be seen in Equation 2.63 that an increase in droplet diameter and/or impact velocity will cause an increase in spread factor.

The model was presented by Pasandideh-Fard et al. [1996], then cited by Adam [2012] and Adam [2013]. It was based on a numerical solution of the Navier-Stokes equations, to model a droplet impacting a stainless steel surface. The numerical model was compared to experiments where a 2.05×10^{-3} m droplet fell onto a stainless steel surface, with an impact velocity of $1\,\mathrm{m\,s^{-1}}$. This spread factor was an improvement from the spread factor proposed by Chandra and Avedisian [1991] which overestimated the values of $d_{\max}$ by 40 %. Chandra and Avedisian [1991]'s work overestimated $d_{\max}$ because they assumed that the characteristic length in the

viscous dissipation function was equal to the height of the spread. Chandra and Avedisian [1991] do not record what the characteristic length is or how it is measured. Pasandideh-Fard et al. [1996] used the boundary layer thickness of the viscous dissipation instead (which is smaller than the height of the spread) to scale the dissipation function. This change by Pasandideh-Fard et al. [1996] lowered the error of the spread factor to 15 %.

Pasandideh-Fard et al. [1996] (and later Adam [2012, 2013]) therefore show the spread factor as:

$$\beta = \sqrt{\frac{\mathrm{We} + 12}{3\,(1 - \cos\theta_a) + \frac{4\mathrm{We}}{\sqrt{\mathrm{Re}}}}}\,, \tag{2.64}$$

where θ_a is the advancing contact angle, d_0 is the diameter of the droplet before impact, and d_max is the maximum extension diameter of the droplet, as shown in Figure 2.10. See Appendix R for derivation. For Equation 2.64, the Weber number (We) and Reynolds number (Re) are defined in Section 2.1, Equation 2.9 and Equation 2.11, respectively.

Pasandideh-Fard et al. [1996] state that the capillary effects (or surface tension effects as stated by Hulse-Smith et al. [2005]) can be neglected if $\mathrm{We} \gg \sqrt{\mathrm{Re}}$. This assumption can be made because the "magnitude of the term $(1 - \cos\theta_a)$... can be, at most, 2. If $\frac{\mathrm{We}}{\sqrt{\mathrm{Re}}}$ is large in comparison, the value of the contact angle will have little effect on β" (Pasandideh-Fard et al. [1996]). This means $u_0^3 d_0 \gg \frac{\sigma_{lg}}{\sqrt{\rho_l \mu_l}}$. In this thesis, horse blood is used and the experiments endeavour to keep the diameter of the droplets constant (Chapter 4); the average droplet diameter was 3.76×10^{-3} m (from 785 droplets). Using these values, the impact velocity would need to be much greater than $0.52\,\mathrm{m\,s^{-1}}$. The droplets in this thesis achieve much greater velocities than $0.52\,\mathrm{m\,s^{-1}}$ thus the capillary effects can be neglected.

In fact, the contact angle does not appear to have significant effect on the maximum spread factor, as shown in Figure 2.12. The influence of the contact angle on the maximum spread factor decreases as the impact velocity and diameter of the droplet increase.

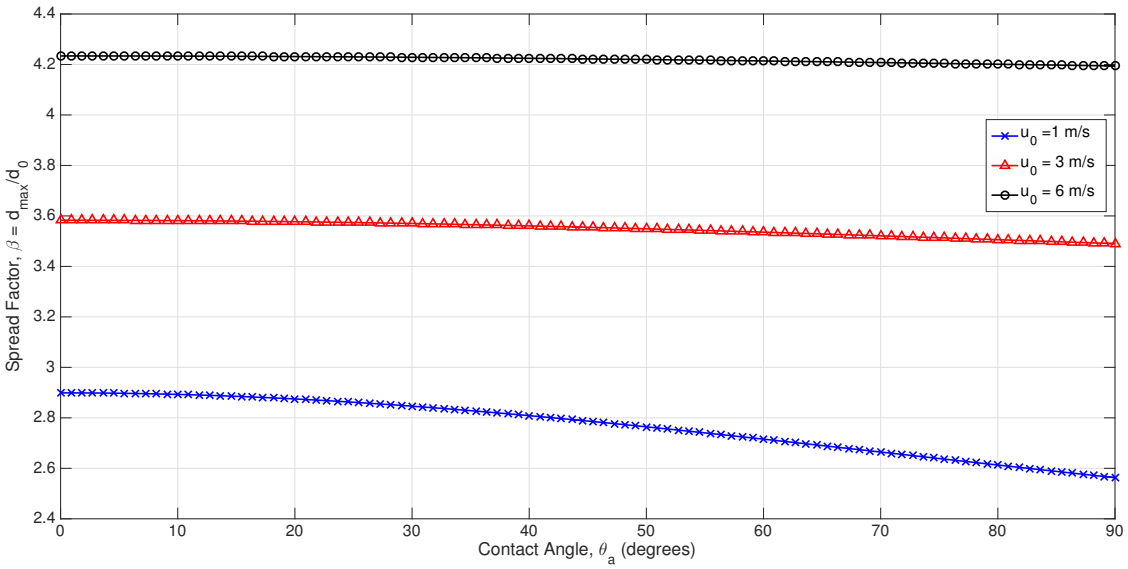

Figure 2.12: The effect of contact angle on the maximum spread factor as proposed by Pasandideh-Fard et al. [1996]. The droplet diameter used is $d_0 = 3.76 \times 10^{-3}$ m.

2.7.4 Spread factor according to Hulse-Smith et al. [2005]

The maximum spread factor was also modelled by Hulse-Smith et al. [2005], using the assumption that the surface tension effects can be neglected because We $\gg \sqrt{\text{Re}}$. The previous subsection shows that this assumption can be used for this thesis as well. Hulse-Smith et al. [2005] also state that the maximum extension of the droplet spread, $d_{\max}$, is equal to the final stain diameter, d_f, as per their experimental work. Laan et al. [2014] agree that d_f being equal to $d_{\max}$ is accepted in the literature. This is a reasonable assumption because in the experimental work by Hulse-Smith et al. [2005], there are three figures showing the high-speed photography of nine different droplets (three of which are on different surfaces). In these photographs, one cannot clearly see a difference in diameter between the bloodstains photographed at 6 milliseconds and again at 20 milliseconds. The resolution of the photographs taken by Hulse-Smith et al. [2005] was not noted.

Hulse-Smith et al. [2005] base their spread factor model on the work by Pasandideh-Fard et al. [1996] using the assumptions that the surface tension effects are negligible and therefore We $\gg \sqrt{\text{Re}}$ and We $\gg 12$. These assumptions reduce Equation 2.64 as follows:

$$\begin{aligned}
\beta &= \frac{d_{\max}}{d_0} \\
&= \sqrt{\frac{\mathrm{We}+12}{3\left(1-\cos\theta_a\right)+\frac{4\mathrm{We}}{\sqrt{\mathrm{Re}}}}} \\
&= \sqrt{\frac{\mathrm{We}+\cancel{12}}{\cancel{3\left(2\right)}+\frac{4\mathrm{We}}{\sqrt{\mathrm{Re}}}}} \\
&= \sqrt{\frac{\mathrm{We}\sqrt{\mathrm{Re}}}{4\mathrm{We}}} \\
&= \sqrt{\frac{\sqrt{\mathrm{Re}}}{4}} \\
&= \frac{1}{2}\mathrm{Re}^{1/4}.
\end{aligned} \tag{2.65}$$

Both Pasandideh-Fard et al. [1996] and Hulse-Smith et al. [2005] neglect to show the reduction of Equation 2.64 to Equation 2.65. Hulse-Smith et al. [2005] then fit Equation 2.65 to experimental data in their work leading to:

$$\beta = \frac{1.11}{2}\mathrm{Re}^{1/4}. \tag{2.66}$$

Again, Equation 2.65 shows an increase in droplet diameter and/or impact velocity will cause an increase in spread factor.

2.7.5 Comparison of spread factors

Before comparing the different spread factors presented in the previous subsections, it must be noted that the spread factor is a ratio of the maximum diameter to the initial droplet diameter ($\beta = \frac{d_{\max}}{d_0}$). This means that an increase in initial droplet diameter should cause the spread factor to decrease. However, in all of the models presented, an increase in droplet diameter causes an increase in spread factor. Therefore, the maximum diameter must change at the same rate as the

initial droplet diameter. This outlines the importance of defining what the maximum diameter is measuring. If the maximum diameter includes the satellite stains then a small droplet with high velocity, striking a rough surface, will have a large $d_{\max}$. This will cause the ratio to break down. The maximum diameter will force the spread factor to increase when the models predict the spread factor to decrease with initial droplet diameter. However, if the measurement of $d_{\max}$ does not include satellite stains, and is only a measurement of the parent stain, then a small droplet impacting a rough surface at high velocity will have a small parent stain. This is because the roughness and high velocity impact would cause droplets to detach from the parent stain. This reasoning indicates that the maximum diameter is a measurement of the parent stain only and is therefore defined as such.

In this section the spread factors are compared over a range of impact velocities ($1\,\mathrm{m\,s^{-1}}$ to $6\,\mathrm{m\,s^{-1}}$) with a droplet of diameter $3.76\times10^{-3}\,\mathrm{m}$. The contact angle was taken to be 90°. The different spread factors were plotted in Figure 2.13.

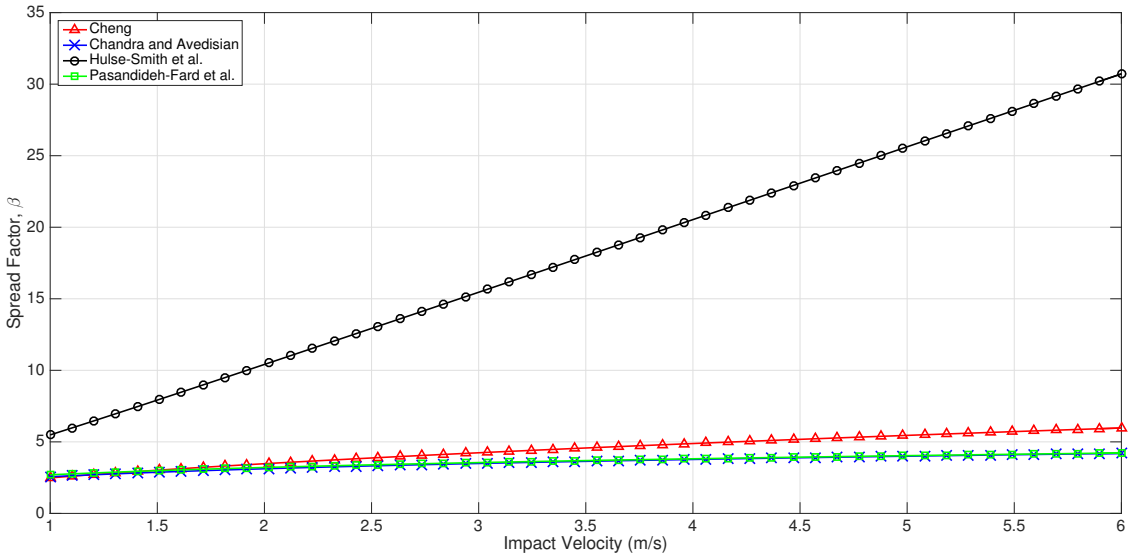

Figure 2.13: A comparison of spread factors for a droplet $d_0 = 3.76\times10^{-3}\,\mathrm{m}$: Cheng [1977] (Equation 2.62), Chandra and Avedisian [1991] (Equation 2.63), Hulse-Smith et al. [2005] without fitting coefficient (Equation 2.65), and Pasandideh-Fard et al. [1996] (Equation 2.64).

It is unclear which of these spread factors are best, however, an alternative spread factor that accounts for surface roughness will be presented in this work. The spread factor presented by

Pasandideh-Fard et al. [1996] has the clearest derivation and thus seems most robust. Therefore, any new derivations of the spread factor in this work will start with the work by Pasandideh-Fard et al. [1996]. A more detailed comparison of the spread factors will be presented in Chapter 6.

2.8 Investigating the evolution of spines

A succinct list of facts has been presented by Boys [2003] with regards to the spines that evolve from droplet impacts:

- the direction of travel of a blood droplet is indicated by the cast-off on the bloodstain;
- if there is no cast-off from the droplet, one can use the spines around the droplet (as they congregate at the far end away from impact) to deduce the direction from which the droplet came;
- the texture of a surface must be considered when analysing a bloodstain pattern that has impacted said surface; and
- the angle at which a blood droplet impacts a surface is a function of the bloodstain's size (Balthazard formula Bevel and Gardner [2001]).

The statistical results from Boys [2003] suggest that: a bloodstain's size increases with drop size, with height (from which the droplet is falling, *i.e.* the impact velocity), and with increased impact velocity. The number of spines on a bloodstain then increases with stain size but decreases with increased impact angle (Boys [2003]). The impact angle is the angle that the substrate makes with the x-axis. The number of spines should decrease with a decrease in impact angle because when a droplet is incoming to a surface on an angle, the blood will be distributed in the direction of travel, rather than evenly around the location of impact. The 'angle' mentioned in Boys [2003] may be with respect to the horizontal. One interesting factor to note is that the droplets were not always spherical as they were falling to the surface, which implies that even at these heights the droplets are oscillating. This phenomenon is studied by Raymond et al. [1996a].

Modelling of spines around a circular bloodstain was carried out by Thoroddsen and Sakakibara [1998], which was based on a surface tension modified Rayleigh-Taylor instability. A visualisation technique was developed by Thoroddsen and Sakakibara [1998] to view the evolution of fingering of a water droplet impacting a glass plate. The visualisation was created from experiments where three flash photographs were taken in quick succession during the spreading of a water droplet. These photographs overlaid on each other showed the evolution of the spines of a water droplet. It was then proposed by Thoroddsen and Sakakibara [1998] that the spines are instabilities of the ring of fluid first touching the surface. Thoroddsen and Sakakibara [1998] also suggested that the spines could be modelled by a surface tension modified Rayleigh-Taylor instability (based on work first proposed by Allen [1975]). A Rayleigh-Taylor instability can occur when a fluid of lower density (air) is pressing on and resisting a fluid of higher density (blood or water, Sharp [1984]). The air pushes against the droplet, causing it to decelerate rapidly. The motion of the droplet spreading radially and decelerating as a result of viscous forces was described by Allen [1975] to exhibit a Rayleigh-Taylor instability.

The model developed by Thoroddsen and Sakakibara [1998] did not use the Weber number to predict the number of spines on the resulting stain. Even though it is commonly used in BPA to describe the formation of spines (Mehdizadeh et al. [2004]; Hulse-Smith et al. [2005]; Knock and Davison [2007]). The Weber number is a dimensionless number used to analyse fluid flows where there are two different fluids interacting; in this case, the blood droplet and the air. It is a measure of the fluid's inertia compared to its surface tension. The Weber number is expressed as (Equation 2.11, Section 2.1):

$$\mathrm{We} = \frac{\rho_l u_0^2 d_0}{\sigma_{lg}}, \tag{2.67}$$

where d_0 is the diameter of the droplet.

There are a few models in the literature that use the Weber number to predict the number of spines on a stain. The models presented by Mehdizadeh et al. [2004], Hulse-Smith et al. [2005], and Knock and Davison [2007] are based on the following relationship between spines, N, and

the Weber number, We:

$$N = C\sqrt{\mathrm{We}} \tag{2.68}$$

where C is a data fitting constant. The Weber number, We, is given by Equation 2.67. The value of C (in Equation 2.68) in models by Mehdizadeh et al. [2004], Hulse-Smith et al. [2005], and Knock and Davison [2007] is different depending on the experiments performed.

Mehdizadeh et al. [2004] derived a model using experiments with water droplets of radius 2.75×10^{-4} m to 6.5×10^{-4} m. The water droplets had impact velocities between $10\,\mathrm{m\,s^{-1}}$ and $50\,\mathrm{m\,s^{-1}}$ and impacted a stainless steel substrate, fixed onto a rotating wheel. The idea was to have the droplet fall vertically and impact the substrate perpendicularly as it accelerated in a circular path parallel to the floor (much like swinging a bat at a ball that is falling downwards). The rotating wheel was used to achieve higher impact velocities. The stainless steel substrates had an average roughness of 3×10^{-9} m or 2.3×10^{-7} m (see Section 2.4 for more information on surface roughness). The relationship found by Mehdizadeh et al. [2004] was:

$$N = 1.14\sqrt{\mathrm{We}}, \tag{2.69}$$

where the coefficient $C = 1.14$ is a result of a curve fit, through data from the experiments of water droplets impacting the steel surfaces. Equation 2.69 agreed with results found by Mehdizadeh et al. [2004] within $\pm$ 3 %.

Porcine blood experiments validated the model by Hulse-Smith et al. [2005]. The droplets had radii from 1.5×10^{-3} m to 2.15×10^{-3} m and the heights used to release the droplets ranged from 0.305 m to 1.219 m. Hulse-Smith et al. [2005] then calculated the impact velocities as ranging from $2.4\,\mathrm{m\,s^{-1}}$ to $4.9\,\mathrm{m\,s^{-1}}$. The different substrates (glass, paper, steel, and plastic) had varying roughnesses, from 3×10^{-9} m to 2.9×10^{-6} m. The following relationship was found by Hulse-Smith et al. [2005]:

$$N = 0.955\sqrt{\mathrm{We}}, \tag{2.70}$$

where the coefficient $C = 0.995$, was found from fitting Equation 2.68 to data from the porcine blood experiments. The value for C is actually an adjustment to Equation 2.69, that fits the experimental data better. This equation was then used to predict droplet diameters in the experiment and succeeded to do so within 5 %. Equation 2.70 is also used by Brownson and Banks [2010].

Brownson and Banks [2010] made an estimation about how the number of spines would change on a bloodstain if the surface tension varied as much as the viscosity (± 4 %). It was found that the number of spines on a vertical impact using a droplet diameter of 4.4×10^{-3} m and impact velocity of $3.8\,\mathrm{m\,s^{-1}}$, would be 103 for a $+4$ % difference in surface tension, and 107 for a -4 % change in surface tension. In the same publication, Brownson and Banks [2010] also found that an average dose of amphetamine increased blood viscosity by 4.1 %. Later, El-Sayed et al. [2011] added different concentrations of warfarin to defibrinated horse blood to find the largest change in the viscosity (20.4%). This addition of warfarin saw a decrease in surface tension from $0.051\,\mathrm{N\,m^{-1}}$ to $0.0486\,\mathrm{N\,m^{-1}}$. Again the final stain diameter and number of spines were calculated based on a droplet of $d_0 = 4.4 \times 10^{-3}$ m and $u_0 = 3.8\,\mathrm{m\,s^{-1}}$. El-Sayed et al. [2011] found that the average number of spines changes from 34.7 to 35.5 spines with the increased concentration of warfarin. As previously discussed, the number of spines is related to the Weber number; so a decrease in surface tension would cause an increased Weber number thus and an increase in spines.

Finally, the model by Knock and Davison [2007] used porcine blood droplets with radius 1.85×10^{-3} m to 2.5×10^{-3} m dripping onto paper. The droplets fell from heights of 0.5 m, 1.0 m, 1.5 m, and 2.0 m which produced impact velocities from $1.82\,\mathrm{m\,s^{-1}}$ to $5.76\,\mathrm{m\,s^{-1}}$. The relationship found by Knock and Davison [2007] was:

$$N = 0.76\sqrt{\mathrm{We}}\sin^3\theta_f, \tag{2.71}$$

where θ_f is the impact angle and the coefficient $C = 0.76$, was achieved from fitting data produced from experiments of porcine blood droplets impacting paper vertically. The R^2 value of that fit was 0.90.

All three models have an increase in spines with an increase of Weber number (as seen in Figure 2.14). This is reasonable because the Weber number will increase with an increase in droplet size and/or droplet impact velocity. The larger the droplet or the faster the droplet is moving before the impact, the more energy the droplet will carry to produce spines. The models only differ by a fitting coefficient because they all use different liquids (notably, different viscosities, which are absent in these models), substrates, and in the case of the work by Mehdizadeh et al. [2004], a different experimental arrangement. All three models rely on manual counts of the spines in order to find the Weber number of the droplet that formed the stain, but conversely these models do include the physical properties of the liquid required to predict the number of spines on a stain.

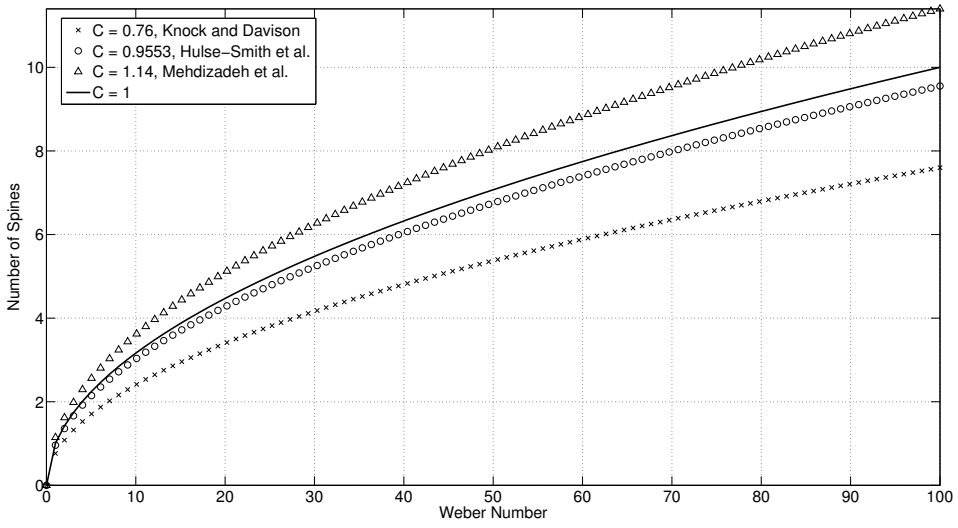

Figure 2.14: Different models for predicting the number of spines on a bloodstain using the Weber number. Data in this figure are from Mehdizadeh et al. [2004], Hulse-Smith et al. [2005], and Knock and Davison [2007]. For reference, the line $C = 1$ is included which would represent the relationship between number of spines and the Weber number without any experimental coefficient.

2.9 Terminal velocity of a droplet

The terminal velocity of a droplet is important to study, especially for passive drops, *i.e.* blood dripping from a stationary source, straight down onto a surface. Understanding when blood droplets reach terminal velocity would make determining impact velocity much simpler. The height from which the droplet has fallen (starting from rest) is also an important variable to understand when investigating terminal velocity. van Boxel [1997], via numerical modelling, found that within 2 m of falling, water droplets of diameter less than 1×10^{-3} m will only achieve 95 % of their terminal velocity. As the droplet diameters increased, the height required to reach terminal velocity also increased rapidly. A droplet of 2×10^{-3} m requires a height of 5.6 m to reach terminal velocity. Free falling human blood was used in experiments by MacDonell [1993] to find the terminal velocity of different sized droplets (see Table 2.2). The terminal velocity of a 0.05 ml droplet was determined to be 7.65 ± 0.3 m s^{-1} (MacDonell [1993]). According to Willis et al. [2001], if a droplet has fallen far enough to achieve terminal velocity, the size of the bloodstain is no longer dependant on the distance of the fall. The units in Table 2.2 have been converted to reflect SI units.

Table 2.2: Characteristics of free falling human blood by MacDonell [1993] (units have been converted to SI units)

Observed diameter (10^{-3} m)	Terminal velocity (m s^{-1})	Distance travelled to reach terminal velocity (m)
1.06	2.29	0.51 - 0.66
1.32	3.32	0.84 - 0.99
2.12	4.69	3.05 - 3.66
4.60	7.65	6.10 - 7.62

A droplet will reach terminal velocity, u_t, when the force of drag, F_d, (or air resistance) is equal to the force of gravity, F_g, acting upon the droplet. The model proposed by Gunn and Kinzer [1949] to express the terminal velocity was developed by equating the force of drag, F_d, to the force of gravity. The force of drag is written as:

$$F_d = \frac{\pi}{2}\kappa\rho_{\text{air}}r^2u_t^2\,, \tag{2.72}$$

where κ is the drag coefficient, ρ_{air} is the density of the air surrounding the droplet, r is the radius of the droplet, and u_t is the terminal velocity. For a solid sphere, $\kappa = 0.47$. The force of gravity, F_g, is written as:

$$F_g = \frac{4}{3}g\pi r^3\left(\rho_{\text{drop}} - \rho_{\text{air}}\right)\,, \tag{2.73}$$

where g is acceleration due to gravity, and ρ_{drop} is the density of the fluid (in the experiment by Gunn and Kinzer [1949] this is distilled water). Equations 2.72 and 2.73 produce an expression for the terminal velocity:

$$u_t^2 = \frac{8gr\left(\rho_{\text{drop}} - \rho_{\text{air}}\right)}{3\rho_{\text{air}}\kappa}\,. \tag{2.74}$$

However, Gunn and Kinzer [1949] noted that during the experimental work, that the applicability of Equation 2.74 may be suspect in reality. This could be caused by the influence of turbulence from other water droplets falling in the vicinity of one another, and the deformations of the droplets during the fall (because the droplets are not rigid spheres). The terminal velocities were then found experimentally by Gunn and Kinzer [1949], at standard pressure (1.01×10^5 Pa) and temperature (20°) settings. The masses of the droplets used in that experiment ranged from 2×10^{-10} kg to 1×10^{-4} kg which is 3.6×10^{-5} m to 2.8×10^{-3} m, in equivalent radius. It should also be noted that in this work the droplets were literally weighed, whereas in more modern studies, high-speed cameras are used and the size of the droplets are normally extrapolated from the photograph or video data (see Knock and Davison [2007]).

The drag coefficient, is known to be a function of the Reynolds number (Sherman [1990], Sirignano [1999], Murray [2012]). This means the drag coefficient in Equation 2.74 should be calculated at every time step of the droplet's fall. Even though the droplet is in a state of constant velocity (because the drag force and gravitational force are equal), the radius of the droplet

is changing slightly from the droplet oscillating through the air, thus the drag coefficient will technically be changing during the droplet's fall. Equation 2.74 is the only model for terminal velocity which depends on the radius of the droplet and the speed of the droplet through the air.

Later, Wobus et al. [1971] proposed three other functions to calculate the terminal velocity. The first model is:

$$u_t = -0.183848\sqrt{\frac{\rho_0}{\rho_{\text{air}}}r}, \tag{2.75}$$

where ρ_0 is the air density at sea level and ρ_{air} is the density of the air. Wobus et al. [1971] makes the assumption that at low altitudes $\frac{\rho_0}{\rho_{\text{air}}} \approx 1$. The negative is placed to indicate directionality as the droplets in this study were falling downwards (Wobus et al. [1971]). This was the approach used by Kessler [1969] and is an evaluation for radii greater than 500 µm. His work was later reviewed and summarised by Kessler [1995]. While the units for radius in Equation 2.75 are micrometres, the units for u_t are metres per second. The coefficient in this model is not only used for fitting to experimental data produced by Gunn and Kinzer [1949], but also accounts for the direction the droplet is travelling (downward, hence the negative sign). For the purposes of studying these models, this unit convention is used.

The second approach, by Wobus et al. [1971], is a piecewise function of simple polynomial fits to experimental data by Gunn and Kinzer [1949] over ranges of r (in µm):

$$u_t = \begin{cases} (-1.202\times10^{-4})r^2, & \text{if } r < 40 \\ (-8.923\times10^{-3})r + 0.1645, & \text{if } 40 \leq r < 200 \\ (-8.033\times10^{-3})r - 0.0135, & \text{if } 200 \leq r \leq 500 \\ -b_1r^3 + b_2r^2 - b_3r + b_4, & \text{if } r > 500 \end{cases}, \tag{2.76}$$

where the fitting constants can be found in Table 2.3. Equation 2.76 was developed by one of the authors (L. R. Koenig) who collaborated in the publication by Wobus et al. [1971].

A more ambitious approach for calculating the terminal velocity, by Wobus et al. [1971], is

Table 2.3: List of fitting constants in the work by Wobus et al. [1971]

b_1	$3.6719974 \times 10^{-10}$
b_2	3.2747328×10^{-6}
b_3	9.566183×10^{-3}
b_4	0.1214986
b_5	2.036791×10^{-15}
b_6	3.815343×10^{-12}
b_7	4.516634×10^{-9}
b_8	8.020389×10^{-7}
b_9	$1.44274121 \times 10^{-3}$

again a piecewise function and is made up of fits to experimental data, from Gunn and Kinzer [1949], over ranges of r (in μm):

$$u_t = \begin{cases} (1.44 \times 10^{-13})r^6 + (8.64 \times 10^{-11})r^5 - (1.197 \times 10^{-4})r^2, & \text{if } r \leq 50 \\ 0.18 - (9 \times 10^{-3})r, & \text{if } 50 < r \leq 230 \\ \frac{0.4}{r-210} - 0.008r - 0.07, & \text{if } 230 < r \leq 450 \\ \frac{5.545}{D} - 9.215 + \frac{0.4}{r-210}, & \text{if } r > 450 \end{cases}, \quad (2.77)$$

where

$$D = b_5 (r-450)^5 - b_6 (r-450)^4 + b_7 (r-450)^3 - b_8 (r-450)^2 + b_9 (r-450) + 1, \quad (2.78)$$

and again the fitting constants can be found in Table 2.3. Equation 2.77 was developed by one of the authors (Hermann B. Wobus) who collaborated in the publication by Wobus et al. [1971]. This model is more robust than the second model because it is continuous in its first derivative (the acceleration of the droplet) and the edges of the experimental data range approach asymptotes, giving a more compact solution for this specific data range. It can be

seen in Equation 2.77 that without the coefficients accounting for the units in the piecewise function, the units analysis would not be correct. For example, in Equation 2.77 in the range $r \leq 50$, if the coefficients were dimensionless, the units in the function would not equate to $\mathrm{m\,s^{-1}}$. Again, for both models shown in Equations 2.76 and 2.77, the velocity is negative to indicate directionality.

Table 2.3 lists all the constants embedded in the fitting polynomials which are used by Wobus et al. [1971].

Lastly, Wobus et al. [1971] states that the terminal velocity also "varies with air density and dynamic viscosity; hence it varies with pressure, temperature and relative humidity" and proposes the viscosity of the air, $\tilde{\mu}_{\text{air}}$, should be calculated as a function of temperature, T (which are in the units of degrees Celsius):

$$\tilde{\mu}_{\text{air}} = 775.7257 - \frac{719813.4}{T + 918.768}. \tag{2.79}$$

Wobus et al. [1971] does not indicate what units are used for $\tilde{\mu}$ in Equation 2.79 nor does the expression yield the accepted value for the dynamic viscosity for air at 25 °C. Equation 2.79 gives $\tilde{\mu} = 184.2$, units unknown, at 25 °C whereas the accepted constant for dynamic viscosity of the air at 25 °C is $\mu_{\text{air}} = 1.8 \times 10^{-5}\,\mathrm{N\,s\,m^{-2}}$ (Batchelor [2000]).

Wobus et al. [1971] also proposed a parameter related to the drag on a droplet (the origin of this formula is not stated by Wobus et al. [1971]):

$$C = \frac{0.2177076}{u_t^2} r + \frac{1817.8}{r\,u_t}, \tag{2.80}$$

which is used in Equation 2.81:

$$\tilde{u}_t = \frac{6\tilde{\mu}_{\text{air}}}{r\rho_{\text{air}}C} - \sqrt{\left(\frac{6\tilde{\mu}_{\text{air}}}{r\rho_{\text{air}}C}\right)^2 + \frac{0.261249r}{\rho_{\text{air}}C}} \tag{2.81}$$

which is a corrected expression for terminal velocity, $\tilde{u}_t$, to account for changes in the air's temperature and pressure. The terminal velocity, u_t, calculated by any method (either Equa-

tion 2.75, Equation 2.76, or Equation 2.77) at standard density and temperature, can be used in Equation 2.81. It is assumed that in Equation 2.81 all the unit analysis is absorbed into the fitting coefficients. It should be noted that the parameter C is undefined if the terminal velocity is zero, however this should not occur physically. However, as the terminal velocity increases, C approaches zero which will cause Equation 2.81 to be undefined. A comparison of Equation 2.75, Equation 2.76, Equation 2.77, and their corresponding corrections using Equation 2.81 are plotted in Figure 2.15.

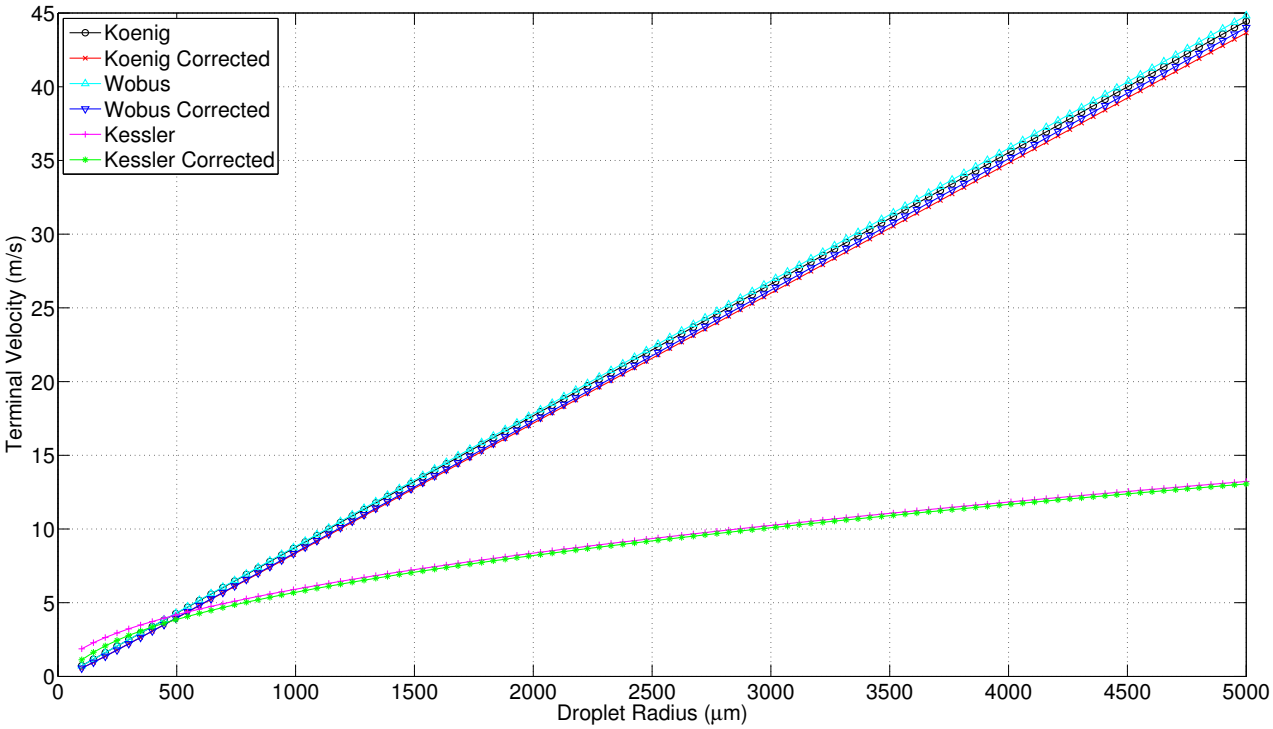

Figure 2.15: The terminal velocity calculated using Equation 2.76 (labelled Koenig), Equation 2.77 (labelled Wobus), and Equation 2.75 (labelled Kessler) with a range of radii from 1×10^{-4} m to 5×10^{-3} m with their respective corrections using Equation 2.81. The absolute value of the terminal velocity is used. All three models can be found in the work by Wobus et al. [1971].

The corrections in Figure 2.15 are expected to be close to their respective models because the models were done at standard pressure and temperature. Equation 2.76 and Equation 2.77 prove to be similar while Equation 2.75 offers very low terminal velocities. The reasons for the

large difference is unknown other than the methodology for deriving Equation 2.75 is different compared to Equations 2.76 and 2.77 (which use piecewise functions). The terminal velocity was also modelled by fitting equations to data, by Berry and Pranger [1974]. A "slip correction" equation (Equation 2.82) was deduced, investigated, modified, and finally written as

$$S = 1.0 + \frac{8.12 \times 10^{-9}}{\rho_{\text{air}} r} \left[1.23 + 0.41 \exp\left(\frac{-0.88 \rho_{\text{air}} r}{8.12 \times 10^{-9}} \right) \right]. \tag{2.82}$$

This is used in a simpler expression for terminal velocity:

$$u_t = \frac{S \text{Re} \mu_{\text{air}}}{2 r \rho_{\text{air}}}, \tag{2.83}$$

where the Reynolds number in Equation 2.83 is determined from experimental data thus this equation is not iterative.

The use for studying the terminal velocity of droplets is for situations where blood is dripping, not when blood droplets are projected by force, for example, in passive stains, drip trails, or gravitational drops. Passive drops are used exclusively in this thesis therefore understanding when a droplet reaches terminal velocity is important.

2.10 Calculating the initial velocity and initial diameter of a blood droplet

Hulse-Smith et al. [2005] suggested two formulae that could be used to calculate the diameter of the droplet at impact, d_0, and the impact velocity of a droplet, u_0, using properties of the bloodstain. The impact velocity and impact diameter can be used to find the source of bloodletting if used in a model to estimate the flight path of the droplet. The two properties inputted into the equations by Hulse-Smith et al. [2005] are the number of spines on a droplet and the final stain diameter. Presently, these properties are measured manually. In Chapter 3, it will be shown that an Automated Spine Counter (ASC) can not only automatically count

spines on a bloodstain (removing human bias), but it can also measure properties of the stain. These properties are stain area, A_{ASC}, stain perimeter, P_{ASC}, inner diameter, d_{in}, and outer diameter, d_{out}. The inner diameter is defined as the diameter of the bloodstain not including spines and the outer diameter is the diameter of the bloodstain including spines. In Chapter 6, it is shown that using the ASC to measure the properties of the stain, in conjunction with a few adjustments to Hulse-Smith et al. [2005]'s equations to calculate u_0 and d_0, is more accurate than current methods. This section will outline how the equations to calculate u_0 and d_0 were initially derived.

Hulse-Smith et al. [2005] started with relationships between, spines on a stain (N) and spread factor of a stain (β), found by Mehdizadeh et al. [2004]. In general these relationships are:

$$\beta = \frac{\mathrm{Re}^{\frac{1}{4}}}{2}, \tag{2.84}$$

and

$$N = \sqrt{\mathrm{We}}, \tag{2.85}$$

where N is the number of spines, Re is the Reynolds number of the flow, We is the Weber number, and β is the spread factor. As previously discussed, the spread factor is the ratio of $d_{\max}$ to d_0. Substituting in the Reynolds number, Weber number, and spread factor gives:

$$\frac{d_{\max}}{d_0} = \frac{1}{2}\left(\frac{\rho_l d_0 u_0}{\mu_l}\right)^{\frac{1}{4}}, \tag{2.86}$$

and

$$N = \sqrt{\frac{\rho_l d_0 u_0^2}{\sigma_{lg}}}. \tag{2.87}$$

With two equations and two unknowns, the droplet diameter and impact velocity can be

found using the method of substitution. Rearranging Equation 2.87 for d_0:

$$\frac{\sigma_{lg}N^2}{\rho_l u_0^2} = d_0\,. \tag{2.88}$$

Then substitute Equation 2.88 into Equation 2.86:

$$\frac{d_{\max}}{d_0} = \frac{1}{2}\left(\frac{\rho u_0}{\mu_l}\right)^{\frac{1}{4}} d_0^{1/4} \tag{2.89}$$

$$d_{\max} = \frac{1}{2}\left(\frac{\rho_l u_0}{\mu_l}\right)^{\frac{1}{4}} d_0^{5/4} \tag{2.90}$$

$$d_{\max} = \frac{1}{2}\left(\frac{\rho_l u_0}{\mu_l}\right)^{\frac{1}{4}} \left(\frac{\sigma_{lg}N^2}{\rho_l u_0^2}\right)^{5/4} \tag{2.91}$$

$$2d_{\max} = \frac{\sigma_{lg}^{5/4} N^{5/2}}{\mu_l^{1/4}\rho_l u_0^{9/4}}\,. \tag{2.92}$$

Now rearrange for u_0:

$$u_0^{9/4} = \frac{\sigma_{lg}^{5/4} N^{5/2}}{2\rho_l d_{\max}\mu_l^{1/4}} \tag{2.93}$$

$$u_0 = \frac{\sigma_{lg}^{5/9} N^{10/9}}{2^{4/9}\rho_l^{4/9} d_{\max}^{4/9}\mu_l^{1/9}} \tag{2.94}$$

$$u_0 = \left(\frac{\sigma_{lg}^5 N^{10}}{2^4\rho_l^4 d_{\max}^4\mu_l}\right)^{1/9} \tag{2.95}$$

$$u_0 = \left(\frac{\sigma_{lg}^5 N^{10}}{16\rho_l^4 d_{\max}^4\mu_l}\right)^{1/9}\,. \tag{2.96}$$

Substitute Equation 2.96 into Equation 2.88:

$$d_0 = \frac{\sigma_{lg} N^2}{\rho_l u_0^2} \tag{2.97}$$

$$d_0 u_0^2 = \frac{\sigma_{lg} N^2}{\rho_l} \tag{2.98}$$

$$d_0 \left(\frac{\sigma_{lg}^5 N^{10}}{16 \rho_l^4 d_{\max}^4 \mu_l} \right)^{2/9} = \frac{\sigma_{lg} N^2}{\rho_l} \tag{2.99}$$

$$d_0 \frac{\sigma_{lg}^{10/9} N^{20/9}}{16^{2/9} \rho_l^{8/9} d_{\max}^{8/9} \mu_l^{2/9}} = \frac{\sigma_{lg} N^2}{\rho_l} \tag{2.100}$$

$$d_0 = \frac{16^{2/9} d_{\max}^{8/9} \mu_l^{2/9}}{\rho_l^{1/9} \sigma_{lg}^{1/9} N^{2/9}} \tag{2.101}$$

$$d_0 = \left(\frac{256 d_{\max}^8 \mu_l^2}{\rho_l \sigma_{lg} N^2} \right)^{1/9}. \tag{2.102}$$

Therefore, the initial droplet diameter and the impact velocity can be described in general as:

$$d_0 = 256^{1/9} \left(\frac{d_{\max}^8}{\rho_l \sigma_{lg}} \right)^{1/9} \left(\frac{\mu_l}{N} \right)^{2/9}, \tag{2.103}$$

and

$$u_0 = \left(\frac{\sigma_{lg}^5 N^{10}}{16 \rho_l^4 d_{\max}^4 \mu_l} \right)^{1/9}. \tag{2.104}$$

Equations 2.103 and 2.104 have been adjusted with fitting constants in previous work (Hulse-Smith et al. [2005]; Knock and Davison [2007]) in order to fit with their specific experimental data. The fitting constants used by Hulse-Smith et al. [2005] adjust Equations 2.103 and 2.104 as follows:

$$d_0 = 0.902 \left(256^{1/9} \right) \left(\frac{d_{\max}^8}{\rho_l \sigma_{lg}} \right)^{1/9} \left(\frac{\mu_l}{N} \right)^{2/9}, \tag{2.105}$$

and

$$u_0 = 1.102 \left(\frac{\sigma_{lg}^5 N^{10}}{16 \rho_l^4 d_{\max}^4 \mu_l} \right)^{1/9}. \tag{2.106}$$

In Chapter 6, a new approximation to these equations is suggested. These new equations do not use fitting constants but rather other properties of the stain. This approach makes the equations more robust and generalised to work with different sets of data, not just one type of experimental data.

2.11 Current methods used in BPA

In crime scenes where there are bloodstain patterns, finding the position of the source of bloodletting is a helpful tool for crime scene investigators to reconstruct the events of a crime (MacDonell [1993]; Bevel and Gardner [2001]). The shape of a bloodstain, for example, can give an indication of which direction the droplet came from (Section 2.3) and therefore where the victim was positioned at the time of the assault or murder. The most popular method to find the source of bloodletting uses straight lines along the major axis of a bloodstain (Figure 2.23). A region of intersection (Figure 2.16), can be identified by attaching a string to each bloodstain according to the bloodstain's impact angle and direction of travel. The impact angle is found using a formula by Balthazard et al. [1939]:

$$\sin\left(\theta_f\right) = \frac{d_i}{d_j}, \tag{2.107}$$

where θ_f is the impact angle, d_i is the minor diameter of the stain (or the width of the stain), and d_j is the major diameter of the stain (or the length of the stain). The method of using a string to find the source of bloodletting is called straight line geometric reconstruction (SLGR) by Murray [2012], but is more commonly known as the string method (by Illes et al. [2005]) or string reconstruction (by Wonder [2007]). This method however, neglects the forces of gravity and drag acting upon a blood droplet during its trajectory because it models the flight of the

droplet as straight lines. Figure 2.16 shows the overhead view of the potential flight paths of blood droplets that would emerge from a bloodletting source in the region of intersection. In reality, all blood droplets will not emerge from one single point, and is why investigators are not looking for a point of intersection. However, there needs to be some validation as to how large the region of intersection can be, *i.e.*, the region of intersection cannot be larger than the average human body. On the other hand, if there are multiple regions of intersection it could imply the victim was moving.

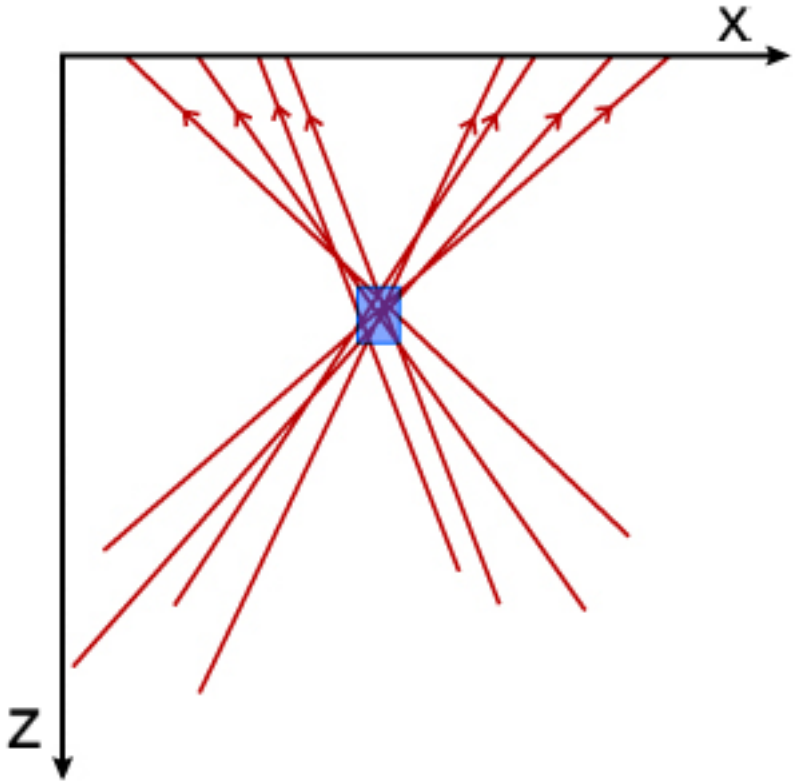

Figure 2.16: An overhead view of the intersection of blood droplet paths by Maloney and Maloney [2009]. The region in the blue square is considered the region of intersection. The arrows show the direction of motion of the droplet. The bloodstain is created on the y plane.

There are two computational implementations of SLGR. The first is called *BACKTRACK*™ and was developed by A. L. Carter in 1992. Illes et al. [2005] notes that the software is best used for downward moving droplets and can estimate the x and y coordinate of the source of bloodletting with “sufficient" accuracy. It is unclear in the article by Illes et al. [2005] as to what

"sufficient" accuracy means. However, the height of the bloodletting source, or the z coordinate, is not as easily estimated and should be used with caution. Figure 2.17 shows the estimation of the z-coordinate, where without the virtual reconstruction of the three upward-moving droplets (strings 21, 22, and 23 in Figure 2.17) the height of the source of bloodletting would have been overestimated.

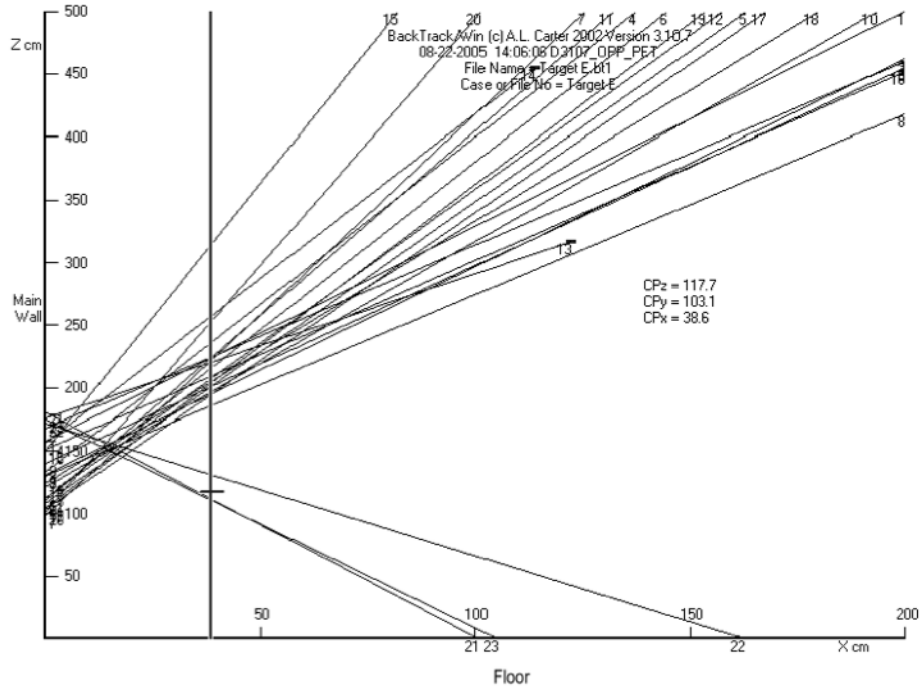

Figure 2.17: A screen capture from Illes et al. [2005] of the trajectory reconstruction produced by *BACKTRACK*™. A view from the side where droplets are moving from right to left. The virtual flight paths of the downward moving droplets are shown to be originating from the ceiling. The three virtual flight paths show to be originating from the floor are upward moving droplets. The intersection of all these virtual flight paths are used to approximate the z coordinate.

According to Buck et al. [2010], it is possible for SLGRs to overestimate the height of a source of bloodletting by up to 2 m. Figure 2.18 illustrates the difference in height of estimated bloodletting using both a straight line to predict the path of the droplet and a curved path. Using a straight line estimation, from the impact angle, has a much higher position for estimated bloodletting. Whereas if the droplet is affected by the forces of gravity and drag, the path will be curved and thus the straight line is overestimating the position of bloodletting. Buck et al. [2010] recommend using ballistic analysis for bloodstains that exhibit an impact angle less than

10°. This ballistic analysis includes the force of gravity in the analysis of the droplet's flight path (which has also been carried out by Knock and Davison [2007]). It should be noted that to carry out ballistic analysis, the droplet's mass and velocity must be known at any one position of the droplet's trajectory.

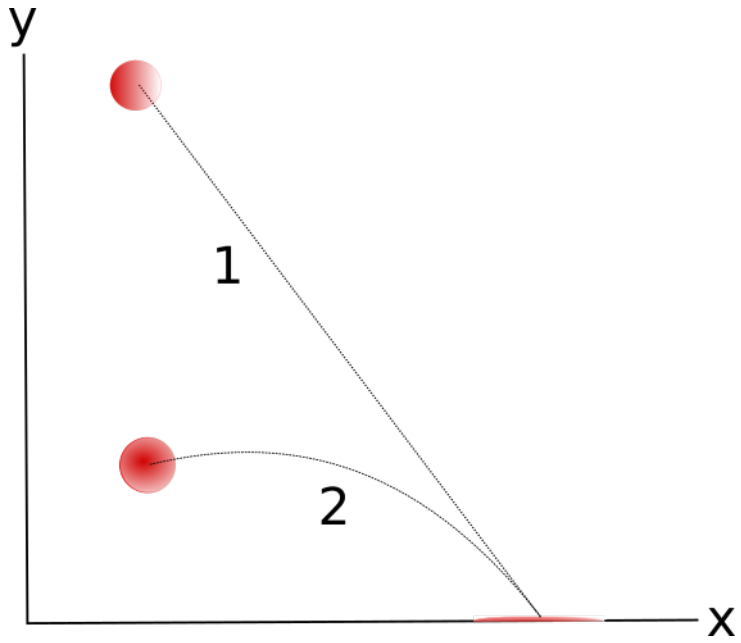

Figure 2.18: Illustration of a droplet's initial position using (1) a straight line geometric reconstruction and (2) a ballistic estimation.

The second computational implementation of the SLGR is *HEMOSPAT*™ created by Maloney in 2006. This is a three-dimensional reconstruction software which has features to detect the bloodstain in a digital photograph, and calculate the source of bloodletting. Maloney et al. [2009] state that the source of bloodletting was found within 0.01 m accuracy and the maximum height offered by the software was 0.151 m away from the source. Another feature of *HEMOSPAT*™ is the ability to record, analyse, and present data about cast-off patterns. Cast-off patterns are bloodstains resulting from droplets being released from an object due to motion (Scientific Working Group on Bloodstain Pattern Analysis [2013]). Two experiments by Maloney et al. [2011a] used a knife for a horizontal cast-off pattern and a swinging hammer for back cast-off, forward cast-off, and then a single impact pattern. *HEMOSPAT*™ was used to analyse the cast-off patterns the same way it would be used to analyse an impact pattern.

However, it is unclear how an investigator would distinguish between these two types of patterns before inputting them into *HEMOSPAT*™, or if *HEMOSPAT*™ is capable of showing whether the different droplets are coming from a single moving object (for example, a swinging knife). *HEMOSPAT*™ is only used in these two experiments by Maloney et al. [2011a] to depict a two-dimensional view of the cast-off patterns.

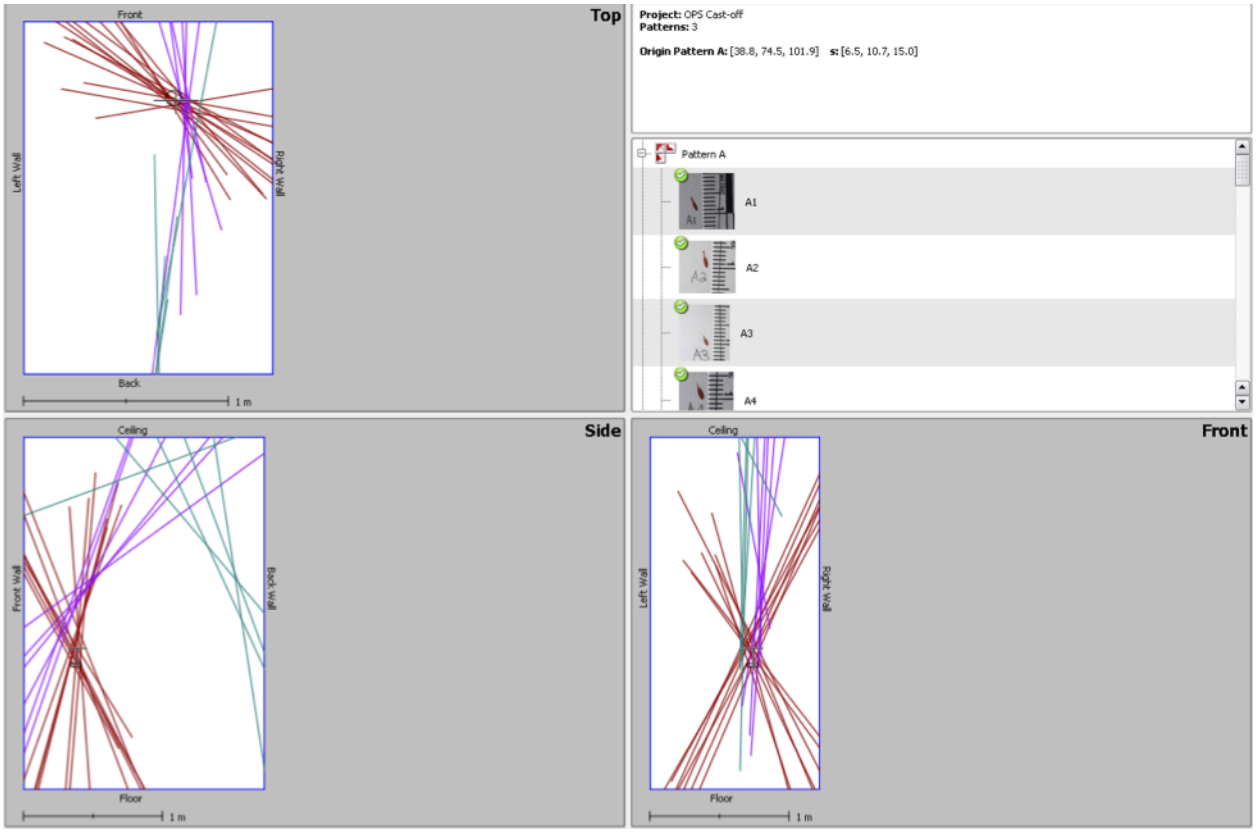

Figure 2.19: A screen capture from Maloney et al. [2011a] of cast-off analysis in *HEMOSPAT*™. Two-dimensional views of the complex cast-off pattern generated by a swinging hammer. Blue lines may indicate the backward-cast off, pink lines for forward cast-off, and red lines for impact trajectories.

Figure 2.19 is a screen capture from *HEMOSPAT*™ showing the analysis of the swinging hammer experiment by Maloney et al. [2011a]. It is not stated in the article what the coloured lines mean, *i.e.*, which colours are the forward cast-off, backward cast-off, and impact trajectories. It is also unclear if the terms "forward cast-off" and "backward cast-off" are referring to cast-off patterns and cessation cast-off patterns, respectively (bloodstains produced from droplets

being released from an object decelerating quickly, Scientific Working Group on Bloodstain Pattern Analysis [2013]). It was shown in the analysis that *HEMOSPAT*™ alone cannot analyse the planar motion of an object's swing (causing the cast-off pattern), but that in conjunction with outside software, some information about the planar motion can be found. *HEMOSPAT*™ has also been tested to analyse "one-sided patterns" (Maloney et al. [2011b]).

A one-sided bloodstain pattern occurs when a portion of the bloodstain is removed or unavailable for analysis. For example, if blood droplets impacted a wall and a chair, but the chair was removed from the scene, that portion of the bloodstain is unavailable for analysis. Fortunately, sometimes the remaining one-sided pattern can still be used to find the source of bloodletting, however this may not work for all situations. Maloney et al. [2011b] used a hammer striking a pool of blood siting on a hockey puck to create the bloodstain.

The known origin, in the form (x, y, z), of the impact was at coordinates (0.3 m, 1.038 m, 0.83 m). The average location from the analysis of 64 one-sided bloodstain patterns using *HEMOSPAT*™ gave a source of bloodletting at (0.244 m, 1.016 m, 0.895 m) which is stated by Maloney et al. [2011b] to be within a range of acceptable limits.

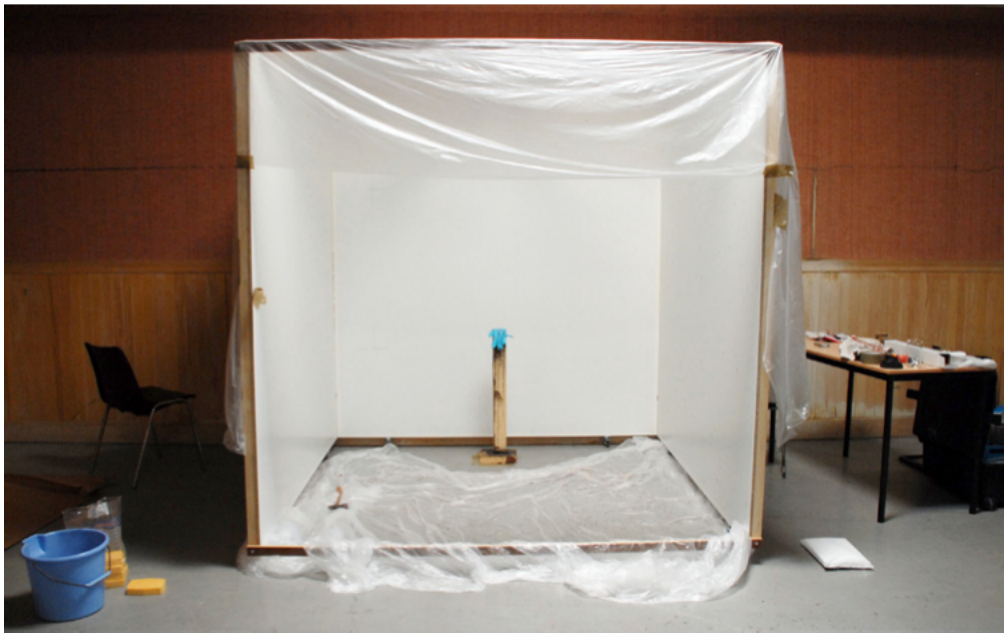

Figure 2.20: Experimental set up by Maloney et al. [2011b] where a pool of blood sitting on a hockey puck is struck with a hammer.

In Figure 2.20 it appears the source of bloodletting is placed close enough to the target wall to ensure the blood droplets will travel in straight lines to the surface. It would be interesting to see the same experiment and analysis repeated with the target moved further away from walls. This would allow the droplet enough flight time so as to let the forces of gravity and drag to have an effect. However, since *HEMOSPAT*™ uses SLGR, the software would fail to estimate at least the height of the source of bloodletting if the target was moved further away.

de Bruin et al. [2011] did a comparison between *BACKTRACK*™ and *HEMOSPAT*™. Nine experiments (three sets of three) were done using a mouse trap striking a pool of blood. The first set of three experiments were performed with the mouse trap 0.5 m away from the wall, and the second set of three experiments were carried out at 1 m away. The last set of three were carried out at 0.5 m away from two perpendicular walls. The distance between the mouse trap and the walls in these experiments is small enough to use SLGR for the analysis (Buck et al. [2010]).

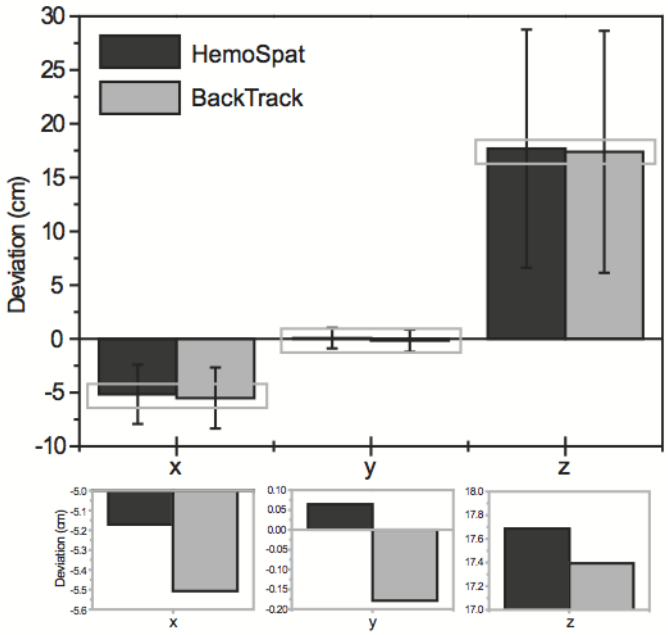

Figure 2.21: A comparison between *BACKTRACK*™ and *HEMOSPAT*™ by de Bruin et al. [2011]. 14 bloodstains were analysed using *HEMOSPAT*™ (dark grey) or *BACKTRACK*™ (light grey). The deviation of the estimated source of bloodletting from the known solution was measured and the mean deviations are shown in this figure. The difference between *BACKTRACK*™ and *HEMOSPAT*™ is enlarged in the small graphs on the bottom.

de Bruin et al. [2011] took 14 bloodstains from the three different experiments and used

BACKTRACK™ and *HEMOSPAT*™ to find the source of bloodletting. Figure 2.21 shows the results of the estimation of the source of bloodletting. The bottom of the figure shows the difference between *BACKTRACK*™ or *HEMOSPAT*™ results. The difference between the software packages are, according to de Bruin et al. [2011], "so small that they are forensically not relevant". However, in Figure 2.21 is it clear that the software packages overestimate the height of the source of bloodletting by over 0.15 m. This overestimation is shown in the bars indicating the deviation in the z-axis. This deviation is far greater than the deviations in the x and y-axes. The recommendations, listed by de Bruin et al. [2011] for using these SLGR software packages are:

- to choose bloodstains that are closest to the presumed position of the blood source;
- to choose large bloodstains (width $>$ 1.5 mm);
- to choose bloodstains that have a distinct elliptical form;
- to use bloodstains from more than one wall; and
- to be cautious in using *BACKTRACK*™ and *HEMOSPAT*™ when the blood source is presumably more than 0.5 m away, horizontally.

These software packages lack analysis of droplets which have fallen vertically, droplets where gravity and drag have affected their flight, and droplets which have fallen onto different surfaces. The analysis of surface roughness can be a method to limit the amount of errors when extracting information from a bloodstain. Considering software packages are approximations, the best analysis of the bloodstains using software will be achieved by reducing the amount of potential errors when investigating the surface. This section of the literature indicates the need for including the forces of gravity and drag, to models that predict the path of droplets from the source of bloodletting, to the stain. It also indicates the need to investigate how surface roughness affects the spread and appearance/shape of stains on surfaces.

2.12 Predicting the position of the source of bloodletting

This section outlines methods of estimating the position of bloodletting with models that include the forces of gravity. This is an advancement from the methods described in Section 2.11 as those methods are based on the string method which does not include the forces of gravity or drag.

It was noted by Williams [2000] that a large number of stains would have to be analysed to have an accurate prediction of the source of bloodletting. A 2 ml blood substitute (water and food dye) target was used and was impacted with a falling cylinder for the purpose of creating bloodstains. The velocity of impact was not recorded. One high-speed camera was used in conjunction with a mirror to give the capabilities of two high speed cameras. The calculations for finding the source of droplets travelling in curved trajectories could not be completed, because the modelling problem proved to be too difficult. However, the recognition of curved trajectories and the need for gravity acting upon the droplets was stated. In a separate paper, Knock and Davison [2007] found the diameter of a given blood droplet before it impacted a surface, and the velocity at which the droplet impacted the surface.

In a two-dimensional system neglecting the drag force on the droplet, an investigator should find the horizontal position of a droplet using the string method, and then find the vertical position of the droplet using the following equation based on kinematics (Knock and Davison [2007]):

$$y_i = y_f - \tan\theta_f \left(x_f - x_i\right) - \frac{g\left(x_f - x_i\right)^2}{2u_0^2 \cos^2\theta_f} \tag{2.108}$$

The variables with a subscript i are pertaining to the blood droplet's initial state and variables with subscript f pertain to the blood droplet's impact on a surface. These variables are shown in Figure 2.22.

The unknowns here are the vertical position of the source (y_i) and the impact velocity (u_0). The angle of impact on the surface, θ_f, can be found using a well-known expression called "the

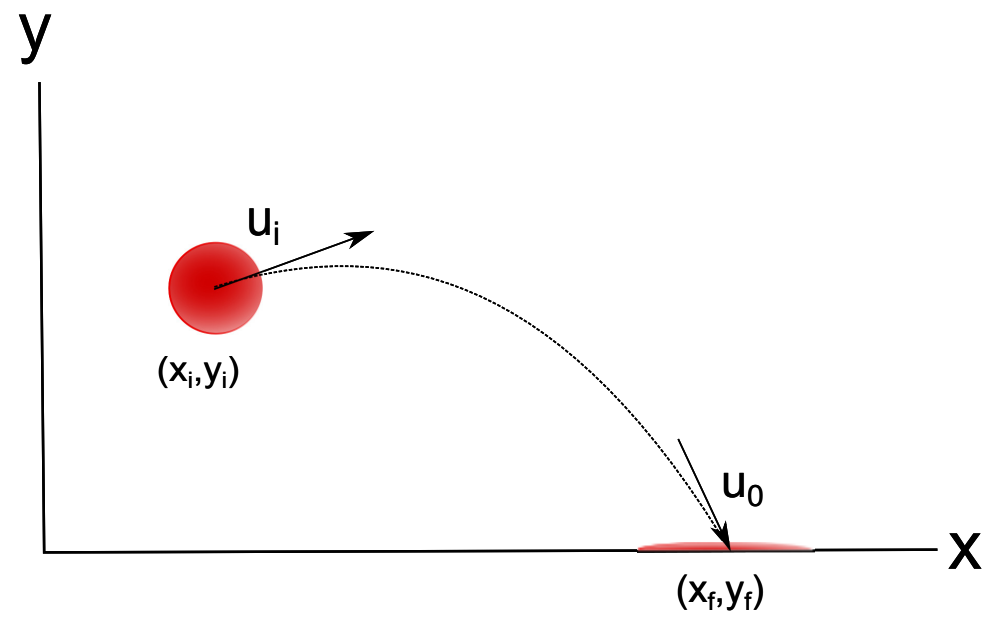

Figure 2.22: Illustration of a droplet before and after it impacts a surface where x_i and y_i are the coordinates of the droplet's initial position and the droplet is given an initial velocity of u_i. The droplet's impact velocity is denoted as u_0 and the droplet's final position (or coordinates of the resulting bloodstain) are denoted by x_f and y_f.

Balthazard formula" as stated by Bevel and Gardner [2001], where:

$$\sin\left(\theta_f\right) = \frac{d_i}{d_j}, \tag{2.109}$$

where θ_f is the impact angle, d_i is the minor diameter of the stain (or the width of the stain), and d_j is the major diameter of the stain (or the length of the stain) as shown in Figure 2.23.

So long as the crime scene investigator is clear about the cartesian coordinate system they are using, and the origin of this coordinate system, the final position of the bloodstain can be found (*i.e.*, x_f and y_f). The initial x-coordinate of the blood droplet can be found using the string method without being subject to the errors of estimating the height of bloodletting. The string is pulled backwards along the major axis (d_j) according to the impact angle. The problem with using the string method to find x_i is that if the trajectory of the blood droplet is curved, there is no way to tell what kind of curve the droplet has followed from the bloodstain alone. The droplet could have passed through a rather flat curve or a curve with a very high apex, therefore this does not prove how far away x_i is, only the line along which x_i lies. This method

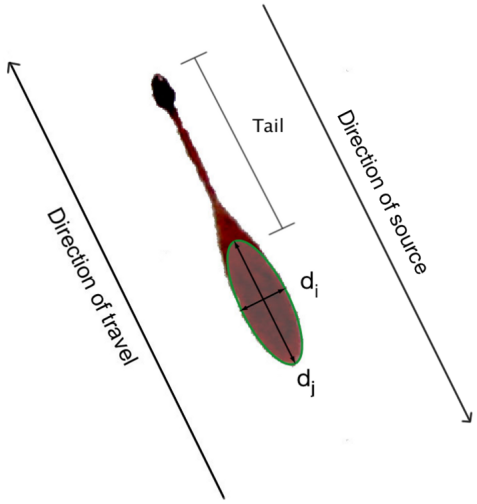

Figure 2.23: An edited depiction (tail of bloodstain is labelled) of classical measuring of bloodstains, where the direction of travel is indicated by the position of the tail of the bloodstain (Maloney and Maloney [2009]). The width of the stain (d_i) and length of the stain (d_j) are also labelled.

will only work in the context of other stains, *i.e.*, if there are multiple strings that intersect with one another. A data fitting method was implemented to find the impact velocity independent of Equation 2.108.

Knock and Davison [2007] focused on the parameter's stain size, denoted by $d_i d_j$, where d_i is the stain's width, d_j is the stain's length, and the number of spines on the stains, denoted by N. In Knock and Davison [2007]'s work, one equation gives information on the stain area being proportional to the impact velocity and the drop diameter, and the other equation shows the number of spines being proportional to impact velocity and the drop diameter.

The expression that makes most physical sense (according to Knock and Davison [2007]) when describing the stain size is given by:

$$\frac{d_i d_j}{d_0^2} = 0.0023\mathrm{Re} + 3.27\,. \tag{2.110}$$

The Reynolds number (Re) is defined in Section 2.1. Equation 2.110 is physically sound because as the size of the droplet and the impact velocity of the droplet tends to zero, the size of the stain tends to zero as well. However, better fits are found using equations that may not be as

physically sound (*i.e.*, when the impact velocity tends to zero, Equation 2.111 does not yield correct results) but can be applicable in the correct limits of the data collected. The equation that Knock and Davison [2007] found worked best for the limits of the collected data was:

$$d_i d_j = 111.74 \left(\mathrm{Re}\sqrt{\mathrm{We}}\right)^{\frac{3}{8}} d_0^2 + 0.00084\,. \tag{2.111}$$

The Weber number (We) is defined in Section 2.1. As for the number of spines, Knock and Davison [2007] found:

$$N = 0.76\sqrt{\mathrm{We}}\sin^3\theta_f\,, \tag{2.112}$$

which can be rearranged to find an expression for estimating the impact velocity:

$$\begin{aligned} N &= 0.76\sqrt{\mathrm{We}}\sin^3\theta_f \\ \frac{N}{0.76\sin^3\theta_f} &= \sqrt{\frac{\rho_l u_0^2 d_0}{\sigma_{lg}}} \\ \frac{\sigma_{lg}}{\rho_l d_0}\left(\frac{N}{0.76\sin^3\theta_f}\right)^2 &= u_0^2 \\ \sqrt{\frac{\sigma_{lg}}{\rho_l d_0}}\left(\frac{N}{0.76\sin^3\theta_f}\right) &= u_0\,. \end{aligned} \tag{2.113}$$

This can be used in Equation 2.111 to solve for d_0, which then can be substituted back into Equation 2.113 to solve for an expression of u_0. Further, setting the fitting coefficients to numbers that are more approximate can give more general expressions of these models. Appendix U shows the derivations (done in this thesis) of the following expressions for droplet diameter and impact velocity:

$$d_0 = \left[\left(\frac{d_i d_j}{100}\right)^8 \left(\frac{\sin^3\theta_f}{N}\right)^6 \left(\frac{\mu_l}{\sqrt{\rho_l \sigma_{lg}}}\right)^3\right]^{2/35} \tag{2.114}$$

and

$$u_0 = \left[\left(\frac{100}{d_i d_j} \right)^8 \left(\frac{\sigma_{lg}^{22}}{\rho_l^{16} \mu_l^3} \right) \left(\frac{N}{\sin^3 \theta_f} \right)^{41} \right]^{1/35}. \tag{2.115}$$

Now, there is an expression for impact velocity, Equation 2.108 can be used to find the height of bloodletting.

An advancement to this work (and the work by Boys [2003]) is the inclusion of air resistance on blood droplets. Without the drag force, the reconstructions of trajectories are limited to parabolas, whereas with the inclusion of drag, other more complex and possibly more accurate reconstructions can be made. Extending to three dimensions is unnecessary, as the horizontal position of the source can be obtained by the string method without major inaccuracy.

To test the model by Knock and Davison [2007] (with the general expression for impact velocity derived in this thesis) one would need experiments that consistently create bloodstains produced from droplets that fly in curved paths. To produce stains with angled impacts, Boys [2003] used water with food colouring (which is in common with the work done by King [2002]) to impact paper placed on an angle. The drop of liquid was released vertically onto the paper to simulate a shallow impact. To produce a curved path consistently perhaps a syringe can be set up on an angle, with a known volume of blood and the blood is forced out of the syringe with some indication of the initial force. There has yet to be conclusive work showing how to identify the difference between the following: a droplet impacting an angled surface perpendicularly, a droplet impacting a horizontal surface at an angle, and a droplet impacting a moving surface perpendicularly.

2.12.1 Errors in calculating the source of bloodletting

In a study by Willis et al. [2001], the variance of the estimated distance fallen, and the variance of the estimated angle of impact were studied. Willis et al. [2001] states that the variance of the height a droplet has fallen can be expressed as a function of the height the droplet has fallen and

the variance in the diameter of the droplet, as shown in Equation 2.116,

$$\sigma_H^2 = \frac{1}{B^2C^2} e^{2CH} \sigma_{d_0}^2 , \tag{2.116}$$

where σ_H^2 is the variance in height the droplet has fallen, $\sigma_{d_0}^2$ is the variance in the droplet's diameter, B and C are constants dependant on the volume and physical properties of the blood droplet, and H is the height the droplet initially fell from. It is not noted if Equation 2.116 can account for a droplet falling at terminal velocity, but the height of the droplet is held within an exponential function. Therefore, as the height the droplet falls from increases, the variance in the height also increases exponentially. It is unclear what values are used for constants B and C (or how they are derived). With these constants unknown it is not possible to test Equation 2.116 for a known height.

Willis et al. [2001] derived another expression (Equation 2.117) describing the variance of the impact angle as a function of the impact angle, length and width of a bloodstain, variance and covariance of the length and width of a bloodstain. So,

$$\sigma_{\theta_f}^2 = \frac{\sin^2\theta_f}{1-\sin^2\theta_f} \left[\frac{\sigma_{d_i}^2}{d_i^2} + \sin^2\theta_f \frac{\sigma_{d_j}^2}{d_i^2} - 2\sin\theta_f \frac{\sigma_{d_i d_j}^2}{d_i^2} \right] , \tag{2.117}$$

where θ_f is the impact angle, $\sigma_{\theta_f}^2$ is the variance of the impact angle, d_i is the width of the bloodstain, d_j is the length of the bloodstain, $\sigma_{d_i}^2$ is the variance of the width of the bloodstain, $\sigma_{d_j}^2$ is the variance of the length of the bloodstain, and $\sigma_{d_i d_j}^2$ is the covariance of the width and length. As the impact angle approaches 90°, the length and the variance of the length approaches the width, and variance of width, respectively. This results in a simplification shown in Equation 2.118:

$$\sigma_{\theta_f}^2 = \frac{\sin^2\theta_f}{1-\sin^2\theta_f} \left[(1+\sin^2\theta_f) \frac{\sigma_{d_i}^2}{d_i^2} - 2\sin\theta_f \frac{\sigma_{d_i d_j}^2}{d_i^2} \right] . \tag{2.118}$$

These formulae should be considered when estimating the source of bloodletting to give the results more context.

2.13 Blood substitute

Ideally, experiments in bloodstain pattern analysis (BPA), should use human blood because that is indicative of what will be found at a crime scene. However, none of the studies cited (Thoroddsen and Sakakibara [1998]; Mehdizadeh et al. [2004]; Hulse-Smith et al. [2005]; Knock and Davison [2007]; Brownson and Banks [2010]), employ the use of human blood. This is because of the health risks associated to experimentation using human blood *i.e.* risk of contracting HIV or hepatitis B or C (Raymond et al. [1996b] and the Advisory Committee on Dangerous Pathogens [2003]). Raymond et al. [1996b] deemed porcine blood to be an acceptable substitute for human blood. Horse blood has also been used in experiments for BPA by Brownson and Banks [2010], El-Sayed et al. [2011], Larkin et al. [2012], and Doom [2012].

Due to health and safety, the experiments in this thesis (Chapter 4) are restricted to the use of horse blood. The purpose of employing a non-biological blood substitute is to avoid unnecessary exposure to harmful infections previously discussed (Raymond et al. [1996b]), when training crime scene investigators and carrying out experiments. The Advisory Committee on Dangerous Pathogens [2003] also noted that bovine tuberculosis and Q fever are risks from cattle blood.

Human blood has been used safely in experiments (Pizzola et al. [1986a,b]; Maloney et al. [2011b]). However, other biological fluids have been used as acceptable alternatives to human blood in crime scene reconstruction, despite their nature as biohazards (Raymond et al. [1996b]; Kendall [2008]; McKechnie [2009]). The Advisory Committee on Dangerous Pathogens [2003] noted that streptococcosis is a risk from pig blood, regardless of it being a food item, but Raymond et al. [1996b] deems porcine blood an acceptable substitute for human blood. Horse blood has also been used as an appropriate substitute for human blood in experimentation (Kendall [2008]; McKechnie [2009]).

Ovine blood has also been used in bloodstain pattern analysis as a substitute for human blood with reportedly “no appreciable difference in results” (Sweet [1993]). But again the Advisory

Committee on Dangerous Pathogens [2003] notes that chlamydiosis is a risk from sheep or goat blood. The whole blood (unmodified blood) viscosity was studied for human, pig, and sheep blood (Laurent et al. [1999]). Laurent et al. [1999] measured the shear stress as a function of shear rate (using a Couette-type thermostated viscometer) to calculate the dynamic viscosity. These viscosities were measured at body temperatures, 37 °C for human blood, 38.5 °C for pig blood, and 39 °C for sheep blood. Figure 2.24 shows these measured viscosities, where sheep blood has the lowest viscosity at all shear rates, and pig blood has the highest viscosity at all shear rates. It is unclear as to how significant the differences in viscosities are for the purpose of BPA.

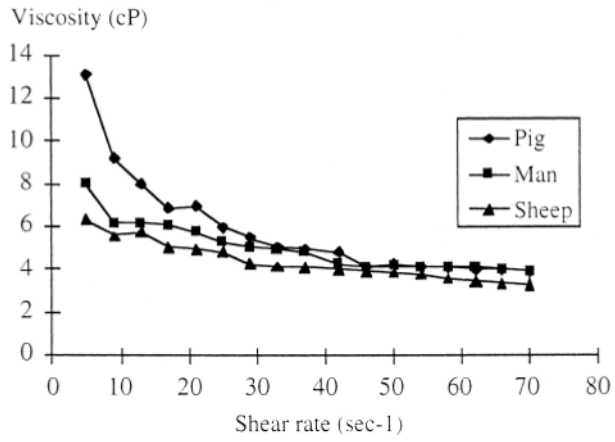

Figure 2.24: Measurements of the average viscosity (over five samples of each species) of human, pig, and sheep blood as a function of shear rate by Laurent et al. [1999]

Laurent et al. [1999] noted that the blood, from all species, begins to behave as a Newtonian fluid once the shear rate rises above $20\,s^{-1}$, because the red blood cells are separating (also known as erythrocyte disaggregation) at higher shear rates.

A non-biological substitute would be useful for the safe training of investigators. Knock [2011] and Balchin [2001] suggest that there is a possible non-biological substitute for blood, using Kollidon VA64, for use in mock crime scene reconstruction.

The substitute used by Knock [2011] was made with Kollidon VA64 and compared to porcine blood which was heated, using a water bath, to 37 °C. Two solutions were made, a 4 % Kollidon VA64 solution and a 6 % Kollidon VA64 solution. Knock [2011] found that plotting

the number of spines and the stain area, against non-dimensional numbers (which would account for physical properties of the liquids) yields the same results for porcine blood, distilled water, and the two Kollidon VA64 solutions.

The viscosity is a function of temperature for non-Newtonian fluids, hence why it is important to replicate the temperature of blood at a crime scene correctly.

The physical properties of blood have been studied at length by Raymond et al. [1996b] and is most commonly cited for the value of surface tension, viscosity and density of human blood (Raymond et al. [1996a]; Hulse-Smith et al. [2005]; Karger et al. [2008]; Larkin et al. [2012]; Ramsthaler et al. [2012]; Attinger et al. [2013]; Kabaliuk et al. [2013]). These properties are important in the analysis of bloodstains because the density, viscosity, and surface tension of blood will affect how the blood interacts with the surface. A summary of the physical properties of blood, water, and Kollidon VA64 can be found in Table 2.4.

The underlined value for pig blood in Table 2.4 was recorded mistakenly as 5.6×10^{-3} in the publication by Knock and Davison [2007], and the values for animal blood cited by Attinger et al. [2013] are species independent.

The values given by Raymond et al. [1996b] for human blood were not measured as a part of the experimental work carried out by that author, rather it is just mentioned as a reference, and it is unclear where the values came from. The values given by MacDonell [1993] for the surface tension and kinematic viscosity were taken from an unpublished work by Seliger [1978]. The density is not recorded by MacDonell [1993] and so the dynamic viscosity cannot be calculated. This is reflected by Balchin [2001] and Knock [2011].

Millington [2001] tried to create a blood substitute for human blood using supermarket bought items (for example, jelly mix, flour, syrup) therefore the consistency of the ingredients of the fluid could vary.

As noted by Balchin [2001], the measurements of the viscosity were performed using a viscometer. Shin and Keum [2002] proposed a new tool to measure the viscosity of blood which is an extended mass-detecting capillary viscometer. This tool works in less than two minutes,

thus the blood can be measured without the use of anticoagulants. The details of how this new viscometer works can be found in the publication by Shin and Keum [2002], and it should be noted that this new method is simple and quick whilst maintaining accuracy in the measurement of viscosity.

The surface tension was measured, by Balchin [2001] using a DU NOUY surface balance. Balchin [2001] also measured the density using a density bottle with known weight. Wallpaper paste and soluble starch (concentrations: 0.65 % to 1 %) were considered in the search for a blood substitute. According to Balchin [2001], the wallpaper paste was inapplicable because it "did not completely dissolve and consequently left a granular residue in the viscometer... giving inaccurate results". It was also found that there were no ingredients on any of the wallpaper paste packaging and therefore it was difficult to know if they had changed between cartons and make. Further, using a market bought product introduces variation between each package that cannot be regulated, similar to the work by Millington [2001]. The soluble starch was inapplicable because the viscosity was too unstable for constant experimentation.

After dropping various liquids vertically onto paper Balchin [2001], showed that Kollidon VA64 7.5 % (density of $1014\,\mathrm{kg\,m^{-3}}$, dynamic viscosity of $3.48 \times 10^{-3}\,\mathrm{N\,s\,m^{-2}}$, and a surface tension of $5.42 \times 10^{-2}\,\mathrm{N\,m^{-1}}$) does match the non-dimensional properties of human blood at room temperature. However, the Kollidon VA64 7.5 % substitute does not match the stain shape and size which is more important for experimentation and the training of forensic investigators. Properties of Kollidon VA64 include (Balchin [2001]):

- being very soluble in hydrophilic (water) and hydrophobic (butanol) liquids;
- being stable when stored at room temperature;
- its viscosity is only affected by temperature (*i.e.* it becomes non-Newtonian) when the concentration is increased, and so at lower concentrations the viscosity will remain the same from 25 °C to 40 °C; and
- it has no acute toxicity.

Balchin [2001] found that a 5 % increase of concentration in Kollidon VA64 will only cause a

$2.33 \times 10^{-6}\,\mathrm{m^2\,s^{-1}}$ increase in viscosity, and the increase is linear. While 7.5 % Kollidon VA64 reportedly had the best matching viscosity to that of blood, the measurement of the viscosity of 7.5% Kollidon VA64 was also found with the highest amount of error (2.9 %). Further, from concentrations 6.5 % to 9 % there was nearly no change in surface tension. The normalisation was calculated by taking the mean of three measurements of the surface tension of Kollidon VA64 (at varying concentrations), and multiplying it by the ratio of the theoretical surface tension value of water, to the experimental surface tension value for water. The normalisation was calculated because the substitute was sticking to the ring during the measurements. Even with this limitation the surface tensions measured were comparable to that of blood.

The density of Kollidon VA64 (7.5 %) at body temperature was $1011\,\mathrm{kg\,m^{-3}}$ and is not accurate (as compared to human blood at body temperature (37 °C), which is $1056\,\mathrm{kg\,m^{-3}}$ to $1061\,\mathrm{kg\,m^{-3}}$). Perhaps trying higher concentrations would achieve the correct density match. There are no data tables for Kollidon VA64 at body temperature so the concentration required to match the density cannot be predicted. According to the data, at room temperature (23 °C to 25 °C), the concentration required would need to be close to 27.6 % to match the density of human blood (Balchin [2001]). In closing, the closest known non-biological substitute to blood, made with Kollidon VA64 of concentration 7.5 %, have the following properties (at 25 °C):

- kinematic viscosity of $3.788 \times 10^{-6}\,\mathrm{m^2\,s^{-1}}$;
- density of $1014\,\mathrm{kg\,m^{-3}}$;
- dynamic viscosity of $3.841 \times 10^{-3}\,\mathrm{N\,s\,m^{-2}}$; and
- surface tension of $5.94 \times 10^{-2}\,\mathrm{N\,m^{-1}}$.

It appears that all properties in the list above (except the density) fall within the ranges of human blood at body temperature given by Raymond et al. [1996b]. It is a little curious as to why the measured properties from MacDonell [1993] are so different or missing. More experimentation looking at the number of spines and the stain size of droplets impacting at an angle should be carried out, to compare the stains from Kollidon VA64 and human blood.

Table 2.4: Comparisons of the physical properties of blood, water, and Kollidon VA64

Substance (cited by)	Temperature (°C)	Dynamic Viscosity ($10^{-3}\,\mathrm{N\,s\,m^{-2}}$)	Density ($\mathrm{kg\,m^{-3}}$)	Surface Tension ($10^{-2}\,\mathrm{N\,m^{-1}}$)
Human Blood (Attinger et al. [2013])	20	6.3	1052-1063	6.1
Human Blood (MacDonell [1993])	25	N/A	N/A	4.9-5.8
Human Blood (Raymond et al. [1996b])	37	3.2-4.4	1056-1061	5.1-6.1
Human Blood (MacDonell [1993])	37	N/A	N/A	2.7-3.4
Human Blood (Hulse-Smith et al. [2005])	37	3.8-5.1	1052-1063	5.1-5.7
Human Blood (Attinger et al. [2013])	37	1.6-5.1	1052-1063	2.7-5.8
Human Blood (Adam [2013])	N/A	4.4	1060	6.2
Pig Blood (fresh) (Raymond et al. [1996b])	37	3.9-5.4	1062	5.1-5.8
Pig Blood (fresh) (Knock and Davison [2007])	37	4.8	1062	5.6
Pig Blood (fresh) (Hulse-Smith et al. [2005])	37	3.4-6.1	1062	5.3-5.8
Horse Blood (Doom [2012])	37	4-49	1045.7-1070.4	4.5-4.6
Horse Blood (Larkin and Banks [2013])	37	4.7	N/A	N/A
Horse Blood (Brownson and Banks [2010])	37	3.29	N/A	N/A
Horse Blood (El-Sayed et al. [2011])	37	3.42-3.42	N/A	5.1
Horse Blood (Larkin et al. [2012])	37	3.47	1062	5.1
Animal Blood (Attinger et al. [2013])	20	8.6	1062	6.5
Animal Blood (Attinger et al. [2013])	37	3-20	1062	5.1
Blood (type undefined, Laan et al. [2014])	37.5	4.8	N/A	N.A
Water (Knock [2011])	25	1.00	1000	6.6-7.25 [Raymond et al. [1996b]]
Water (Attinger et al. [2013])	37	0.7	993	7.0
Kollidon VA64 (7.5%) (Balchin [2001])	37	2.007	1011	6.0

Chapter 3

Computational tools developed

3.1 Automation of counting spines on vertical impact drip stains

3.1.1 Motivation

In crime scenes where there are bloodstain patterns, finding the position of the source of bloodletting is a helpful tool for crime scene investigators (CSIs) to reconstruct the events at a crime (MacDonell [1993]; Bevel and Gardner [2001]). Currently, finding the source of bloodletting is accomplished by using straight line reconstructions (MacDonell [1993]; Bevel and Gardner [2001]) which ignore the effects of gravity on a blood droplet's trajectory (Knock and Davison [2007]). The inaccuracy caused by ignoring the effects of gravity can lead to finding the source of bloodletting up to 2 m higher than the correct source (Buck et al. [2010]). Therefore, it is necessary to include the forces of gravity and drag.

In order to include the effects of gravity on the trajectory of a bloodstain it is necessary to know the impact velocity of the droplet (Knock and Davison [2007]; Attinger et al. [2013]). Further, to include the effects of drag on a droplet, the size of the droplet must be known (Attinger et al. [2013]). It has been shown that the impact velocity of a blood droplet can be

determined from the area and number of spines on a bloodstain (Hulse-Smith et al. [2005]; Knock and Davison [2007]). A spine is defined as a thin ligament that emerges from the raised rim of a droplet spreading (Kieser et al. [2013], Scientific Working Group on Bloodstain Pattern Analysis [2013]; see Figure 3.1).

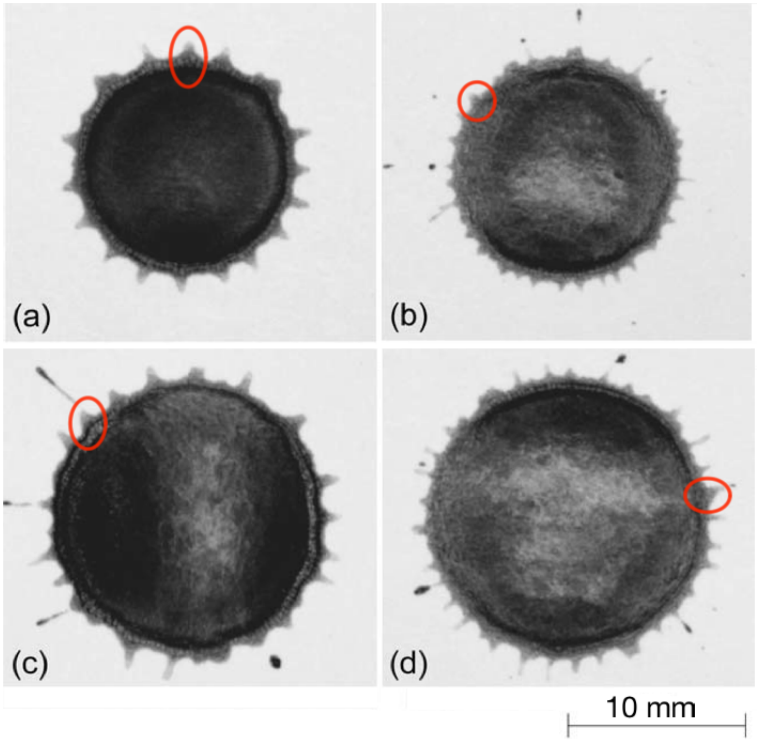

Figure 3.1: Porcine bloodstains produced by Hulse-Smith et al. [2005]. Blood droplets impacted a paper surface vertically, and exhibited spines. Droplet radii, r, and height h are as follows: a) $r = 1.85 \times 10^{-3}$ m, $h = 0.305$ m, b) $r = 1.5 \times 10^{-3}$ m, $h = 1.219$ m, c) $r = 2.15 \times 10^{-3}$ m, $h = 0.61$ m, d) $r = 1.85 \times 10^{-3}$ m, $h = 1.219$ m. Examples of spines are highlighted by the circles.

The two unknowns in this problem then are the impact velocity, u_0, and the droplet diameter, d_0. Section 2.10 shows Equations 2.103 and 2.104 (without fitting constants) which are suggested in the literature to calculate u_0 and d_0 from the stain diameter (it is not clear which diameter) and the number of spines on a stain.

Currently, the size of a bloodstain at a crime scene is determined manually and the number of spines are not determined. The impact speed and size of the droplet are also determined manually in laboratory work. This is time consuming and can invite human error (Attinger

et al. [2013]). The purpose of this section is to demonstrate an Automated Spine Counter (ASC, Section 3.1.5) that can be used to automatically determine the area and number of spines on bloodstains in the field of bloodstain pattern analysis (BPA).

3.1.2 Strategy

The aim of the Automated Spine Counter (ASC) is to provide BPA with a tool that inputs bloodstains and automatically outputs the number of spines on the bloodstain along with other stain properties such as the stain area, perimeter, outer diameter, and inner diameter. The intention of this program is to deal with the vertical impacts first (which produce circular stains, as shown by Pizzola et al. [1986a]) then to move on to angled impacts (which produce elliptical stains, as shown by Pizzola et al. [1986b]) in future work. The advantage of such a tool is that the spines are determined consistently as opposed to an investigator counting the spines manually which could introduce human error. Also the automation saves time. In order to automate the measurement of the bloodstain size and determine the number of spines the following strategy is used:

1. Experiments are carried out in order to generate data to develop a model. These experiments used single horse blood droplets that impact a paper substrate vertically (described in Chapter 4).
2. An automated spine counter is developed using MATLAB. It is used to count the spines on a bloodstain from a digital photograph, in order to find a correlation between the number of spines and the Weber number (Section 3.1.5).
3. The accuracy of the model is validated by comparing it to existing models in the literature for counting spines and also comparing it to manual counts of spines, shown in Section F.2 and Section F.3.

3.1.3 Survey

The literature supporting this section can be found in Chapter 2, but in short the models that the ASC will be compared against are based on the following relationship between spines, N, and the Weber number, We:

$$N = C\sqrt{\mathrm{We}} \tag{3.1}$$

where C is a data fitting constant. The Weber number, We, is given by:

$$\mathrm{We} = \frac{\rho_l u_0^2 d_0}{\sigma_{lg}}, \tag{3.2}$$

where d_0 is the droplet diameter, u_0 is velocity of the droplet, ρ_l is the density of the droplet, and σ_{lg} is the surface tension of the droplet. The value of C (in Equation 3.1) for models by Mehdizadeh et al. [2004], Hulse-Smith et al. [2005], and Knock and Davison [2007] are different depending on the experiments performed.

Mehdizadeh et al. [2004] derived the following model:

$$N = 1.14\sqrt{\mathrm{We}}. \tag{3.3}$$

A different relationship was found by Hulse-Smith et al. [2005]:

$$N = 0.955\sqrt{\mathrm{We}}. \tag{3.4}$$

Finally, the model by Knock and Davison [2007]:

$$N = 0.76\sqrt{\mathrm{We}}. \tag{3.5}$$

See Section 2.8 for a review of these models.

3.1.4 Experimental technique

The purpose of the horse blood experiments is to produce data of horse bloodstains to validate the computational analysis presented in this section. The experimental method for this work can be found in Chapter 4. The horse bloodstains used in this section are from the horse blood droplets that impacted conditioned paper (Appendix A), vertically. This data is used to validate the model described in Section 3.1.5.

3.1.5 Computational determination of stain properties

This subsection describes the procedure of measuring the size of a bloodstain and counting the spines on a bloodstain in a digital photograph (collected from the experiments, Chapter 4). The Automatic Spine Counter (ASC) described in this section collects the following information from the experimental data: the inner diameter of the bloodstain; the outer diameter of the bloodstain; and the number of spines on the bloodstain.

The analysis of the resulting bloodstains from horse blood experiments (Chapter 4) and pig blood experiments (data collected by Davison [2005]) was carried out using built-in image analysis functions from MATLAB. These tools convert digital photographs to binary images to isolate the stain in an image. The properties of these binary regions can be used to find the stain area and number of spines on the stain.

Measurement of the number of spines, area, perimeter, inner diameter, and outer diameter of a stain

Before using the ASC on the digital photographs, some manual preprocessing must be performed. First, the conversion factor from pixels to centimetres is measured using the ruler in the photograph (see Figure 3.2).

Next, the bloodstain is cropped out to isolate it from the rest of the photograph (see Figure 3.3). This cropped photo is now ready for the ASC. The ASC will start the analysis by

Figure 3.2: Photograph of the resulting bloodstain from a horse blood droplet, of radius 2.3×10^{-3} m, falling from a height of 0.5 m.

converting the colour image to a binary image (Figure 3.4) using the MATLAB function **im2bw** (MathWorks [2015a]).

Figure 3.3: Bloodstain cropped from digital photograph

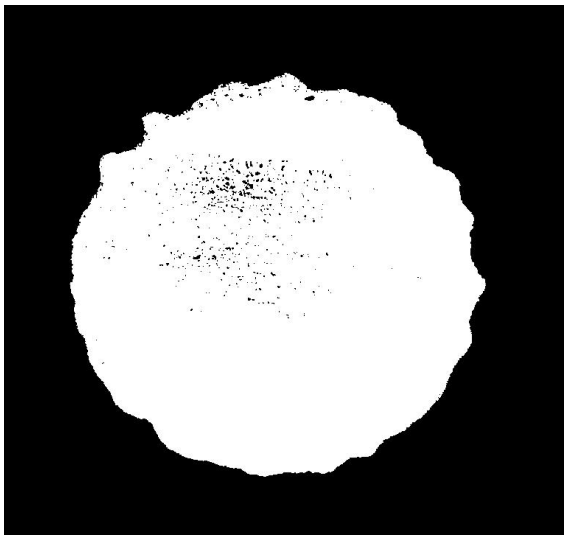

Figure 3.4: Bloodstain converted to binary image.

It should be noted that MATLAB has difficulty extracting the image of the bloodstain when there is a lot of reflection off the stain because of the flash from the camera, therefore some stains needed alternative lighting. Using a small handheld work light is sufficient for lighting the stain. Further, the steel substrates tend to cause low contrast between the blood and the substrate which is difficult for MATLAB to distinguish. In these cases, the colour of the photograph

would be adjusted manually to increase contrast before being used in the automated process.

The line drawn along the outer edge of the bloodstain (Figure 3.5) is performed using **bwboundaries** in MATLAB (a function that traces the edges of a region in a binary image MathWorks [2014b]) and then the properties (*i.e.*, the centroid and area of the region) inside this edge are retrieved using **regionprops** in MATLAB.

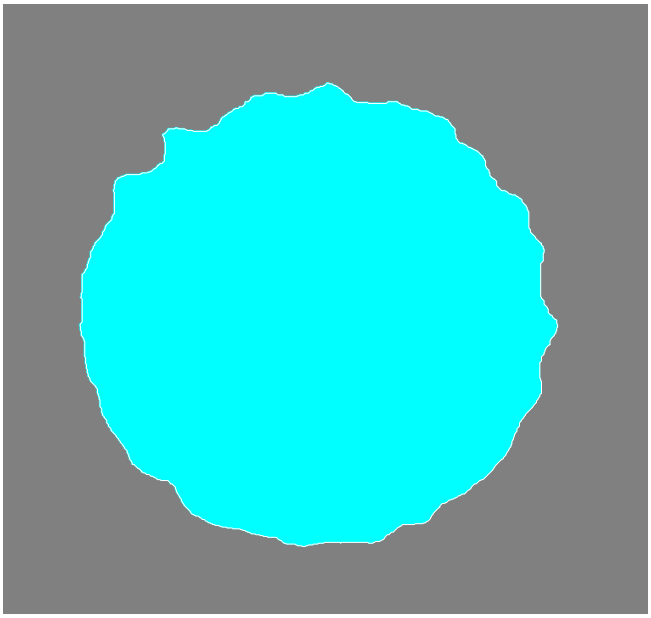

Figure 3.5: Edge and region of bloodstain visualised in MATLAB.

The following steps are used to identify the local maxima on the edge of the bloodstain:

1. The centroid of the region shown in Figure 3.5 (a shape measurement performed by **regionprops** that specifies the x and y coordinate of the centre of mass of a region MathWorks [2014d]) is found and the radii to every point along the edge of the region is calculated.
2. A circle (using **viscircles**, a MATLAB function to create circles with a specified centre and radius MathWorks [2014c]) is drawn on the inside of the region, depicting the inner diameter, using the closest point on the edge (or the smallest radii) to the centroid.
3. Using the largest radii, a circle is drawn on the outside of the region, depicting the outer diameter, using the farthest point on the edge (or the largest radii) to the centroid as shown

in Figure 3.6.

Figure 3.6 is the same as Figure 3.5 but with the inner and outer diameters labelled, along with the spines identified.

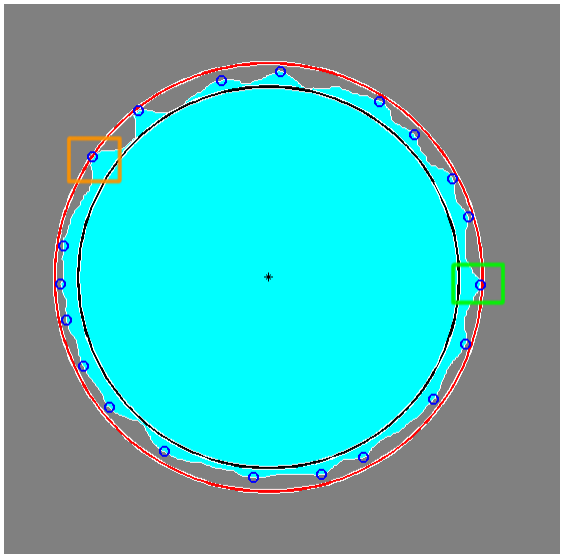

Figure 3.6: Identified spines, inner (black circle) and outer diameter (red circle) overlaid on the bloodstain. The green and orange squares identifies spines on the bloodstain that corresponds with the peaks in the green and orange squares in Figure 3.7. There are 20 spines identified on this stain.

Since the radii to every point on the edge is known, this can be plotted. These data points are smoothed using a Savitsky-Golay filter. This filter smooths data in a vector or matrix by estimating neighbouring data points with low-degree polynomials using a linear least-squares method. In MATLAB, the function is **sgolayfilt** MathWorks [2014a]. This filter was used because it is proficient at smoothing noisy data and is often used with peak data MathWorks [2014f]. Peaks in this graph (see Figure 3.7) are points of largest radii or points furthest from the centre of the region. These are spines on the bloodstain. In order for a peak to be defined as a spine, the following method is used. To explain this mathematically, let the radii on the edge of the bloodstain be denoted as r_i and the mean of all the radii on the edge of the stain is $\bar{r}$. The maximum radius is denoted as $\max_{i \in n} r_i$ and the minimum radius is $\min_{i \in n} r_i$. In order for a peak to be chosen is must be larger than a threshold, $\mathbb{T}$:

$$\mathbb{T} = 0.9\,(\bar{r})\,, \tag{3.6}$$

and the peak must be larger than its surrounding data points by the following selection value, $\mathbb{S}$:

$$\mathbb{S} = \frac{\max_{i\in n} r_i - \min_{i\in n} r_i}{50}\,. \tag{3.7}$$

Equations 3.6 and 3.7, respectively, were found from testing and checking during the development of this tool.

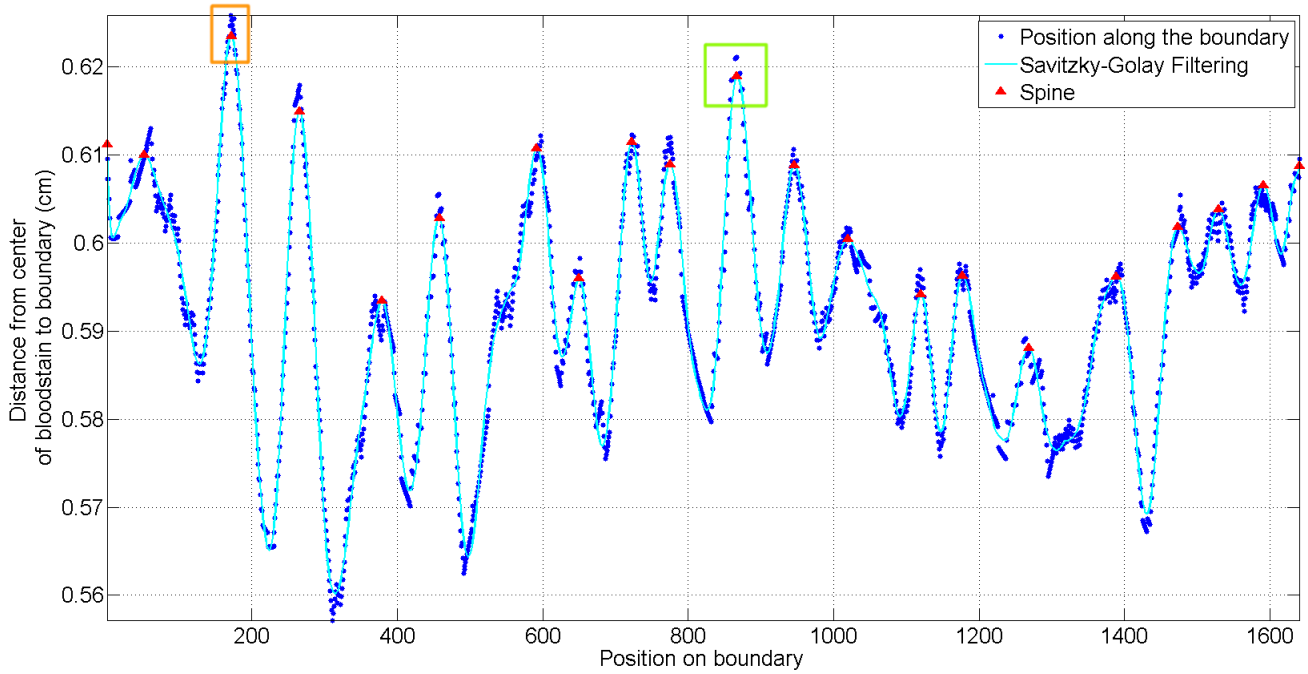

Figure 3.7: Distances from the centre of the bloodstain to the edge of the bloodstain with a Savitsky-Golay filter and identified peaks. The green and orange squares identifies peaks that corresponds with spines on the edge of the bloodstain in the green and orange squares in Figure 3.6. There are 20 spines identified in this example.

3.1.6 Conclusion

This section showed the design of an Automated Spine Counter which has the capability of measuring the spines, area, perimeter, inner and outer diameter, of a bloodstain. This program

was formulated using various MATLAB tools and has proven to improve the speed and accuracy of the vertical bloodstain analysis during the course of this thesis. A comparison of this program against the conventional manual counting of spines can be found in Appendix F. There it is shown that the ASC does not yield statistically different results when counting spines as compared to manual counting. This is an advantage because the ASC is faster, consistent, and removes human variability. Further, Appendix I shows a comparison between the ASC and *ImageJ* which shows that the ASC yields the same measurements for stain area for the bloodstains. It also shows that the ASC has more capabilities than *ImageJ* as it can measure more properties of the stains (inner and outer bloodstain) and can measure the perimeter of the stain more accurately.

3.2 Automation of estimating the droplet properties at impact

3.2.1 Motivation

In order to retrieve the diameter and impact velocity of the droplet from the high-speed videos, a program was written in MATLAB. The program is broken down into two parts: retrieving the diameter of the droplet, and tracking the droplet to calculate the velocity. For brevity, the program will be referred to as the Diameter and Velocity Video Processor (DVVP).

3.2.2 Retrieving droplet diameter

The high-speed video, of the falling droplet being analysed, is read into MATLAB and the frames where the droplet is falling are kept. This means frames at the beginning of the video where the droplet has not entered the view of the camera yet are not loaded and frames at the end of the video when the droplet begins deforming from impact are also not loaded.

The user is asked to measure a known distance within the frame of the video (using the

ruler tool in MATLAB, measuring how many pixels are in a known distance on the physical ruler in the video). This gives the number of pixels per centimetre in the high-speed video (see Figure 3.8).

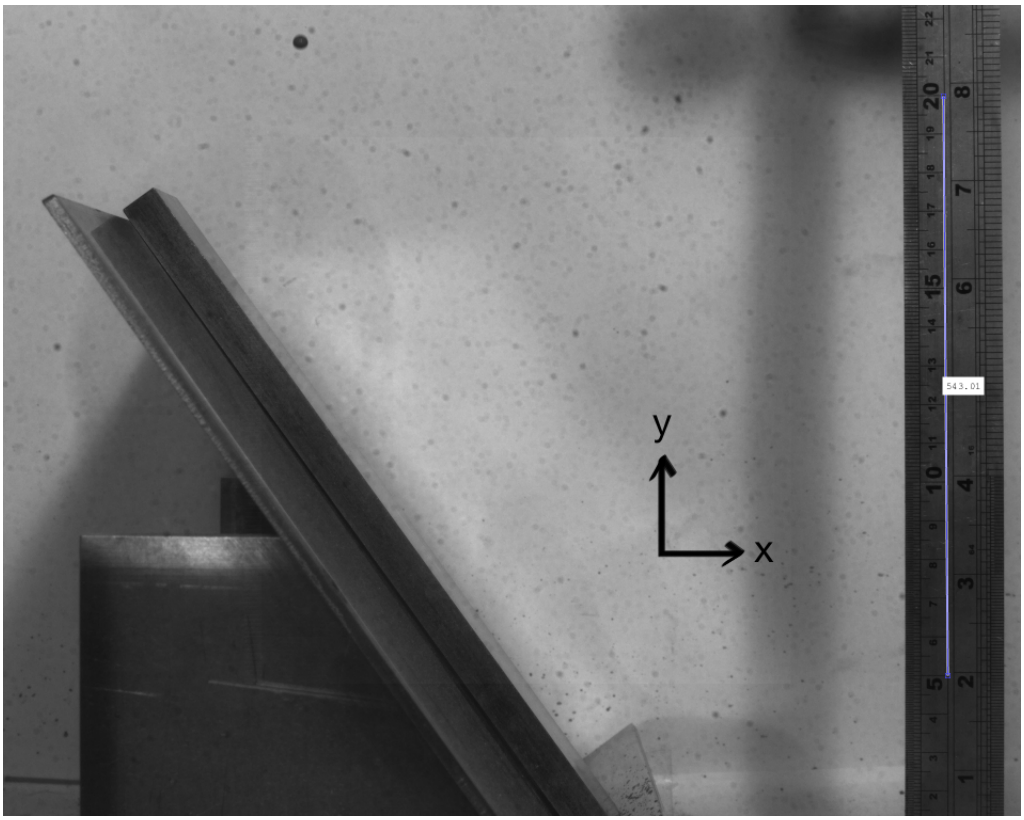

Figure 3.8: Screenshot from the DVVP showing the user measuring, in pixels, a known distance on the physical ruler in the high-speed video.

This needs to be carried out for every video because if experiments are performed on different days, the distance of the high-speed camera to the droplet impact may have changed slightly, changing the focus of the camera. Also, using different ramps to simulate impact angles will change the position of the droplet impact and thus the camera needs refocusing.

Next, the user is then asked to draw a box around the droplet and its anticipated flight downwards (see Subfigure 3.9a). The dimensions and position of this box are saved into MATLAB and are used to crop out parts of the frame that are not needed for retrieving the diameter or velocity of the droplet.

With all the information from the previous subsection, the droplet diameter can be estimated.

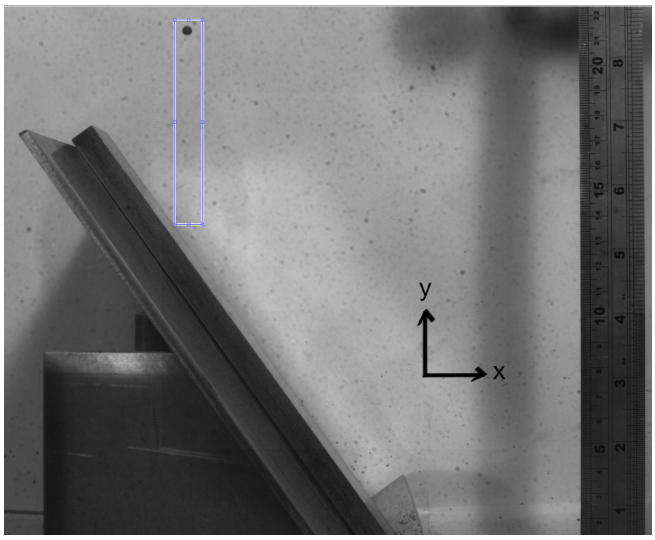

(a) Screenshot from the DVVP showing the user outlining where the droplet is expected to fall in the frame.

(b) Screenshot from the DVVP showing the program cropping the high-speed video frame and outlining the droplet found.

Figure 3.9: Screenshots from the DVVP showing the program successfully finding the droplet within the high-speed video and preparing to track the droplet.

Using the cropped rectangle (Subfigure 3.9b), the function **imfindcircles** is used to locate the droplet. The user must confirm if the droplet has been located correctly.

If the droplet has been located correctly the frame is cropped again (around the droplet) and converted to binary. Then **regionprops** as described being used by the ASC (Section 3.1) is used to estimate the diameter of the droplet.

3.2.3 Retrieving the impact velocity

Once the diameter of the droplet has been estimated, each frame of the droplet's fall is converted to a binary image and in each frame, **regionprops** is used to estimate the position of the droplet (from the centre of the droplet).

The x and y vectors were adjusted to start at zero as shown in Figure 3.10. The y-coordinates decrease smoothly as expected but the x shows a slight curve around the line $x = 0$. This can either be caused by the droplet not falling directly straight down or could be from radial distortions of the droplet (oscillations) as it falls. Figure 3.11 depicts the velocity of the droplet.

The velocity of the droplet was calculated by using the mean of the tracked velocity over three frames:

$$u_i = \frac{\sqrt{(x_{i+2} - x_i)^2 + (y_{i+2} - y_i)^2}}{t_{i+2} - t_i}, \tag{3.8}$$

where i is the time step, x is the x-coordinate of the droplet, y is the y-coordinate of the droplet, t is time, and u is the velocity. The mean of the last three velocity calculations is the estimated impact velocity:

$$u_0 = \frac{u_{n-2} + u_{n-1} + u_n}{3}, \tag{3.9}$$

where u_0 is the impact velocity and n is the last time step in the high-speed video. Using Equation 3.9 is the method used in literature for finding the impact velocity in high-speed videos (Davison [2005]; Knock and Davison [2007]).

Both Figure 3.10 and Figure 3.11 are from the analysis of a blood droplet of radius 2.024×10^{-3} m falling from a height of 0.5 m.

It should be noted that the scatter in Figure 3.11 is not related to pixilation, *i.e.* an error in finding the centroid of the droplet in one pixel rather than another pixel. To prove this the following argument is made: There are 60 frames captured in the video, resulting in a video length of 0.012 s and 2×10^{-4} s between each frame. The first tracked velocity is $5.54\,\mathrm{m\,s^{-1}}$ thus the distance that droplet has traveled in one frame can be calculated as 1.1×10^{-3} m, which is approximately 4 pix (since the high-speed video has a scale of $3.62 \times 10^3\,\mathrm{pix\,m^{-1}}$). The impact velocity is calculated using the movement over 3 frames (Equation 3.9) or 12 pix. If the centroid of the droplet is chosen (by the DVVP) to be off by ± 1 pix then the distance the droplet is traveling in each frame can be incorrect by $\pm 2.75 \times 10^{-4}$ m. The error in finding the tracked velocity then would be $\pm 1.4\,\mathrm{m\,s^{-1}}$. If the scatter in the velocity was caused by pixilation, the range of tracked velocities would be from $4.14\,\mathrm{m\,s^{-1}}$ to $6.94\,\mathrm{m\,s^{-1}}$ which is not seen in Figure 3.11. This also shows that the DVVP is finding the centroid of the droplet to

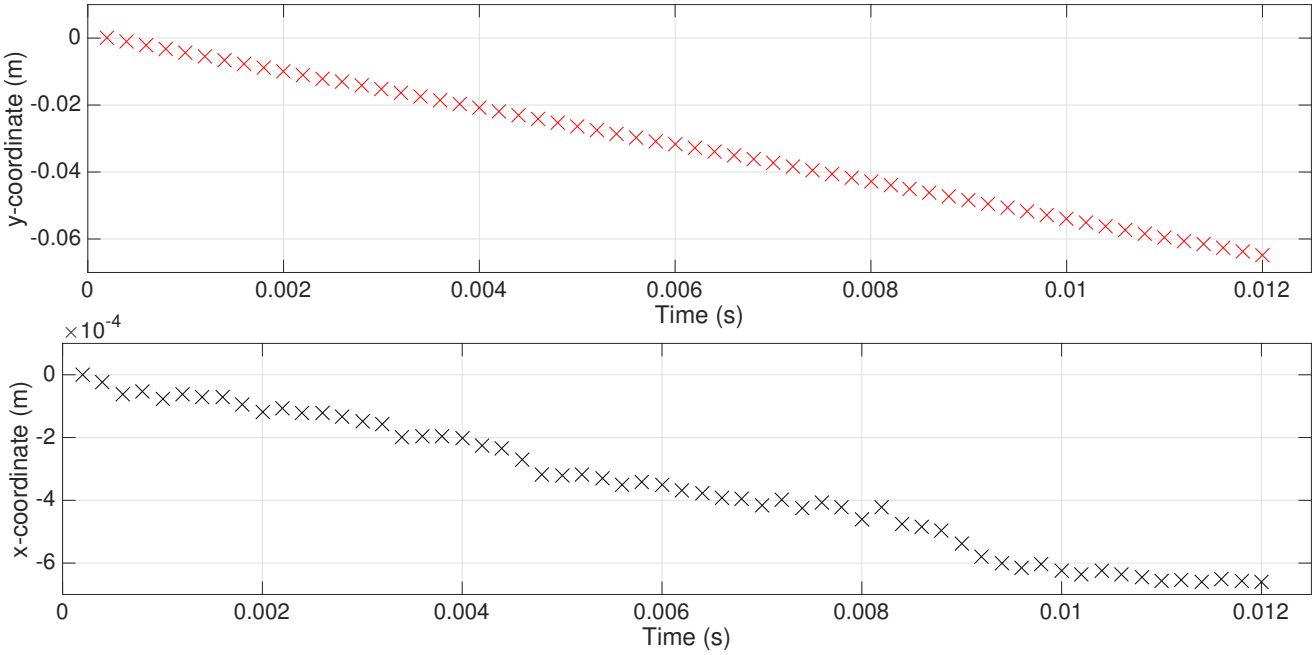

Figure 3.10: x and y position of a horse blood droplet, with diameter 4.00×10^{-3} m, falling from a height of 2.0 m to impact a roughened steel substrate.

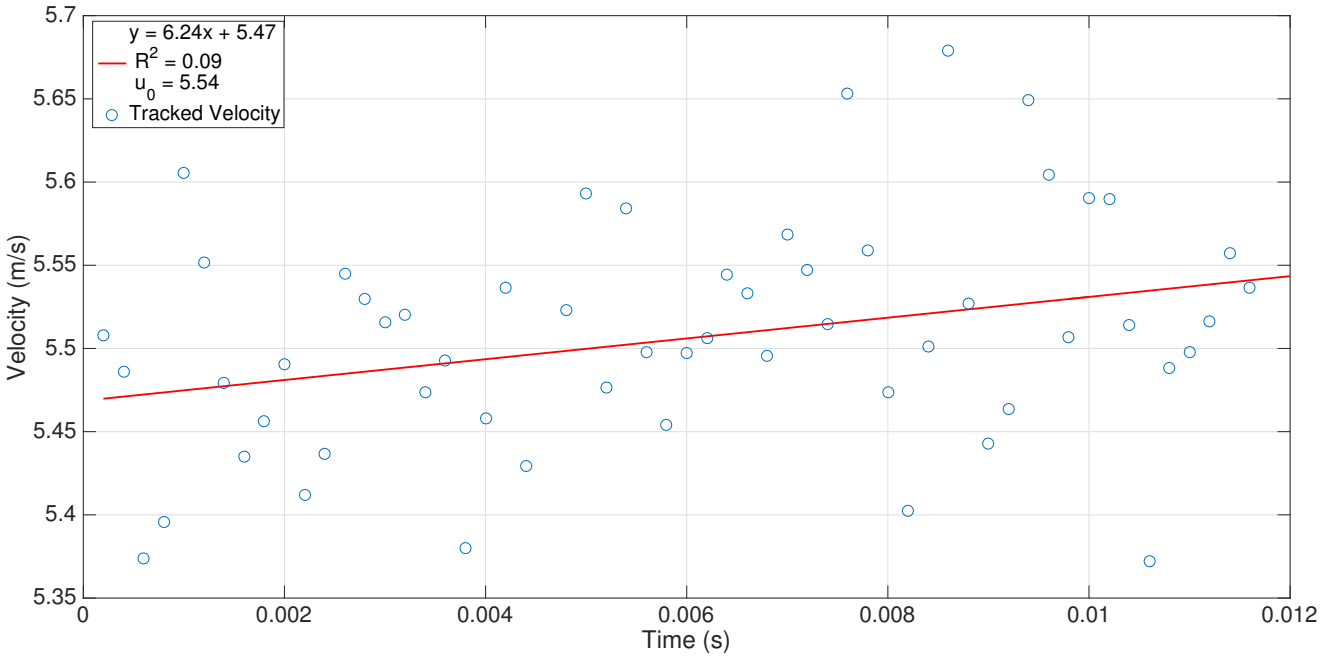

Figure 3.11: Plot of the velocity of the droplet tracked in every frame of the high-speed video, with a linear fit. The impact velocity is calculated using Equation 3.9.

better than 1 pix accuracy.

3.2.4 Testing the accuracy of the DVVP

Ball bearings of known diameter were used to test the accuracy of the DVVP. The results from the *Phantom Camera Control* software were also compared to the results from the DVVP.

Table 3.1 shows a comparison of the DVVP to the PCC when estimating the diameter of the droplet before impact. The number of pixels per centimetre in the high-speed video is also provided. It can be seen that the DVVP can not only estimate the known ball bearing diameters to a good accuracy but it is also estimating the diameter much better than the PCC. For example, comparing the results from the PCC and the DVVP estimating the diameter of the 4.00×10^{-3} m, it can be seen that the DVVP has 0 % error whereas the PCC has 2.50 % error. The percent error is calculated using Equation B.1 (Appendix B).

Table 3.1: Comparing the estimated of droplet diameter, d_0, by *Phantom Camera Control* software (PCC) and the Diameter and Velocity Video Processor (DVVP).

True Diameter (m)	pix cm^{-1}	d_0 estimated by PCC (m)	% error	d_0 estimated by DVVP (m)	% error
3.175×10^{-3}	36.1	3.600×10^{-3}	13.39	3.220×10^{-3}	1.42
4.00×10^{-3}	36.1	4.100×10^{-3}	2.50	4.000×10^{-3}	0.00
4.75×10^{-3}	36.2	5.000×10^{-3}	5.26	4.750×10^{-3}	0.00
5.00×10^{-3}	36.1	5.800×10^{-3}	16.00	5.500×10^{-3}	10.00

Table 3.2 shows a comparison of the estimated impact velocity as carried out by the PCC and by the DVVP. It appears that for larger ball bearings and smaller ball bearings there is a larger percent difference between the two programs and their estimations. However, for the ball bearing of diameter 4.00×10^{-3} m (which is best used to test the diameter of the droplets in these experiments) the percent difference is not as large. The percent error is calculated using Equation B.2 (Appendix B).

Further, the DVVP is an automated process that is quicker than manual clicking on the

Table 3.2: Comparing the estimated of impact velocity, u_0, by *Phantom Camera Control* software (PCC) and the Diameter and Velocity Video Processor (DVVP).

True Diameter (m)	u_0 estimated by PCC ($\mathrm{m\,s^{-1}}$)	u_0 estimated by DVVP ($\mathrm{m\,s^{-1}}$)	% difference
3.175×10^{-3}	3.69	3.08	17.93
4.00×10^{-3}	3.22	3.37	4.68
4.75×10^{-3}	3.23	3.40	5.26
5.00×10^{-3}	3.68	3.27	11.67

bottom of the droplet in every frame in PCC which could introduce human error. Using the DVVP eliminates any human error by automatically tracking the centroid of the droplet in every frame.

3.2.5 Conclusion

The DVVP is a MATLAB based tool that has been developed in this thesis to eliminate human error in the analysis of high-speed videos. The DVVP does not rely on the user to track the droplet manually or measure the size of the droplet manually. Instead the DVVP will find the droplet in each frame and use image analysis tools to measure properties of the droplet and track the droplet in the frame. The DVVP has been shown to be more accurate in estimating the diameter of ball bearings. The DVVP also cuts down analysis time significantly, running the DVVP will take on average 2.3 min but it most cases will be much faster (as quickly as 19.7 s). A direct comparison of the speed of using the DVVP to PCC on the same video is 57 s (DVVP) compared to 5 min (PCC).

Chapter 4

Experimental methodology

4.1 Motivation

In order to investigate how the roughness of a surface alters the shape and size of a bloodstain drops of blood are dripped from known heights onto a variety of substrates at different angles. These experiments are restricted to the use of horse blood because of the health risks associated with human blood (Chapter 2). However, in the literature, horse blood is used and has been accepted as an appropriate substitute for human blood. The data collected from these experiments are:

- diameter of blood droplet before impact;
- impact velocity of the droplet;
- area of the bloodstain;
- perimeter of the bloodstain;
- inner diameter of the bloodstain (*i.e.*, diameter not including spines, Subfigure 4.13a);
- outer diameter of the bloodstain (*i.e.*, diameter including spines, Subfigure 4.13b);
- the number of spines on the bloodstain;
- length of the bloodstain;
- minor diameter of the bloodstain; and

- major diameter of the bloodstain.

4.2 Experimental method

Similar to experiments carried out by Hulse-Smith et al. [2005] and Knock and Davison [2007], a single blood droplet was dripped via pipette (Figure 4.1) from a known height onto a substrate. The blood in the pipette was heated to 37 °C in a water bath to emulate the temperature of blood in the body (Knock and Davison [2007]; Brownson and Banks [2010]; El-Sayed et al. [2011]; Larkin et al. [2012]; Attinger et al. [2013]). To prevent coagulation the blood was stirred regularly whilst the temperature was being controlled. The full laboratory setup can be seen in Figure 4.2. The heights used were 0.5 m, 1.0 m, 1.5 m, and 2.0 m. While the droplets are being formed by pressing them out of a pipette, the droplet is not "pushed" out of the pipette. The droplet is allowed to form at the end of the pipette and filming does not begin until the gravitational forces overcome the surface tension forces to allow the droplet to fall from the pipette.

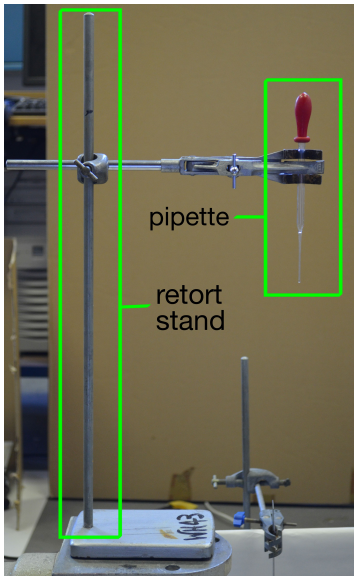

Figure 4.1: Pipette mounted onto retort stand, used to drip single droplets onto a known substrate from a known height.

The droplet impacts were filmed using a Phantom V12, black and white, high-speed camera

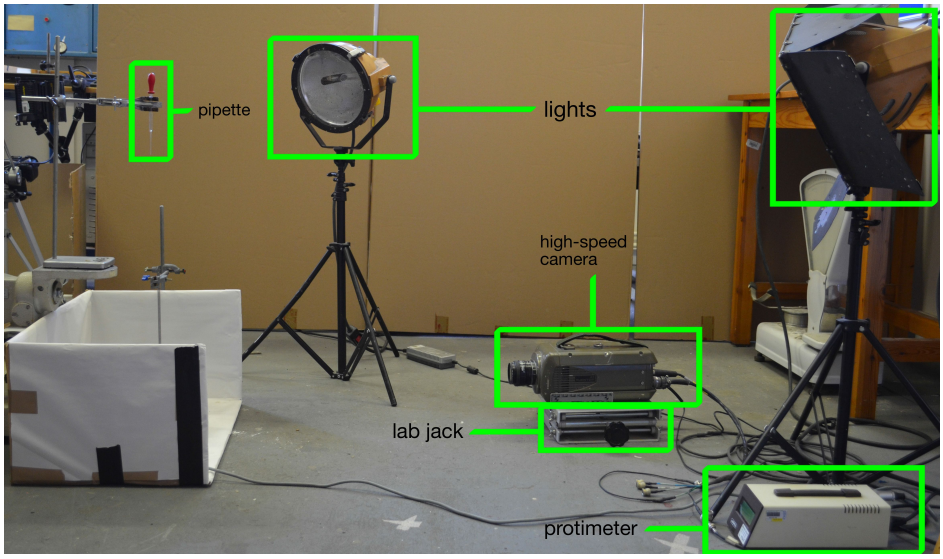

Figure 4.2: Laboratory setup for dripping single droplets onto different substrates.

(Figure 4.3) at 5000 frames per second with an exposure of 40 µs. To accommodate the high frame rate of the high-speed camera, the experiment was lit using two 1000 W lights (shown in Figure 4.2). The resolution of the high-speed video was 960×544 pixels. The high-speed camera is 0.3 m away from the droplet impact and is fitted with a 50 mm lens. The resulting bloodstains were photographed using a 58 mm Canon Zoom Lens, which is 0.25 m away from the stain (Figure 4.4). This gives digital images with a resolution of 4272×2848 pixels. The digital photographs of the stains were taken between 30 s and 60 s of the droplet impacting the surface. In both the high-speed videos and the digital photographs, a ruler was used for scale which allowed measurements to be made to ± 0.05 cm following the rule of measuring to half the smallest division on a measuring device. The distances of the cameras from the resulting bloodstain and droplet impacts are approximate because during experiments, sometimes the cameras need to be moved slightly to ensure the best photograph or video is captured.

This high-speed video setup was used to collect the impact velocity and diameter of the droplets. The droplet was tracked manually in the *Phantom Camera Control* software in the last ten frames of the droplet's fall. The mean of the last three velocity measurements are taken as the impact velocity. The diameter is measured in the videos as well (ten frames before impact) using the measuring tool in the *Phantom Camera Control* software. The average resolution of

the high-speed videos and digital photographs can be found in Table E.1.

Figure 4.3: Phantom V12, black and white, high-speed camera, mounted onto a lab jack.

Figure 4.4: Canon camera fitted with a 58 mm lens used to photograph the resulting stains.

The angles of impact were 90°, 72°, 54°, 36°, and 18° (see Figure 4.5). Scientific Working Group on Bloodstain Pattern Analysis [2013] defines the angle of impact as the acute angle at which a droplet strikes a target.

The angle of impact is measured with respect to the y-axis. These angles of impact were obtained by placing the substrate onto a small ramp at that angle. Figure 4.6 shows the different

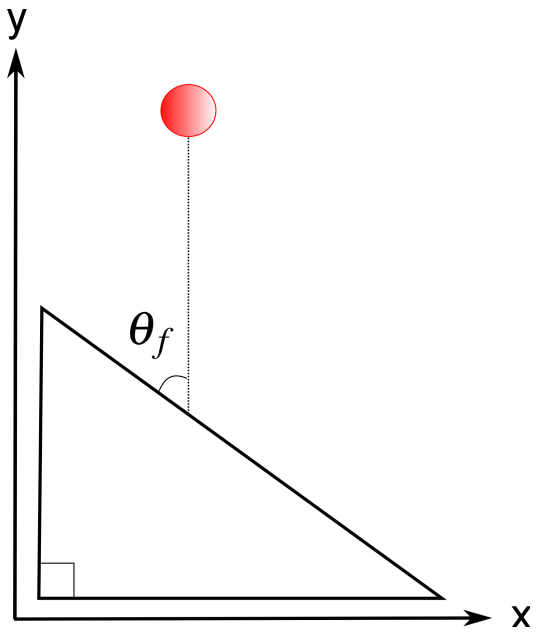

Figure 4.5: Illustration of a droplet impacting a ramp at impact angle θ_f.

angled ramps. The substrates are placed onto the ramp, lined up underneath the pipette. To keep stray droplets from splashing around in the lab and also to reflect light inwards towards the impact, a white box is used to house the impacts. For scale, a ruler also is placed in the box with the substrate, which can be seen by the high-speed camera (Figure 4.7).

A protimeter is also placed inside the box to measure the temperature and humidity of the lab setup whilst the experiments are occurring (Figures 4.8a and 4.8b). The two 1000 W lights generate a lot of heat when switched on, therefore during the experiments the lights are only switched on during filming with the high-speed camera (*i.e.* they are switched on right before the droplet is released from the pipette, then they are shut off immediately after impact).

Figure 4.9 shows the fluctuations of temperature and humidity when the lights are turned on and off during experiments over a full day. It can be seen that the temperature does fluctuate up and down (this is caused by the work lights being turned on and off), however the temperature is in a range of 12 °C and does not stray far from room temperature. Further, this is the temperature of the laboratory space, not of the substrate itself. Therefore, these fluctuations are not affecting the conditions of the blood impacting the surface. Lastly, the blood temperature is controlled

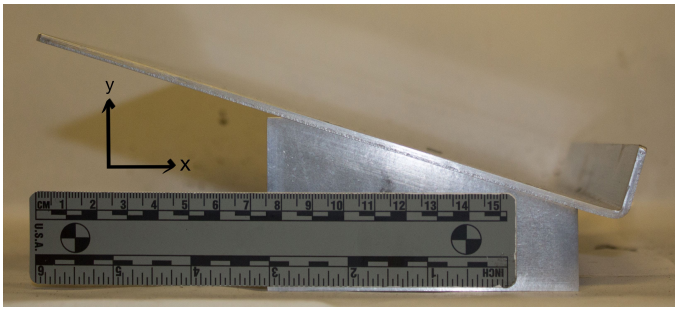

(a) $\theta_f = 72°$ ramp.

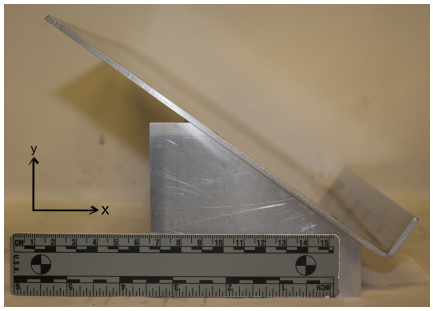

(b) $\theta_f = 54°$ ramp.

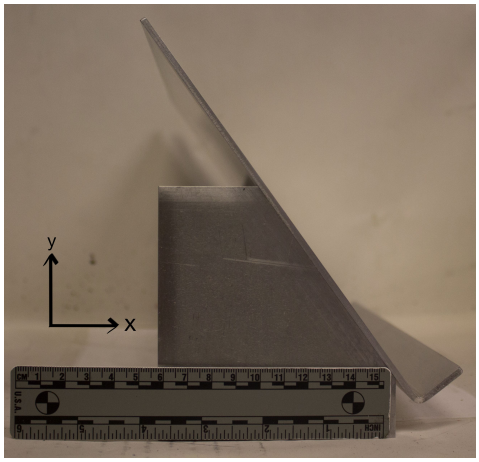

(c) $\theta_f = 36°$ ramp.

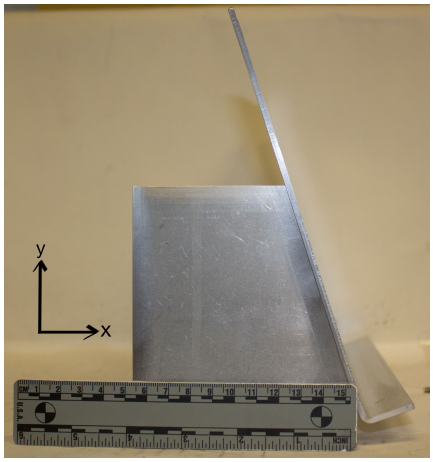

(d) $\theta_f = 18°$ ramp.

Figure 4.6: Ramps upon which substrates are placed to achieve angled impacts.

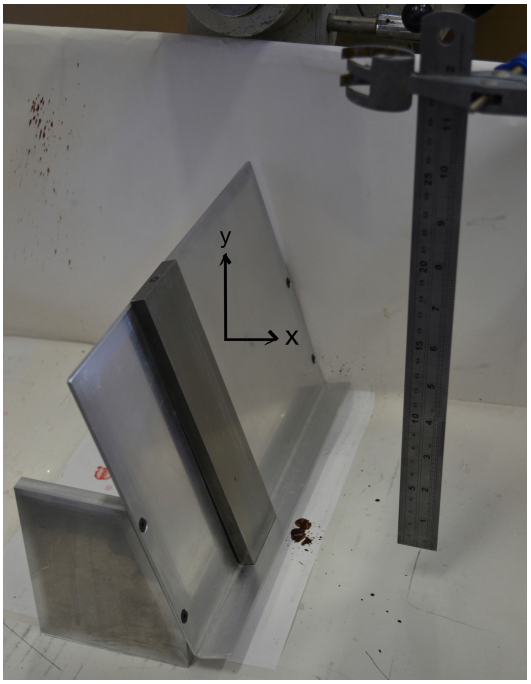

Figure 4.7: Steel substrate placed onto $\theta_f = 18°$ ramp.

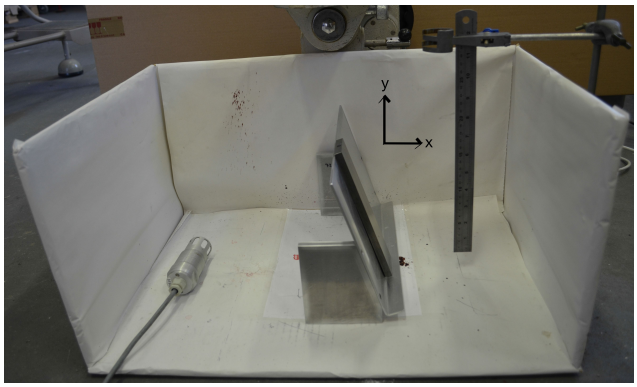

(a) Side view of white box with ramp, substrate, ruler, and protimeter placed inside

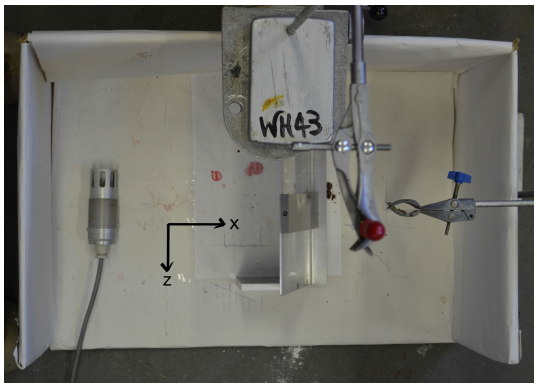

(b) Overhead view of the white box with the ramp, substrate, ruler, and protimeter.

Figure 4.8: Apparatus set up in the white box.

to 37 °C and photographs are taken within a minute of the impact, another counter measure to ensure the conditions of the laboratory are not affecting the formation of the bloodstains.

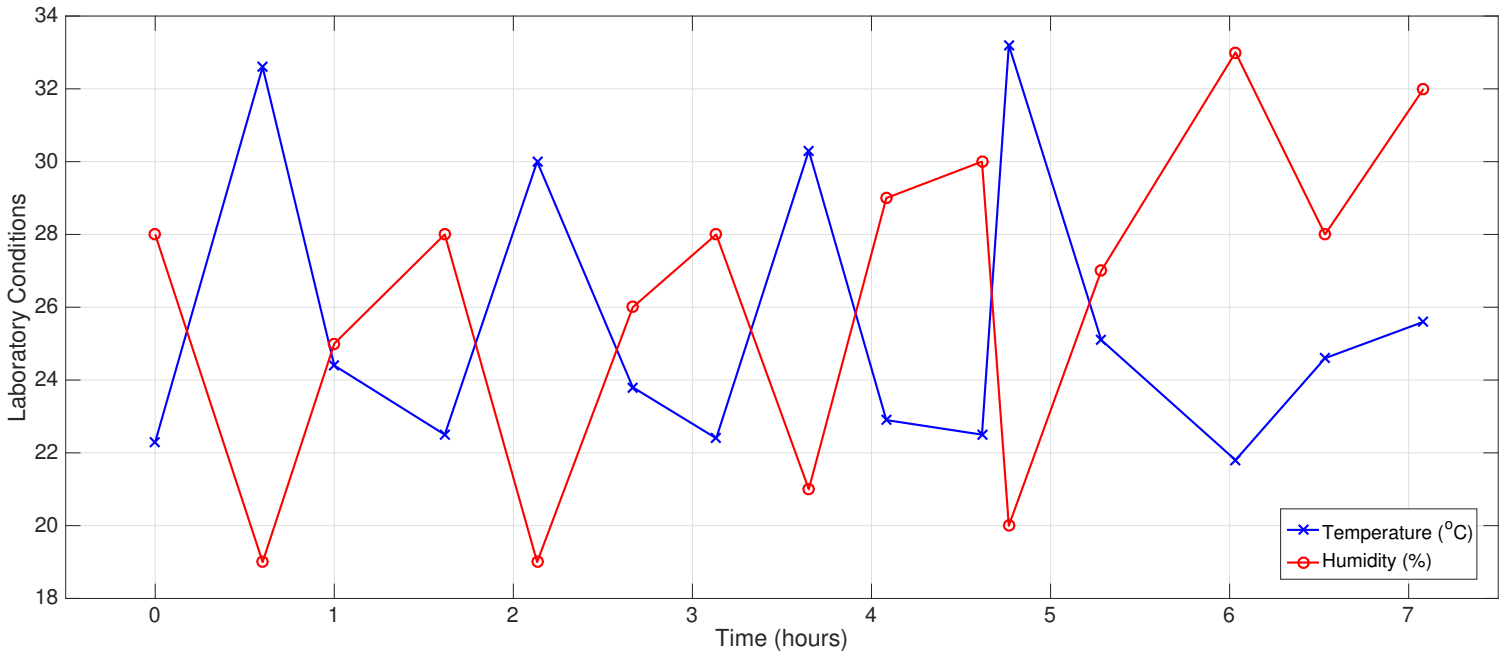

Figure 4.9: Temperature and humidity in the lab setup as measured by a protimeter during a day of experiments.

Different substrates, paper and steel, were used. The conditioned paper was conditioned to British Standard BS EN 20187:1993 (British Standard [1993], see Appendix A). Unconditioned paper was included for comparison. Paper has a roughness of $R_a = 1.3 \times 10^{-8}$ m (as measured

by a Surtronic surface roughness tester). The steel substrates had different roughness values of: $R_a = 0\,\text{m}$, $1.6 \times 10^{-6}\,\text{m}$, $3.2 \times 10^{-6}\,\text{m}$, and $6.3 \times 10^{-6}\,\text{m}$. The roughnesses of the substrates were calculated using Equation 4.4. The definition of roughness can be found in Section 2.4. It should be noted that the steel substrates were thick enough to be completely rigid during impact.

The steel plates were roughened using a milling technique. When milling, a rotary cutter is moved across a surface, cutting as it rotates around a circle of a known diameter. The dimensions of the steel substrates were: 0.2 m by 0.05 m by 0.01 m.

The substrates being used in this work are all the same size, with a geometric area of $A_{geo} = 0.01\,\text{m}^2$.

Calculating the actual area (A_{ac}) uses the following assumptions:

- all the grooves milled into the surface are exactly the same width (x in Figure 4.10) and height (h in Figure 4.10) across the entire surface; and
- the grooves are perfectly symmetrical and triangular.

These assumptions are made clearer in Figure 4.10

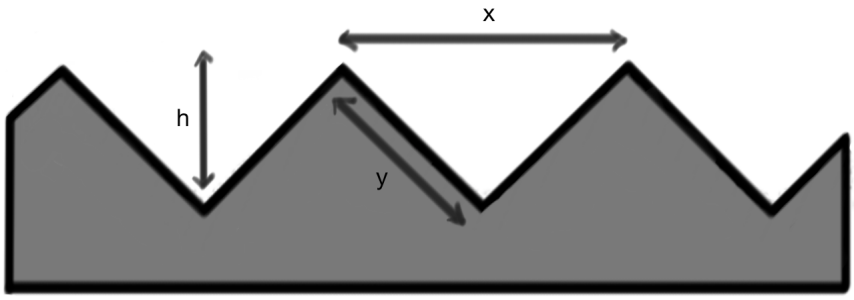

Figure 4.10: Illustration of assumed triangular grooves on the roughened surfaces used in this work.

A Profile Projector PJ 300 was used to measure the number of peaks (p) over a known distance (l) along the surface, and was also used to measure the height of a peak (h) and the distance between peaks (x). In order to calculate $\mathbb{R}$, the actual area of the roughened surfaces must be measured. To achieve this, the distance y in Figure 4.10 is calculated using Pythagorean theorem:

$$y^2 = \left(\frac{x}{2}\right)^2 + h^2 \tag{4.1}$$

$$y = \sqrt{\frac{x^2}{4} + h^2}\,. \tag{4.2}$$

The area of any pleat (which is a rectangle) on either side of a peak can then be calculated by multiplying y by the width of the surface, W. This area is illustrated in Figure 4.11.

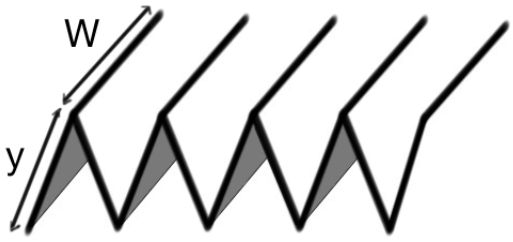

Figure 4.11: Illustration of a theoretical roughened surface.

Across the full length of the surface (L) each peak will have a slope on either side, except the first and last peaks. To find the total number of peaks (P) across the length of the surface (L), a ratio was used:

$$P = \frac{pL}{l}\,, \tag{4.3}$$

where p is the number of peaks measured (by the Profile Projector PJ 300) over a known distance (l).

Therefore, the actual area of the roughened surface, A_{ac}, will be the sum of all the areas of each slope:

$$\begin{aligned} A_{ac} &= 2yW\,(P-1) \\ &= 2W\sqrt{\frac{x^2}{4}+h^2}\,(P-1) \\ &= 2W\sqrt{\frac{x^2}{4}+h^2}\left(\frac{pL}{l}-1\right). \end{aligned} \tag{4.4}$$

In this thesis, the R_a value is used because the Surtronic used to measure the surface roughness of paper outputs this roughness parameter, and a Profile Projector PJ 300 was used to measure certain properties of the steel substrates that are easily used to find an R_a value. It should be noted that surface roughness is not the only parameter that promotes secondary droplets. Increasing the radii of the droplet (r), the impact speed (u_0), and the roughness of the surface (R_a) will all encourage splashing of the droplet on impact.

There were only two steel plates for each roughness which meant, after the photograph of the resulting bloodstain had been taken, the steel substrate had to be cleaned. The steel substrates were cleaned using a 1 % Virkon solution (to remove any biological material from the substrate). Then the steel substrates were cleaned with a Mykal degreaser wipe and left to dry for at least five minutes before their next use. For each height, five to ten trials were performed. For vertical impacts, only five trials were performed. For angled impacts onto paper or onto the smooth steel surface only five trials were performed. For angled impacts onto the roughened steel substrates (R_a = 1.6×10^{-6} m, 3.2×10^{-6} m, and 6.3×10^{-6} m), ten trials were performed: five with the droplet impacting against the grain of the surface finish and five impacting with the grain.

4.3 Recommendations to improve experimental methods

Improvements to the experimental method include having a second person to aid with the experiments. This person can be used to continually wash the steel substrates as they are being used. If possible a third person can be used to take the still photographs and maintain the

database of digital photographs as they are being produced. These additions would cut the time of experiments greatly. Further, the user should be wary of the ruler casting a shadow over the droplets flight path downwards. Lastly, the user should be careful not to save the videos with the droplet too close to the top of the window when it is entering the shot. The droplet should be fully in view before saving the video.

4.4 Experimental results

From the above experiments, different variations of drip stains emerged. This section will lay out the different types of drip stains, their major properties, and how they were measured.

4.4.1 Circular bloodstains

Circular bloodstains often occur when blood droplets impact the surface perpendicularly. They exhibit spines, have an inner diameter, an outer diameter, a total stain area, and total stain perimeter. Figure 4.12 shows a few bloodstains with the examples of spines labeled in blue circles.

The inner and outer diameter of a bloodstain can be seen (labeled as green circles) in Figure 4.13. In this thesis, the inner diameter is the distance from the centre of the stain to the closest edge of the stain (inner radius), multiplied by two. Similarly, the outer diameter is the distance from the centre of the stain to the farthest edge (normally to the end of the longest spine), multiplied by two. Generally, in the literature, these definitions are not clearly stated or these properties are not measured at all.

The stain area is defined to be the area of the bloodstain (which is an irregular shape because of the spines). The ASC (from Chapter 3) measures the area to include the spines of a bloodstain. When using *ImageJ*, the spines are also included. In other work (using porcine blood) Davison [2005] used the following formula to calculate the stain area:

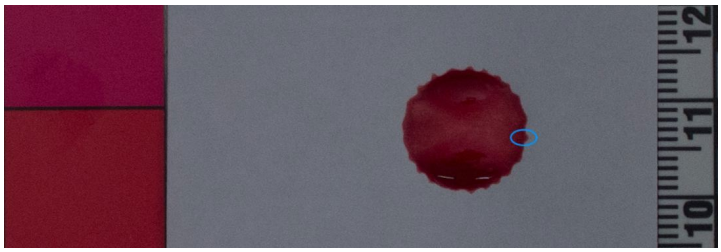

(a) $H = 0.5\,\text{m}$, $d_0 = 4.0 \times 10^{-3}\,\text{m}$, $u_0 = 3.03\,\text{m}\,\text{s}^{-1}$, $N = 25$

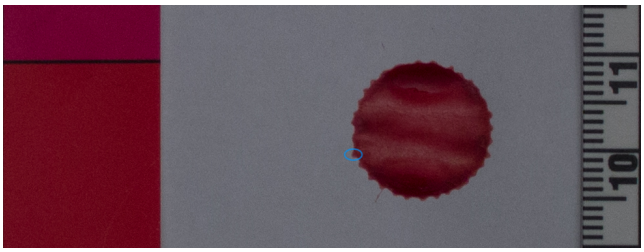

(b) $H = 1.0\,\text{m}$, $d_0 = 4.2 \times 10^{-3}\,\text{m}$, $u_0 = 4.38\,\text{m}\,\text{s}^{-1}$, $N = 32$

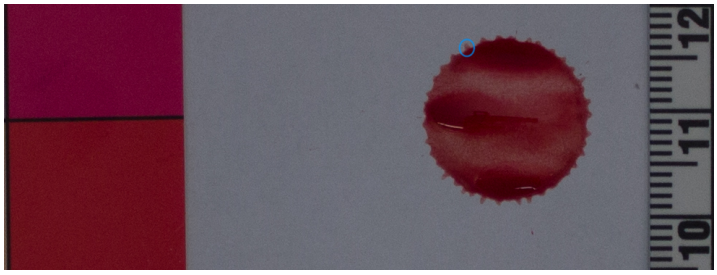

(c) $H = 1.5\,\text{m}$, $d_0 = 4.4 \times 10^{-3}\,\text{m}$, $u_0 = 4.86\,\text{m}\,\text{s}^{-1}$, $N = 35$

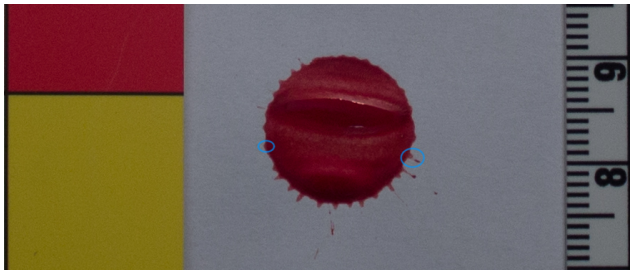

(d) $H = 2.0\,\text{m}$, $d_0 = 4.1 \times 10^{-3}\,\text{m}$, $u_0 = 5.32\,\text{m}\,\text{s}^{-1}$, $N = 29$

Figure 4.12: Resulting drip stains from droplets (with diameter, d_0, and impact velocity, u_0) falling from different heights, H, onto unconditioned paper. The number of spines, N, reported was counted by the Automated Spine Counter (ASC, Chapter 3).

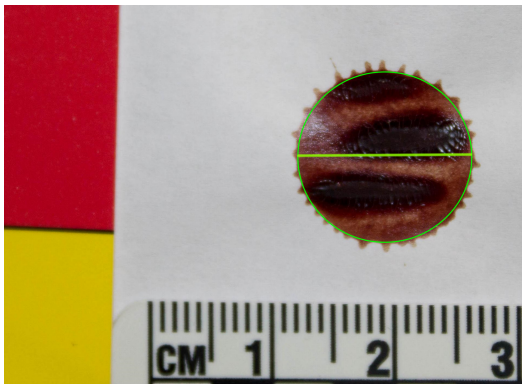

(a) $d_{\text{in}} = 0.014\,\text{m}$

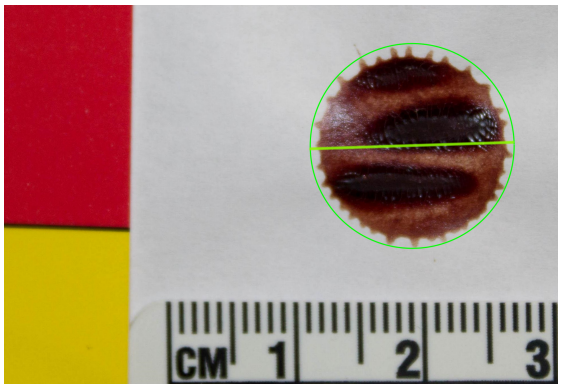

(b) $d_{\text{out}} = 0.016\,\text{m}$

Figure 4.13: Resulting bloodstain from a droplet of diameter $4.4 \times 10^{-3}\,\text{m}$, falling from 1.5 m onto conditioned paper, impacting at a velocity of $5.43\,\text{m}\,\text{s}^{-1}$. The ASC found 31 spines on this stain. The inner diameter and outer diameter was also measured by the ASC. Note: there is a spine that may appear to extend outside the measured outer diameter (in Subfigure 4.13b). The spine has a satellite stain right outside the outer diameter, the satellite stain is not apart of the spine.

$$A_{\mathrm{DAV}} = \pi d_i d_j \,, \tag{4.5}$$

where d_i is the width of the bloodstain and d_j is the length of the bloodstain. It is unclear if Davison [2005] has measured the stain area including spines. For example, a porcine blood droplet (of diameter 4.3×10^{-4} m) that has fallen a height of 0.5 m to impact unconditioned paper with a velocity of $3.018\,\mathrm{m\,s^{-1}}$. Below are the calculated stain areas for the same porcine bloodstain using different methods:

- Equation 4.5: $A_{\mathrm{DAV}} = 1.77 \times 10^{-4}\,\mathrm{m}^2$
- *ImageJ*: $A_{\mathrm{IJ}} = 1.898 \times 10^{-4}\,\mathrm{m}^2$
- ASC (Chapter 3): $A_{\mathrm{ASC}} = 1.837 \times 10^{-4}\,\mathrm{m}^2$

The difference in areas between the calculation by Davison [2005] and the estimations *ImageJ* and the ASC shows the need for defining clearly how the area is being measured. Further, this shows the requirement for stain properties to be measured using a computational tool, rather than manually, to remove any human error.

In the case of the bloodstain in Figure 4.13, the ASC yields a stain area of $1.593 \times 10^{-4}\,\mathrm{m}^2$ whereas *ImageJ* gives $1.65 \times 10^{-4}\,\mathrm{m}^2$ for the stain area. The difference in stain area is explained in Appendix I where it is shown that the ASC is more accurate and faster than *ImageJ*.

When no spines are observed on the stains (see Figure 4.14) only the stain area is recorded. In the case of the bloodstain in Figure 4.14, the stain area as measured by the ASC is A_{ASC}=$1.867 \times 10^{-4}\,\mathrm{m}^2$ and as measured by *ImageJ* is A_{IJ}=$1.987 \times 10^{-4}\,\mathrm{m}^2$. In this instance, the percent difference between the stain area measured by the ASC and by *ImageJ* is 6.2 %.

The ASC can still find the inner and outer diameter of a stain without spines however because the edge of the stain is not perfectly smooth. Its inner and outer diameter, as measured by the ASC (in Figure 4.15), is 1.352×10^{-2} m and 1.613×10^{-2} m, respectively. Figure 4.15 shows the inner and outer diameter of the bloodstain in Figure 4.14 as measured by the ASC. The area of this bloodstain as calculated by the ASC is $1.894 \times 10^{-4}\,\mathrm{m}^2$ and as calculated by ImageJ is $1.995 \times 10^{-4}\,\mathrm{m}^2$ (the difference in stain area is explained in Appendix I).

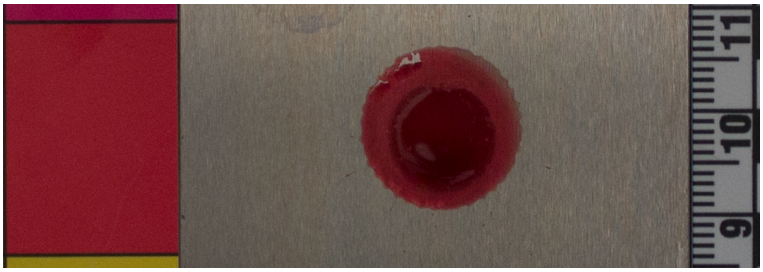

Figure 4.14: Bloodstain from a droplet of diameter 3.64×10^{-3} m, impacting a smooth steel surface with velocity $5.10\,\mathrm{m\,s^{-1}}$. This bloodstain has no spines.

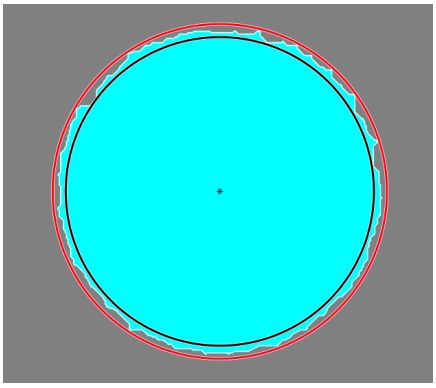

Figure 4.15: Analysis (by the ASC) of the bloodstain shown in Figure 4.14.

Conversely, some bloodstains (particularly those formed on rougher surfaces) can exhibit very chaotic spines and satellite stains. For these stains, it is very difficult to find a consistent way to count the number of spines on the stain, therefore only the stain area is measured which does not include satellite stains. An example of this is shown in Figure 4.16.

In Figure 4.16, the area of the stain as measured by *ImageJ* is 1.430×10^{-4} m^2 (as shown in Subfigure 4.16b, outlined in yellow). The stain diameter as measured by the ASC (shown in Subfigure 4.16c) is 1.461×10^{-4} m^2. The inner diameter of this stain as measured by the ASC (also shown in Subfigure 4.16c) is 1.201×10^{-2} m and the outer diameter is 1.843×10^{-2} m.

4.4.2 Elliptical bloodstains

When investigating elliptical bloodstains, there are a few properties to take into account.

Figure 4.17a shows an elliptical stain formed from a blood droplet that has impacted unconditioned paper with an angle of impact of 18°.

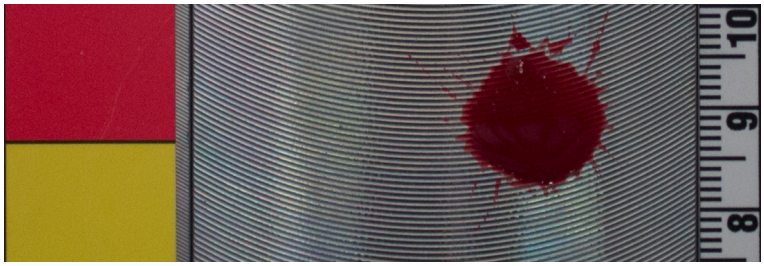

(a) Digital photograph of the stain.

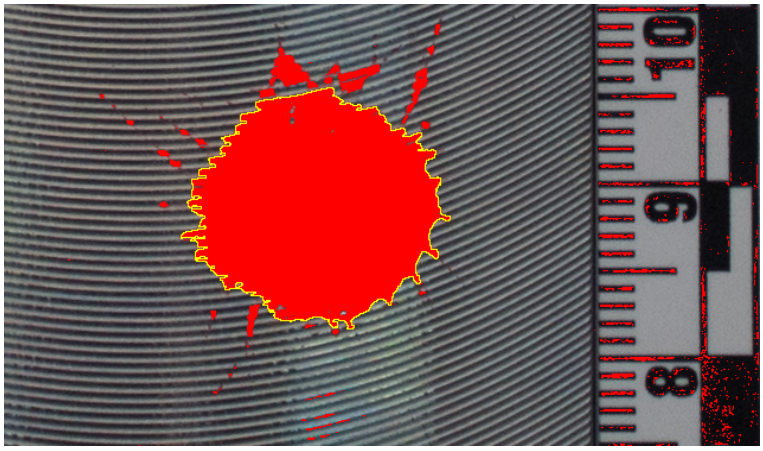

(b) View of the stain in *ImageJ* with a colour filter in order to find the edges of the stain.

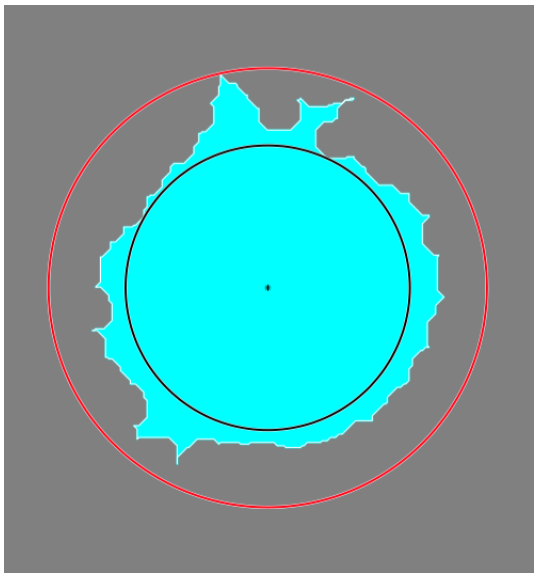

(c) Analysis of the stain using the ASC.

Figure 4.16: Bloodstain from a droplet impacting a steel substrate of roughness R_a = 6.3×10^{-6} m. The droplet's diameter before impact was 3.84×10^{-3} m and its impact velocity was $5.56\,\mathrm{m\,s^{-1}}$.

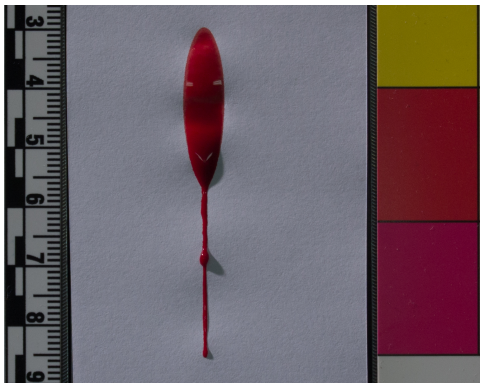

(a) Original digital photograph.

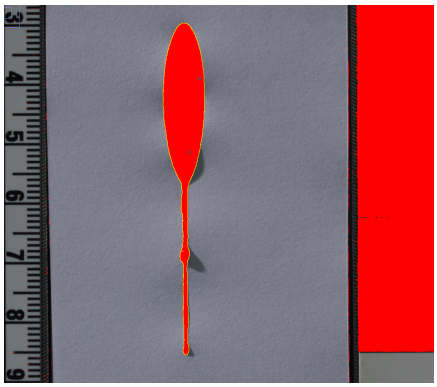

(b) Stain area and perimeter measurement in *ImageJ*.

Figure 4.17: Drip stain from a droplet of diameter 3.46×10^{-3} m, impact velocity of $3.15\,\mathrm{m\,s^{-1}}$, impacting unconditioned paper at an angle of impact, 18°.

In this work, the full stain area and perimeter was found using *ImageJ* (see Subfigure 4.17b) with the wand tool. Next, an ellipse estimation (with major and minor axis known) was used to approximate the main body of the stain (also done in *ImageJ*). The criterion for measuring the ellipses was first to have the estimated ellipse directly on the top point of the stain, then the ellipse must fit the perimeter everywhere on the stain except where the tail of the stain joins the main body of the stain. The full length of the stain was measured (from the top of the main body of the stain to the end of the tail), and finally the tail length (from the bottom of the ellipse to the end of the tail) is calculated by subtracting the major axis of the ellipse approximation from the full length of the stain. It should be noted that the difference between a spine and a tail is that tails tend to curve towards each other (following the shape of an ellipse) whereas spines radiate away from the centre of the stain not facing each other. For example, the bloodstain in Figure 4.17 has the following dimensions (the subscript *IJ* indicates the measurement is done by *ImageJ*):

- full stain area, $A_{\mathrm{IJ}} = 1.686 \times 10^{-4}\,\mathrm{m}^2$;
- full stain perimeter, $P_{\mathrm{IJ}} = 1.216 \times 10^{-1}\,\mathrm{m}$;
- full length, $L_{\mathrm{IJ}} = 5.580 \times 10^{-2}\,\mathrm{m}$;
- minor axis, $a_{\mathrm{IJ}} = 6.970 \times 10^{-3}\,\mathrm{m}$;

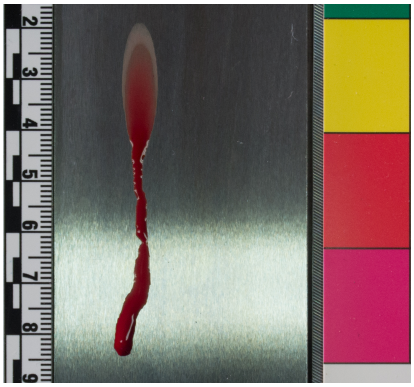

(a) Original digital photograph.

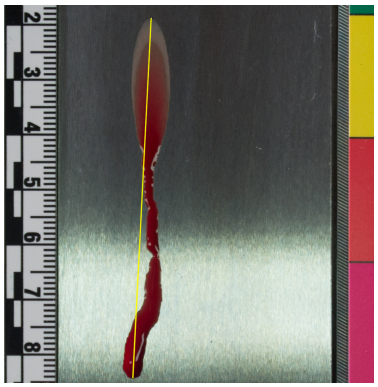

(b) Stain length measurement in *ImageJ*.

Figure 4.18: Resulting drip stain from a droplet of diameter 3.26×10^{-3} m, impacting a smooth steel surface with velocity $3.11\,\mathrm{m\,s^{-1}}$. The angle of impact is 18°.

- major axis, $b_{\mathrm{IJ}} = 2.666 \times 10^{-2}$ m; and
- tail length, $l_{\mathrm{IJ}} = 2.914 \times 10^{-2}$ m.

The tails of elliptical stains can vary depending on the type of surface and the impact velocity of the droplet. There have been two variations of tails found in the experiments in this thesis:

- curved tails; and
- multiple tails.

While these types of tails may have been observed in the literature, it has never been defined or discussed. Subfigure 4.18a is not an example of a curved tail, rather it is a draining effect. The blood is being pulled down by gravity creating a flow pattern. For analysis, the length of the stain is measured from the stop of the stain to the longest part of the stain (which may not be in the exact direction of impact, because of the tail draining off to the left). This is shown in Subfigure 4.18b.

The bloodstain in Figure 4.18 has the following dimensions:

- full stain area, $A_{\mathrm{IJ}} = 2.176 \times 10^{-4}\,\mathrm{m^2}$;
- full stain perimeter, $P_{\mathrm{IJ}} = 1.603 \times 10^{-1}$ m;
- full length, $L_{\mathrm{IJ}} = 6.542 \times 10^{-2}$ m;
- minor axis, $a_{\mathrm{IJ}} = 6.890 \times 10^{-3}$ m;
- major axis, $b_{\mathrm{IJ}} = 2.562 \times 10^{-2}$ m; and

- tail length, $l_{\mathrm{IJ}} = 4.050 \times 10^{-2}$ m.

Figure 4.19 is an example of both multiple tails and curved tails. This blood droplet has fallen from a height of 2.0 m, impacting at an angle of 18°, onto a substrate of roughness 6.3×10^{-6} m, with the grain. This stain has a main elliptical body but instead of having one tail that extends out the end of the major axis of the ellipse, it has two tails out the sides of the ellipse. These tails still indicate directionality. For analysis, the length of the stain that is measured is the longest distance across the stain (from the top of the ellipse to the end of the longest tail).

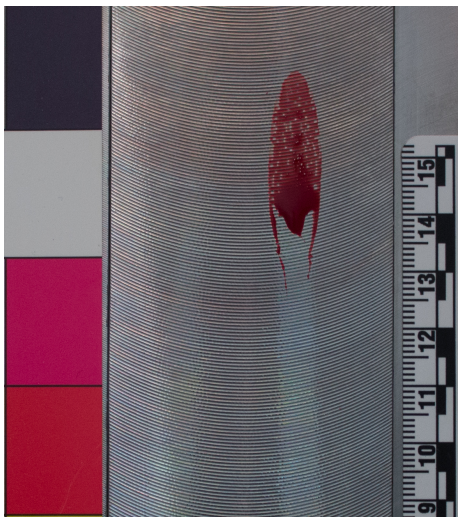

Figure 4.19: Resulting drip stain from a droplet of diameter 3.9×10^{-3} m, impacting a steel substrate of roughness $R_a = 6.3 \times 10^{-6}$ m (with the grain) with velocity 5.44 m s^{-1} at 18°. This bloodstain has two tails.

The bloodstain in Figure 4.19 has the following dimensions:

- full stain area, $A_{\mathrm{IJ}} = 2.187 \times 10^{-4}$ m^2;
- full stain perimeter, $P_{\mathrm{IJ}} = 1.348 \times 10^{-1}$ m;
- full length, $L_{\mathrm{IJ}} = 3.943 \times 10^{-2}$ m;
- minor axis, $d_i = 9.060 \times 10^{-3}$ m;
- major axis, $d_j = 2.887 \times 10^{-2}$ m; and
- tail length, $l_{\mathrm{IJ}} = 1.056 \times 10^{-2}$ m.

The difference between an elliptical stain having two tails (that are curved towards each

other) and a circular stain with two spines is that spines tend to radiate out from the centre of the stain whereas tails tend to follow the direction of impact. In cases, where one tail is longer than the other, this may be caused by droplets not falling strictly down towards the substrate or could be caused by oscillations in the droplet before impact causing the droplet to be non-spherical upon impact.

4.4.3 Miscellaneous stains

There are other stains where ellipses would be expected (from angled impacts) but they do not occur. Three instances have been observed:

- stream;
- non-stick (with ellipse invisible); and
- non-stick (with ellipse visible).

Figure 4.20 is an example of a stream stain. For analysis, only the length (measurement from the very first instance of the stain to the last instance of the stain) is measured in *ImageJ*.

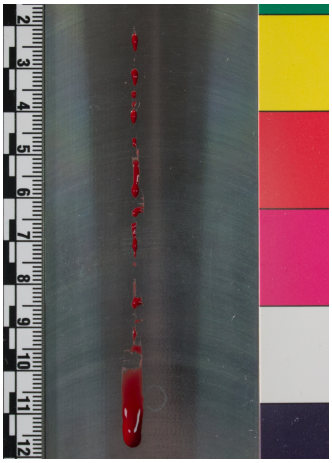

Figure 4.20: Resulting drip stain from a droplet of diameter 3.14×10^{-3} m, impacting a steel substrate of roughness 1.6×10^{-6} m (against the grain) with velocity $3.13\,\mathrm{m\,s^{-1}}$ at 18°. The total length of this drip stain is 9.753×10^{-2} m.

Figure 4.21 is an example of a blood droplet that has failed to "stick" to the substrate and create a stain. There is a small amount of blood that indicates where the initial contact was

made with the substrate and the bottom third of the ellipse can be seen before the tail, but the main body of the stain (the ellipse) is missing.

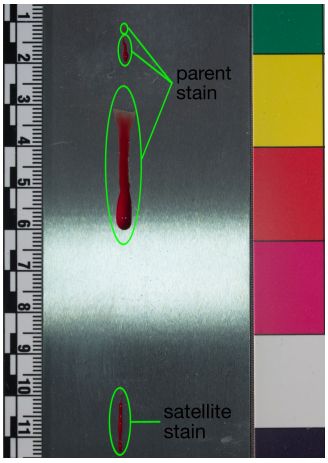

Figure 4.21: Bloodstain from a droplet of diameter 3.26×10^{-3} m, impacting a smooth steel surface with velocity $3.12\,\mathrm{m\,s^{-1}}$ at an angle of 18°.

The stain area in this case was measured by adding the areas of the three distinct parts of the parent stain. The satellite stain at the bottom is ignored. The bloodstain in Figure 4.21 has the following dimensions:

- full stain area, $A_{\mathrm{IJ}} = 9.170 \times 10^{-5}\,\mathrm{m}^2$;
- full stain perimeter, $P_{\mathrm{IJ}} = 4.001 \times 10^{-2}$ m; and
- full length, $L_{\mathrm{IJ}} = 4.908 \times 10^{-2}$ m.

Figure 4.22 is an example of a non-stick stain where the ellipse is still visible on the substrate. This is also an example of a stain with two tails and one tail is longer than the other. In analysis, the measurements are identical to the measurements taken for other elliptical stains, except the total stain area is not measured because the stain has not stuck to the substrate. It is possible that rougher surfaces yield visible ellipses more than smooth surfaces because as the blood is spreading along the surface, the blood gets trapped in the grooves of the substrate.

The bloodstain in Figure 4.22 has the following dimensions:

- full length, $L_{\mathrm{IJ}} = 6.912 \times 10^{-2}$ m;
- minor axis, $a_{\mathrm{IJ}} = 9.720 \times 10^{-3}$ m;

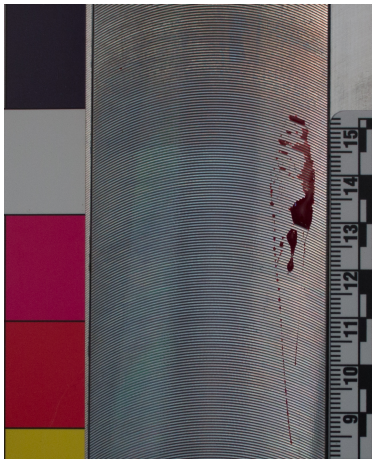

Figure 4.22: Bloodstain from a droplet of diameter 3.96×10^{-3} m, impacting a steel surface of roughness 6.3×10^{-6} m with velocity $5.46\,\mathrm{m\,s^{-1}}$ at 18°.

- major axis, $b_{\mathrm{IJ}} = 2.810 \times 10^{-2}$ m; and
- tail length, $l_{\mathrm{IJ}} = 4.102 \times 10^{-2}$ m.

4.5 Error Analysis

The programs described in Chapter 3 and the analysis carried out in *ImageJ* rely heavily on the conversions of digital photographs (or still frames from high-speed videos) to binary photographs. In order to convert a colour photograph to binary, the computer must decide (given a threshold) if the colour of a pixel is closer to white or black. If the computer decides the luminance of a pixel is greater than the given threshold it will give that pixel a value of 1 (for white). If the computer decides the opposite, it will give the pixel a value of 0 (for black). This will result in a binary photograph, with pixels of values 1 or 0. By converting the photographs (or in the case of the DVVP, the still frames) to binary, the error of drawing the boundary of a stain or droplet part way through a pixel is eliminated. The **regionprops** function in the ASC and DVVP (Chapter 3) measures stain properties by counting discrete pixels. For example, the area of a stain is measured by counting the number of white pixels in an image. Since this is an absolute figure, there is no error involved in measuring these stain properties. Another example is finding the centroid of a droplet, since the photograph is binary, the centre of mass of the

droplet in a still frame is not subject to error (as it would be if the user needed to choose the centre of mass manually). If, however, the centroid were incorrect by one pixel, the potential error in calculating the impact velocity would be $\pm 25\,\%$. Section 3.2 shows that this error in pixilation is not seen in the calculation of velocity by the DVVP.

In *ImageJ*, however, there is a larger human element to measuring the major and minor diameter of an elliptical stain. To measure these properties the user must impose an ellipse onto the stain using the criterion that the imposed ellipse must match the entire perimeter of the stain, except where the tail meets the main body of the stain (more detail in Section 4.4). If this criterion is not adhered to and the user imposes an ellipse that overestimates the main body of the stain, the percent error in the major and minor diameter would be maximum $2\,\%$. If the user imposes an ellipse that underestimates the main body of the stain, the error in the major diameter would have an upper limit of $8\,\%$ and in the minor diameter $18\,\%$. The error decreases with increased impact angle as the stains become more circular and so overestimating yields errors in major and minor diameter of at most $5\,\%$ and underestimating at most $1\,\%$.

These errors will only occur if the user does not adhere to the criterion advised for imposing an ellipse onto the stain. This error analysis is further evidence of the need for computational tools, such as the programs presented in Chapter 3, to automate the measurements of stains, specifically elliptical stains, to eliminate the human errors in measuring stain properties.

4.6 Summary

This chapter has outlined the procedure to follow in order to replicate the experiments used in this thesis. It showed the different substrates used, at different impact angles, from different heights. The curved milling of the steel substrates should not be seen as a limitation of these experiments. It will be shown in Chapter 5 that the directionality of the milling does not affect the shape or size of the stains. These experiments used horse blood heated at $37\,^{\circ}\mathrm{C}$. To avoid wasting blood, a magnetic stirrer in a beaker over a heater should be used instead of a water

bath. The blood in a beaker in a water bath leaves the blood stagnant which creates a film of dried blood on the edges of the beaker.

4.6.1 New definitions of stain properties

There is no formal definition of a tail. Tails and spines must be separate definitions because spines can radiate in all directions around a stain. Tails will indicate the directionality of a droplet (in cases of angled impact between 30° and 50° as stated by James et al. [2005]). On parent stains, the tail points away from the origin whereas on satellite stains, the tail points towards the origin. The tails investigated in this thesis are on parent stains.

In these experiments, spines are seen on stains resulting form impact angles 90° and 72°. Spines are emitted from the centre of the stain, in all directions around the stain. The mathematical definition of spines was discussed in Section 3.1. Tails are exhibited in these experiments on stains resulting from 54°, 36°, and 18°. Tails tend to curve inwards towards each other, in the direction of the impact. This is the main difference between spines and tails.

Other types of stains that have not been defined by the Scientific Working Group on Bloodstain Pattern Analysis [2013], but have been observed in these experiments, include stream stains, and the non-stick stains. A stream is type of stain that does not exhibit an elliptical "head". It is just a long and thicker stain, like a brushstroke, down a substrate. Often, at the top of a stream stain, the surface tension of the blood tends to keep the little speckled droplets of blood together. This occurs because the steel substrates are non-absorbent so the substrate (like paper would do) is not latching onto the droplet during impact, the droplet is simply sliding down the surface, leaving a trail behind on the steel substrate. The non-stick stains are in two categories (ellipse visible or invisible) because with increased roughness the ellipse becomes more visible as the droplet is being caught in the grooves of a substrate and staying in place.

Chapter 5

Results of the horse blood experiments

5.1 Context

This chapter outlines the results of the horse blood experiments from Chapter 4. The beginning of this chapter has a reminder of the non-dimensional numbers investigated in these results. These non-dimensional numbers give a description of the fluid flow in these experiments. Then, there is a general overview presented of the data, collected during the experiments. Later, the results are broken down into subsections which investigate the relationships between impact properties and stain properties. The impact properties are: impact velocity, u_0, impact angle, θ_f, and the roughness of the substrates given by their R_a values (see Sections 2.4 and 4.2). The stain properties are: stain area, stain perimeter, number of spines and tails, major and minor diameters of the stain, and the length of the stain.

5.2 Fluid Flow

The non-dimensional numbers used in this results section were introduced in Chapter 2, Section 2.1. These terms are different combinations of the impact velocity, u_0, the initial droplet diameter, d_0, and some known constants of horse blood (*i.e.* the density of the fluid, $\rho_l = 1062\,\mathrm{kg\,m^{-3}}$, the surface tension of the fluid, $\sigma_{lg} = 5.1 \times 10^{-2}\,\mathrm{N\,m^{-1}}$, the dynamic viscos-

ity of the fluid, $\mu_l = 4.7 \times 10^{-3}\,\mathrm{N\,s\,m^{-2}}$, and the acceleration due to gravity, $g = 9.81\,\mathrm{m\,s^{-2}}$). See Table 2.4 for a list of the physical properties of blood and their citations. The values for density have been cited from Raymond et al. [1996b]; Hulse-Smith et al. [2005]; Knock and Davison [2007]; Larkin et al. [2012]; Attinger et al. [2013]. The values for surface tension have been cited from El-Sayed et al. [2011]; Larkin et al. [2012]; Attinger et al. [2013]. The values of dynamic viscosity are cited from averaged measurements by Hulse-Smith et al. [2005]. It should be noted that the blood used in the experiments (Chapter 4) was collected from the same supplier used by Hulse-Smith et al. [2005] and Knock and Davison [2007].

The first non-dimensional number to be investigated in each of the following sections is the capillary number:

$$\mathrm{Ca} = \frac{\mu_l u_0}{\sigma_{lg}}. \tag{5.1}$$

Next, the Reynolds number:

$$\mathrm{Re} = \frac{\rho_l u_0 d_0}{\mu_l}. \tag{5.2}$$

Multiplying the Reynolds number by the capillary number yields the Weber number:

$$\mathrm{We} = \frac{\rho_l u_0^2 d_0}{\sigma_{lg}}. \tag{5.3}$$

Next, the Bond number:

$$\mathrm{Bo} = \frac{\rho_l g d_0^2}{\sigma_{lg}}. \tag{5.4}$$

Finally, the ratio of the Weber number to the Bond number yields the Froude number:

$$\hat{\mathrm{Fr}} = \frac{u_0}{\sqrt{g d_0}}. \tag{5.5}$$

In general, certain ranges of non-dimensional numbers indicate different types of flow.

Capillary numbers (Equation 5.1) greater than 10^{-5} are considered high (Section 2.1). This means the viscous forces of the droplet are dominating the surface tension forces. Reynolds numbers (Equation 5.2) lower than 5×10^5 are considered to be laminar as opposed to turbulent (Section 2.1). Weber numbers (Equation 5.3) greater than five indicate that the surface tension forces are being dominated by inertial forces and this encourages the spread to rip away from the surface (Section 2.1). A critical Bond number (Equation 5.4) of 11.22 occurs when the surface tension forces are being overcome by the initial droplet diameter (Section 2.1). Froude numbers (Equation 5.5) greater than one are described as supercritical with strong jumps in the flow (Section 2.1).

All of the droplets in this results chapter (785 droplets) have high capillary numbers ($0.266 \leq \text{Ca} \leq 0.603$), viscous forces are dominating the surface tension forces yielding laminar flow ($2.13 \times 10^3 \leq \text{Re} \leq 6.30 \times 10^3$), with surface tensions being dominated by inertial forces, due to high velocity rather than large diameter ($5.95 \times 10^2 \leq \text{We} \leq 3.79 \times 10^3$ and $1.90 \leq \text{Bo} \leq 4.08$), and finally all are described as supercritical flow ($15.0 \leq \text{Fr} \leq 32.1$).

5.3 General view of the data

The following subsections provide a general overview of the data collected from the horse blood experiments (Chapter 4). The overview presents the mean impact velocities ($\bar{u_0}$) of droplets falling from different heights, onto different substrates, with different impact angles. All the impact velocities, u_0, and droplet diameters, d_0, were obtained using the Diameter and Velocity Video Processor (DVVP, Chapter 3).

The resulting bloodstains from droplets impacting substrates at 90° and 72° had the following properties measured: outer stain diameter, d_{out}, final stain area, A_{ASC}, perimeter of the stain, P_{ASC}, and number of spines, N. These were estimated by the Automated Spine Counter (ASC, Chapter 3). However, the resulting bloodstains from droplets impact substrates at 54°, 36°, and 18° are more elliptical and thus had the following properties measured: minor diameter, d_i, major

diameter, d_j, final stain area, A_{IJ}, and stain perimeter, P_{IJ}. These properties were estimated using *ImageJ*. The elliptical stains exhibited tails instead of spines, which were counted manually from the experiments.

It should be mentioned that the experimental design (Chapter 4) purposely used a very small range of initial diameters in these experiments (*i.e.* it was endeavoured to have the same sized droplet for every repeat). Therefore, there may be a lack of correlation with the initial droplet diameters because there was not enough variation in the droplet diameters to see certain phenomenon occurring in the results. The mean droplet diameter (estimated from 785 droplets) was 3.76×10^{-3} m with a variance of 9.97×10^{-8} m^2.

Statistical properties (minimum, maximum, mean) of the droplets and bloodstains used in these experiments can be found in Appendix E in tables organised by impact angle and substrate. They are separated into tables of general statistics of stain properties, then into statistics of the non-dimensional properties, and also the coefficients of variation in the stain properties. Further, the resolution of the digital photographs, resolution of the high-speed videos, and the calculated circularity of the stains (Equation 2.17, Section 2.1) can also be found in Appendix E, in Table E.1.

For each combination of height, impact angle, and substrate, five to six repetitions were carried out (except on conditioned paper, with 10 repetitions). Before presenting the overview of the data collected, two comparisons were performed:

1. Is there a difference in stain shape or size when a droplet impacts conditioned paper versus unconditioned paper?
2. Is there a difference in stain shape or size when a droplet impacts a roughened steel substrate, with or against the grain?

The question of conditioning paper substrates is addressed in Appendix G. A statistical comparison of stain properties on conditioned and unconditioned paper was carried out. The stain properties tested were stain area, stain perimeter, inner and outer diameters, and the number of spines. It was found that the conditioning of the paper does not have an effect on the number

of spines, outer diameter, or stain perimeter. The conditioning does have an effect on the inner diameter and stain area but the effect is small compared to the significant effect of the height on the stain properties. Appendix G concluded that the conditioning of paper does not have an effect on stain shape and size.

The question of direction of the grain of roughened steel substrates was dealt with using statistical testing as well. A one-way ANOVA test was used to check if the direction of the grain (on roughened steel substrates) had an effect on a given stain property by investigating the resulting p-values. Definitions of the one-way ANOVA test and p-values can be found in Appendix C. The one-way ANOVA test was used on each stain property for the different impact angles in the experiments. The resulting p-values of the one-way ANOVA tests can be found in the tables of Appendix D. For each test, none of the p-values indicated very strong evidence ($p \leq 0.01$) against the null hypothesis. This means none of the ANOVA tests showed very strong evidence that the direction of the grain had an effect on the stain properties being tested.

From these statistical tests, it can be concluded that the conditioning of paper substrates and the direction of the grain of roughened steel substrates do not affect the stain shape or size in this range of experiments.

5.3.1 Droplets impacting at 90°

Table 5.1 shows the number of repeats performed for droplets impacting different substrates at 90°. Only four repeats onto unconditioned paper at 1.0 m are included in this data set because one of the droplets had a bubble inside, causing an abnormal stain (see Figure 5.1). The large outer stain diameter was an outlier in the data set and thus was removed. There are 59 bloodstains in total in this portion of the results.

None of the bloodstains on smooth steel exhibited any spines. There was no digital photograph of one of the stains formed on smooth steel, falling from 1.0 m, therefore there are only four repeats at that height. 19 bloodstains, on smooth steel, are accepted for this portion of the results (Table 5.1).

Table 5.1: Number of repeats (reps) and mean impact velocities ($\bar{u_0}$) of droplets impacting substrates at 90°. The range of droplet diameters in this data set is 3.2×10^{-3} m to 4.3×10^{-3} m.

Substrate	Roughness (10^{-6} m)	Height (m)	$\bar{u_0}$ (m s^{-1})	reps
paper	1.3	0.5	3.16	15
		1.0	4.42	14
		1.5	5.26	15
		2.0	6.05	15
steel	0	0.5	2.97	5
		1.0	4.14	4
		1.5	5.04	5
		2.0	5.55	5
	1.6	0.5	2.92	5
		1.0	4.13	5
		1.5	5.04	5
		2.0	5.53	6
	3.2	0.5	2.97	5
		1.0	4.12	5
		1.5	5.06	5
		2.0	5.58	6
	6.3	0.5	2.98	5
		1.0	4.14	5
		1.5	5.04	5
		2.0	5.61	5

Figure 5.1: Resulting stain from a droplet with a bubble formed inside. $H = 1.0\,\text{m}$, $d_0 = 3.76 \times 10^{-3}\,\text{m}$, $u_0 = 4.26\,\text{m s}^{-1}$, $d_{\text{out}} = 2.73 \times 10^{-2}\,\text{m}$.

Statistical properties of the bloodstains in this section can be found in Appendix E in Tables E.2, E.3, E.4, E.5, and E.6.

5.3.2 Droplets impacting at 72°

Table 5.2 shows the number of repeats performed for droplets impacting different substrates at 72°.

Table 5.2: Number of repeats (reps) and mean impact velocities ($\bar{u_0}$) of droplets impacting substrates at 72°. The range of droplet diameters in this data set is 3.1×10^{-3} m to 4.5×10^{-3} m.

Substrate	Roughness (10^{-6} m)	Height (m)	$\bar{u_0}$ (m s^{-1})	reps
paper	1.3	0.5	3.09	5
		1.0	4.18	5
		1.5	4.90	4
		2.0	5.63	5
steel	0	0.5	3.18	5
		1.0	4.19	5
		1.5	4.99	5
		2.0	5.60	6
	1.6	0.5	3.10	10
		1.0	4.22	10
		1.5	5.00	10
		2.0	5.61	10
	3.2	0.5	3.10	10
		1.0	4.21	10
		1.5	4.99	10
		2.0	5.60	10
	6.3	0.5	3.09	10
		1.0	4.18	11
		1.5	4.96	11
		2.0	5.62	10

For impacts onto paper ($R_a = 1.3 \times 10^{-6}$ m) at 72°: At each height, five repeats were performed, except 1.5 m where four repeats were accepted. One of the repeats in this set of testing had a bubble within the droplet (similar to Figure 5.1) which caused the outer diameter to be excessively large and producing more satellite stains than normal (see Subfigure 5.2a). Therefore, it was an outlier in this data set. A comparison of the omitted bloodstain and an

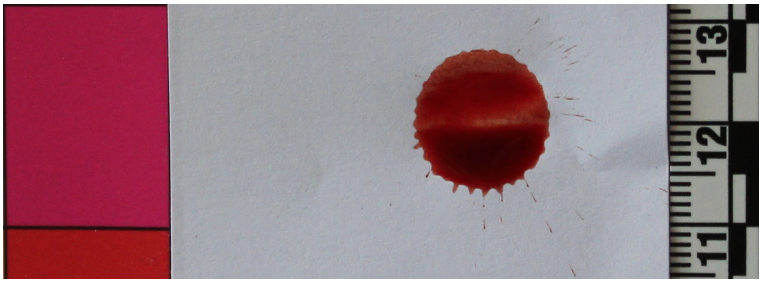

(a) The omitted bloodstain resulting from a droplet with $d_0 = 3.22 \times 10^{-3}$ m and $u_0 = 4.88\,\mathrm{m\,s^{-1}}$. The outer diameter is $d_{\mathrm{out}} = 2.89 \times 10^{-2}$ m.

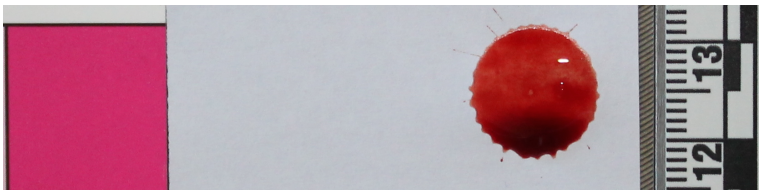

(b) The accepted bloodstain resulting from a droplet with $d_0 = 3.13 \times 10^{-3}$ m and $u_0 = 4.85\,\mathrm{m\,s^{-1}}$. The outer diameter is $d_{\mathrm{out}} = 1.42 \times 10^{-2}$ m.

Figure 5.2: Resulting bloodstains from droplets falling from a height of $H = 1.5$ m impacting unconditioned paper at 72°.

accepted bloodstain is shown in Figure 5.2.

Statistical properties of the bloodstains in this section can be found in Appendix E in Tables E.7, E.8, E.9, E.10, and E.11.

5.3.3 Droplets impacting at 54°

Table 5.3 shows the number of repeats performed for droplets impacting different substrates at 54°. None of the bloodstains at this angle were omitted.

Statistical properties of the bloodstains in this section can be found in Appendix E, in Tables E.12, E.13, E.14, E.15, and E.16.

5.3.4 Droplets impacting at 36°

Table 5.4 shows the number of repeats performed for droplets impacting different substrates at 36°.

For impacts from 1.0 m onto smooth steel ($R_a = 0$ m), four of the six repeats were accepted

Table 5.3: Number of repeats (reps) and mean impact velocities ($\bar{u_0}$) of droplets impacting substrates at 54°. The range of droplet diameters in this data set is 3.3×10^{-3} m to 4.4×10^{-3} m.

Substrate	Roughness (10^{-6} m)	Height (m)	$\bar{u_0}$ (m s^{-1})	reps
paper	1.3	0.5	3.41	5
		1.0	4.28	5
		1.5	4.98	7
		2.0	5.62	5
steel	0	0.5	3.23	5
		1.0	4.23	5
		1.5	5.01	5
		2.0	5.61	5
	1.6	0.5	3.27	10
		1.0	4.29	10
		1.5	5.03	10
		2.0	5.59	10
	3.2	0.5	3.28	10
		1.0	4.27	10
		1.5	5.04	10
		2.0	5.62	10
	6.3	0.5	3.28	10
		1.0	4.27	10
		1.5	5.04	10
		2.0	5.63	10

Table 5.4: Number of repeats (reps) and mean impact velocities ($\bar{u_0}$) of droplets impacting substrates at 36°. The range of droplet diameters in this data set is 3.6×10^{-3} m to 4.3×10^{-3} m.

Substrate	Roughness (10^{-6} m)	Height (m)	$\bar{u_0}$ ($\mathrm{m\,s^{-1}}$)	reps
paper	1.3	0.5	3.24	5
		1.0	4.13	5
		1.5	4.89	5
		2.0	5.58	5
steel	0	0.5	3.20	5
		1.0	4.20	4
		1.5	4.93	5
		2.0	5.54	5
	1.6	0.5	3.20	10
		1.0	4.21	9
		1.5	4.93	10
		2.0	5.56	10
	3.2	0.5	3.21	10
		1.0	4.17	9
		1.5	4.91	10
		2.0	5.55	10
	6.3	0.5	3.23	10
		1.0	4.19	11
		1.5	4.95	9
		2.0	5.56	10

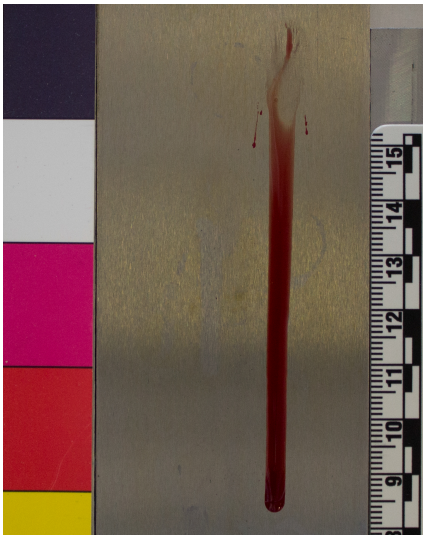

(a) Resulting bloodstain of a droplet with $d_0 = 3.82 \times 10^{-3}$ m and $u_0 = 4.15\,\mathrm{m\,s^{-1}}$.

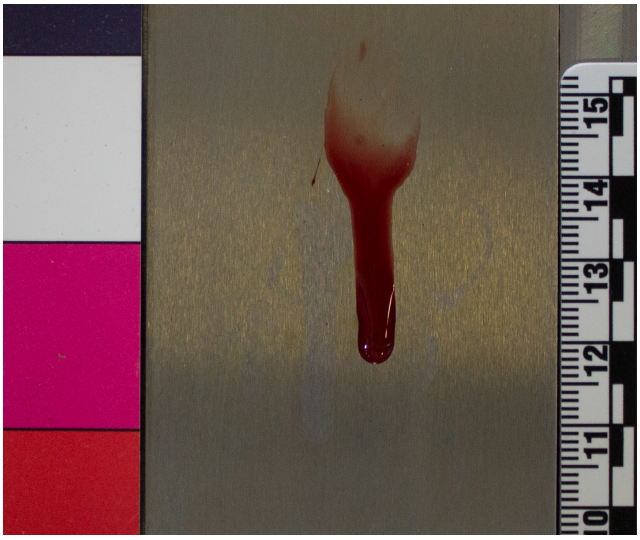

(b) Resulting bloodstain of a droplet with $d_0 = 4.17 \times 10^{-3}$ m and $u_0 = 4.17\,\mathrm{m\,s^{-1}}$.

Figure 5.3: Resulting bloodstains from droplets falling from a height of $H = 1.0$ m impacting smooth steel at 36°. Subfigure 5.3a is described as a "stream" (Chapter 4).

because the first two repeats produced streams. This is shown in Figure 5.3. Subfigure 5.3a shows what is described as a "stream" in Chapter 4. This bloodstain was removed from the dataset because it was an anomaly in the data set and was probably caused by the substrate not being completely dry before use in the experiment. Subfigure 5.3b shows what the rest of the repeats in this section looked like.

Statistical properties of the bloodstains in this section can be found in Appendix E in Tables E.17, E.18, E.19, E.20, and E.21.

5.3.5 Droplets impacting at 18°

Table 5.5 shows the number of repeats performed for droplets impacting different substrates at 18°. None of the bloodstains at this angle were omitted.

Statistical properties of the bloodstains in this Subsection can be found in Appendix E in Tables E.22, E.23, E.24, E.25, and E.26.

Table 5.5: Number of repeats (reps) and mean impact velocities ($\bar{u_0}$) of droplets impacting substrates at 18°. The range of droplet diameters in this data set is 3.1×10^{-3} m to 4.3×10^{-3} m.

Substrate	Roughness (10^{-6} m)	Height (m)	$\bar{u_0}$ ($\mathrm{m\,s^{-1}}$)	reps
paper	1.3	0.5	3.16	5
		1.0	4.28	5
		1.5	4.75	5
		2.0	5.59	5
steel	0	0.5	3.14	5
		1.0	4.33	5
		1.5	4.68	5
		2.0	5.59	6
	1.6	0.5	3.15	12
		1.0	4.32	10
		1.5	4.90	10
		2.0	5.40	10
	3.2	0.5	3.17	10
		1.0	4.29	10
		1.5	4.92	10
		2.0	5.36	10
	6.3	0.5	3.13	11
		1.0	4.29	10
		1.5	5.01	10
		2.0	5.58	11

5.4 Effect of impact velocity and impact angle on various stain properties

The next five subsections will investigate the effect of impact velocity, u_0, and impact angle, θ_f, on stain properties such as stain area, stain perimeter, the number of spines and tails, the major diameter, the minor diameter, and the full length of the stain. Each subsection will have a plot of the data, averaged over each height. The different symbols in the plots indicate different substrate roughness (see Section 2.4). Recall, paper has a surface roughness of $R_a = 1.3 \times 10^{-6}$ m (depicted as stars in the plots). There are four steel substrates: one smooth steel substrate ($R_a = 0$ m, depicted as diamonds in the plots), and three roughened steel substrates: $R_a = 1.6 \times 10^{-6}$ m, $R_a = 3.2 \times 10^{-6}$ m, and $R_a = 6.3 \times 10^{-6}$ m (depicted as, squares, triangles, and circles, respectively). The different coloured symbols indicate different impact angles: green is 90°, dark blue is 72°, red is 54°, pink is 36°, and light blue is 18°. In each plot, a line of best fit is used. The R^2 values in the following subsections range from 0.40 to 0.79, which are lower than the accepted $R^2 = 0.9$, but they do give an indication as to general linear relationships between the different combinations of u_0 and θ_f with the various stain properties. Lastly, each plot in this section includes error bars that represent the standard error. The standard error gives an indication as to how well the mean of the data is estimated and is described as the standard deviation divided by the square root of the sample size.

5.4.1 Effect of u_0 and θ_f on stain area

With an increase in velocity there should be an increase in stain area because a higher impact velocity yields more energy, which helps the droplet spread farther onto a surface. A decrease in impact angle will increase the stain area because when a droplet impacts an angled substrate, gravity will help the droplet spread farther by pulling the droplet down the incline. These expectations are seen in Figure 5.4. The line of best fit has an R^2 value of 0.40, which is not

indicative of a strong linear relationship, but this is caused by the variability in the experimental data and a linear relationship can be fitted to the data, if the scatter in the data is random and not systematic. It can also be seen in Figure 5.4 that a decrease in impact angle (36°, the pink symbols, and 18°, the light blue symbols) causes more variation in the stain area. Perpendicular impacts are more controlled, when the droplet impacts a substrate, it will spread in all directions equally. Whereas for more angled impacts (54° and lower) gravity acts to pull the droplet down the substrate, causing more elliptical stains which vary more in length. Similar to a decrease in θ_f, an increase in u_0 causes more variability in the stain areas. This is caused by the increased energy inputted into the impacts, making the impacts less controlled.

Lastly, the paper substrates are seen in Figure 5.4 to show the least amount of variability. Paper will behaves more consistently than the steel surfaces because while it has a very low roughness parameter ($R_a = 1.3 \times 10^{-6}$ m), it does have a level of absorbency that "cushions" the droplet upon impact. The paper absorbs some of the blood, and some of the droplet's kinetic energy, at impact, resulting in fewer and slower satellite droplets. Whereas steel, being completely non-yielding and non-absorbent the impact will be more abrupt. Hence the lower roughness values would decrease the variability in the stain.

It should be noted that the stain area does not include satellite stains, only the parent stain is measured. With increased roughness there should be an increase in satellite stains (which are not measured in this thesis). Since parts of the droplet are detaching from the parent stain and forming satellite stains, the overall area of the parent stain decreases with an increase in roughness. The same phenomenon is observed with an increase in velocity (more energy during impact causes more satellite stains, thus smaller parent stains). This phenomenon is not observed on paper because the absorbency of the paper tends to hold the droplet down on the surface during spreading and if there is enough energy for droplets to exit at the maximum extension of the spread, then satellite droplets will exit but the spread will generally not be interrupted as on steel surfaces and so the parent stain will grow as normal and then eject satellite stains. Whereas steel surfaces will tend to eject satellite drops and then retract on the surface.

Another effect of the roughness on the stain area is that increased roughness will cause more variability in the stain area, to a certain limit. It has been observed in some stains (on surfaces with lower R_a values) where the droplet is retracting after impact. This causes the parent stain to be smaller than expected. Physically, this is caused by surface tension attempting to keep the droplet as spherical as possible. Rougher surfaces, however, behave more like paper because as the droplet is spreading along the surface the blood is entering deeper and larger grooves on the surface, trapping the blood (much like how paper is absorbing the blood as it spreads). This prohibits the droplet from retracting along the surface. This is shown in Figure 5.4 where roughened steel substrates of $R_a = 1.6 \times 10^{-6}$ m and $R_a = 3.2 \times 10^{-6}$ m increases in variability, then the variability decreases again with $R_a = 6.3 \times 10^{-6}$ m.

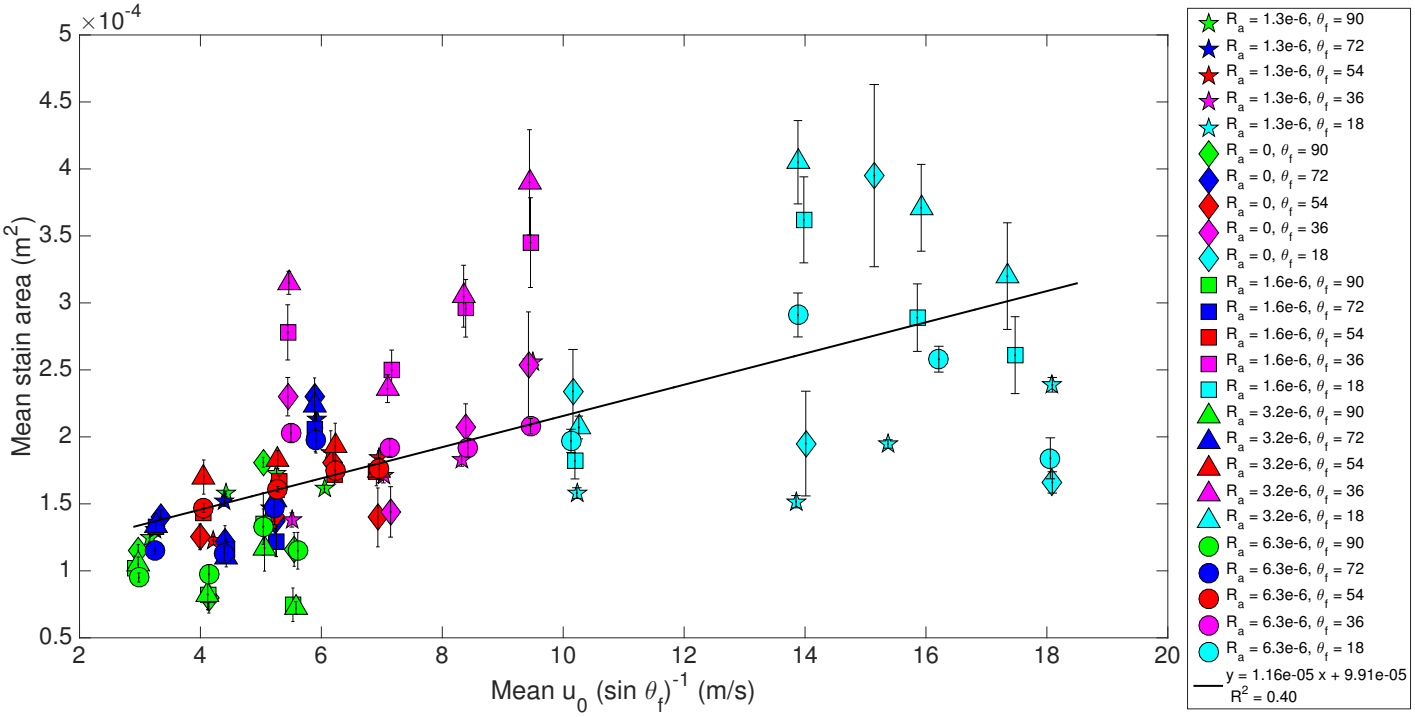

Figure 5.4: The effect of impact velocity and impact angle on the mean area of the stains from droplets impacting different surfaces at different angles. The data has been averaged at each height and the error bars represent the standard error.

The stain area of bloodstains on smooth steel however seem to fluctuate more than the stain area on paper. Figure 5.5 shows an example of a bloodstain from each height fallen. It appears that the droplet in Subfigure 5.5c has a larger area and a larger amount of retraction

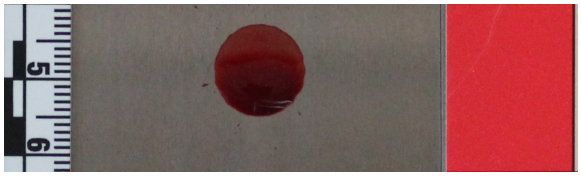

(a) Droplet of $d_0 = 3.73 \times 10^{-3}$ m, with $u_0 = 2.96\,\mathrm{m\,s^{-1}}$, and $A_{\mathrm{ASC}} = 1.16 \times 10^{-4}\,\mathrm{m^2}$.

(b) Droplet of $d_0 = 3.30 \times 10^{-3}$ m, with $u_0 = 4.07\,\mathrm{m\,s^{-1}}$, and $A_{\mathrm{ASC}} = 1.14 \times 10^{-4}\,\mathrm{m^2}$.

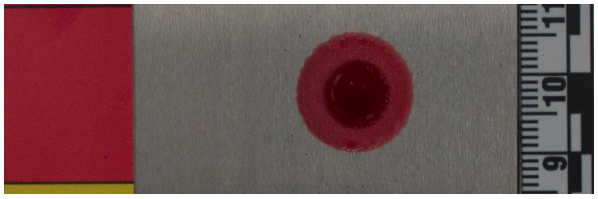

(c) Droplet of $d_0 = 3.62 \times 10^{-3}$ m, with $u_0 = 5.07\,\mathrm{m\,s^{-1}}$, and $A_{\mathrm{ASC}} = 1.78 \times 10^{-4}\,\mathrm{m^2}$.

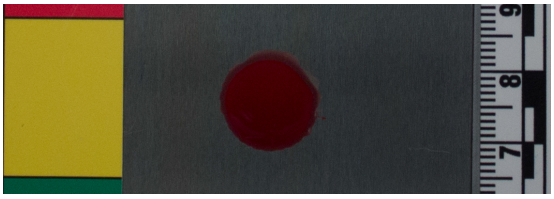

(d) Droplet of $d_0 = 3.41 \times 10^{-3}$ m, with $u_0 = 5.58\,\mathrm{m\,s^{-1}}$, and $A_{\mathrm{ASC}} = 1.55 \times 10^{-4}\,\mathrm{m^2}$.

Figure 5.5: Four droplets impacting smooth steel from four different heights.

after impact. It is unclear at this time why this stain specifically is different from the others. According to the raw experimental data, the impacts at $H = 0.5\,\mathrm{m}$ and $H = 1.0\,\mathrm{m}$ were done in one day, $H = 1.5\,\mathrm{m}$ on another day, and finally $H = 2.0\,\mathrm{m}$ also on another day. It is possible that some conditions in the lab may have changed over the different experimental days. Future work should endeavour to account for temperature and humidity in the laboratory (as these variables were not controlled in these experiments, see Chapter 4) during these experiments to ensure these variables are not affecting the drying of the stain.

Further, statistical tests (see Appendix C) were performed on the averaged data to check if the stain areas resulting from different impact angles are statistically different. First, the Levene's test showed that the stain areas come from normal distribution with the same variance ($p = 0.7309$). This allows for the use of a three-way ANOVA test to be used which yielded the following results:

- the impact angle affects the stain area ($F_{4,88} = 29.57$, $p = 0$);
- the height from which the droplet has fallen has an effect on the stain area ($F_{3,88} = 4.61$, $p = 0.0048$); and
- the roughness of the surface has an effect on the stain area ($F_{4,88} = 2.98$, $p = 0.0234$).

To supplement the ANOVA test, a Tukey test was performed. The Tukey test indicates if the

means of groups of stain areas are statistically different from each other. With regards to impact angle, the Tukey test shows that the means of the stain areas resulting from impact angles 18° and 36° are not statistically different. Further, the means of the stain areas resulting from 72° are not statistically different from 54° and 90° but 54° and 90° are different from each other. In this case, 72° bridges the gap between 54° and 90°.

With regards to the height from which the droplet has fallen, a Tukey test indicates that the mean stain areas from droplets that have fallen 0.5 m are statistically different from those that have fallen from 1.5 m and 2.0 m. However, 1.0 m bridges the gap between all four heights.

For the roughness of the substrates, the ANOVA test indicated that the roughness has an effect on the stain area, but the F-statistic shows that the effect of substrate roughness is not as strong as the other factors. A Tukey test indicates that the mean stain areas of all the different substrates are not statistically different. Figure 5.6 shows the stain areas on paper alone to show how the data collapses without the variability of the steel substrates.

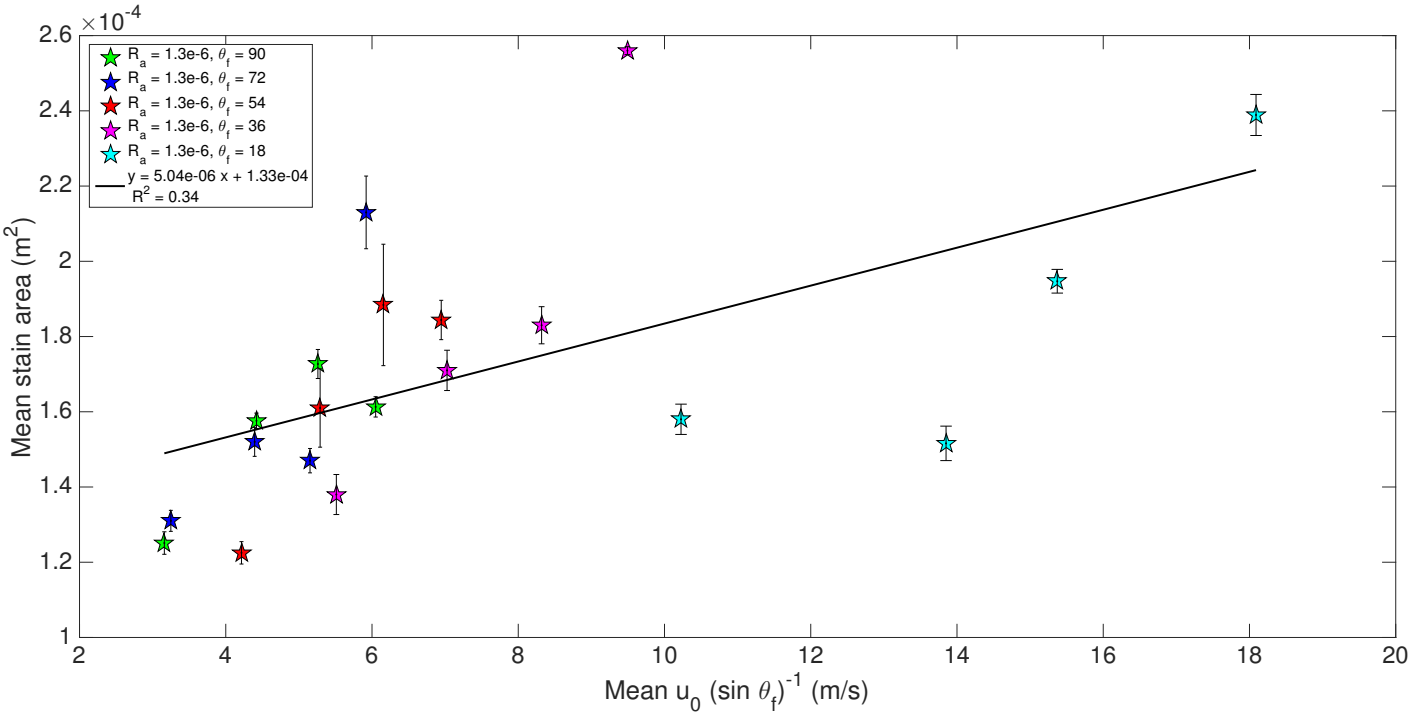

Figure 5.6: The effect of impact velocity and impact angle on the mean area of the stains from droplets impacting paper at different angles. The data has been averaged at each height and the error bars represent the standard error.

Finally, other non-dimensional numbers were tested in an attempt to find a combination of impact properties that would collapse the stain area data better (Table V.1). Figure 5.7 shows an improved correlation to the Bond number as opposed to the impact velocity alone, yielding an R^2 value of 0.47.

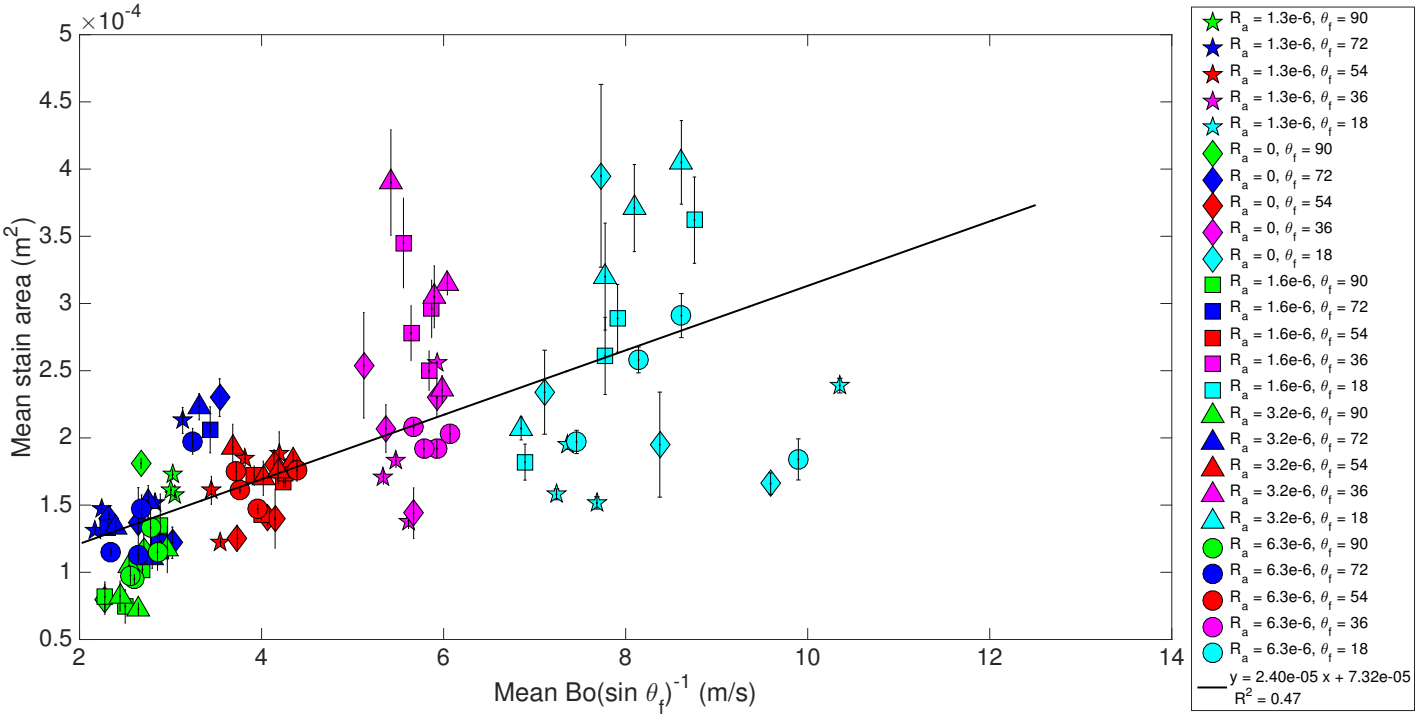

Figure 5.7: The effect of Bond number (Equation 5.4) and impact angle on the mean area of the stains from droplets impacting different surfaces at different angles. The data has been averaged at each height and the error bars represent the standard error.

5.4.2 Effect of u_0 and θ_f on stain perimeter

An increase in u_0 and decrease in θ_f should cause an increase in stain perimeter. This is because an increase in energy into the impact will make stains more variable, further, a decrease in impact angle tends to elongate stains, giving them a larger perimeter. These expectations are shown in Figure 5.8. The line of best fit has an R^2 value of 0.53. Again, this is not a good linear fit, but because of the variability in the stain perimeters, this is acceptable for depicting a linear relationship. It can also be seen in Figure 5.8 that paper has the least variable perimeter of all the substrates. This is caused by its absorbent nature, discussed in Subsection 5.4.1. The increase in

variability with increase in substrate roughness (up to a limit of $R_a = 6.3 \times 10^{-6}$ m) is also seen, and is similar to stain area.

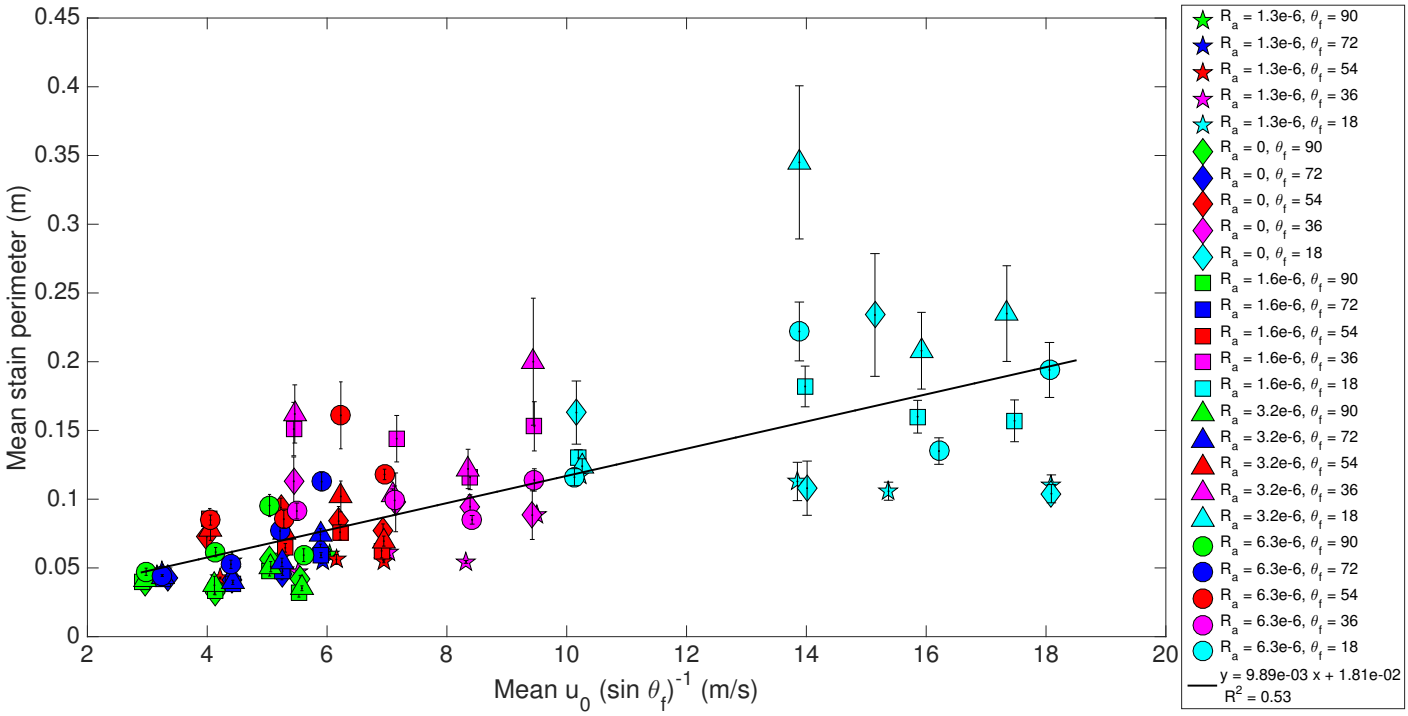

Figure 5.8: The effect of impact velocity and impact angle on the mean perimeter of the stains from droplets impacting different surfaces at different angles. The data has been averaged at each height and the error bars represent the standard error.

Again, statistical tests (see Appendix C) were performed on the averaged data to check if the stain perimeters resulting from different impact angles are statistically different. First, the Levene's test showed that the stain perimeters come from normal distribution with the same variance ($p = 0.7142$). This allows for the use of a three-way ANOVA test to be used which yielded the following results:

- the impact angle affects the stain perimeter ($F_{4,88} = 40.57$, $p = 0$);
- the roughness of the surface has an effect on the stain perimeter ($F_{4,88} = 5.35$, $p = 0.0007$); and
- the height from which the droplet has fallen does not have an effect on the stain perimeter ($F_{3,88} = 1.23$, $p = 0.3033$).

A Tukey test is used to show if the mean stain perimeters of certain groups of data are

statistically different from each other. With regards to the impact angle, 72° seems to bridge the gap between 90° and 54°. Whereas, 36° is statistically different to all other impact angles, and 18° is also statistically different from all other impact angles.

With regards to substrates, a Tukey test showed that paper has statistically different mean stain perimeters as compared to roughened steel of $R_a = 3.2 \times 10^{-6}$ m and $R_a = 6.3 \times 10^{-6}$ m. The smooth steel substrate and roughened steel of $R_a = 1.6 \times 10^{-6}$ m seem to bridge the gap between all substrates in this Tukey test.

There is no statistical difference in the mean stain perimeters with respect to height the droplet has fallen. This reaffirms the result found in the three-way ANOVA test (where height did not effect the stain perimeter). This is an interesting point to make when looking at Figure 5.8, since the height does not affect the stain perimeter, this means the impact velocity does not effect the stain perimeter. Therefore, the increase in stain perimeter is mostly driven by the impact angle. The three-way ANOVA test affirms this notion as well, as the impact angle has the highest F-statistic. This can also be seen graphically, in Figure 5.9 where the dependency on impact angle has been removed and the data shows clearly that there is no dependency on impact velocity.

Finally, other non-dimensional numbers were tested in an attempt to find a combination of impact properties that would collapse the stain perimeter data better (Table V.1). Figure 5.10 shows an improved correlation to the Bond number as opposed to the impact velocity alone, yielding an R^2 value of 0.59.

5.4.3 Effect of u_0 and θ_f on the number of spines and tails

Before investigating the effects of u_0 and θ_f on the number of spines and tails, it should be noted that the stains resulting from 90° and 72° exhibit spines, whereas stains resulting from 54°, 36°, and 18° exhibit tails. The data sets are merged together because accounting for the impact angle in this study links the spines and tails on the stains. Figure 5.11 shows the trends expected. An increase in impact velocity and impact angle does increase the number of spines and tails.

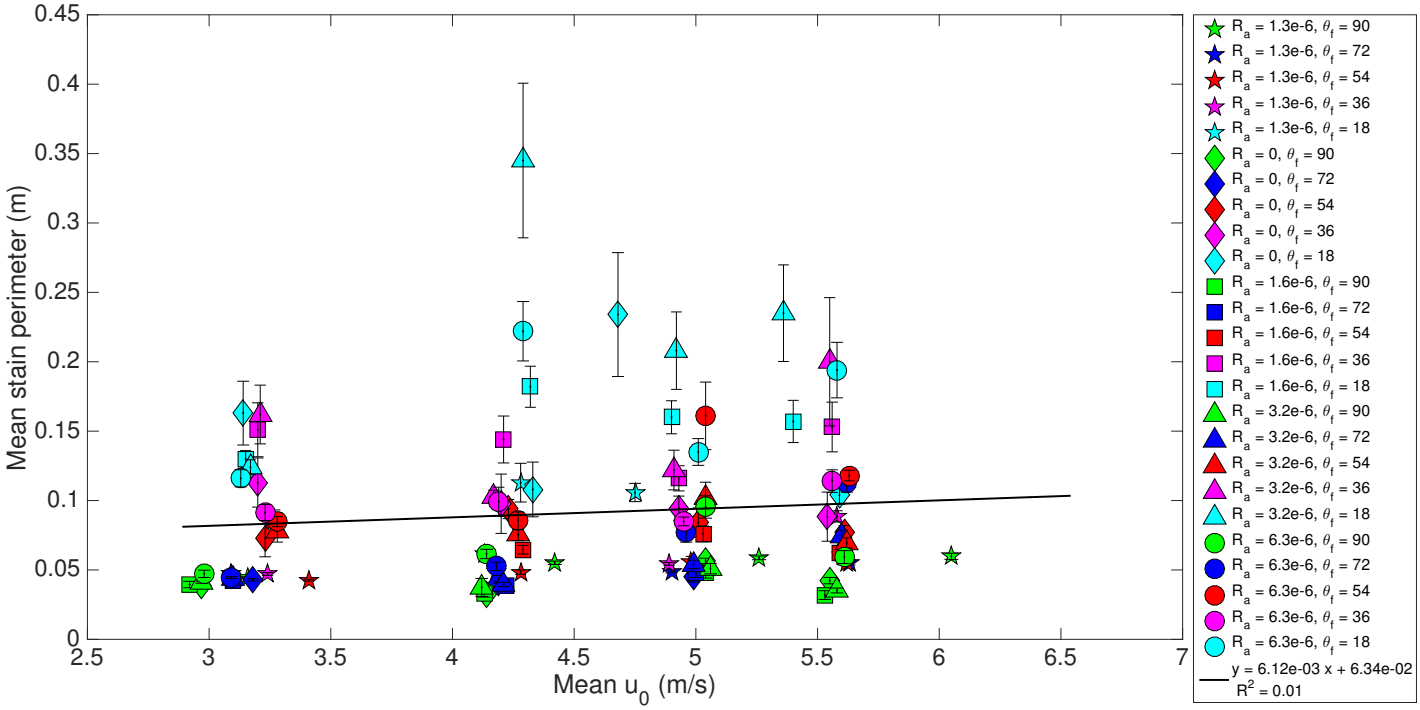

Figure 5.9: The effect of impact velocity on the mean perimeter of the stains from droplets impacting different surfaces at different angles. The data has been averaged at each height and the error bars represent the standard error.

The lower impact angles (specifically 18°) are all grouped together, regardless of the roughness of the substrates. Paper shows the most amount of spines and tails (because of its absorbent nature), whereas smooth steel exhibits the least amount of spines and tails. The roughness limit is shown slightly in Figure 5.11, where (disregarding paper) an increase of roughness seems to increase the number of spines/tails up to $R_a = 6.3 \times 10^{-6}\,\mathrm{m}$ where the number of spines/tails decreases again.

It would appear, in Figure 5.11, that there is a critical velocity around $u_0 = 2\,\mathrm{m\,s^{-1}}$, where for stains resulting from a velocity lower than $2\,\mathrm{m\,s^{-1}}$ the number of spines/tails is independent of velocity or impact angle. Stains resulting from velocities larger than $2\,\mathrm{m\,s^{-1}}$ develop a dependency on velocity and angle. The stains resulting from 18° and 36° are grouped so tightly together because these stains very rarely have more than one tail. There is not much variability in the number of tails for these stains. At impact angles great than 36° however, there is far more variability. In fact, stains resulting from impacts at 54° seem to be stains that transition

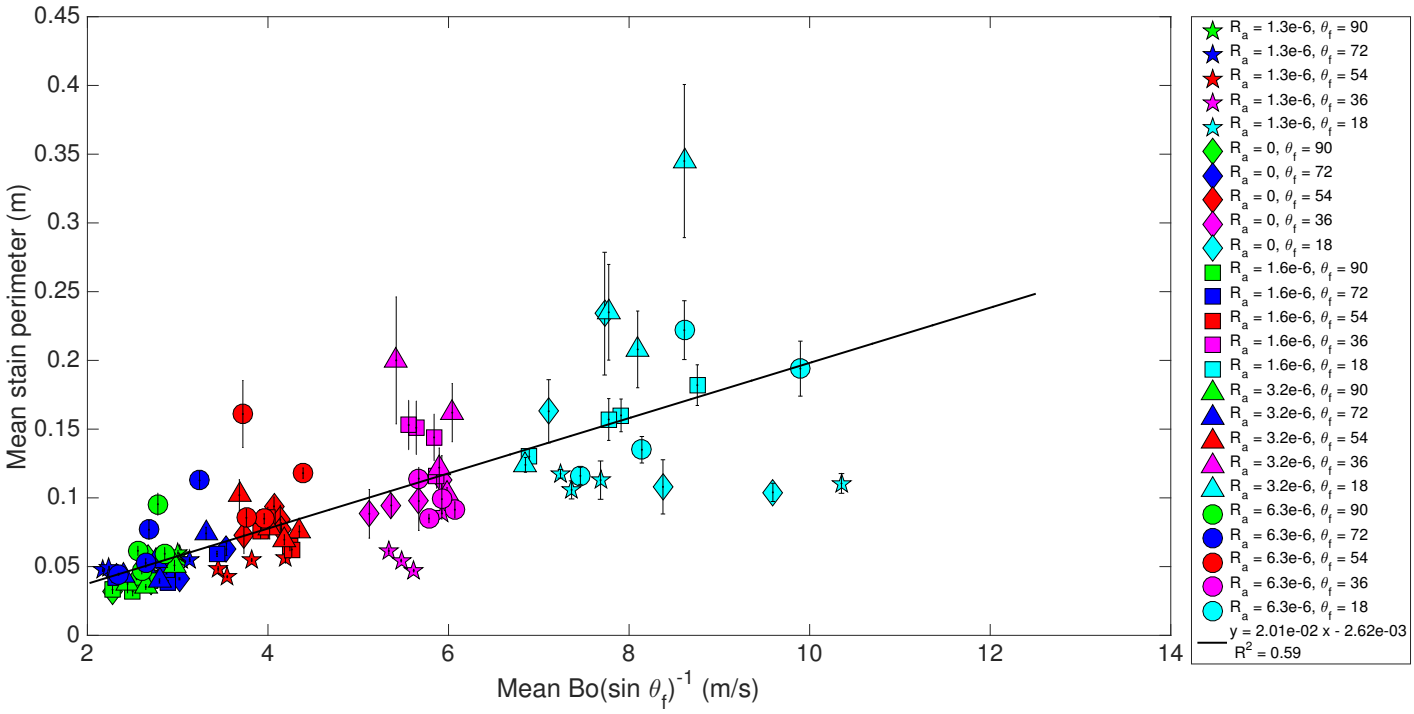

Figure 5.10: The effect of Bond number (Equation 5.4) and impact angle on the mean perimeter of the stains from droplets impacting different surfaces at different angles. The data has been averaged at each height and the error bars represent the standard error.

from having tails, to having spines.

The averaged data was used in statistical tests (Appendix C) to investigate if the number of spines and tails are effected by impact angle, height (impact velocity), and surface roughness. The result of a Levene's test ($p = 0.5111$) indicates that a three-way ANOVA test can be used. The three-way ANOVA test yields the following results:

- the impact angle affects the number of spines and tails ($F_{4,88} = 35.01$, $p = 0$);
- the roughness of the surface has an effect on the number of spines and tails ($F_{4,88} = 12.55$, $p = 0$); and
- the height from which the droplet has fallen does not have an effect on the number of spines and tails ($F_{3,88} = 2.06$, $p = 0.1115$).

A Tukey test was used to check if the mean number of spines/tails of certain groups of data are statistically different. With regards to the impact angles, the number of spines and tails fall into two categories, impact angles 18°, 36°, and 54° (all statistically the same). Then 72°

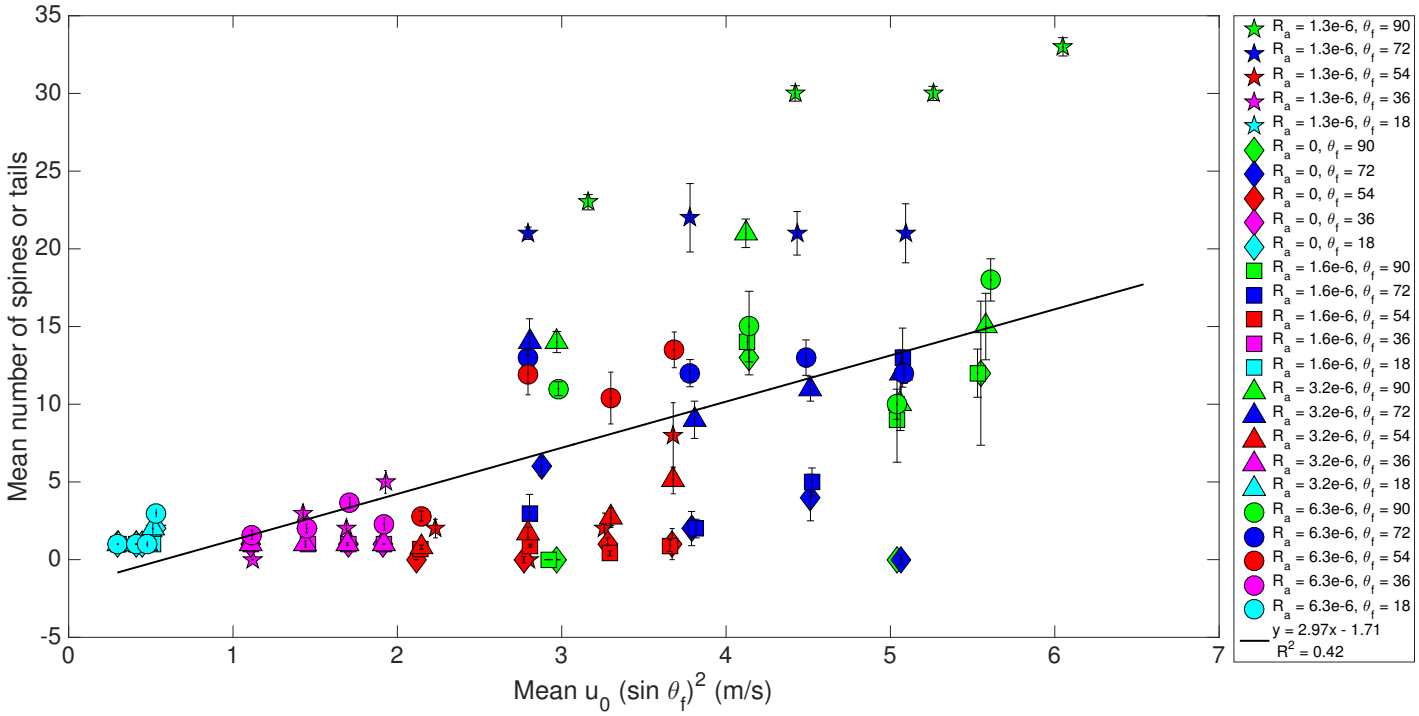

Figure 5.11: The effect of impact velocity and impact angle on the mean number of spines and tails of the stains from droplets impacting different surfaces at different angles. The data has been averaged at each height and the error bars represent the standard error.

and 90° (statistically the same). This is expected as the perpendicular impacts (90° and 72°) had spines and these spines were measured by the ASC (Chapter 3). The other impact angles resulted in more elliptical stains with tails, which were counted manually.

When using the Tukey test for surface roughness, it is shown that number of spines/tails on paper substrates is statistically the same as roughened steel substrates of $R_a = 6.3 \times 10^{-6}$ m. Further, $R_a = 3.2 \times 10^{-6}$ m appears to bridge the gap between all of the steel substrates but it should be noted that $R_a = 6.3 \times 10^{-6}$ m is statistically different from smooth steel and $R_a = 1.6 \times 10^{-6}$ m.

Another Tukey test showed mean numbers of spines/tails from all four heights are statistically the same. For reference, Figure 5.12 shows how the number of spines and tails collapses better when plotting paper alone. Paper has a level of absorbency that causes more consistent stains.

Finally, other non-dimensional numbers were tested in an attempt to find a combination of impact properties that would collapse the stain perimeter data better (Table V.1). Figure 5.13

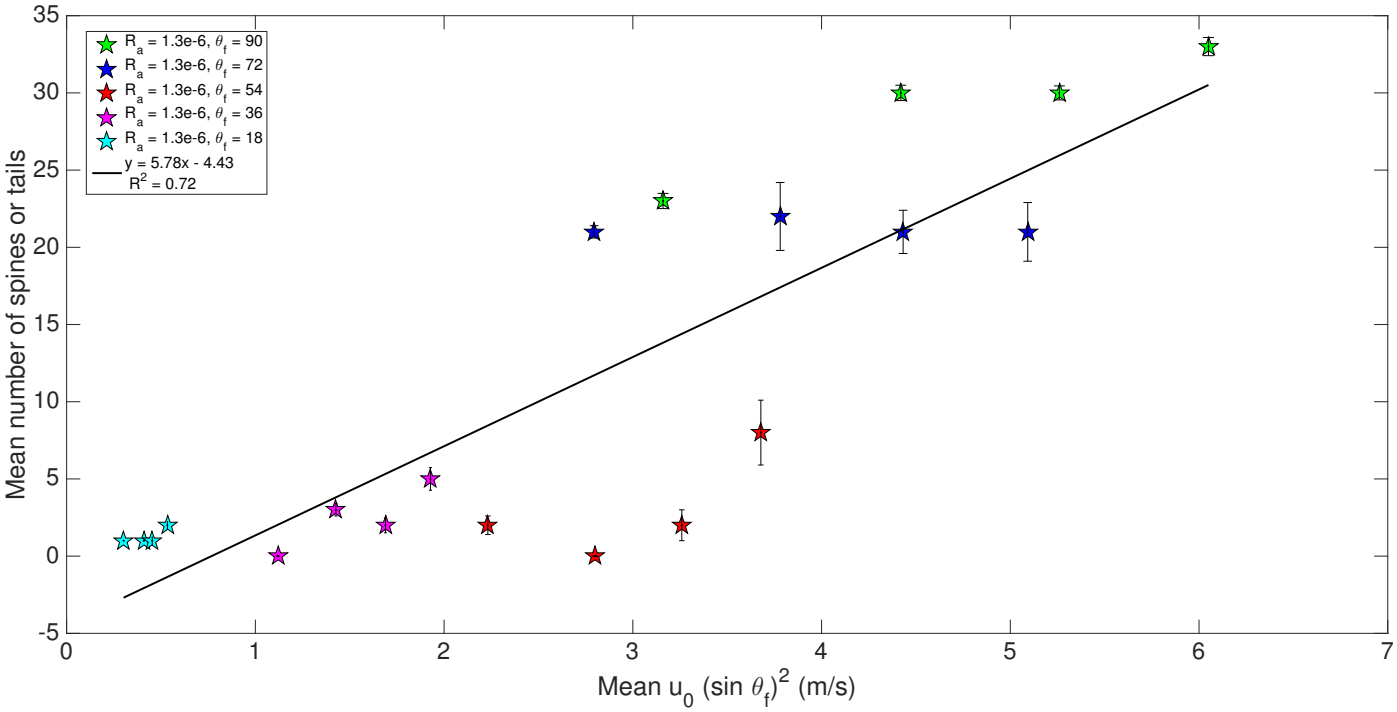

Figure 5.12: The effect of impact velocity and impact angle on the mean number of spines and tails of the stains from droplets impacting paper at different angles. The data has been averaged at each height and the error bars represent the standard error.

shows an improved correlation to the Froude number as opposed to the impact velocity alone, yielding an R^2 value of 0.43.

5.4.4 Effect of u_0 and θ_f on the major diameter of stains

It should be noted that the stains resulting from 90° and 72° are circular in shape, thus these stains do not have a major diameter explicitly. Instead, the outer diameter, d_{out}, was measured by the ASC on these stains and used in this comparison against the major diameter of the more elliptical stains from impact angles 54°, 36°, and 18°.

In this subsection it is seen that the major diameter of these stains are driven by the impact angle. Figure 5.14 shows a good linear relationship ($R^2 = 0.79$) between the impact properties and the major diameter. As expected, a decrease in impact angle creates more elongated stains. Further, greater impact velocities will input more energy into the impacts, also elongating the stains. Lastly, the more circular stains (green and dark blue symbols) are more variable

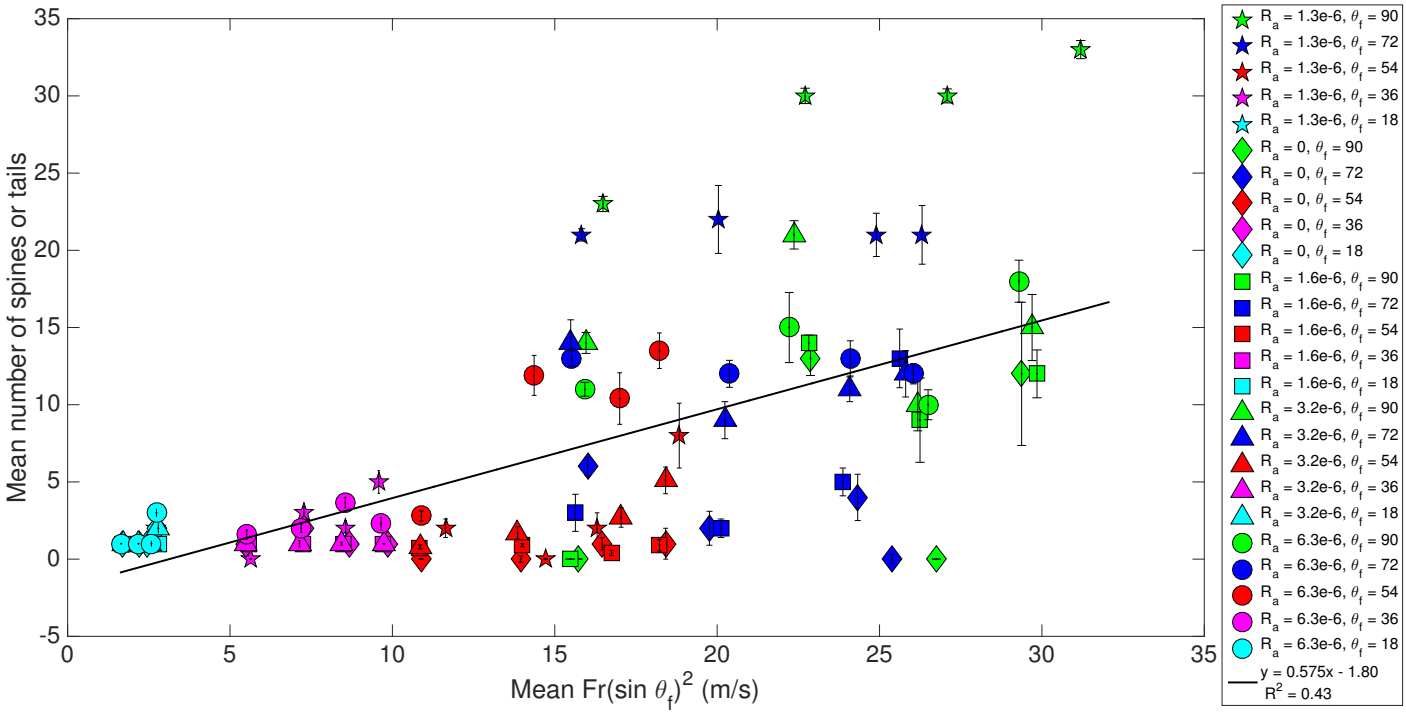

Figure 5.13: The effect of Froude number (Equation 5.5) and impact angle on the mean number of spines and tails on stains from droplets impacting different surfaces at different angles. The data has been averaged at each height and the error bars represent the standard error.

because the energy is directed in all directions equally instead of being forced down the substrate according to the impact angle. For angled impacts, gravity is pulling the droplet down causing a draining effect. The more perpendicular impacts have less of a spreading rate because the droplet is spreading in all directions. This means that perpendicular impacts have a shorter distance for surface tension to act and stabilise the spreading.

Levene's test yields a p-value of 0.6396, permitting the use of a three-way ANOVA test which produces the following results:

- the impact angle affects the major diameter ($F_{4,88} = 165.16$, $p = 0$);
- the height from which the droplet has fallen has an effect on the major diameter ($F_{3,88} = 16.3$, $p = 0$); and
- the roughness of the surface has an effect on the major diameter ($F_{4,88} = 3.29$, $p = 0.0147$).

A Tukey test shows that the mean major diameters of the stains resulting from impact angles

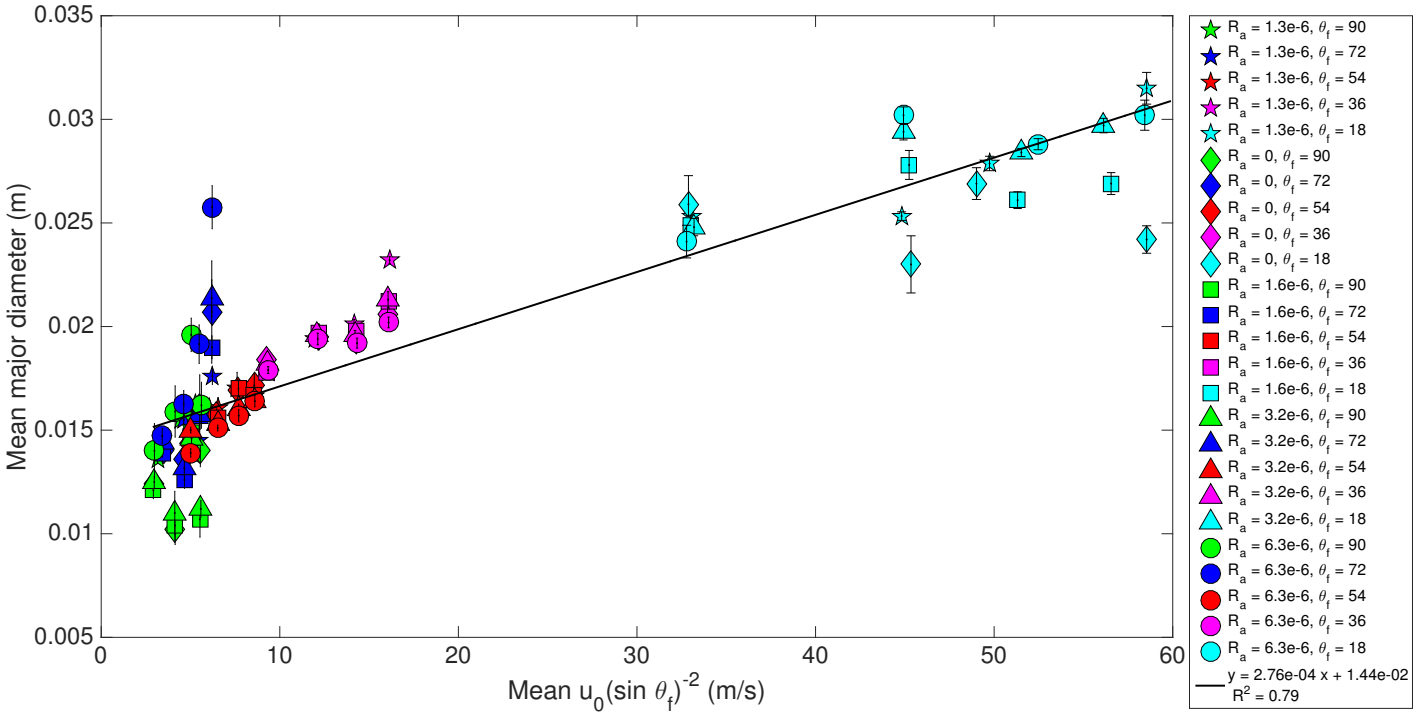

Figure 5.14: The effect of impact velocity and impact angle on the mean major diameter of the stains from droplets impacting different surfaces at different angles. The data has been averaged at each height and the error bars represent the standard error.

54° and 72° are statistically the same. The other impact angles yield statistically different mean major diameters.

Further, a Tukey test indicates that the roughest steel substrate yields statistically different mean major diameters to smooth steel and steel of $R_a = 1.6 \times 10^{-6}$ m but is statistically the same as paper.

Lastly, the smaller heights (0.5 m and 1.0 m) yield mean major diameters that are statistically the same then the larger heights (1.5 m and 2.0 m) have mean major diameters that are grouped together.

Other combinations of non-dimensional numbers were tested in an attempt to collapse the data better (Table V.1). After testing correlations between the major stain diameter and non-dimensional numbers, it was found that the Reynolds number (with the impact angle) collapses the data slightly better than the impact velocity alone. The Bond number also collapses the data better. Both the Reynolds number and the Bond number yield an R^2 value of 0.80. This is

shown in Figures 5.15 and 5.16.

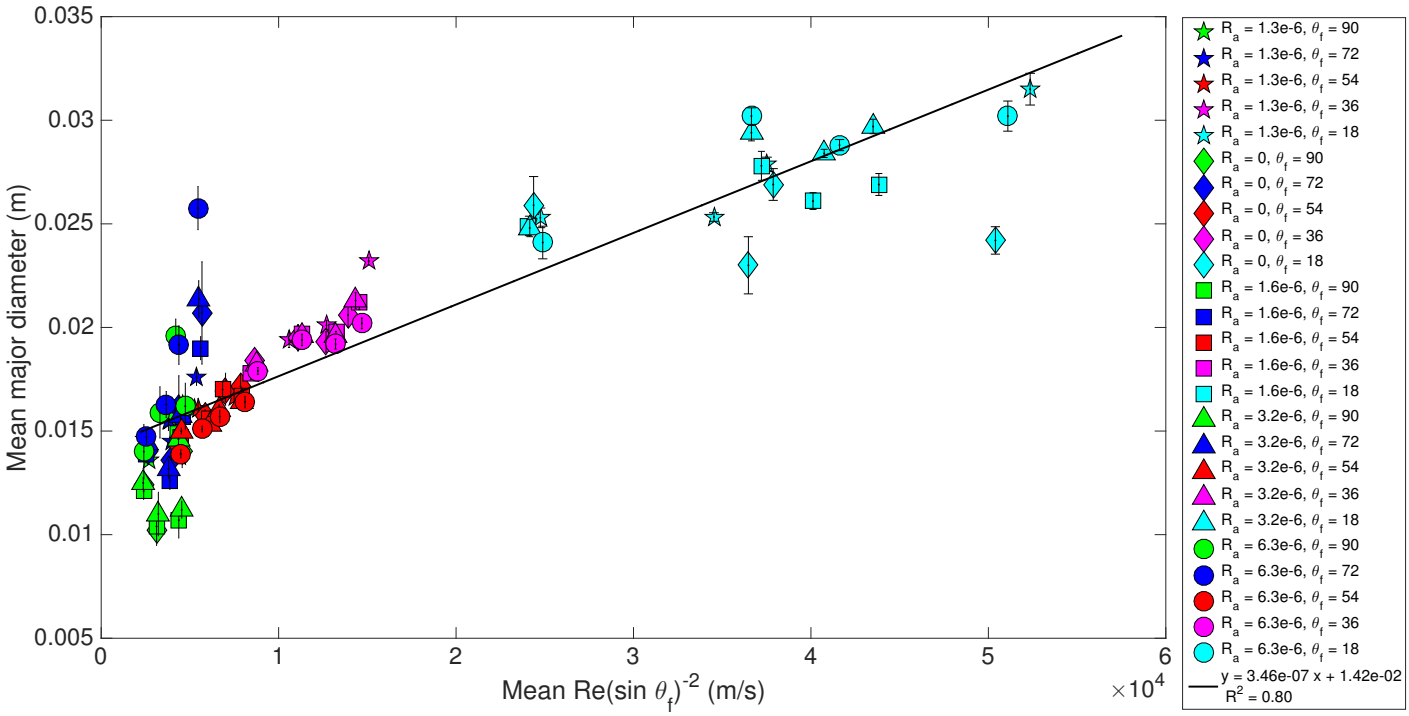

Figure 5.15: The effect of the Reynolds number and impact angle on the mean major diameter of the stains from droplets impacting different surfaces at different angles. The data has been averaged at each height and the error bars represent the standard error.

5.4.5 Effect of u_0 and θ_f on the minor diameter of stains

Similar to the previous subsection, the stains resulting from 90° and 72° are circular compared to the elliptical stains from impact angles 54°, 36°, and 18°. Again, the outer diameter, d_{out}, of these circular stains were measured by the ASC. This outer diameter is used in comparison to the minor diameter of the more elliptical stains .

The minor diameter of these stains have opposite relationships than those seen with major diameter. Figure 5.17 shows this, where an increase in impact angle (and increase in impact velocity) causes an increase in minor diameter. This is because with an increase impact angle, the stains are becoming shorter and therefore wider (moving from ellipses to circles). As mentioned in the previous subsection, the more perpendicular impacts (green and dark blue symbols) show more variability because the energy of the impact is directed in all directions

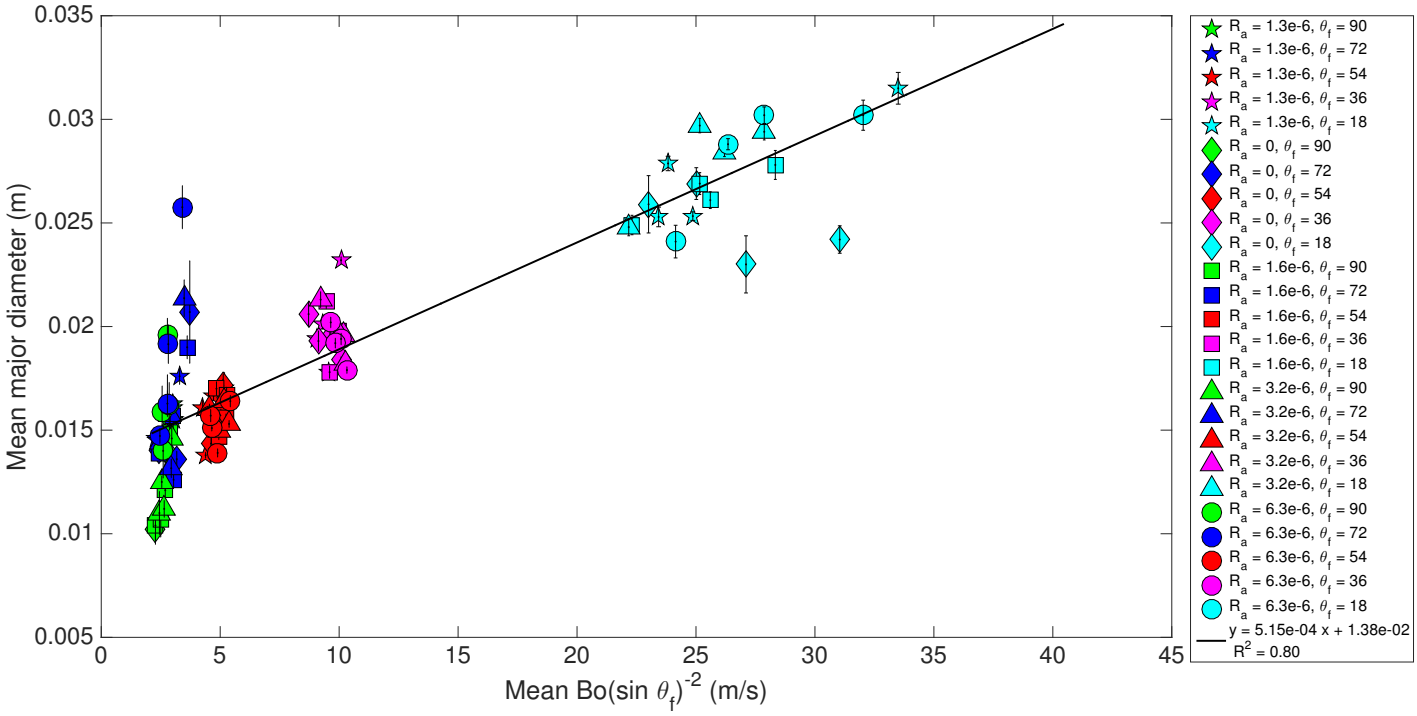

Figure 5.16: The effect of the Bond number and impact angle on the mean major diameter of the stains from droplets impacting different surfaces at different angles. The data has been averaged at each height and the error bars represent the standard error.

during impact instead of being prescribed down the substrate. Figure 5.17 shows that the impact velocity with the impact angle gives a correlation of $R^2 = 0.65$.

A three-way ANOVA test is used (as Levene's test allows, with $p = 0.0684$) and yields the following results:

- the impact angle affects the minor diameter ($F_{4,88} = 70.76$, $p = 0$);
- the height from which the droplet has fallen has an effect on the minor diameter ($F_{3,88} = 11.97$, $p = 0$); and
- the roughness of the surface has no effect on the minor diameter ($F_{4,88} = 2.28$, $p = 0.0674$).

A Tukey test shows that the mean minor diameters of stains resulting from impact angles 36° and 54° are statistically the same, the other impact angles are statistically different. Interestingly, the Tukey test also shows the increase in mean minor diameter with impact angle. Except at 90°, where the mean minor diameter of the stains is actually smaller than the mean minor

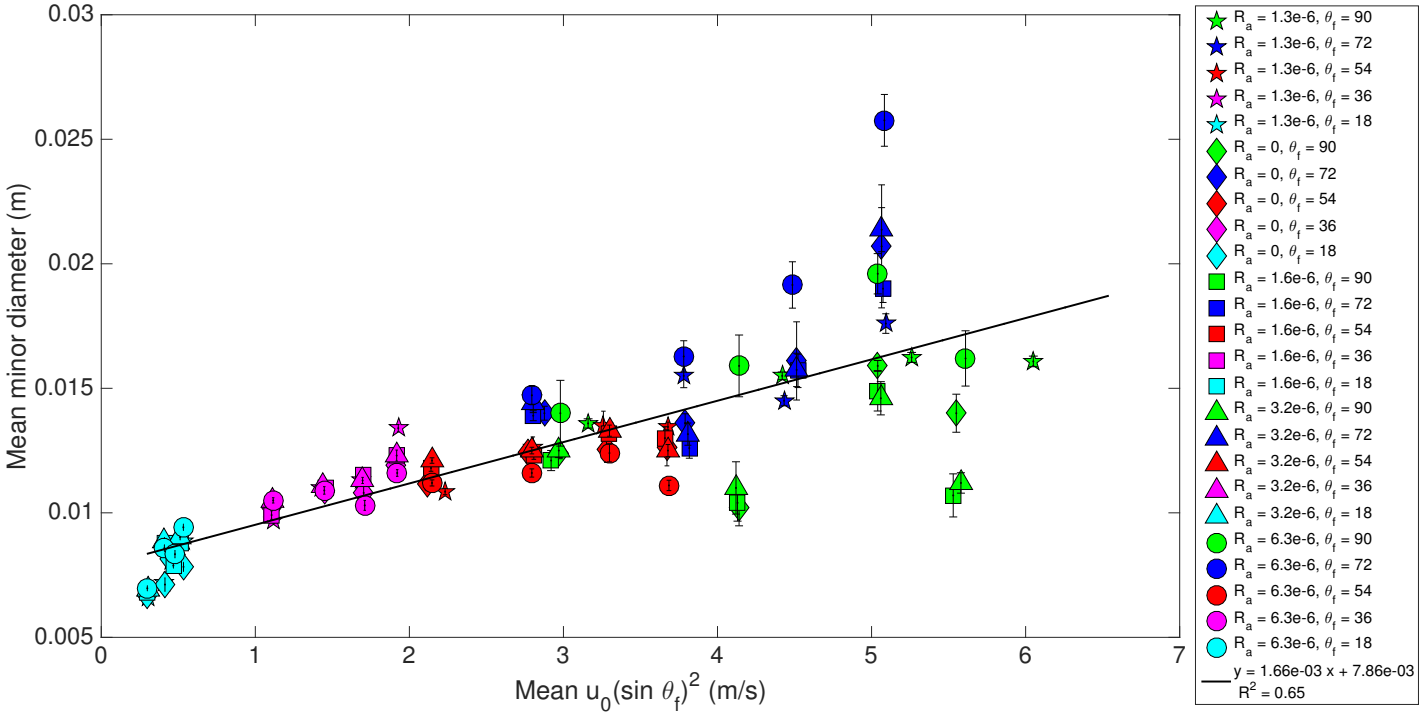

Figure 5.17: The effect of impact velocity and impact angle on the mean minor diameter of the stains from droplets impacting different surfaces at different angles. The data has been averaged at each height and the error bars represent the standard error.

diameters of stains from 72°. The reason for this is unknown but can be seen graphically in Figure 5.17 (where the dark blue symbols, 72°, have larger minor diameters as compared to the green symbols, 90°).

Another Tukey test shows that there is no statistical difference between the mean minor diameters on different substrates, which reaffirms the findings of the three-way ANOVA test. Similar to the results of the mean major diameters, the smaller heights (0.5 m and 1.0 m) are grouped together but statistically different to the larger heights (1.5 m and 2.0 m) which are grouped together.

Finally, other non-dimensional numbers were tested in an attempt to find a combination of impact properties that would collapse the minor diameter data better (Table V.1). Figure 5.18 shows an improved correlation to the Froude number as opposed to the impact velocity alone, yielding an R^2 value of 0.43.

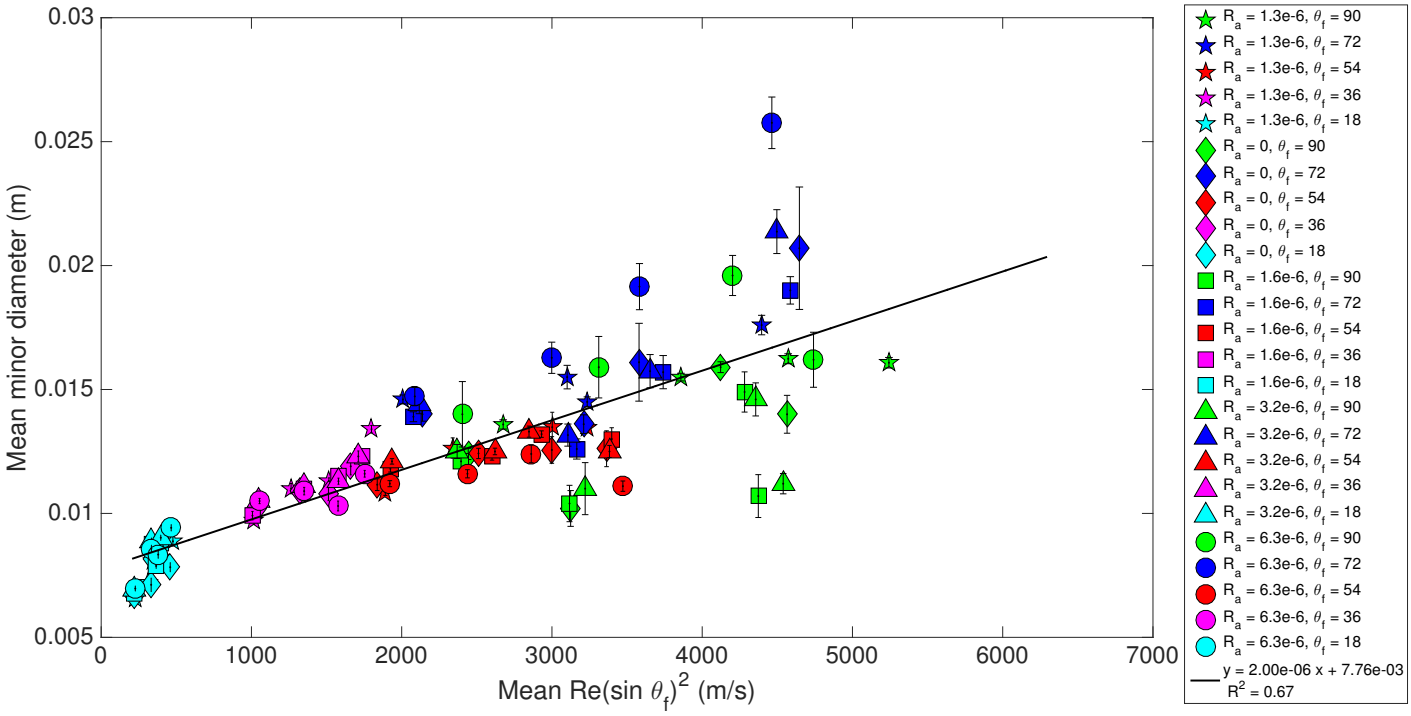

Figure 5.18: The effect of Reynolds number and impact angle on the mean minor diameter of stains from droplets impacting different surfaces at different angles. The data has been averaged at each height and the error bars represent the standard error.

5.4.6 Effect of u_0 and θ_f on the length of stains

The length of the stain is measured as the distance from the top of the stain to the end of the longest tail and thus includes and is larger than the major diameter. There is an increase in the length of stains (and variability in length) with a decrease in impact angle because of gravity pulling the droplet down the substrate. Further, there is an increase in length of stains with an increase in impact velocity (because the impacts have more energy). These notions are seen in Figure 5.19 where a good linear relationship ($R^2 = 0.70$ is shown between impact properties and the length of the stain. It would also be reasonable to expect that increased surface roughness (or absorbency, in the case of paper) would lower the length of the stains (as the droplet will not spread as far down the substrate). This is seen as well in Figure 5.19 where the roughest steel, $R_a = 6.3 \times 10^{-6}$ m, (circles) and paper substrates (stars) are associated with smaller lengths of stains.

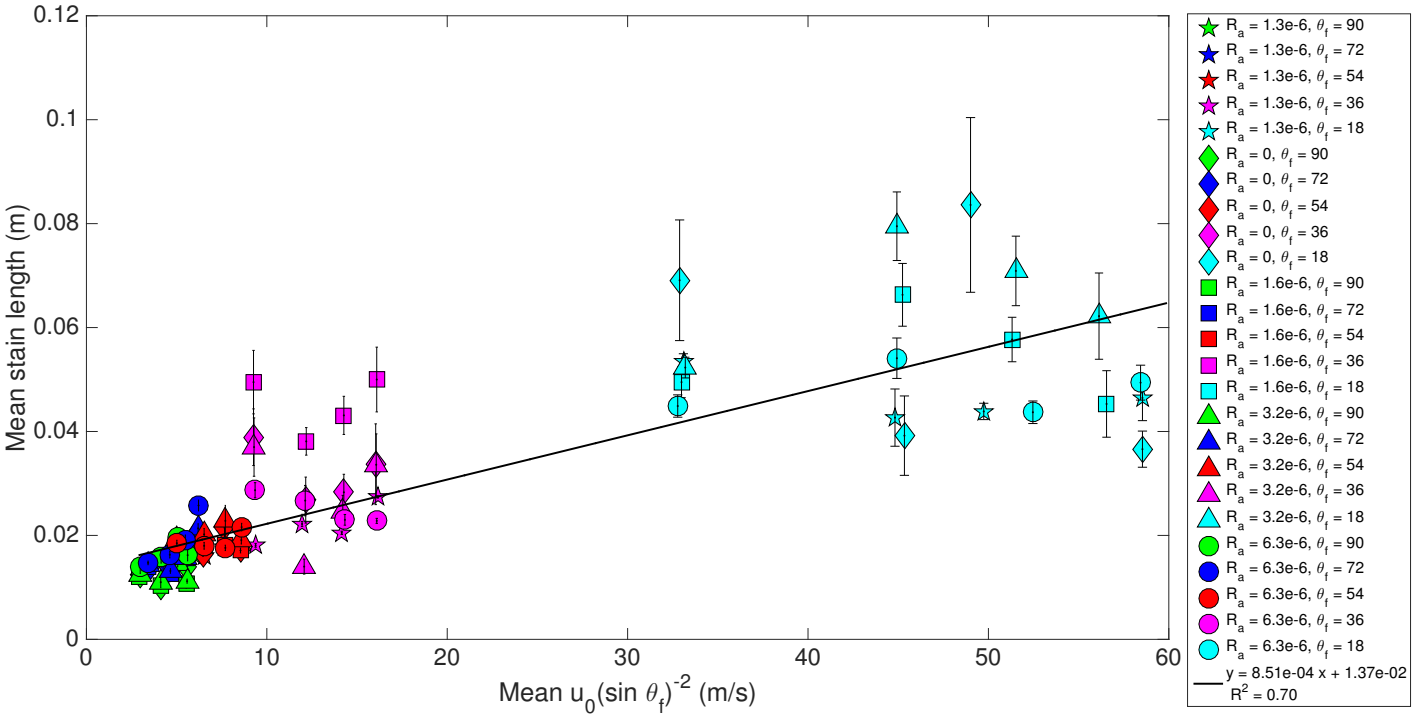

Figure 5.19: The effect of impact velocity and impact angle on the mean length of the stains from droplets impacting different surfaces at different angles. The data has been averaged at each height and the error bars represent standard error.

A Levene's test indicates ($p = 0.6619$) that a three-way ANOVA test can be used. The results of the ANOVA are as follows:

- the impact angle affects the length of the stain ($F_{4,88} = 90.64$, $p = 0$);
- the roughness of the surface does not have an effect on the length of the stain ($F_{4,88} = 1.86$, $p = 0.1245$); and
- the height from which the droplet has fallen has does not have an effect on the length of the stain ($F_{3,88} = 0.53$, $p = 0.6656$).

A Tukey test indicates that the mean length of stains resulting from impact angles 90°, 72°, and 54° are statistically the same. However, the mean length of stains resulting from 36° are statistically different and stains resulting from 18° are statistically different again.

Another Tukey test indicates that the mean length of the stains on different substrates are statistically the same, which is in agreement with the three-way ANOVA test. The same is true for the Tukey test regarding the height from which the droplet has fallen. There is no statistical

difference between the mean length of stains, when grouped by height.

Finally, other non-dimensional numbers were tested in an attempt to find a combination of impact properties that would collapse the minor diameter data better (Table V.1). Figure 5.20 shows an improved correlation to the Bond number as opposed to the impact velocity alone, yielding an R^2 value of 0.76.

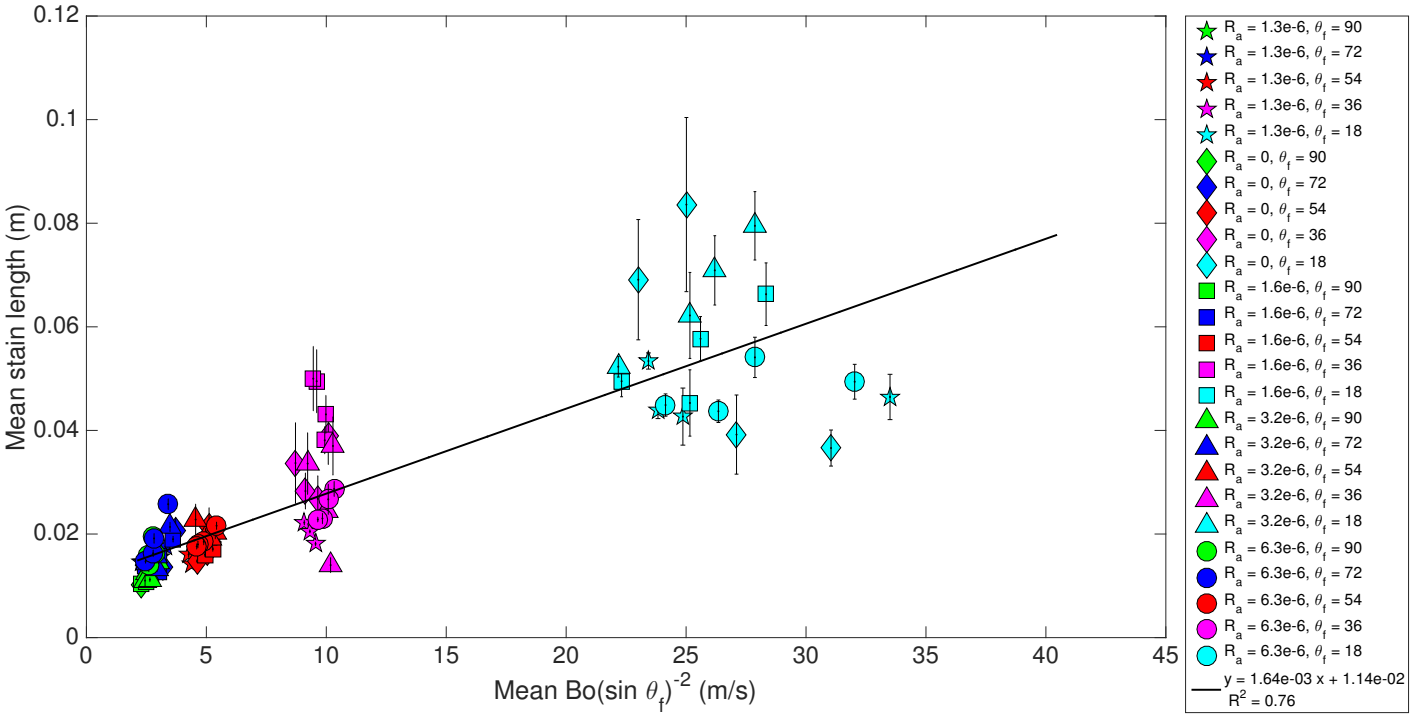

Figure 5.20: The effect of the Bond number and impact angle on the mean length of the stains from droplets impacting different surfaces at different angles. The data has been averaged at each height and the error bars represent standard error.

5.5 Statistical results

The Tukey tests give an indication of groups of data that are statistically similar or different. Regarding the impact angles the following facts can be stated:

- Impact angles 90° and 72° are statistically the same for all stain properties except the major and minor diameters.
- Impact angles 72° and 54° are statistically the same for all stain properties bar the number

of spines and tails and the minor diameter.

- Impact angles 54° and 36° are statistically the same for the number of tails, and minor diameter.
- Impact angles 36° and 18° are statistically the same for stain area and the number of tails.
- Stains resulting from impact angle 18° are the most exclusive, being statistically different for the most stain properties.

Regarding surface roughness the following facts can be stated:

- Smooth steel, steel of $R_a = 1.6 \times 10^{-6}$ m and steel of $R_a = 3.2 \times 10^{-6}$ m are statistically the same for all stain parameters.
- Paper is statistically the same as smooth steel and steel of $R_a = 1.6 \times 10^{-6}$ m for all stain parameters except major diameter.
- Paper is statistically the same as steel of $R_a = 6.3 \times 10^{-6}$ m for all parameters except stain perimeter.
- Paper is statistically the same as steel of $R_a = 3.2 \times 10^{-6}$ m for minor diameter and length of stains only.
- The roughest steel substrate is statistically the same as smooth steel and steel of $R_a = 1.6 \times 10^{-6}$ m for all stain parameters except major diameter.
- Roughened steel of $R_a = 3.2 \times 10^{-6}$ m is the most exclusive substrate, being statistically different for most stain properties.

Lastly, regarding the height from which the droplet has fallen, the Tukey tests revealed the following:

- The heights are divided into two groups (0.5 m with 1.0 m and 1.5 m with 2.0 m) for the stain area and major and minor diameters.

5.6 Summary

This chapter has outlined the results of the experiments carried out in Chapter 4. The flow of the droplets during impact were described to be laminar with inertial forces dominating the surface tension forces. 785 horse blood droplets of very similar diameter ($\bar{d_0} = 3.76 \times 10^{-3}$ m) were impacted onto five different substrates, at five different impact angles, from four different heights. Each combination of height, impact angle, and substrate had approximately five repeats performed. When studying the substrates it was found that conditioning paper substrates and the direction of grain on roughened substrates do not affect the stain properties.

By plotting the data and using statistical tests, it was found that the impact angle, roughness of a substrate, and impact velocity of a droplet almost always have an effect on stain shape and size. There are only a few cases were these factors do not affect stain properties. Surface roughness does not affect minor diameter and the length of a stain.

For all stain properties, the experimental data behaved in a physically sensible manner and in agreement with literature. For example, increases in impact velocity should impart more energy to the impacts, making the stain properties larger and more irregular. This is seen in all stain properties. Further, increases in impact angle should elongate stains (causing larger stain lengths and major diameters) which is seen in these results as well. Lastly, surface roughness should cause stains to be more irregular. This was also seen the results up to a limit of roughness ($R_a = 6.3 \times 10^{-6}$ m). Roughness promotes satellite stains but these results are only concerned with the parent stain. This caused some stain properties to be less variable where more complexity was expected.

Further, it was found that smooth steel and roughened steel of $R_a = 1.6 \times 10^{-6}$ m and steel of $R_a = 3.2 \times 10^{-6}$ m are statistically the same for all stain parameters. This means in further testing only one substrate is needed to represent these ranges of roughnesses. The impact angle has shown to affect all stain properties and needs to be included in all modelling of stain properties. Section 5.5 shows some important statistical findings that can be used to cut down

the number of experiments needed in certain ranges of angles or substrates.

Finally, the effects of impact angle, surface roughness, and impact velocity (while in some specific instances can be ignored) should be included in modelling of the spreading of a droplet onto surfaces. A spread factor has been suggested in this thesis that accounts for these three factors. The derivation and performance of this spread factor can be found in Chapter 6.

Chapter 6

Mathematical expressions developed for BPA

6.1 Motivation for new spread factor

The spread factor of a droplet has been investigated in the literature (Section 2.7). The spread factor is generally derived from the conservation of energy of a droplet during impact (Section 2.6). However, there are no spread factors in the literature that include the effect of surface roughness or impact angle. This chapter will show the derivation of a model to predict the spread factor, beginning with the conservation of energy, that includes the effect of surface roughness and impact angle. It should be clear that the model derived in this thesis includes the energies of the impact only. Therefore, the time scale covered here is from the moment the droplet first comes into contact with the substrate all the way to the moment the droplet settles on the substrate and stops moving. Because of this short time scale, the effect of the force of drag can be neglected as it would be a calculation of the drag on the droplet at an infinitesimally small height above the surface.

6.2 Derivation of a new spread factor

Starting with the conservation of energy (Equation 2.33), this thesis will make the same assumptions as Rein [1993], where the potential energy before and after impact is negligible. Hence the conservation of energy of a droplet's impact is:

$$E_K + E_S = E_S' - E_\theta + E_D\,, \tag{6.1}$$

where E_K, and E_S are the kinetic and surface energy of the droplet before impact, E_S' is the surface energy of the droplet during impact, E_θ is the energy lost along the contact line (*i.e.* it is the work done by the substrate onto the droplet), and E_D is the energy due to the deformation of the droplet.

As stated in Chapter 2 (Equation 2.34), the kinetic energy of a droplet before impact, E_K, is (Chandra and Avedisian [1991]; Pasandideh-Fard et al. [1996]; Roisman et al. [2002]; Adam [2012]):

$$E_K = \frac{\pi}{12}\rho_l d_0^3 u_0^2\,, \tag{6.2}$$

where ρ_l is the density of the droplet, d_0 is the diameter of the droplet before impact, and u_0 is the impact velocity of the droplet. The first modification to these generic energy equations, for the purposes of deriving a new spread factor, is to account for the impact angle of the droplet. The sine of the impact angle, θ_f has been added in with the impact velocity:

$$E_K = \frac{\pi}{12}\rho_l d_0^3 u_0^2 \left(\sin\theta_f\right)^2\,. \tag{6.3}$$

The term $\left(\sin\theta_f\right)^2$ was added to the velocity to allow the energy terms to account for the impact angle. This term was chosen specifically after testing other variations of impact angle and it proved to work best for this model. There are other energy terms in this chapter that have the same modifications with the velocity and those terms have been modified for the same

reason. Again from Chapter 2 (Equation 2.36), the surface energy, E_S, is (Engel [1955]; Chandra and Avedisian [1991]; Pasandideh-Fard et al. [1996]; Roisman et al. [2002]; Adam [2012]):

$$E_S = \sigma_{lg} \pi d_0^2 \,, \tag{6.4}$$

where d_0 is the diameter of the droplet before impact and σ_{lg} is the surface tension of the fluid against the air. See Appendix M for derivation of Equation 6.4.

The surface energy of the droplet during the impact (also Chapter 2, Equation 2.42), E_S', is given by:

$$E_S' = \pi \sigma_{lg} \left(\frac{d_{\max}^2}{4} + \frac{2d_0^3}{3d_{\max}} \right) , \tag{6.5}$$

where σ_{lg} is the surface tension, $d_{\max}$ is the maximum diameter of the droplet, d_0 is the diameter of the droplet before impact.

The energy along the contact line, E_θ, is adapted (in this thesis) from work by Roisman et al. [2002] (Equation 2.44) where the advancing contact angle is replaced with the contact angle on a rough surface (see Section 2.5):

$$E_\theta = \frac{\pi}{4} d_{\max}^2 \sigma_{lg} \cos\theta_{rough} \,, \tag{6.6}$$

where again σ_{lg} is the surface tension, $d_{\max}$ is the maximum diameter of the droplet, and $\cos\theta_{rough}$ is defined as the contact angle on a rough surface. The expression for the contact angle on a rough surface, θ_{rough}, is by Carey [1992] (as seen in Chapter 2, Equation 2.30) but has yet to be used in a spread factor:

$$\cos\theta_{rough} = \frac{A_{ac}}{A_{geo}} \cos\theta_Y \,, \tag{6.7}$$

where A_{ac} is the actual surface area of a surface, A_{geo} is the geometric surface area (Section 2.4), and the ratio of these two areas is denoted as $\mathbb{R}$.

From Section 2.4 the actual surface roughness can be calculated using the formula:

$$A_{ac} = 2W\sqrt{\frac{x^2}{4}+h^2}\left(\frac{pL}{l}-1\right), \tag{6.8}$$

where W is the width of the substrate, L is the length of the substrate, x is the distance between peaks along the substrate, h is the height of each peak on the substrate, p is the number of peaks measured over a known distance, l. With regards to the substrates used in this thesis, a Profile Projector PJ 300 was used to measure x, h, p, and l. From Chapter 4, the steel substrates have the dimensions $W = 0.05\,\text{m}$ and $L = 0.2\,\text{m}$ and thus have a geometric area of $A_{geo} = WL = 0.01\,\text{m}^2$. The paper substrates and smooth steel substrates were assumed to have an actual surface area equal to their geometric surface area, thus both have a $\mathbb{R} = 1$.

Using Equation 6.8, the following $\mathbb{R}$ values were calculated for the roughened steel substrates:

- Steel of $R_a = 1.6 \times 10^{-6}\,\text{m}$: $\mathbb{R} = 1.32$;
- Steel of $R_a = 3.2 \times 10^{-6}\,\text{m}$: $\mathbb{R} = 1.15$; and
- Steel of $R_a = 6.3 \times 10^{-6}\,\text{m}$: $\mathbb{R} = 1.02$.

Looking back to Equation 6.7, θ_Y is the value of the equilibrium contact angle in the ideal situation where a substrate is smooth, rigid, homogenous, and insoluble, with constant interfacial tensions (Section 2.5). When blood impacts a substrate, wetting is occurring which means $0° < \theta_Y < 90°$ (Section 2.5). The assumption will be made here that $\theta_Y = 45°$ thus $\cos\theta_Y = \sqrt{2}/2$. Including this assumption, and substituting Equation 6.7 into Equation 6.6, the energy lost along the contact line becomes:

$$E_\theta = \frac{\pi}{4} d_{\max}^2 \sigma_{lg}\left(\frac{\sqrt{2}}{2}\mathbb{R}\right). \tag{6.9}$$

Lastly, the deformation energy selected for this spread factor is by Pasandideh-Fard et al. [1996]:

$$E_D = \frac{\pi \rho_l u_0^2 d_0 d_{\max}^2}{3\sqrt{\mathrm{Re}}}, \tag{6.10}$$

where ρ_l is the density of the fluid, u_0 is the impact velocity of the droplet, d_0 is the diameter of the droplet before impact, and Re is the Reynolds number (as defined by Equation 2.9). The same modification of accounting for the impact angle, θ_f, (as carried out for the kinetic energy) is suggested here:

$$E_D = \frac{\pi \rho_l u_0^2 \left(\sin\theta_f\right)^2 d_0 d_{\max}^2}{3\sqrt{\mathrm{Re}}\sqrt{\sin\theta_f}}. \tag{6.11}$$

This deformation energy was chosen over the other options in Chapter 2 because it can be seen in the conservation of energy that the energies before impact will be driven mostly by the kinetic energy before impact and thus, to conserve energy correctly, another energy during impact needed to be large enough to balance Equation 6.1. For a droplet with $d_0 = 3.69 \times 10^{-3}\,\mathrm{m}$ and $u_0 = 3.28\,\mathrm{m\,s^{-1}}$ impacting paper perpendicularly (thus $\mathbb{R} = 1$, see Section 2.4 and $\theta_f = 90°$), and physical constants of $\rho_l = 1062\,\mathrm{kg\,m^{-3}}$, $\sigma_{lg} = 5.1 \times 10^{-2}\,\mathrm{N\,m^{-1}}$, and $\mu_l = 4.7 \times 10^{-3}\,\mathrm{N\,s\,m^{-2}}$ the terms in the conservation of energy become:

- $E_K = 1.50 \times 10^{-4}\,\mathrm{J}$ (Equation 6.3);
- $E_S = 2.18 \times 10^{-6}\,\mathrm{J}$ (Equation 6.4);
- $E_S' = 6.90 \times 10^{-6}\,\mathrm{J}$ (Equation 6.5);
- $E_\theta = 4.43 \times 10^{-6}\,\mathrm{J}$ (Equation 6.9); and
- $E_D = 1.33 \times 10^{-4}\,\mathrm{J}$ (Equation 6.11).

Note, the larger terms are the kinetic energy of the droplet before impact and the deformation of the droplet during impact because they both have a density term and a velocity squared term. The deformation of the droplet suggested by Roisman et al. [2002] does not give an energy large enough to balance the conservation of energy. Recall, Equation 2.57:

$$E_D = \frac{2\pi\sigma_{lg}}{5}\left(\frac{\mathrm{We}}{\mathrm{Re}}\right)\left[\frac{1}{27}\left(\frac{d_0^8}{d_{\max}^6}\right) + \frac{d_0^4}{d_{\max}^2}\right], \tag{6.12}$$

would produce an energy of $E_D = 2.29 \times 10^{-8}\,\mathrm{J}$ which is too small. Substituting Equations 6.3, 6.4, 6.5, 6.9, and 6.11 into Equation 6.1:

$$E_K + E_S = E_S' - E_\theta + E_D$$

$$\frac{\pi}{12}\rho_l d_0^3 u_0^2 \left(\sin\theta_f\right)^2 + \sigma_{lg}\pi d_0^2 = \pi\sigma_{lg}\left(\frac{d_{\max}^2}{4} + \frac{2d_0^3}{3d_{\max}}\right) - \frac{\pi}{4}d_{\max}^2\sigma_{lg}\left(\frac{\sqrt{2}}{2}\mathbb{R}\right) + \frac{\pi\rho_l u_0^2\left(\sin\theta_f\right)^2 d_0 d_{\max}^2}{3\sqrt{\mathrm{Re}}\sqrt{\sin\theta_f}}.$$

Divide all terms by $\pi\sigma_{lg}d_0^2$:

$$\frac{1}{12\sigma_{lg}}\rho_l d_0 u_0^2\left(\sin\theta_f\right)^2 + 1 = \left(\frac{d_{\max}^2}{4d_0^2} + \frac{2d_0}{3d_{\max}}\right) - \frac{1}{4d_0^2}d_{\max}^2\left(\frac{\sqrt{2}}{2}\mathbb{R}\right) + \frac{\rho_l u_0^2\left(\sin\theta_f\right)^2 d_0 d_{\max}^2}{3d_0^2\sigma_{lg}\sqrt{\mathrm{Re}}\sqrt{\sin\theta_f}}$$

$$\frac{\mathrm{We}\left(\sin\theta_f\right)^2}{12} + 1 = \left(\frac{d_{\max}^2}{4d_0^2} + \frac{2d_0}{3d_{\max}}\right) - \frac{1}{4d_0^2}d_{\max}^2\left(\frac{\sqrt{2}}{2}\mathbb{R}\right) + \frac{\mathrm{We}\left(\sin\theta_f\right)^2 d_{\max}^2}{3d_0^2\sqrt{\mathrm{Re}}\sqrt{\sin\theta_f}}.$$

Now recall that the spread factor is the ratio of $d_{\max}$ to d_0:

$$\frac{\mathrm{We}\left(\sin\theta_f\right)^2}{12} + 1 = \left(\frac{\beta^2}{4} + \frac{2}{3\beta}\right) - \frac{\beta^2}{4}\left(\frac{\sqrt{2}}{2}\mathbb{R}\right) + \frac{\beta^2\mathrm{We}\left(\sin\theta_f\right)^2}{3\sqrt{\mathrm{Re}}\sqrt{\sin\theta_f}}$$

$$\frac{\mathrm{We}\left(\sin\theta_f\right)^2}{12} + 1 = \beta^2\left(\frac{1}{4} - \frac{\sqrt{2}}{8}\mathbb{R} + \frac{\mathrm{We}\left(\sin\theta_f\right)^2}{3\sqrt{\mathrm{Re}}\sqrt{\sin\theta_f}}\right) + \frac{2}{3\beta}$$

$$\frac{\mathrm{We}\left(\sin\theta_f\right)^2}{12} + 1 = \beta^2\left(\frac{1}{4} - \frac{\sqrt{2}}{8}\mathbb{R} + \frac{\mathrm{We}\left(\sin\theta_f\right)^{3/2}}{3\sqrt{\mathrm{Re}}}\right) + \frac{2}{3\beta}.$$

Using our test droplet again, with $d_0 = 3.69 \times 10^{-3}\,\mathrm{m}$, $u_0 = 3.28\,\mathrm{m\,s^{-1}}$, $\mathbb{R} = 1$, and $d_{\max} = 1.25 \times 10^{-2}\,\mathrm{m}$, it can be seen that the inverse of β is small compared to the other terms in this equation (Weber number is in the order of 10^3, where β is in the order 10^{-1}). It can also be seen that as $\beta \to \infty$ the last term on the right hand side tends to zero. Therefore, the $2/(3\beta)$ term will be neglected.

$$\frac{\mathrm{We}\left(\sin\theta_f\right)^2}{12}+1=\beta^2\left(\frac{1}{4}-\frac{\sqrt{2}}{8}\mathbb{R}+\frac{\mathrm{We}\left(\sin\theta_f\right)^{3/2}}{3\sqrt{\mathrm{Re}}}\right)+\frac{2}{\cancel{3}\beta}$$

$$\mathrm{We}\left(\sin\theta_f\right)^2+12=\beta^2\left(3-\frac{3\sqrt{2}}{2}\mathbb{R}+\frac{4\mathrm{We}\left(\sin\theta_f\right)^{3/2}}{\sqrt{\mathrm{Re}}}\right)$$

$$\sqrt{\frac{\mathrm{We}\left(\sin\theta_f\right)^2+12}{3\left(1-\frac{\sqrt{2}}{2}\mathbb{R}\right)+\frac{4\mathrm{We}\left(\sin\theta_f\right)^{3/2}}{\sqrt{\mathrm{Re}}}}}=\beta\,. \tag{6.13}$$

This spread factor has been derived from the conservation of energy but includes a term that accounts for the roughness of substrates and it also accounts for the impact angle of the droplet. The magnitudes of the terms in Equation 6.13 can be investigated using the test droplet again: $d_0 = 3.69\times10^{-3}\,\mathrm{m}$, $u_0 = 3.28\,\mathrm{m\,s^{-1}}$, $\mathbb{R}=1$, and $d_{\max} = 1.25\times10^{-2}\,\mathrm{m}$. Thus the values of the terms are as follows:

- $\mathrm{We}\left(\sin\theta_f\right)^2 = 826.7$;
- $3\left(1-\frac{\sqrt{2}}{2}\mathbb{R}\right) = 0.88$;
- $4\mathrm{We}\left(\sin\theta_f\right)^{3/2} = 3306.8$; and
- $\sqrt{\mathrm{Re}} = 52.3$.

These magnitudes indicate that $\mathrm{We}\left(\sin\theta_f\right)^2 \gg 12$ and $\frac{4\mathrm{We}\left(\sin\theta_f\right)^{3/2}}{\sqrt{\mathrm{Re}}} \gg 3\left(1-\frac{\sqrt{2}}{2}\mathbb{R}\right)$ which indicates that a simplified version of Equation 6.13 is possible:

$$\begin{aligned}\beta &= \sqrt{\frac{\mathrm{We}\left(\sin\theta_f\right)^2 + \cancel{12}}{\cancel{3\left(1-\frac{\sqrt{2}}{2}\mathbb{R}\right)} + \frac{4\mathrm{We}\left(\sin\theta_f\right)^{3/2}}{\sqrt{\mathrm{Re}}}}} \\ &= \sqrt{\frac{\mathrm{We}\left(\sin\theta_f\right)^2}{\frac{4\mathrm{We}\left(\sin\theta_f\right)^{3/2}}{\sqrt{\mathrm{Re}}}}} \\ &= \sqrt{\frac{\left(\sin\theta_f\right)^{1/2}}{\frac{4}{\sqrt{\mathrm{Re}}}}} \\ &= \frac{1}{2}\mathrm{Re}^{1/4}\left(\sin\theta_f\right)^{1/4}. \end{aligned} \tag{6.14}$$

This simplified version of the new spread factor model will be tested in the next section.

6.3 Test spread factors against experimental data

The spread factors were tested against experimental data by plotting the experimental spread factor. Normally, the spread factor is calculated using the ratio $\beta = d_{\max}/d_0$, however, the spread factor model assumes that the spread is occurring in both directions (width, i, and length, j). Thus, the spread factor ratio used to test the models will be $\beta = \bar{d}/d_0$, where $\bar{d}$ is the average of d_i and d_j for every stain. The models either given in the literature (Chapter 2) or the model derived in this thesis, shown in Section 6.2 were compared to the experimental spread factors.

As a reminder, the spread factors being tested are the following:

$$\beta = 0.816\mathrm{We}^{\frac{1}{4}}\left(1+\frac{1}{2\mathrm{Fr}}\right)^{\frac{1}{4}}, \tag{6.15}$$

developed by Cheng [1977], where We is the Weber number and Fr is the Froude number (see Section 2.1). Another spread factor by Chandra and Avedisian [1991]:

$$\beta \approx \sqrt{\frac{\frac{\mathrm{We}}{3}+4}{1-\cos\theta_a}}, \tag{6.16}$$

where θ_a is the advancing contact angle. This spread factor was then improved by Pasandideh-Fard et al. [1996]:

$$\beta = \sqrt{\frac{\mathrm{We}+12}{3\left(1-\cos\theta_a\right)+\frac{4\mathrm{We}}{\sqrt{\mathrm{Re}}}}}, \tag{6.17}$$

where Re is the Reynolds number (Section 2.1). Finally, the correct and more general version (*i.e.*, without a fitting constant) of Hulse-Smith et al. [2005]'s spread factor:

$$\beta = \frac{1}{2}\mathrm{Re}^{1/4}. \tag{6.18}$$

All of these will be tested, along side Equation 6.13, against the experimental data from this thesis. Figure 6.1 shows the spread factors plotted against the Reynolds number. First off, it shows the spread factor proposed by Chandra and Avedisian [1991] has a large amount of variation and overestimates the experimental spread factor greatly. This was explained by Pasandideh-Fard et al. [1996] to be caused by using an incorrect characteristic length in the model (Section 2.7). However, even with the improvements to Chandra and Avedisian [1991]'s work (Section 2.7), Pasandideh-Fard et al. [1996]'s spread factor fares much better along with Hulse-Smith et al. [2005]'s general spread factor. Figure 6.2 shows the same results, but uses the Weber number instead.

Figures 6.3 and 6.4 removes the spread factors that overestimate the data set greatly, to show a closer look at how the spread factor by Cheng [1977], Hulse-Smith et al. [2005], Pasandideh-Fard et al. [1996], and the spread factor developed in this thesis fare against the experimental data. Again, these plots are against the Reynolds number and Weber number respectively.

It should be noted that the models by Hulse-Smith et al. [2005] and Pasandideh-Fard et al. [1996] yield nearly identical spread factors so the points showing the Hulse-Smith et al. [2005] model are hiding behind the points showing thePasandideh-Fard et al. [1996] model in the plots. Figures 6.5 and 6.6 show, specifically, how Equation 6.13 is failing at lower impact angles. Equation 6.13 is producing the correct impact velocity but is underestimating the spread factor.

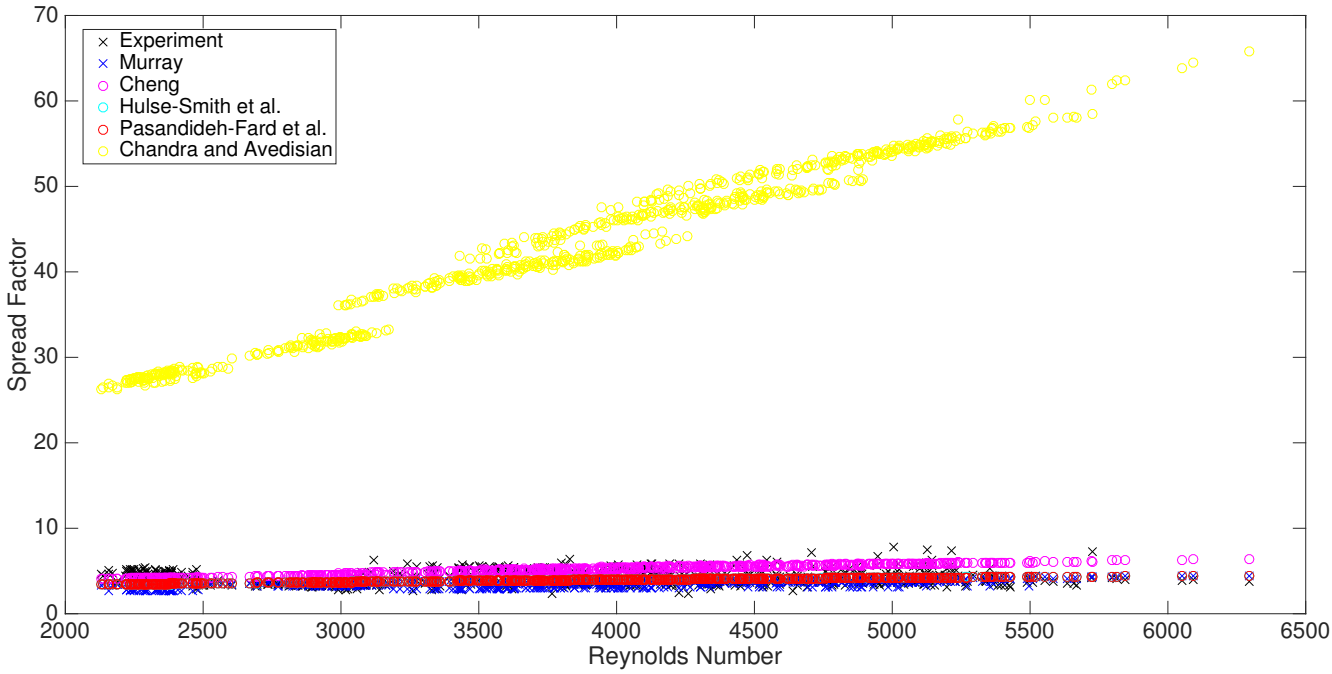

Figure 6.1: A comparison of spread factors against experimental data using the Reynolds number: Cheng [1977] (Equation 6.15), Chandra and Avedisian [1991] (Equation 2.63), Hulse-Smith et al. [2005] (Equation 6.18), Pasandideh-Fard et al. [1996] (Equation 2.64), and Murray (Equation 6.13).

To remedy this, it was considered to multiply the spread factor by a dimensionless coefficient that is based on the measured properties of the stain.

The coefficient trialled to help Equation 6.13 perform better at lower impact angles was $\left(\frac{\bar{d}}{d_i d_j}\right)^2$. This coefficient was chosen because it gives Equation 6.13 more dependancy on the final diameter of the droplet's spread in both directions. Equation 6.13 then becomes:

$$\beta = \left(\frac{\bar{d}}{d_i d_j}\right)^2 \sqrt{\frac{\mathrm{We}\left(\sin\theta_f\right)^2 + 12}{3\left(1 - \frac{\sqrt{2}}{2}\mathbb{R}\right) + \frac{4\mathrm{We}\left(\sin\theta_f\right)^{3/2}}{\sqrt{\mathrm{Re}}}}}. \tag{6.19}$$

This adjustment to the spread factor model allows the model to behave better for lower impact angles. Figures 6.7 and 6.8 show the improvement of Equation 6.19 particularly regarding lower impact angles.

Figures 6.9 and 6.10 are the same plots as shown in Figures 6.3 and 6.4, but using the new spread factor model, with the coefficient added, shown in Equation 6.19. These plots show that

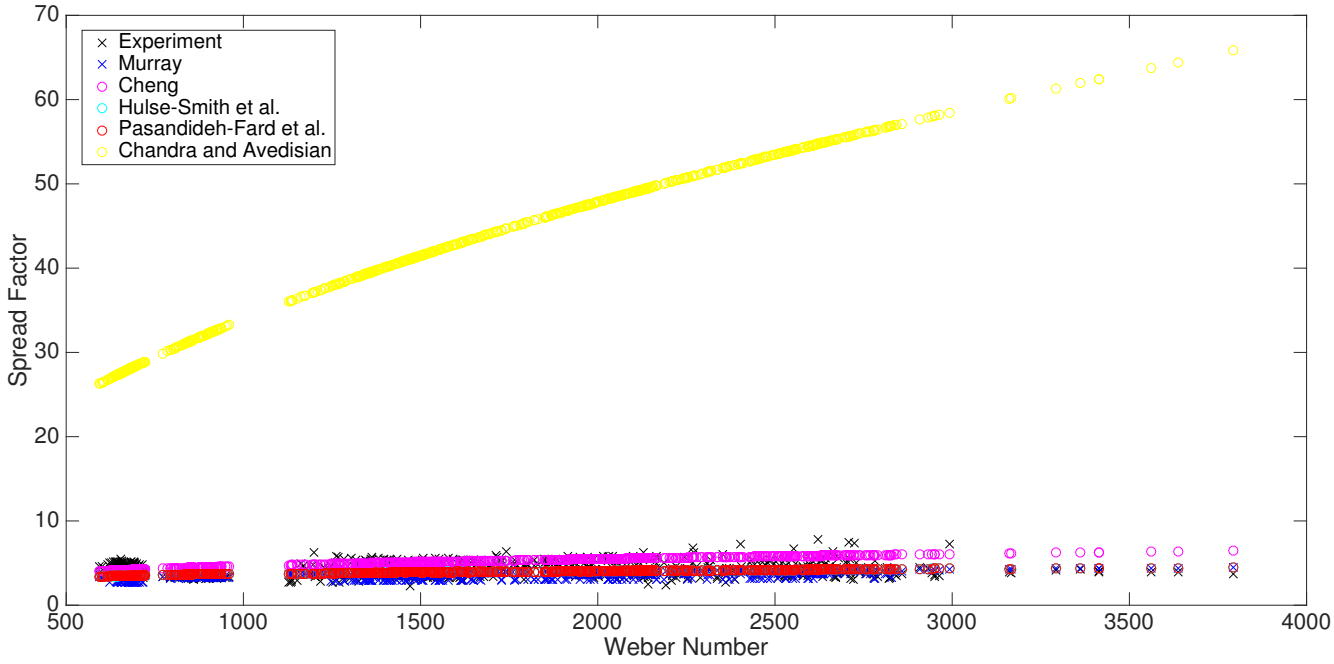

Figure 6.2: A comparison of spread factors against experimental data using the Weber number: Cheng [1977] (Equation 6.15), Chandra and Avedisian [1991] (Equation 2.63), Hulse-Smith et al. [2005] (Equation 6.18), Pasandideh-Fard et al. [1996] (Equation 2.64), and Murray (Equation 6.13).

Equation 6.19 no longer underestimates the experimental spread factor and does better to give a larger range of spread factors, as shown in the experimental spread factors. The spread factor models offered by Cheng [1977], Hulse-Smith et al. [2005], and Pasandideh-Fard et al. [1996] do not give a large enough range of spread factors to cover all of the experimental spread factor range.

Figures 6.9 and 6.10 also show that the models offered by Hulse-Smith et al. [2005] (Equation 6.18) and Pasandideh-Fard et al. [1996] (Equation 2.64) fail to replicate large experimental spread factors wheres the model offered by Cheng [1977] (Equation 6.15) fails to replicate smaller experimental spread factors. The adjusted model proposed in this thesis can produce a larger range of spread factors, making it more effective in replicating experimental spread factors. Lastly, a comparison of the simplified version of the proposed model (Equation 6.14) to the adjusted model is shown. Equation 6.14 will also be adjusted using the same coefficient, $\left(\bar{d}/d_i d_j\right)^2$, meaning it will become:

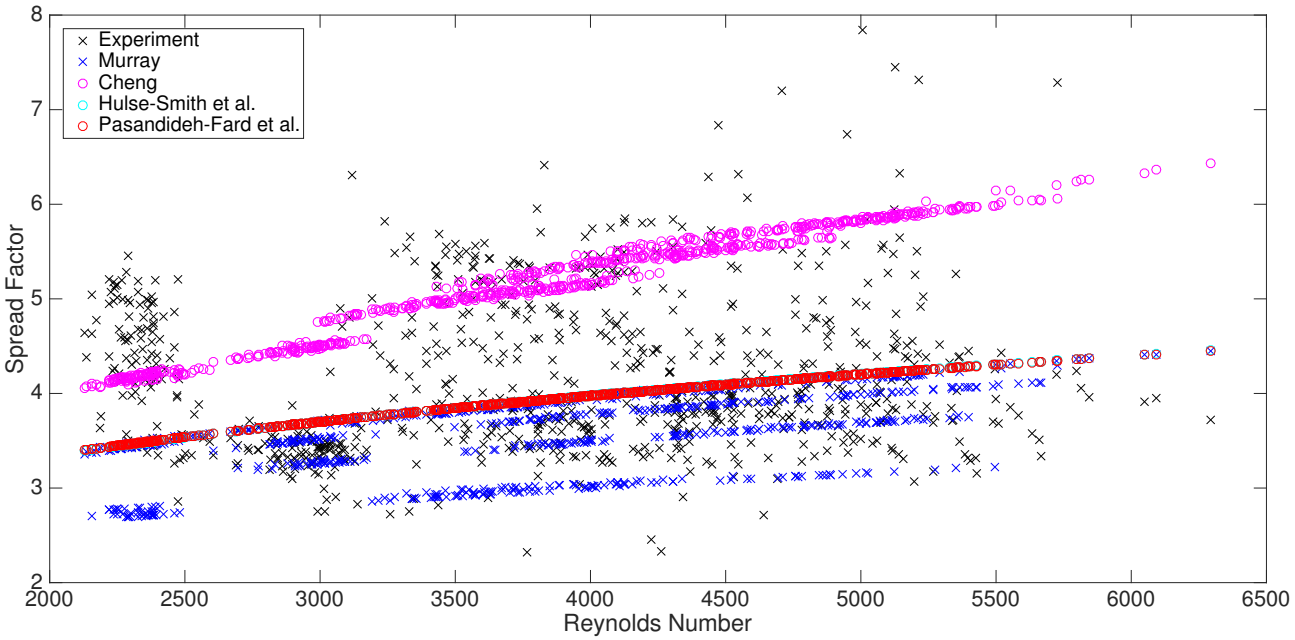

Figure 6.3: A comparison of spread factors against experimental data using the Reynolds number: Cheng [1977] (Equation 6.15), Hulse-Smith et al. [2005] (Equation 6.18), Pasandideh-Fard et al. [1996] (Equation 2.64), and Murray (Equation 6.13).

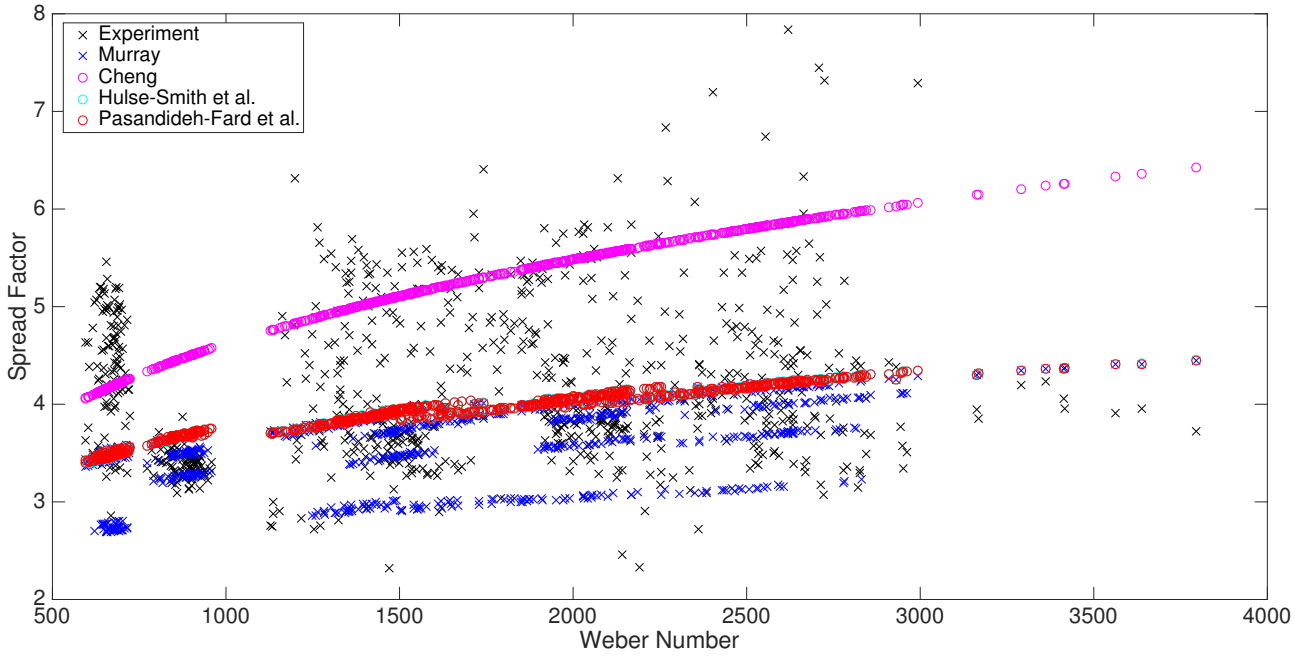

Figure 6.4: A comparison of spread factors against experimental data using the Weber number: Cheng [1977] (Equation 6.15), Hulse-Smith et al. [2005] (Equation 6.18), Pasandideh-Fard et al. [1996] (Equation 2.64), and Murray (Equation 6.13).

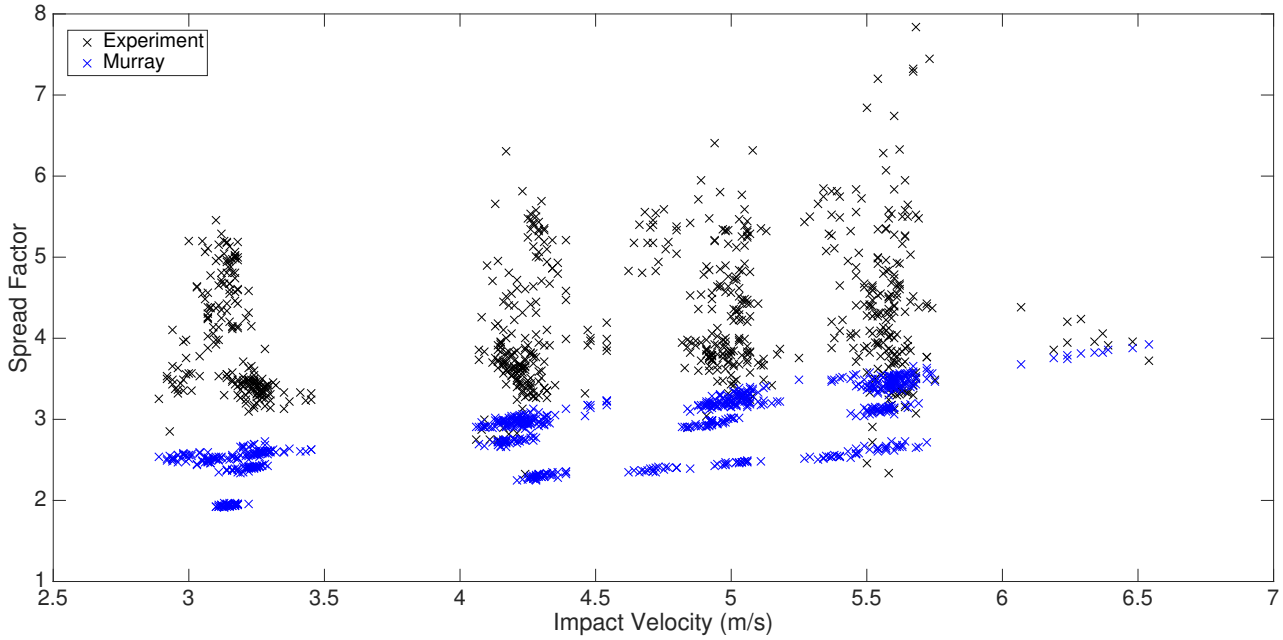

Figure 6.5: Comparing Equation 6.13 (Murray) to the experimental spread factors over impact velocity.

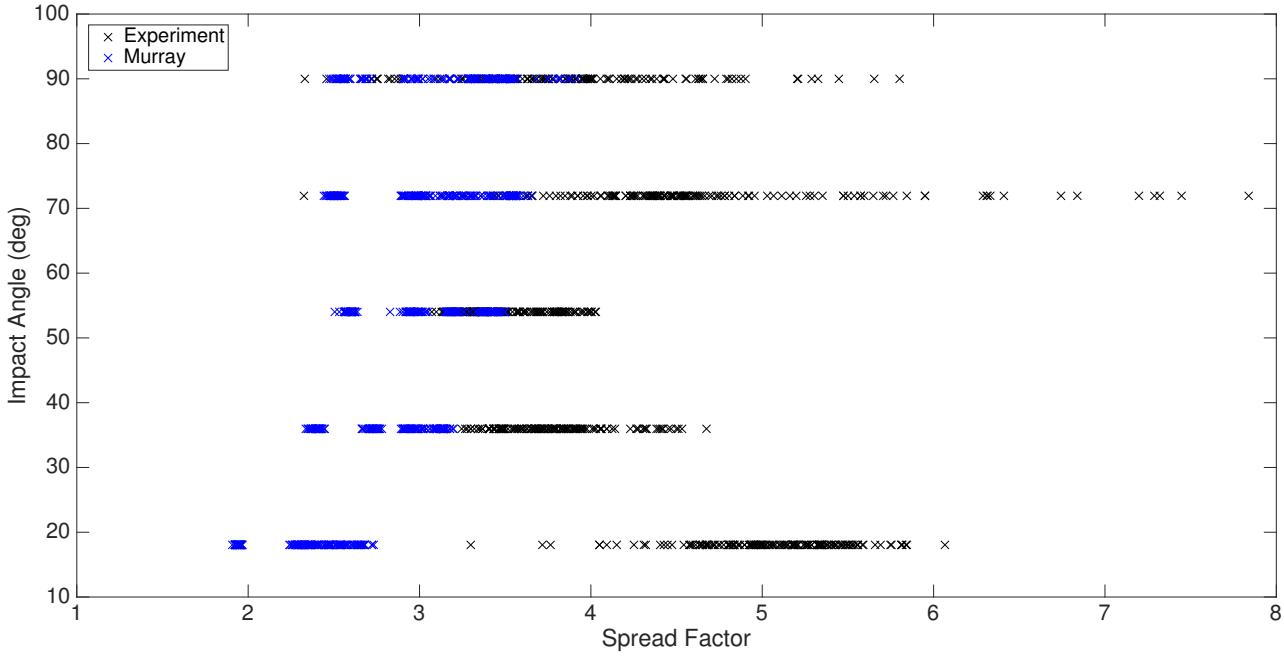

Figure 6.6: Comparing Equation 6.13 (Murray) to the experimental spread factors over impact angle.

$$\beta = \frac{1}{4}\left(\frac{\bar{d}}{d_i d_j}\right)^2 \mathrm{Re}^{1/4}\left(\sin\theta_f\right)^{1/4}. \tag{6.20}$$

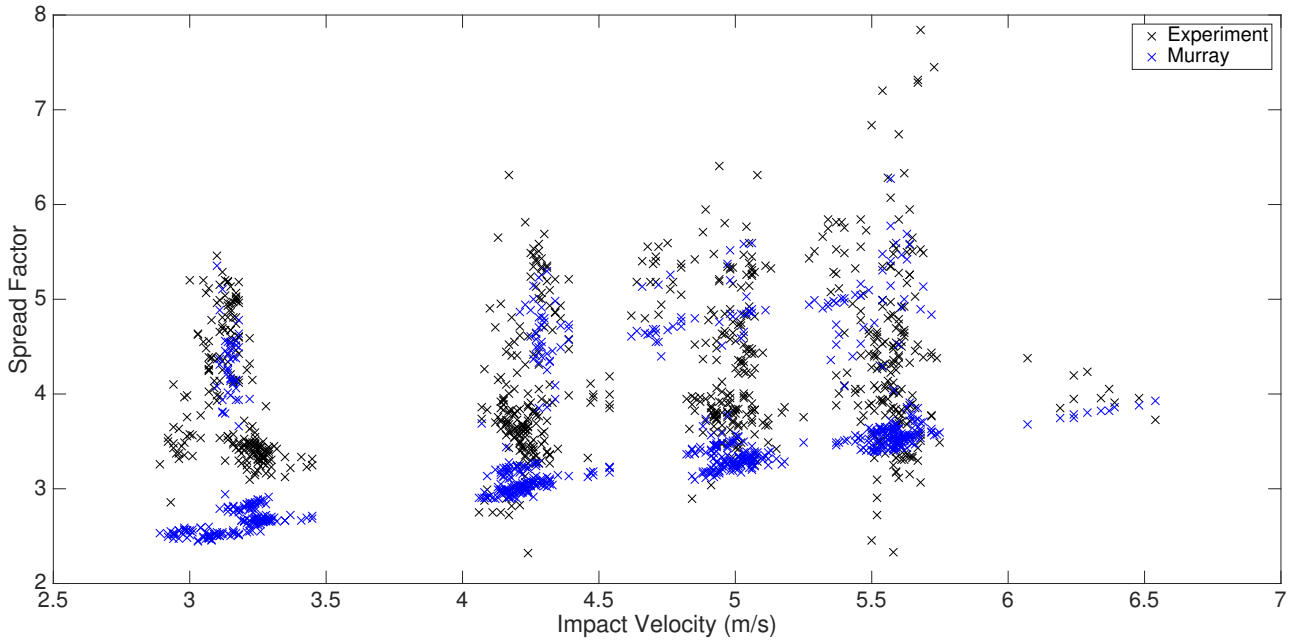

Figure 6.7: Comparing Equation 6.19 (Murray) to the experimental spread factors over impact velocity. This spread factor model includes the adjustment coefficient.

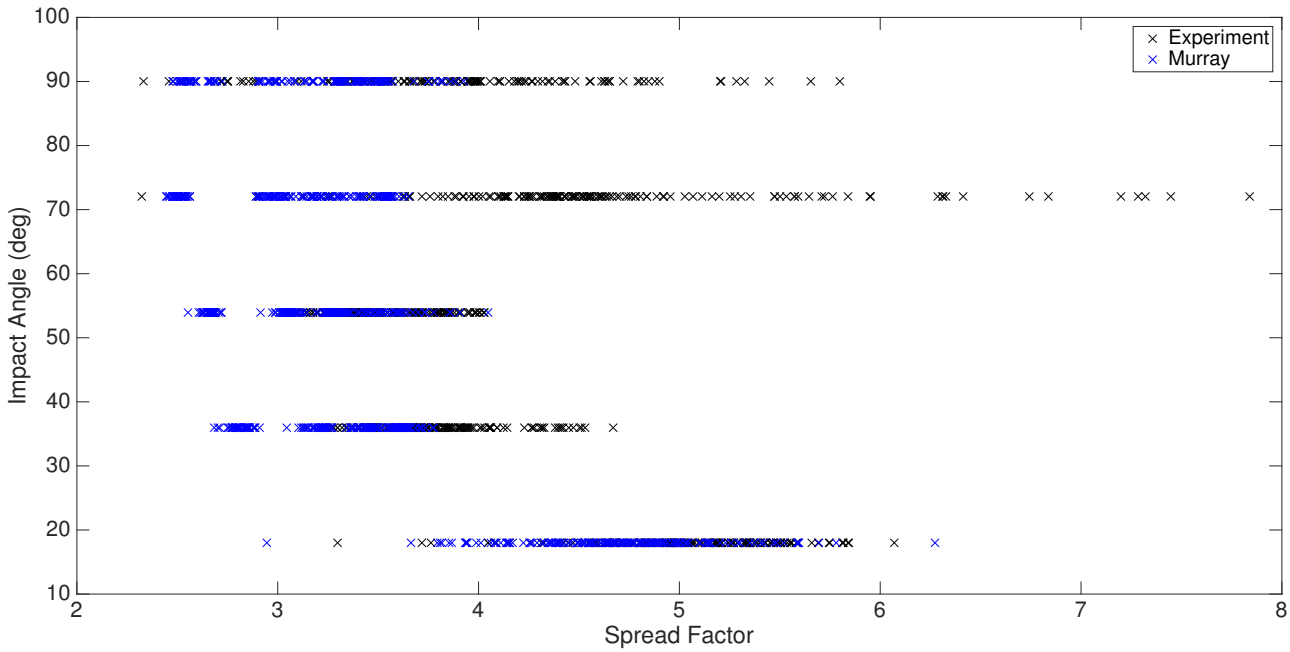

Figure 6.8: Comparing Equation 6.19 (Murray) to the experimental spread factors over impact angle. This spread factor model includes the adjustment coefficient.

Figure 6.11 shows the models plotted against a 1:1 ratio line for the experimental spread factor, meaning the goal is for the spread factor models to produce spread factors as close to the

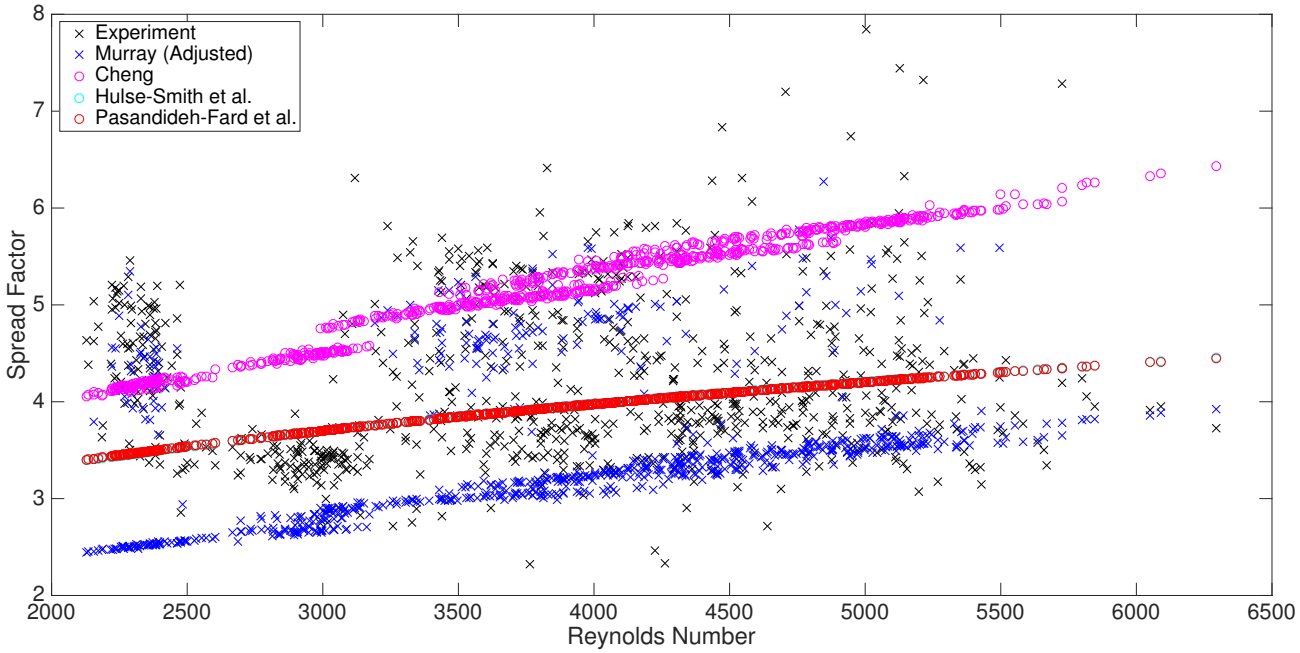

Figure 6.9: A comparison of spread factors against experimental data using the Reynolds number: Cheng [1977] (Equation 6.15), Hulse-Smith et al. [2005] (Equation 6.18), Pasandideh-Fard et al. [1996] (Equation 2.64), and Murray (Equation 6.19) with the adjustment coefficient added.

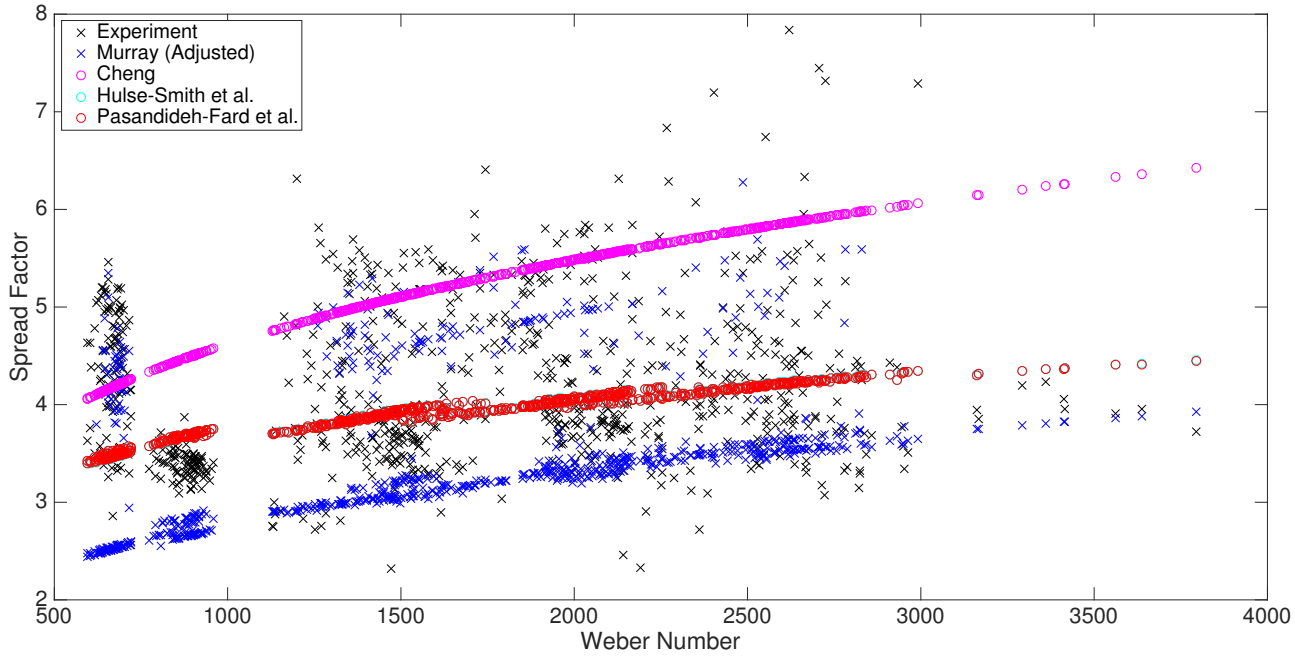

Figure 6.10: A comparison of spread factors against experimental data using the Weber number: Cheng [1977] (Equation 6.15), Hulse-Smith et al. [2005] (Equation 6.18), Pasandideh-Fard et al. [1996] (Equation 2.64), and Murray (Equation 6.19) with the adjustment coefficient added.

1:1 line as possible. This plot is very noisy, so a line of best fit was drawn through each spread factor model and their R^2 values are reported. These lines of best fit are show in Figure 6.12.

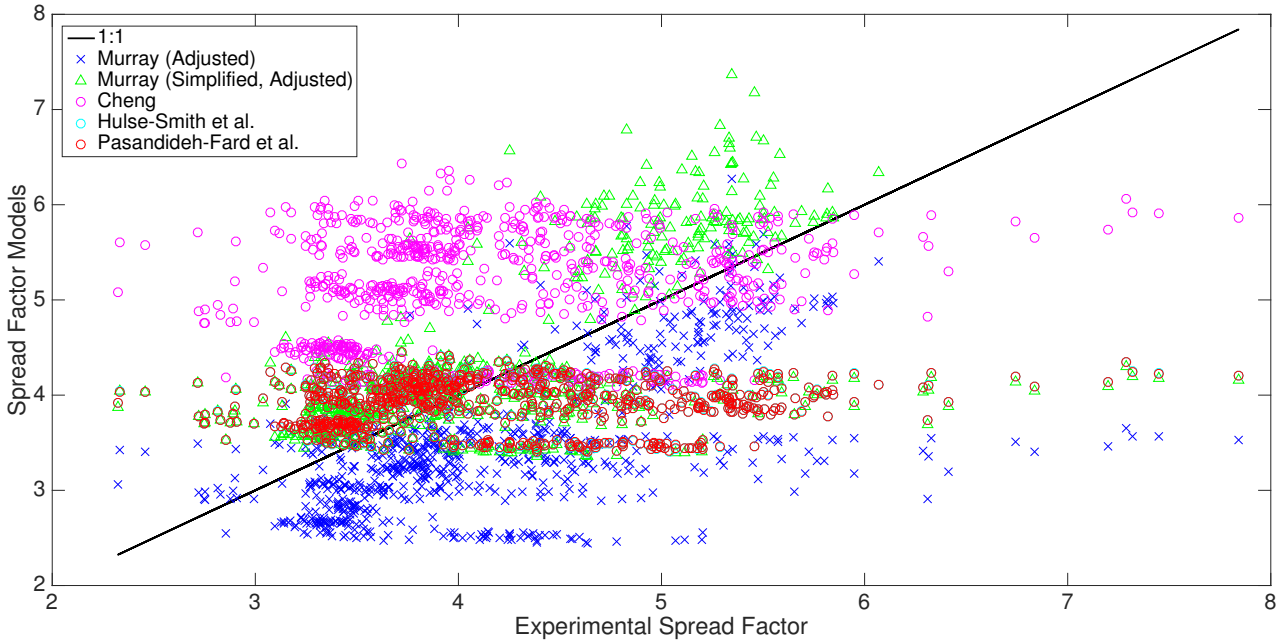

Figure 6.11: A comparison of all spread factor models against the experimental spread factor.

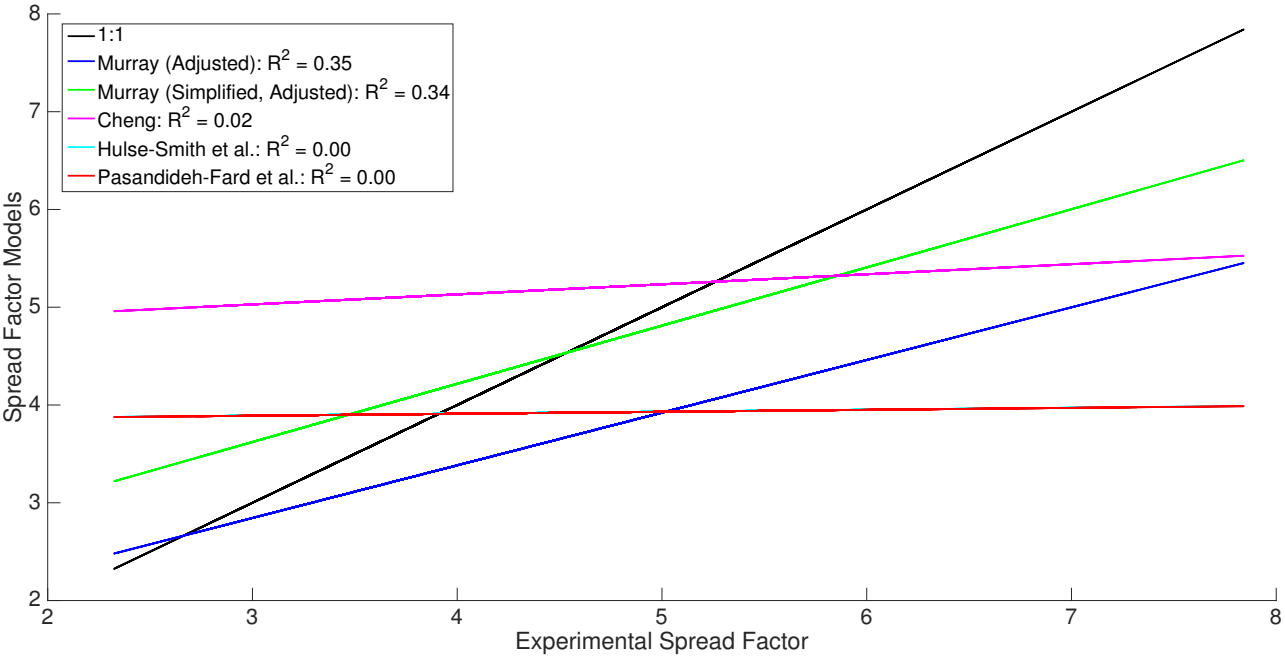

Figure 6.12: The lines of best fit for each model, and their R^2 values, compared against the experimental factor.

In conclusion, Figure 6.12 shows that the proposed spread factor model in this thesis, performs better that the models offered in literature. The line of best fit through the spread factors from the simplified model (Equation 6.20) is closest to the 1:1 experimental spread factor line. However, this simplified model may not be robust enough to work with substrates of different roughnesses (outside of the data set in these experiments) thus it may be wise to start with the model described by Equation 6.19 first before using a simplified model.

6.4 Motivation for new impact velocity and droplet diameter equations

The purpose of developing new impact velocity and droplet diameter equations is to improve on the current equations in the literature (Chapter 2) by avoiding the use of fitting constants. The current equations for impact velocity and droplet diameter were developed mathematically then adjusted to fit the specific experiments carried out by Hulse-Smith et al. [2005]. This makes the equation unusable for another experimental data set (especially if the experiments are carried out using a different type of animal blood). To that end, the following sections will outline a new set of equations for calculating the impact velocity and droplet diameter that is more generic and uses only the properties of the stain.

6.5 Calculating the impact velocity and droplet diameter

In the literature review (Chapter 2) a pair of equations were suggested to calculate the droplet diameter, d_0, and impact velocity of a droplet, u_0. Using fitting constants for their experimental data, Hulse-Smith et al. [2005] write these equations as:

$$d_0 = 0.902\left(256^{1/9}\right)\left(\frac{d_{\max}^8}{\rho_l \sigma_{lg}}\right)^{1/9}\left(\frac{\mu_l}{N}\right)^{2/9}, \tag{6.21}$$

and

$$u_0 = 1.102 \left(\frac{\sigma_{lg}^5 N^{10}}{16 \rho_l^4 d_{\max}^4 \mu_l} \right)^{1/9}, \tag{6.22}$$

where σ_{lg} is the surface tension of the fluid, N is the number of spines on the stain, ρ_l is the density of the fluid, μ_l is dynamic viscosity of the fluid, and $d_{\max}$ is the maximum diameter of the stain. Hulse-Smith et al. [2005] does not define how $d_{\max}$ is measured.

There are also a pair of similar equations based on the work of Knock and Davison [2007] that were derived in this thesis. Section 2.12 shows the work by Knock and Davison [2007] on which the derivation carried out is based on. Appendix U shows the full derivation of the following:

$$d_0 = \left[\left(\frac{d_i d_j}{100} \right)^8 \left(\frac{\sin^3 \theta_f}{N} \right)^6 \left(\frac{\mu_l}{\sqrt{\rho_l \sigma_{lg}}} \right)^3 \right]^{2/35} \tag{6.23}$$

and

$$u_0 = \left[\left(\frac{100}{d_i d_j} \right)^8 \left(\frac{\sigma_{lg}^{22}}{\rho_l^{16} \mu_l^3} \right) \left(\frac{N}{\sin^3 \theta_f} \right)^{41} \right]^{1/35}, \tag{6.24}$$

where d_i is the minor diameter of the stain, d_j is the major diameter of the stain, and θ_f is the impact angle.

Both sets of equations by Hulse-Smith et al. [2005] (Equations 6.21 and 6.22) and Knock and Davison [2007] (Equations 6.23 and 6.24) are reliant on fitting constants that allow those specific equations to match best with their experimental work.

6.6 Testing new equations for impact velocity and droplet diameter

The purpose of this section is to demonstrate that equations to calculate the impact velocity and initial droplet diameter based on measured properties of bloodstains are more accurate than

equations that use fitting constants.

In order test the accuracy of the equations, 5 participants counted the number of spines on 40 bloodstains on paper. The ASC (Chapter 3) was also included to count the number of spines on the 40 stains.

Since, the participants of the manual counting did not measure a maximum diameter of the bloodstains, the outer diameter, d_{out}, of each stain (as measured by the ASC) was used instead. With this first adjustment the formulae for calculating d_0 and u_0 were (also shown in Chapter 2 as Equations 6.21 and 6.22):

$$d_0 = 0.902\,(265)\left[\frac{d_{\text{out}}^8}{\rho\sigma}\left(\frac{\mu}{N}\right)^2\right]^{\frac{1}{9}}, \tag{6.25}$$

and

$$u_0 = 1.102\left(\frac{1}{16}\right)\left[\frac{N^{10}\sigma^5}{(\rho d_{\text{out}})^4\,\mu}\right]^{\frac{1}{9}}. \tag{6.26}$$

Table 6.1 shows the mean percent error of calculating d_0 and u_0 using Equations 6.25 and 6.26.

Table 6.1: The average percent error of calculating d_0 and u_0 using Equations 6.25 and 6.26 with different methods of counting spines.

Method	% Error in d_0	% Error in u_0
Participant 1a	13.2	30.0
Participant 2	13.9	27.8
Participant 3	15.6	29.9
Participant 4	15.4	30.9
Participant 1b	14.3	35.0
Participant 5	15.8	29.4
ASC	14.2	28.3

It can be seen that the number of spines as counted by the ASC yields the third lowest percent error in determining the initial diameter and the second lowest percent error in determining the impact velocity. It was considered that the fitting coefficients used by Hulse-Smith et al. [2005]

may not be appropriate for this data. Instead of doing another data fit to find new coefficients, it was considered to remove the coefficients completely and multiply both Equation 2.103 and Equation 2.104 by a ratio of other properties of the stain (all measured by the ASC). A few combinations of properties were investigated. For example, $\frac{d_{\text{out}}P_{ASC}}{\pi A_{ASC}}$ or $\frac{d_{\text{in}}P_{ASC}}{\pi A_{ASC}}$ or the circularity of the stain defined as $\frac{4\pi A_{ASC}}{P_{ASC}^2}$. These equations were considered because they are properties measured by the ASC (Chapter 3) and have not been tested in other models. The best combination found (that satisfied dimensional analysis) was $\frac{d_{\text{out}}}{d_{\text{in}}}$. It was also found that using the inner diameter instead of the outer diameter (in Equations 6.25 and 6.26) also lowered the percent error of calculating the initial diameter (from 14.2 % to 7.6 %) and impact velocity (from 28.3 % to 10.6 %). The new equations for calculating the initial drop diameter and impact velocity are then:

$$d_0 = \frac{d_{\text{out}}}{d_{\text{in}}}(265)\left[\frac{d_{\text{in}}^8}{\rho\sigma}\left(\frac{\mu}{N}\right)^2\right]^{\frac{1}{9}}, \tag{6.27}$$

and

$$u_0 = \frac{d_{\text{out}}}{d_{\text{in}}}\left(\frac{1}{16}\right)\left[\frac{N^{10}\sigma^5}{(\rho d_{\text{in}})^4\mu}\right]^{\frac{1}{9}}. \tag{6.28}$$

An obvious disadvantage to these new equations is that they have not been tested with different impact angles and thus have not been compared to the equations derived from Knock and Davison [2007]'s work. However, these new equations yield an average percent error (for d_0 and u_0) of 7.6 % and 10.6 % over 40 bloodstains. Not only is the percent error lower with the new equations, but these equations no longer depend on fitting constants, instead they are solely built from properties of blood and properties of the bloodstain. It should be noted that the whole number 265 and 16 in Equations 6.27 and 6.28 are not fitting constants, but numbers that fall out during the derivation of the equations (see Section 2.10).

Chapter 7

Conclusions

7.1 Summary

A large scale experiment was carried out in this thesis that employed 785 bloodstains to understand the effect of surface roughness on the size and shape of a bloodstain. In order to analyse this large amount of data quickly and accurately, two computational tools were developed in this thesis. The data analysis demonstrated a need for new definitions of spines, tails, stream stains, and non-stick stains.

This work showed that the roughness of a substrate does alter the shape and size of a bloodstain. In general, increased roughness tends to create more chaotic stains, up to a limit of roughness ($R_a = 6.3 \times 10^{-6}$ m). At this point, the roughness promotes more satellite stains and the parent stain reverts to a more controlled state (similar to bloodstains formed on paper). It was also seen in this work that the impact angle influences the shape and size of a bloodstain. For every stain property studied in Chapter 5, the impact angle always had the largest effect on the shape and size of the stain as compared to the surface roughness or the impact velocity. Lastly, analysis of the data demonstrated a need for accounting for impact angle and surface roughness when modelling the spread factor of a bloodstain. Starting from the conservation of energy, this thesis derived a new spread factor that accounts for impact angle and substrate

roughness, which has not yet been seen in the literature.

7.2 Contributions

This section outlines the contributions made by this thesis. As the field of BPA expands and more experimental work is undertaken to understand bloodstains better, it is hoped that the contributions of this thesis will help in the accuracy and speed of analysis, whilst emphasising the need for BPA methodologies to be derived from an understanding of fundamental physics.

7.2.1 Large experimental data set

This thesis has collected a large range of horse bloodstains (Chapter 4) impacting different substrates at different angles. These stains are accompanied by high-speed video footage of each droplet's impact. This data set can be used for future testing in BPA.

7.2.2 Classification of stain properties

New definitions of spines and tails are presented. Further, other stains such as a stream and non-stick stains (only seen on steel substrates) are named and discussed (Chapter 4). Quantitatively, a spine is a disturbance, still connected to the parent stain. Spines will radiate, from the centre of the stain, in all directions around a stain. Qualitatively, the new mathematical definition of a spine has been developed (Chapter 3). In the ASC, spines are selected if and only if they are larger than a threshold (Equation 3.6) and the spine must be larger than other peaks closest to the spine by a selection value (Equation 3.7). A tail is a protrusion, connected to the parent stain, that is pulled out by gravity indicating the direction of the impact. If there are multiple tails they tend to curve inwards towards each other. A stream stain is a stain where an elliptical head has not formed, the droplet has just rolled down the substrate, leaving a single stroke of small speckled stains behind. A non-stick stain is a stain where the elliptical head of the stain is predominantly missing. On smoother steel substrates, the elliptical head may be invisible

entirely. On rougher steel substrates, the elliptical head may have an outline.

7.2.3 Irrelevance of conditioning paper and the direction of milling

This work showed that the conditioning of paper, as per British Standard [1993] (Appendix A), yields the same bloodstains as unconditioned paper (Chapter 5). Hence there is no need to spend time and money conditioning paper for experiments in BPA. It was shown that the direction of impact with respect to the milling of the steel substrates (either with the grain or against the grain) did not influence the stain shape or size (Chapter 5). Hence there is no need to perform repeats in both directions in experiments in BPA.

7.2.4 The Diameter and Velocity Video Processor (DVVP)

The Diameter and Velocity Video Processor (DVVP) was developed in this thesis (Chapter 3) to extract the impact velocity and droplet diameter of a blood droplet from high-speed videos. Using the high-speed footage of the droplet's descent toward a substrate, the DVVP can measure the droplet's diameter before impact and track the droplet in the video to calculate its impact velocity. The DVVP carries out these measurements automatically which saves a considerable amount of time as compared to using the *Phantom Camera Control* (PCC) software. In the PPC software, the user must attempt to click on the same point on a droplet in every frame, then export the data in a cumbersome type workflow in order to arrive at an impact velocity. The PCC software also invites a lot of human error because the user may not be clicking on the same point on the droplet every frame or may not be measuring the diameter of a droplet directly on the edge of the droplet. The DVVP eliminates these errors by tracking the centroid of the droplet in every frame of the video and by using image processing to extract the diameter from the video frame.

7.2.5 The Automated Spine Counter (ASC)

The Automated Spine Counter (ASC) was developed in this thesis (Chapter 3) to estimate stain properties from bloodstains that were produced from vertical impacts (90° and 72° in this case). The ASC is capable of measuring stain area, stain perimeter, inner and outer diameter, and count the number of spines, on stains that have impacted paper and steel. It does so automatically, using a digital photograph of the stain, and it measures these properties faster, more accurately, and more consistently, than manual methods. Further, it can measure more stain properties than *ImageJ*, as *ImageJ* cannot measure the inner and outer diameter of a stain nor can it count spines. The ASC eliminates human error and subjectivity when measuring these stain properties. There is a mathematical criterion that selects spines on a stain, and there is no ambiguity about how the other stain properties are measured. Lastly, a mathematical definition of a spine, as opposed to a subjective definition, was borne from the development of the ASC.

7.2.6 Relationships discovered between impact properties and stain properties

The stain properties investigated in this thesis are: stain area, stain perimeter, inner and outer diameter (of circular stains), number of spines (on circular stains) and tails (on elliptical stains), major and minor diameter (of elliptical stains), and finally the length of an elliptical stain. The impact properties investigated are: the impact velocity of a droplet, the droplet diameter before impact, the impact angle, and the roughness of the substrate being impacted.

An analysis of impact properties versus stain properties was shown using statistics, presenting the notion that some substrates and some impact angles have similar behaviour. For example, regarding stain area and major and minor diameters of stains, droplets with fall heights 0.5 m and 1.0 m tend to yield statistically the same stains, while 1.5 m and 2.0 m are also grouped together statistically. Further, the impact angles tend to yield stains that are statistically similar in most stain properties to a neighbouring impact angle. For example 90° and 72° yield statistically

the same stains with regards to all stain properties except major and minor diameters of the stains. However, 18° is the most statistically dissonant impact angle, being statistically different from the other impact angles for almost all of the stain properties, bar stain area and number of spines. Lastly, the surface roughnesses showed the interesting phenomenon that paper and roughened steel of $R_a = 6.3 \times 10^{-6}$ m yield the same stains statistically with respect to all stain properties except stain perimeter. This confirms the theory discussed in Chapter 5 where roughness promotes disorder in stains up to a certain limit ($R_a = 6.3 \times 10^{-6}$ m) where the stains begin ejecting satellite stains, at which point the parent stain reverts to a more controlled shape and size.

The dependency of stain properties on some impact angles or surface roughnesses was studied in Chapter 5. Stain area was found to increase with a decrease in impact angle and increase in impact velocity. Further, the variability of the stain area increases with increased roughness, up to a limit of $R_a = 6.3 \times 10^{-6}$ m. Stain perimeter shows the same relationships as stain area but the increase in stain perimeter is driven solely by impact angle, not impact velocity. The stain length also shows the same relationships but the variability is not only caused by the roughness of the surface, but also caused by lower impact angles. The number of spines and tails on stains increases with increased impact angle and impact velocity. There is a sharp change in variability once the impact angle becomes larger than 36° because by impacts at 54° the stains begin exhibiting spines instead of tails. The major and minor diameters of stains, expectedly, behaved in opposite ways. It was seen that the major diameter of stains would increase with decrease in impact angle and increase in impact velocity. Conversely, an increase in impact angle (and impact velocity) gave an increase in minor diameter. Both the major and minor diameters show more variability with circular stains (*i.e.*, 90° and 72°) opposed to elliptical stains (54°, 36°, and 18°).

7.2.7 Novel spread factor

The new model for predicting spread factor accounted for impact angle, and the roughness of a non-absorbent substrate which has not been seen in literature. The new spread factor (Chapter 6, Equation 6.13) was derived from the laws of conservation of energy of a droplet's impact. Equation 6.13 models the spread of droplets better than the other spread factors found in literature. Spread factors are normally only used for stains resulting from vertical impacts. By accounting for impact angle, this new spread factor can be used on stains from all impact angles. However, Chapter 6, has shown that for lower impact angles (particularly 18°), Equation 6.13 seems to fail. This is possibly caused by the equation not being flexible enough for the increased length of the stain.

7.2.8 Two novel equations to calculate u_0 and d_0

Two new equations were developed in this thesis, that can be used to calculate droplet diameter (Equation 6.27) and impact velocity (Equation 6.28) from properties of a stain alone. In the literature, equations for calculating d_0 and u_0 tend to have fitting constants to adjust the equations to fit the experimental data. This makes the equation unusable for other experimental data sets. Therefore, two new equations were derived that do not have fitting constants and it was shown in Chapter 6 that the new pair of equations could predict the droplet diameter and impact velocity more accurately (over the range of experimental data in this thesis) than the equations suggested in literature. The performance of these equations outside this experimental data range is unknown.

7.3 Future Work

Topics for future work should include:

- a version of the ASC that can estimate stain properties on elliptical stains;

- further development of the new spread factor, to model elliptical stains better;
- a version of a pair of equations that can calculate impact velocity and droplet diameter using stain properties of elliptical stains on different substrates; and
- an investigation of stains formed on substrates with a higher roughness factor and substrates that are more absorbent than paper.

References

Adam, C. D. (2012). Fundamental studies of bloodstain formation and characteristics. *Forensic Science International*, 219:76–87.

Adam, C. D. (2013). Experimental and theoretical studies of the spreading of bloodstains on painted surfaces. *Forensic Science International*, 229:66–74.

Advisory Committee on Dangerous Pathogens (2003). *Infection at work: Controlling the risks - A guide for employers and the self employed on identifying, assessing and controlling the risks of infection in the workplace*. Health and Safety Executive.

Ahmed, G., Sellier, M., Lee, Y. C., Jermy, M., and Taylor, M. (2013). Modeling the spreading and sliding of power-law droplets. *Colloids and Surfaces A: Physicochemical and Engineering Aspects*, 432:2–7.

Allen, R. F. (1975). The role of surface tension in splashing. *Journal of Colloid and Interface Science*, 51(2):350–351.

Attinger, D., Moore, C., Donaldson, A., Jafari, A., and Stone, H. A. (2013). Fluid dynamics topics in bloodstain pattern analysis: Comparative review and research opportunities. *Forensic Science International*, 231:375–396.

Balchin, M. (2001). The search for a blood substitute for forensic science work for its use in bloodstain analysis. Master's thesis, Cranfield University.

Balthazard, V., Piédeliévre, R., Desoille, H., and Dérobert, L. (1939). Étude des gouttes de sang projeté. In *XXIIe Congrés de Médicine Légale de langue Francaise*, Paris.

Berry, E. X. and Pranger, M. R. (1974). Equations for calculating the terminal velocities of water drops. *Journal of Applied Meteorology*, 13(1):108–113.

Boys, C. (2003). Blood spatter analysis using the effects of drop size to determine point of origin. Master's thesis, Cranfield University.

British Standard (1993). Paper, board, and pulps - standard atmosphere for conditioning and testing and procedure for monitoring the atmosphere and conditioning of samples.

Brownson, D. A. C. and Banks, C. E. (2010). Crime scene investigation i: The effect of drug contaminated bloodstains on bloodstain pattern analysis. *Analytical Methods*, 2:1885–1889.

Buck, U., Kneubuehl, B., Näther, S., Albertini, N., Schmidt, L., and Thali, M. (2010). 3D bloodstain pattern analysis: Ballistic reconstruction of the trajectories of blood drops and determination of the centres of origin of the bloodstains. *Forensic Science International*, 206:22–28.

Chandra, S. and Avedisian, C. T. (1991). On the collision of a droplet with a solid surface. *Proceedings of the Royal Society of London A*, 432(1884):13–41.

Cheng, L. (1977). Dynamic spreading of drops impacting onto a solid surface. *Industrial & Engineering Chemistry Process Design and Development*, 16(2):192–197.

Davison, M. (2005). Determining the position of the source of blood spatter including the effects of gravity. Msc thesis, Cranfield University.

de Bruin, K. G., Stoel, R. D., and Limborgh, J. C. M. (2011). Improving the point of origin determination in bloodstain pattern analysis. *Journal of Forensic Science*, 56(6):1476–1482.

Ding, M. and Kantzas, A. (2007). Capillary number correlations for gas-liquid systems. *Journal of Canadian Petroleum Technology*, 46(2).

Doom, S. (2012). Bloodstain pattern analysis: To improve the accuracy when estimating the height of the blood source from stains originating from acute angled impacts. Master's thesis, Cranfield University.

El-Sayed, M., Brownson, D. A. C., and Banks, C. E. (2011). Crime scene investigation ii: The effect of warfarin on bloodstain pattern analysis. *Analytical Methods*, 3:1521–1524.

Engel, O. G. (1955). Waterdrop collisions with solid surfaces. *Journal of Research of the National Bureau of Standards*, 5(5):281–298.

Eral, H. B., 't Mannetje, D. J. C. M., and Oh, J. M. (2013). Contact angle hysteresis: a review of fundamentals and applications. *Colloid and Polymer Science*, 291:247–260.

Ford, R. E. and Furmidge, C. G. L. (1967a). The formation of dropls from viscous newtonian liquids sprayed through fan-jet nozzles. *British Journal of Applied Physics*, 18.

Ford, R. E. and Furmidge, C. G. L. (1967b). The formation of drops from viscous water-in-oil emulsions sprayed through fan-jet nozzles. *British Journal of Applied Physics*, 18.

Ford, R. E. and Furmidge, C. G. L. (1967c). Impact and spreading of spray drops on foliar surfaces. *Journal of the Society for Chemical Industry*, 25:417–432.

Gao, L. and McCarthy, T. J. (2006). Contact angle hysteresis explained. *American Chemical Society*, 22:6234–6237.

Gharenhkhani, S., Sadeghinezhad, E., Kazi, S. N., Yarmand, H., Badarudin, A., Safaei, M. R., and Zubir, M. N. M. (2015). Basic effects of pulp refining on fiber properties - a review. *Carbohydrate Polymers*, 115:785–803.

Gunn, R. and Kinzer, G. D. (1949). The terminal velocity of fall for water droplets in stagnant air. *Journal of Meteorology*, 6(4):243–248.

Harper, E. Y., Grube, G. W., and Chang, I.-D. (1972). On the breakup of accelerating liquid drops. *Journal of Fluid Mechanics*, 52:565–591.

Hulse-Smith, L., Mehdizadeh, N. Z., and Chandra, S. (2005). Deducing drop size and impact velocity from circular bloodstains. *Journal of Forensic Science*, 50:1.

Illes, M. B., Carter, A. L., Laturnus, P. L., and Yamashita, A. B. (2005). Use of the BACKTRACK computer program for bloodstain pattern analysis of stains from downward-moving drops. *Canadian Society of Forensic Science*, 38(4):213–218.

Kabaliuk, N., Jermy, M., Williams, E., Laber, T., and Taylor, M. (2014). Experimental validation of a numerical model for predicting the trajectory of blood drops in typical crime scene conditions, including droplet deformation and breakup, with a study of the effect of indoor air currents and wind on typical spatter drop trajectories. *Forensic Science International*, 245:107–120.

Kabaliuk, N., Jermy, M. C., Morison, K., Stotesbury, T., Taylor, M. C., and Williams, E. (2013). Blood drop size in passive dripping from weapons. *Forensic Science International*, 228:75–82.

Karger, B., Rand, S., Fracasso, T., and Pfeiffer, H. (2008). Bloodstain pattern analysis-casework experience. *Forensic Science International*, 181:15–20.

Kendall, M. M. (2008). The bloodstain pattern analysis on shoes from kicking incidents. Master's thesis, Cranfield University.

Kessler, E. (1969). On the distribution and continuity of water substance in atmospheric circulations. *Meterological Monographs*, 10(32):88.

Kessler, E. (1995). On the continuity and distribution of water substance in atmospheric circulations. *Atmospheric Research*, 38(1-4):109–145.

King, S. (2002). Determination of the source of bloodstains. Master's thesis, Cranfield University.

Knock, C. (2011). Blood substitute for bloodstain pattern analysis. Unpublished.

Knock, C. and Davison, M. (2007). Predicting the position of the source of bloodstains for angled impacts. *Journal of Forensic Science*, 52(5):1044–1049.

Laan, N., de Bruin, K., Bartolo, D., Josserand, C., and Bonn, D. (2014). Maximum diameter of impacting liquid droplets. *Physics Review Applied*, 2.

Larkin, B. A. J. and Banks, C. E. (2013). Preliminary study on the effect of heated surfaces upon bloodstain pattern analysis. *Journal of Forensic Sciences*, 58(5):1289–1296.

Larkin, B. A. J., El-Sayed, M., Brownson, D. A. C., and Banks, C. E. (2012). Crime scene investigation iii: Explorining the effects of drugs of abuse and neurotransmitters on bloodstain pattern analysis. *Anal*, 4:721–729.

Laurent, A., Durussel, J. J., Dufaux, J., Penhouët, L., Bailly, A. L., Bonneau, M., and Merland, J. J. (1999). Effects of constrast media on blood rheology: Comparison in humans, pigs, and sheep. *Cardiovascular and Interventional Radiology*, 22:62–66.

Liu, P. S. K. and Megaw, W. J. (1986). Spread factors for oil-based and water droplets. *Journal of Aerosol Science*, 17(2):169–177.

Maloney, A., Campbell, T., and Killeen, J. (2011a). Visualization of cast-off patterns using 3d modelling software. *Journal of the Association for Crime Scene Reconstruction*, 17(4):49–56.

Maloney, A. and Maloney, K. (2009). Hemospat bloodstain pattern analysis software.

Maloney, A., Nicloux, C., Maloney, K., and Heron, F. (2011b). One-sided impact spatter and area-of-origin calculations. *Journal of Forensic Identification*, 61(2):123–135.

Maloney, K., Killeen, J., and Maloney, A. (2009). The use of HemoSpat to include bloodstains located on nonorthogonal surfaces in area-of-origin calculations. *Journal of Forensic Identification*, 59(5):513–524.

Marmur, A. (1994). Thermodynamic aspects of contact angle hysteresis. *Advances in Colloid and Interface Science*, 50:121–141.

MathWorks (2014a). Documentation center: Digital filter implementation – sgolayfilt. www.mathworks.co.uk/help/signal/ref/sgolayfilt.html.

MathWorks (2014b). Documentation center: Object analysis – bwboundaries. www.mathworks.co.uk/help/images/ref/bwboundaries.html.

MathWorks (2014c). Documentation center: Object analysis – viscircles. www.mathworks.co.uk/help/images/ref/viscircles.html.

MathWorks (2014d). Documentation center: Region and image properties – regionprops. www.mathworks.co.uk/help/images/ref/regionprops.html.

MathWorks (2014e). Documentation center: Statistics toolbox – anova1. www.mathworks.co.uk/help/stats/anova1.html.

MathWorks (2014f). Filtering and smoothing data. www.mathworks.co.uk/help/curvefit/smoothing-data.html.

MathWorks (2015a). Documentation center: Image processing toolbox – im2bw. uk.mathworks.com/help/images/ref/im2bw.html.

MathWorks (2015b). Documentation center: Statistics toolbox – kstest. uk.mathworks.com/help/stats/kstest.html.

McKechnie, A. L. (2009). Blood spatter patterns from kicking injuries. Master's thesis, Cranfield University.

Mehdizadeh, N. Z., Chandra, S., and Mostaghimi, J. (2004). Formation of fingers around the edges of a drop hitting a metal plate with high velocity. *Journal of Fluid Mechanics*, 510:353–373.

Millington, J. (2001). Development of a synthetic blood substitute for use in forensic science teaching. Master's thesis, London Metropolitan University.

Moita, A. S., Herrmann, D., and Moreira, A. L. N. (2014). Experimental characterisation of the post-impact behaviour of non-newtonian droplets. In *17th International Symposium on Applications of Laser Techniques to Fluid Mechanics*, Lisbon, Portugal.

Moita, A. S. and Moreira, A. L. (2002). The dynamic behaviour of single droplets impacting onto a flat surface. In *ILASS*.

Murray, R. (2012). Computational and laboratory investigations of a model of blood droplet flight for forensic applications. Master's thesis, Faculty of Science, University of Ontario Institute of Technology.

Oliver, J. F., Huh, C., and Mason, S. G. (1980). An experimental study of some effects of solid surface roughness on wetting. *Colloids and Surfaces*, 1:79–104.

Pasandideh-Fard, M., Qiao, Y. M., Chandra, S., and Mostaghimi, J. (1996). Capillary effects during droplet impact on a solid surface. *Physics of Fluids*, 8(3):650–659.

Pizzola, P. A., Roth, S., and Forest, P. R. D. (1986a). Blood droplet dynamics – I. *Journal of Forensic Sciences*, 31:36–49.

Pizzola, P. A., Roth, S., and Forest, P. R. D. (1986b). Blood droplet dynamics – II. *Journal of Forensic Sciences*, 31:50–64.

Ramsthaler, F., Schmidt, P., Bux, R., Potente, S., Kaiser, C., and Kettner, M. (2012). Drying properties of bloodstains on common indoor surfaces. *International Journal of Legal Medicine*, 126:739–746.

Raymond, M. A., Smith, E. R., and Liesegang, J. (1996a). Oscillating blood droplets—implications for crime scene reconstruction. *Science & Justice*, 36:161–171.

Raymond, M. A., Smith, E. R., and Liesegang, J. (1996b). The physical properties of blood—forensic considerations. *Science & Justice*, 36:153–160.

Rein, M. (1993). Phenomena of liquid drop impact on solid and liquid surfaces. *Fluid Dynamics Research*, 12:61–93.

Roisman, I. V., Rioboo, R., and Tropea, C. (2002). Normal impact of a liquid drop on a dry surface: model for spreading and receding. *Proceedings of the Royal Society of London A*, 458:1411–1430.

Saylor, J. R. and Bounds, G. D. (2012). Experimental study of the role of the weber and capillary numbers on mesler entrainment. *American Institute of Chemical Engineers*, 58(12):3841–3851.

Scientific Working Group on Bloodstain Pattern Analysis (2013). Recommended terminology. Accessed: 15 May 2015.

Seliger, L. (1978). Forensic considerations of the physical properties of human blood. Unpublished Independent Study Report from Elmira College.

Sharp, D. H. (1984). An overview of rayleigh-taylor instability. *Physica D: Nonlinear Phenomena*, 12:3–10.

Shin, S. and Keum, D.-Y. (2002). Measurement of blood viscosity using mass-detecting sensor. *Biosensors & Bioelectronics*, 17:383–388.

Shuttleworth, R. and Bailey, G. L. J. (1948). The spreading of a liquid over a rough solid. *Discussions of the Faraday Society*, 3:16–22.

State of Florida v. Dieter Riechmann (2000). Supreme Court of Florida. SC89564, SC93236.

Stow, C. D. and Hadfield, M. G. (1981). An experimental investigation of fluid flow resulting from the impact of a water frop with an unyielding dry surface. *Proceedings of the Royal Society of London A*, 373:419–441.

Sweet, M. J. (1993). Velocity measurements of projected bloodstains from a medium velocity impact source. *Canadian Society of Forensic Science*, 26(3):103–110.

Thoroddsen, S. T. and Sakakibara, J. (1998). Evolution of the fingering patther of an impacting drop. *Physics of Fluids*, 10(6):1359–1374.

van Boxel, J. H. (1997). Numerical model for the fall speed of raindrops in a rainfall simulator. *Workshop on Wind and Water Erosion*.

Warren R. Horinek v. The State of Texas (1998). Court of Appeals of Texas, Fort Worth. 2-96-565-CR.

Wenzel, R. N. (1936). Resistence of solid surfaces to wetting by water. *Industrial & Engineering Chemistry*, 28(8):988–994.

Williams, A. (2000). Prediction of the source of blood spatters. Master's thesis, Cranfield University.

Willis, C., Piranian, A. K., Donaggio, J. R., Barnett, R. J., and Rowe, W. F. (2001). Errors in the estimation of the distance of fall and angles of impact blood drops. *Forensic Science International*, 123:1–4.

Wobus, H. B., Murray, F. W., and Loenig, L. R. (1971). Caluation of the terminal velocity of water drops. *Journal of Applied Meteorology*, 10(4):751–754.

Wolansky, G. and Marmur, A. (1999). Apparent contact angles on rough surfaces: the wenzel equation revisited. *Colloids and Surfaces*, 156:381–388.

Worthington, A. M. (1876). On the forms assumed by dropls of liquids falling vertically on a horiztonal plate. *Proceedings of the Royal Society of London*, 25:261–272.

Wågberg, L. and Westerlind, C. (2000). Spreading of droplets of different liquids on specially structred papers. *Nordic Pulp and Paper Research*, 15(5):598–606.

Bibliography

Acheson, D. J. (1990). *Elementary Fluid Dynamics*. Oxford Applied Mathematics and Computing Science Series. Oxford University Press, New York.

Batchelor, G. K. (2000). *An Introduction to Fluid Dynamics*. Cambridge University Press.

Bergman, T. L., Lavine, A. S., Incropera, F. P., and DeWitt, D. P. (2011). *Fundamentals of heat and mass trasnfer*. John Wiley & Sons, 7th edition.

Bevel, T. and Gardner, R. M. (2001). *Bloodstain Pattern Analysis: With an Introduction to Crime Scene Reconstruction*. CRC Press, New York, 2nd edition.

Carey, V. P. (1992). *Liquid-vapor phase-change phenomena*. Hemisphere Publishing Corporation.

Croft, H. T., Falconer, K. J., and Guy, R. K. (1991). *Unsolved Problems in Geometry*. Springer-Verlag.

Holman, J. P. (2010). *Heat transfer*. McGraw-Hill, 10th edition.

James, S. H., Kish, P. E., and Sutton, T. P. (2005). *Principles of Bloodstain Pattern Analysis: Theory and Practice*. Taylor & Francis Group.

Kieser, J., Taylor, M., and Carr, D. (2013). *Essentials of Forensic Science: Forensic Biomechanics*. Wiley-Blackwell.

Li, D. (2008). *Encyclopedia of Microfluids and Nanofluidics*. Springer.

MacDonell, H. L. (1993). *Bloodstain Patterns*. Laboratory of Forensic Science.

Sherman, F. S. (1990). *Viscous Flow*. McGraw-Hill.

Sirignano, W. A. (1999). *Fluid Dynamics and Transport of Droplets and Sprays*. Cambridge University Press.

Spiegel, M. R., Lipschutz, S., and Liu, J. (2009). *Mathematical Handbook of Formulas and Tables*. McGraw-Hill Companies, Inc., 3rd edition.

Weiss, N. A. (1995). *Introductory Statistics*. Addison-Wesley Publishing Company, Inc., 4th edition.

Weiss, N. A. (2002). *Elementary Statistics*. Pearson Education Inc., 5th edition.

Weiss, N. A. (2012). *Elementary Statistics*. Pearson Education Inc., 8th edition.

White, F. M. (1991). *Viscous Fluid Flow*. McGraw-Hill.

White, F. M. (1999). *Fluid Mechanics*. McGraw-Hill.

Wonder, A. Y. (2001). *Blood Dynamics*. Academic Press.

Wonder, A. Y. (2007). *Bloodstain Pattern Evidence: Objective Approaches and Case Applications*. Elsevier Academic Press.

Worthington, A. M. (1908). *A study of splashes*. Longmans, Green, and Co.

Appendix A

British Standards

In Europe, experiments need to be carried out at a specific standard. In this thesis, paper is one of the substrates used in the horse blood experiments. The paper must be conditioned to the requirements of British Standard EN 20187:1993 (British Standard [1993]). This standard has the following requirements:

- the paper must be conditioned to a temperature of 23 °C $\pm$ 1 °C;
- the paper must be conditioned to a humidity of 50 % $\pm$ 2 %;
- the conditioning, if performed in an area of good air circulation, needs to be carried out over a 4 hour period.

The conditioning of the paper in this thesis was performed in an environmental chamber over a minimum of 4 hours to the above requirements.

Appendix B

Calculating percent error and percent difference

The percent error is used to determine how close an experimental measurement (s_{exp}) is to the accepted or known value (s_{ac}). To calculate the percent error the following formula is used:

$$\%\,error = \frac{\left|s_{ac} - s_{exp}\right|}{s_{ac}}. \tag{B.1}$$

The percent difference is used to determine how different two measurements are from each other. Let the first measurement be denoted as s_1 and the second measurement be denoted as s_2. To calculate the percent difference the following formula is used:

$$\%\,difference = \frac{|s_1 - s_2|}{\frac{1}{2}(s_1 + s_2)}. \tag{B.2}$$

Appendix C

Definitions of statistical tests

C.1 Interpretation of the p-value

The p-value is a probability value that indicates how to interpret the null hypothesis, H_0, stated by a given statistical test. The p-value will indicate whether or not there is evidence that the null hypothesis should be accepted or rejected (Weiss [1995]). It is also a measurement of how significant statistical results are. Table C.1 shows how the p-values is interpreted as suggested by Weiss [1995] and Weiss [2002].

Table C.1: Guidelines on how to interpret the p-value from statistical tests.

p-value	Evidence against H_0
$p > 0.10$	Weak or none
$0.05 < p \leq 0.10$	Moderate
$0.01 < p \leq 0.05$	Strong
$p \leq 0.01$	Very strong

Generally, a p-value greater than 0.05 does not provide evidence against the null hypothesis, whereas the p-value less than or equal to 0.05 indicates there is evidence against the null hypothesis (Weiss [1995]). For simplicity in this thesis, and what is widely accepted, p-values less than or equal to 0.05 will result in the rejection of the null hypothesis and p-values greater than 0.05 are acceptance of the null hypothesis.

C.2 Levene's Test

The null hypothesis stated by the Levene's test is that the columns of the data set come from normal distributions with the same variance. In MATLAB, the function used is **vartestn**, with the explicit use of Levene's test (as opposed to Bartlett's test which is the default). If the Levene's test shows that the data set does come a normal distribution with the same variance, then that data set can be used in an analysis of variance test (ANOVA test, Section C.4). The Levene's test will output a p-value. If the p-value is less than or equal to 0.05 then the data does not come from a normal distribution with the same variance. If the p-value is greater than 0.05, then the data set does come from a normal distribution with the same variance.

C.3 One-sample Kolmogorov-Smirnov test

In order to check if a data set comes from a standard normal distribution, a Kolmogorov-Smirnov test is carried out. In MATLAB, the function used is **kstest** (MathWorks [2015b]). The null hypothesis states that the data set comes from a standard normal distribution. To use this test the data inputed into the function **kstest** must be centred and scaled correctly. To do this the z-score of each data point must be found:

$$\hat{z} = \frac{x - \hat{\mu}}{\hat{\sigma}} \tag{C.1}$$

where $\hat{z}$ is the z-scores of the data in x, $\hat{\mu}$ is the mean of vector x, and $\hat{\sigma}$ is the standard deviation of x. The vector from Equation C.1 can then be used in function **kstest** to test for a standard normal distribution. **kstest** will output a p-value for interpretation.

C.4 Analysis of variance Test (ANOVA)

A one-way ANOVA test is a method for comparing the means of several data populations using only one factor (Weiss [2012]). The data used in this test must come from normal distributions with the same variance (see Section C.2). In MATLAB, the **anova1** function uses the null hypothesis that the data populations have the same means (MathWorks [2014e]). To compare more than one factor the MATLAB function **anovan** must be used. When more than one factor is used, an interaction p-value is produced. This p-value is used to understand if one variable is dependent on another variable in the ANOVA test. The null hypothesis for interaction is that the variables are interacting therefore if the p-value is greater than 0.05 then there is not sufficient evidence agains the null hypothesis. These results will be reported with the F-statistic (which indicates the significance of the p-value) and degrees of freedom (the degrees of freedom of that variable and the error).

In short, if a variable has a p-value greater than 0.05, then that variable does not have an effect on the result being investigated. Similarly, if the interaction p-value is greater than 0.05 then there is no interaction between the variables being investigated.

C.5 Tukey Test

The Tukey test is a post-hoc statistics test that is normally done after an ANOVA test (see C.4). This test compares the means of the columns in a data set. It will confirm if different groups in the data have statistically different means. In MATLAB, the function used is **multcompare**.

Appendix D

Testing the effect of grain direction: Results of the one-way ANOVA

The stain properties measured in Table D.1 were performed by the ASC. The properties are stain area, A_{ASC}, stain perimeter, P_{ASC}, outer diameter, d_{out}, and number of spines, N.

Table D.1: Results of a one-way ANOVA test regarding grain direction for an impact angle of 72°.

Roughness (10^{-6} m)	Stain property	p-value
1.6	d_{out}	0.8682
	A_{ASC}	0.4609
	P_{ASC}	0.7629
	N	0.5982
3.2	d_{out}	0.1150
	A_{ASC}	0.1351
	P_{ASC}	0.2025
	N	0.7152
6.3	d_{out}	0.8072
	A_{ASC}	0.2016
	P_{ASC}	0.8151
	N	0.0392

The stain properties measured in Tables D.2, D.3, and D.4 were performed by *ImageJ*. The properties are stain area, A_{IJ}, stain perimeter, P_{IJ}, length of the stain, L_{IJ}, major diameter, d_j, and minor diameter, d_i. The number of tails were counted manually, N.

Table D.2: Results of a one-way ANOVA test regarding grain direction for an impact angle of 54°.

Roughness (10^{-6} m)	Stain property	p-value
1.6	L_{IJ}	0.3911
	A_{IJ}	0.6638
	P_{IJ}	0.8939
	d_i	0.9896
	d_j	0.2428
	N	0.5145
3.2	L_{IJ}	0.1472
	A_{IJ}	0.0301
	P_{IJ}	0.6030
	d_i	0.1897
	d_j	0.8066
	N	0.3263
6.3	L_{IJ}	0.6484
	A_{IJ}	0.2481
	P_{IJ}	0.4309
	d_i	0.3146
	d_j	0.3704
	N	0.0516

Table D.3: Results of a one-way ANOVA test regarding grain direction for an impact angle of 36°.

Roughness (10^{-6} m)	Stain property	p-value
1.6	L_{IJ}	0.3000
	A_{IJ}	0.4331
	P_{IJ}	0.4096
	d_i	0.4291
	d_j	0.3668
	N	0.9744
3.2	L_{IJ}	0.3443
	A_{IJ}	0.8572
	P_{IJ}	0.2634
	d_i	0.7441
	d_j	0.7316
	N	0.7008
6.3	L_{IJ}	0.6960
	A_{IJ}	0.3558
	P_{IJ}	0.9483
	d_i	0.0953
	d_j	0.6672
	N	0.5026

Table D.4: Results of a one-way ANOVA test regarding grain direction for an impact angle of 18°.

Roughness (10^{-6} m)	Stain property	p-value
1.6	L_{IJ}	0.2886
	A_{IJ}	0.9568
	P_{IJ}	0.4376
	d_i	0.7877
	d_j	0.7162
	N	0.2869
3.2	L_{IJ}	0.0045
	A_{IJ}	0.0016
	P_{IJ}	0.0017
	d_i	0.2732
	d_j	0.2940
	N	0.0309
6.3	L_{IJ}	0.0305
	A_{IJ}	0.8629
	P_{IJ}	0.3277
	d_i	0.1790
	d_j	0.8062
	N	0.3651

Appendix E

Raw statistics from experimental data used in Chapter 5

The tables in this appendix detail some simple statistics of the experimental data, broken up by substrate and impact angle.

Table E.1: The resolution of high-speed videos and digital photographs gathered from conducting the experiments in Chapter 4 and the circularity of the stains resulting from the experiments.

Substrate	Roughness (10^{-6} m)	Impact Angle	Circularity	Average resolution of high-speed videos (pix cm^{-1})	Average resolution of digital photographs (pix cm^{-1})
paper	1.3	90°	0.67	44.4	360.01
steel	0		0.86	35.8	153.51
	1.6		0.84	35.7	153.51
	3.2		0.72	35.7	153.51
	6.3		0.37	35.5	153.77
paper	1.3	72°	0.80	40.0	193.29
steel	0		0.85	39.7	193.29
	1.6		0.83	39.7	192.20
	3.2		0.75	39.8	192.42
	6.3		0.46	39.8	194.21
paper	1.3	54°	0.81	36.0	184.38
steel	0		0.34	36.0	189.81
	1.6		0.48	36.0	188.06
	3.2		0.40	36.0	188.06
	6.3		0.22	36.0	188.12
paper	1.3	36°	0.64	36.0	175.84
steel	0		0.34	36.0	185.10
	1.6		0.23	36.0	182.77
	3.2		0.24	36.0	181.71
	6.3		0.30	36.0	182.44
paper	1.3	18°	0.20	35.5	160.28
steel	0		0.17	35.0	159.03
	1.6		0.14	32.6	164.83
	3.2		0.12	32.4	164.85
	6.3		0.14	35.6	160.63

(a) Measured droplet and stain properties

	u_0 ($\mathrm{m\,s^{-1}}$)	d_0 (10^{-3} m)	$d_{\max}$ (10^{-2} m)	A_{ASC} (10^{-4} $\mathrm{m^2}$)	P_{ASC} (10^{-2} m)	N
Min	3.40	3.22	1.25	1.11	3.99	20
Max	5.21	4.26	1.76	1.97	7.05	36

(b) Calculated non-dimensional properties

	β	Ca (10^{-1})	Re (10^3)	We (10^3)	Bo	$\hat{\mathrm{Fr}}$
Min	3.40	2.76	2.47	0.681	2.12	15.8
Max	5.22	6.03	6.30	3.79	3.71	32.1

(c) Coefficients of variation (in percentages)

Height	u_0	d_0	$d_{\max}$	A_{ASC}	N
0.5 m	3.21	2.02	5.29	9.25	8.32
1.0 m	2.65	3.67	3.73	4.84	6.18
1.5 m	4.08	6.71	4.78	8.65	5.8
2.0 m	6.7	8.96	5.13	6.48	6.97

Table E.2: Statistical properties of the experimental data from droplets impacting paper at 90°.

(a) Measured droplet and stain properties

	u_0 ($\mathrm{m\,s^{-1}}$)	d_0 (10^{-3} m)	$d_{\max}$ (10^{-2} m)	A_{ASC} (10^{-4} $\mathrm{m^2}$)	P_{ASC} (10^{-2} m)
Min	2.94	3.30	0.933	0.669	2.91
Max	5.59	3.80	1.66	1.91	6.07

(b) Calculated non-dimensional properties

	β	Ca (10^{-1})	Re (10^3)	We (10^3)	Bo	Fr
Min	2.72	2.71	2.33	0.630	2.22	15.5
Max	4.64	5.15	4.77	2.45	2.95	30.5

(c) Coefficients of variation (in percentages)

Height	u_0	d_0	$d_{\max}$	A_{ASC}
0.5 m	0.934	3.14	4.09	9.01
1.0 m	1.6	2.35	14.2	28.7
1.5 m	0.858	1.06	3.06	4.58
2.0 m	0.714	5.19	12.2	24.3

Table E.3: Statistical properties of the experimental data from droplets impacting smooth steel at 90°.

(a) Measured droplet and stain properties

	u_0 ($\mathrm{m\,s^{-1}}$)	d_0 (10^{-3} m)	$d_{\max}$ (10^{-2} m)	A_{ASC} (10^{-5} $\mathrm{m^2}$)	P_{ASC} (10^{-2} m)	N
Min	2.89	3.22	0.788	3.47	2.14	0
Max	5.58	3.86	1.64	19.0	5.62	17

(b) Calculated non-dimensional properties

	β	Ca (10^{-1})	Re (10^3)	We (10^3)	Bo	$\hat{\mathrm{Fr}}$
Min	2.33	2.66	2.29	0.616	2.12	15.0
Max	4.47	5.14	4.69	2.39	3.04	30.6

(c) Coefficients of variation (in percentages)

Height	u_0	d_0	$d_{\max}$	A_{ASC}	N
0.5 m	0.709	3.54	7.48	20.1	NaN
1.0 m	1.41	3.95	15.8	30.3	8.38
1.5 m	0.585	2.69	12.2	38.5	66.3
2.0 m	0.806	4.28	19.9	41	31.6

Table E.4: Statistical properties of the experimental data from droplets impacting roughened steel ($R_a = 1.6 \times 10^{-6}$ m) at 90°.

(a) Measured droplet and stain properties

	u_0 ($\mathrm{m\,s^{-1}}$)	d_0 (10^{-3} m)	$d_{\max}$ (10^{-2} m)	A_{ASC} (10^{-5} $\mathrm{m^2}$)	P_{ASC} (10^{-2} m)	N
Min	2.92	3.26	0.788	5.67	2.94	4
Max	5.64	3.97	1.64	17.4	6.33	24

(b) Calculated non-dimensional properties

	β	Ca (10^{-1})	Re (10^3)	We (10^3)	Bo	$\hat{\mathrm{Fr}}$
Min	2.20	2.69	2.19	0.597	2.17	15.3
Max	4.61	5.20	4.83	2.51	3.23	30.5

(c) Coefficients of variation (in percentages)

Height	u_0	d_0	$d_{\max}$	A_{ASC}	N
0.5 m	1.00	6.37	5.07	11.39	10.53
1.0 m	1.17	5.07	21.41	30.56	9.85
1.5 m	0.73	4.74	10.23	32.86	39.39
2.0 m	0.89	3.75	8.96	15.68	35.27

Table E.5: Statistical properties of the experimental data from droplets impacting roughened steel ($R_a = 3.2 \times 10^{-6}$ m) at 90°.

(a) Measured droplet and stain properties

	u_0 ($\mathrm{m\,s^{-1}}$)	d_0 (10^{-3} m)	$d_{\max}$ (10^{-2} m)	A_{ASC} (10^{-5} $\mathrm{m^2}$)	P_{ASC} (10^{-2} m)	N
Min	2.95	3.24	1.20	7.64	4.17	6
Max	5.65	3.92	2.17	17.5	11.2	22

(b) Calculated non-dimensional properties

	β	Ca (10^{-1})	Re (10^3)	We (10^3)	Bo	$\hat{\mathrm{Fr}}$
Min	3.35	2.72	2.19	0.603	2.14	15.5
Max	5.80	5.20	4.88	2.53	3.14	30.3

(c) Coefficients of variation (in percentages)

Height	u_0	d_0	$d_{\max}$	A_{ASC}	N
0.5 m	0.63	5.58	21.01	8.00	9.09
1.0 m	0.70	4.27	17.40	16.30	34.25
1.5 m	1.48	4.04	9.25	22.32	21.25
2.0 m	0.58	3.57	15.28	26.71	16.57

Table E.6: Statistical properties of the experimental data from droplets impacting roughened steel ($R_a = 6.3 \times 10^{-6}$ m) at 90°.

(a) Measured droplet and stain properties

	u_0 ($\mathrm{m\,s^{-1}}$)	d_0 (10^{-3} m)	$d_{\max}$ (10^{-2} m)	A_{ASC} (10^{-4} $\mathrm{m^2}$)	P_{ASC} (10^{-2} m)	N
Min	3.03	3.11	1.40	1.23	4.44	13
Max	5.74	3.99	2.89	2.34	5.85	27

(b) Calculated non-dimensional properties

	β	Ca (10^{-1})	Re (10^3)	We (10^3)	Bo	$\hat{\mathrm{Fr}}$
Min	3.89	2.79	2.13	0.595	1.98	17.1
Max	8.97	5.29	5.18	2.74	3.25	30.0

(c) Coefficients of variation (in percentages)

Height	u_0	d_0	$d_{\max}$	A_{ASC}	N
0.5 m	1.81	2.44	2.78	4.76	4.34
1.0 m	0.40	6.34	6.84	5.69	22.01
1.5 m	0.70	2.52	37.23	4.89	11.97
2.0 m	1.13	4.40	5.01	10.14	21.05

Table E.7: Statistical properties of the experimental data from droplets impacting paper at 72°.

(a) Measured droplet and stain properties

	u_0 ($\mathrm{m\,s^{-1}}$)	d_0 (10^{-3} m)	$d_{\max}$ (10^{-2} m)	A_{ASC} (10^{-5} $\mathrm{m^2}$)	P_{ASC} (10^{-2} m)	N
Min	3.12	3.15	1.26	6.60	3.56	0
Max	5.61	4.14	2.17	25.6	7.70	10

(b) Calculated non-dimensional properties

	β	Ca (10^{-1})	Re (10^3)	We (10^3)	Bo	$\hat{\mathrm{Fr}}$
Min	3.44	2.88	2.26	0.663	2.03	17.0
Max	5.59	5.17	5.19	2.67	3.50	28.2

(c) Coefficients of variation (in percentages)

Height	u_0	d_0	$d_{\max}$	A_{ASC}	N
0.5 m	1.52	3.15	4.47	8.27	23.96
1.0 m	0.84	6.25	6.22	21.42	138.33
1.5 m	0.95	7.31	21.82	42.38	81.44
2.0 m	1.16	8.38	31.83	15.84	223.61

Table E.8: Statistical properties of the experimental data from droplets impacting smooth steel at 72°.

(a) Measured droplet and stain properties

	u_0 ($\mathrm{m\,s^{-1}}$)	d_0 (10^{-3} m)	$d_{\max}$ (10^{-2} m)	A_{ASC} (10^{-4} $\mathrm{m^2}$)	P_{ASC} (10^{-2} m)	N
Min	2.94	3.07	0.913	0.535	2.63	0
Max	5.72	4.27	2.22	2.60	7.25	22

(b) Calculated non-dimensional properties

	β	Ca (10^{-1})	Re (10^3)	We (10^3)	Bo	$\hat{\mathrm{Fr}}$
Min	2.32	2.71	2.14	0.606	1.92	15.9
Max	5.72	5.27	5.52	2.91	3.72	29.2

(c) Coefficients of variation (in percentages)

Height	u_0	d_0	$d_{\max}$	A_{ASC}	N
0.5 m	1.52	3.15	4.47	8.27	23.96
1.0 m	0.84	6.25	6.22	21.42	138.33
1.5 m	0.95	7.31	21.82	42.38	81.44
2.0 m	1.16	8.38	31.83	15.84	223.61

Table E.9: Statistical properties of the experimental data from droplets impacting roughened steel ($R_a = 1.6 \times 10^{-6}$ m) at 72°.

(a) Measured droplet and stain properties

	u_0 ($\mathrm{m\,s^{-1}}$)	d_0 (10^{-3} m)	$d_{\max}$ (10^{-2} m)	A_{ASC} (10^{-5} $\mathrm{m^2}$)	P_{ASC} (10^{-2} m)	N
Min	3.06	3.17	0.960	5.52	2.84	3
Max	5.65	4.08	2.64	25.6	9.58	21

(b) Calculated non-dimensional properties

	β	Ca (10^{-1})	Re (10^3)	We (10^3)	Bo	$\hat{\mathrm{Fr}}$
Min	2.90	2.82	2.23	0.632	2.05	16.4
Max	6.74	5.20	5.21	2.71	3.40	29.7

(c) Coefficients of variation (in percentages)

Height	u_0	d_0	$d_{\max}$	A_{ASC}	N
0.5 m	1.52	3.15	4.47	8.27	23.96
1.0 m	0.84	6.25	6.22	21.42	138.33
1.5 m	0.95	7.31	21.82	42.38	81.44
2.0 m	1.16	8.38	31.83	15.84	223.61

Table E.10: Statistical properties of the experimental data from droplets impacting roughened steel ($R_a = 3.2 \times 10^{-6}$ m) at 72°.

(a) Measured droplet and stain properties

	u_0 ($\mathrm{m\,s^{-1}}$)	d_0 (10^{-3} m)	$d_{\max}$ (10^{-2} m)	A_{ASC} (10^{-5} $\mathrm{m^2}$)	P_{ASC} (10^{-2} m)	N
Min	3.03	3.15	1.34	7.06	3.96	4
Max	5.73	4.07	3.06	24.8	13.6	18

(b) Calculated non-dimensional properties

	β	Ca (10^{-1})	Re (10^3)	We (10^3)	Bo	$\hat{\mathrm{Fr}}$
Min	3.95	2.79	2.16	0.602	2.03	16.7
Max	7.84	5.28	5.21	2.72	3.38	29.9

(c) Coefficients of variation (in percentages)

Height	u_0	d_0	$d_{\max}$	A_{ASC}	N
0.5 m	1.52	3.15	4.47	8.27	23.96
1.0 m	0.84	6.25	6.22	21.42	138.33
1.5 m	0.95	7.31	21.82	42.38	81.44
2.0 m	1.16	8.38	31.83	15.84	223.61

Table E.11: Statistical properties of the experimental data from droplets impacting roughened steel ($R_a = 6.3 \times 10^{-6}$ m) at 72°.

(a) Measured droplet and stain properties

	u_0 ($\mathrm{m\,s^{-1}}$)	d_0 (10^{-3} m)	A_{IJ} (10^{-4} $\mathrm{m^2}$)	P_{IJ} (10^{-2} m)	d_j (10^{-2} m)	d_i (10^{-2} m)	L_{IJ} (10^{-2} m)	N
Min	3.29	3.33	1.12	4.01	1.35	1.04	1.34	0
Max	5.66	4.35	2.28	6.57	1.87	1.47	2.06	15

(b) Calculated non-dimensional properties

	Ca (10^{-1})	Re (10^3)	We (10^3)	Bo	$\hat{\mathrm{Fr}}$
Min	3.03	2.82	0.854	2.26	17.1
Max	5.22	5.19	2.70	3.86	29.2

(c) Coefficients of variation (in percentages)

Height	u_0	d_0	A_{IJ}	d_j	d_i	L_{IJ}	N
0.5 m	1.97	1.05	5.43	2.29	2.53	3.00	55.90
1.0 m	7.99	5.12	16.39	8.62	8.39	8.62	NaN
1.5 m	1.04	1.99	6.75	3.27	2.61	4.92	70.83
2.0 m	0.82	3.16	6.34	3.16	3.19	3.07	62.83

Table E.12: Statistical properties of the experimental data from droplets impacting paper at 54°.

(a) Measured droplet and stain properties

	u_0 ($\mathrm{m\,s^{-1}}$)	d_0 (10^{-3} m)	A_{IJ} (10^{-4} $\mathrm{m^2}$)	P_{IJ} (10^{-1} m)	d_j (10^{-2} m)	d_i (10^{-2} m)	L_{IJ} (10^{-2} m)	N
Min	3.19	3.58	0.928	0.474	1.35	1.00	1.38	0
Max	5.64	4.33	2.11	1.18	1.87	1.41	3.59	5

(b) Calculated non-dimensional properties

	Ca (10^{-1})	Re (10^3)	We (10^3)	Bo	$\hat{\mathrm{Fr}}$
Min	2.94	2.60	0.773	2.62	16.2
Max	5.20	5.49	2.84	3.83	28.7

(c) Coefficients of variation (in percentages)

Height	u_0	d_0	A_{IJ}	d_j	d_i	L_{IJ}	N
0.5 m	0.89	4.26	17.14	5.92	4.74	5.53	NaN
1.0 m	0.56	3.11	9.81	3.72	3.74	6.25	223.61
1.5 m	0.57	3.48	13.62	6.87	9.57	37.83	149.07
2.0 m	0.39	4.82	35.13	7.19	12.83	8.46	223.61

Table E.13: Statistical properties of the experimental data from droplets impacting smooth steel at 54°.

(a) Measured droplet and stain properties

	u_0 ($\mathrm{m\,s^{-1}}$)	d_0 (10^{-3} m)	A_{IJ} (10^{-4} $\mathrm{m^2}$)	P_{IJ} (10^{-1} m)	d_j (10^{-2} m)	d_i (10^{-2} m)	L_{IJ} (10^{-2} m)	N
Min	3.21	3.75	1.18	0.478	1.41	1.01	1.41	0
Max	5.72	4.33	2.12	1.41	1.92	1.45	2.30	3

(b) Calculated non-dimensional properties

	Ca (10^{-1})	Re (10^3)	We (10^3)	Bo	$\hat{\mathrm{Fr}}$
Min	2.96	2.84	0.848	2.87	16.0
Max	5.27	5.58	2.94	3.83	28.6

(c) Coefficients of variation (in percentages)

Height	u_0	d_0	A_{IJ}	d_j	d_i	L_{IJ}	N
0.5 m	1.18	2.68	8.98	3.49	3.50	8.66	69.01
1.0 m	1.52	3.21	7.45	3.85	3.86	12.95	35.14
1.5 m	1.39	2.38	13.42	6.39	3.15	8.79	129.10
2.0 m	1.22	4.11	19.11	7.22	11.15	8.51	133.02

Table E.14: Statistical properties of the experimental data from droplets impacting roughened steel ($R_a = 1.6 \times 10^{-6}$ m) at 54°.

(a) Measured droplet and stain properties

	u_0 ($\mathrm{m\,s^{-1}}$)	d_0 (10^{-3} m)	A_{IJ} (10^{-4} $\mathrm{m^2}$)	P_{IJ} (10^{-1} m)	d_j (10^{-2} m)	d_i (10^{-2} m)	L_{IJ} (10^{-2} m)	N
Min	3.24	3.58	1.11	0.535	1.43	1.13	1.50	0
Max	5.75	4.41	3.34	1.87	1.76	1.47	4.76	9

(b) Calculated non-dimensional properties

	Ca (10^{-1})	Re (10^3)	We (10^3)	Bo	$\hat{\mathrm{Fr}}$
Min	2.99	2.83	0.846	2.62	16.3
Max	5.30	5.66	2.96	3.97	29.8

(c) Coefficients of variation (in percentages)

Height	u_0	d_0	A_{IJ}	d_j	d_i	L_{IJ}	N
0.5 m	0.71	2.27	23.66	2.91	2.89	31.45	52.70
1.0 m	1.01	2.79	11.65	3.42	3.35	17.62	73.63
1.5 m	1.63	2.06	28.09	5.21	5.32	41.35	74.18
2.0 m	1.14	6.00	16.20	5.60	6.15	12.36	53.46

Table E.15: Statistical properties of the experimental data from droplets impacting roughened steel ($R_a = 3.2 \times 10^{-6}$ m) at 54°.

(a) Measured droplet and stain properties

	u_0 ($\mathrm{m\,s^{-1}}$)	d_0 (10^{-3} m)	A_{IJ} (10^{-4} $\mathrm{m^2}$)	P_{IJ} (10^{-1} m)	d_j (10^{-2} m)	d_i (10^{-2} m)	L_{IJ} (10^{-2} m)	N
Min	3.22	3.65	1.35	0.675	1.26	1.02	1.47	1
Max	5.67	4.44	2.18	3.24	1.77	1.42	2.56	21

(b) Calculated non-dimensional properties

	Ca (10^{-1})	Re (10^3)	We (10^3)	Bo	$\hat{\mathrm{Fr}}$
Min	2.97	2.69	0.808	2.72	16.2
Max	5.23	5.67	2.95	4.03	28.7

(c) Coefficients of variation (in percentages)

Height	u_0	d_0	A_{IJ}	d_j	d_i	L_{IJ}	N
0.5 m	1.47	3.38	6.93	4.55	3.45	9.75	36.89
1.0 m	0.76	1.97	3.99	3.00	4.52	11.43	34.41
1.5 m	1.38	2.43	12.50	6.05	9.02	9.22	50.72
2.0 m	0.69	3.66	14.78	5.34	5.91	10.57	26.88

Table E.16: Statistical properties of the experimental data from droplets impacting roughened steel ($R_a = 6.3 \times 10^{-6}$ m) at 54°.

(a) Measured droplet and stain properties

	u_0 ($\mathrm{m\,s^{-1}}$)	d_0 (10^{-3} m)	A_{IJ} (10^{-4} $\mathrm{m^2}$)	P_{IJ} (10^{-1} m)	d_j (10^{-2} m)	d_i (10^{-2} m)	L_{IJ} (10^{-2} m)	N
Min	3.20	3.78	1.24	0.443	1.69	0.921	1.70	0
Max	5.66	4.22	2.59	1.01	2.39	1.37	2.78	7

(b) Calculated non-dimensional properties

	Ca (10^{-1})	Re (10^3)	We (10^3)	Bo	$\hat{\mathrm{Fr}}$
Min	2.95	2.77	0.817	2.92	16.1
Max	5.22	5.40	2.82	3.64	28.0

(c) Coefficients of variation (in percentages)

Height	u_0	d_0	A_{IJ}	d_j	d_i	L_{IJ}	N
0.5 m	1.06	3.69	8.62	3.44	3.50	4.53	NaN
1.0 m	0.61	3.83	7.00	4.23	4.22	4.63	29.88
1.5 m	1.26	1.56	6.02	2.70	2.65	3.41	60.86
2.0 m	1.23	2.12	0.92	1.63	2.45	1.68	34.23

Table E.17: Statistical properties of the experimental data from droplets impacting paper at 36°.

(a) Measured droplet and stain properties

	u_0 ($\mathrm{m\,s^{-1}}$)	d_0 (10^{-3} m)	A_{IJ} (10^{-4} $\mathrm{m^2}$)	P_{IJ} (10^{-1} m)	d_j (10^{-2} m)	d_i (10^{-4} m)	L_{IJ} (10^{-2} m)	N
Min	3.14	3.69	1.04	0.593	4.42	0.990	1.95	0
Max	5.65	4.21	4.02	1.59	5.57	1.28	6.14	3

(b) Calculated non-dimensional properties

	Ca (10^{-1})	Re (10^3)	We (10^3)	Bo	$\hat{\mathrm{Fr}}$
Min	2.89	2.91	0.844	2.78	15.6
Max	5.21	5.06	2.63	3.62	28.9

(c) Coefficients of variation (in percentages)

Height	u_0	d_0	A_{IJ}	d_j	d_i	L_{IJ}	N
0.5 m	1.69	1.24	13.96	1.67	1.72	31.37	37.27
1.0 m	1.25	4.97	26.06	6.42	6.40	33.01	66.67
1.5 m	0.54	2.84	19.09	5.66	5.89	27.40	63.89
2.0 m	1.37	3.25	34.58	6.50	6.47	51.50	0.00

Table E.18: Statistical properties of the experimental data from droplets impacting smooth steel at 36°.

(a) Measured droplet and stain properties

	u_0 ($\mathrm{m\,s^{-1}}$)	d_0 (10^{-3} m)	A_{IJ} ($10^{-4}\,\mathrm{m^2}$)	P_{IJ} (10^{-1} m)	d_j (10^{-2} m)	d_i (10^{-2} m)	L_{IJ} (10^{-2} m)	N
Min	3.11	3.74	1.52	0.690	1.57	0.873	1.90	0
Max	5.69	4.32	5.14	2.78	2.32	1.34	9.00	3

(b) Calculated non-dimensional properties

	Ca (10^{-1})	Re (10^3)	We (10^3)	Bo	$\hat{\mathrm{Fr}}$
Min	2.87	2.70	0.793	2.86	15.6
Max	5.24	5.36	2.81	3.81	28.7

(c) Coefficients of variation (in percentages)

Height	u_0	d_0	A_{IJ}	d_j	d_i	L_{IJ}	N
0.5 m	1.61	3.24	23.42	5.42	5.44	39.03	35.14
1.0 m	1.17	2.97	17.80	4.38	4.39	20.68	53.03
1.5 m	1.00	3.73	22.99	4.36	4.36	27.09	52.70
2.0 m	1.10	2.97	30.71	5.07	5.09	39.20	0.00

Table E.19: Statistical properties of the experimental data from droplets impacting roughened steel ($R_a = 1.6 \times 10^{-6}$ m) at 36°.

(a) Measured droplet and stain properties

	u_0 ($\mathrm{m\,s^{-1}}$)	d_0 (10^{-3} m)	A_{IJ} ($10^{-4}\,\mathrm{m^2}$)	P_{IJ} (10^{-1} m)	d_j (10^{-2} m)	d_i (10^{-2} m)	L_{IJ} (10^{-2} m)	N
Min	3.14	3.62	1.81	0.607	1.75	1.01	0.258	1
Max	5.60	4.28	5.98	5.48	2.35	1.36	8.36	3

(b) Calculated non-dimensional properties

	Ca (10^{-1})	Re (10^3)	We (10^3)	Bo	$\hat{\mathrm{Fr}}$
Min	2.89	2.91	0.846	2.68	15.5
Max	5.16	5.25	2.70	3.74	29.7

(c) Coefficients of variation (in percentages)

Height	u_0	d_0	A_{IJ}	d_j	d_i	L_{IJ}	N
0.5 m	1.36	1.80	8.63	2.52	2.48	48.01	0.00
1.0 m	0.61	1.53	13.23	1.40	1.29	30.87	53.03
1.5 m	1.33	3.48	23.98	3.43	3.44	41.49	35.14
2.0 m	0.85	32.83	28.38	5.08	5.09	49.55	0.00

Table E.20: Statistical properties of the experimental data from droplets impacting roughened steel ($R_a = 3.2 \times 10^{-6}$ m) at 36°.

(a) Measured droplet and stain properties

	u_0 ($\mathrm{m\,s^{-1}}$)	d_0 (10^{-3} m)	A_{IJ} (10^{-4} $\mathrm{m^2}$)	P_{IJ} (10^{-1} m)	d_j (10^{-2} m)	d_i (10^{-2} m)	L_{IJ} (10^{-2} m)	N
Min	3.18	3.84	1.67	0.616	1.71	0.959	1.92	1
Max	5.60	4.33	2.49	1.70	2.19	1.25	5.40	5

(b) Calculated non-dimensional properties

	Ca (10^{-1})	Re (10^3)	We (10^3)	Bo	$\hat{\mathrm{Fr}}$
Min	2.93	2.92	0.857	3.01	15.7
Max	5.16	5.36	2.76	3.83	28.4

(c) Coefficients of variation (in percentages)

Height	u_0	d_0	A_{IJ}	d_j	d_i	L_{IJ}	N
0.5 m	0.81	1.96	10.61	2.85	3.20	16.00	52.70
1.0 m	1.32	2.20	11.86	4.67	4.58	36.67	49.13
1.5 m	6.50	3.29	8.05	4.07	5.87	12.64	30.86
2.0 m	3.25	3.53	9.35	3.72	4.03	8.53	54.42

Table E.21: Statistical properties of the experimental data from droplets impacting roughened steel ($R_a = 6.3 \times 10^{-6}$ m) at 36°.

(a) Measured droplet and stain properties

	u_0 ($\mathrm{m\,s^{-1}}$)	d_0 (10^{-3} m)	A_{IJ} (10^{-4} $\mathrm{m^2}$)	P_{IJ} (10^{-1} m)	d_j (10^{-2} m)	d_i (10^{-3} m)	L_{IJ} (10^{-2} m)	N
Min	3.15	3.21	1.37	4.80	0.780	2.43	6.33	1
Max	5.63	4.35	2.50	6.62	1.53	3.29	9.30	2

(b) Calculated non-dimensional properties

	Ca (10^{-1})	Re (10^3)	We (10^3)	Bo	$\hat{\mathrm{Fr}}$
Min	2.90	2.29	0.667	2.10	17.1
Max	5.19	5.49	2.83	3.86	29.1

(c) Coefficients of variation (in percentages)

Height	u_0	d_0	A_{IJ}	d_j	d_i	L_{IJ}	N
0.5 m	0.41	2.84	5.70	4.19	3.68	6.54	0.00
1.0 m	1.26	2.45	6.76	1.82	2.38	28.87	0.00
1.5 m	1.60	2.09	3.62	2.80	3.92	8.02	39.12
2.0 m	0.70	5.70	5.11	5.43	5.17	21.05	34.23

Table E.22: Statistical properties of the experimental data from droplets impacting paper at 18°.

(a) Measured droplet and stain properties

	u_0 ($\mathrm{m\,s^{-1}}$)	d_0 (10^{-3} m)	A_{IJ} (10^{-4} $\mathrm{m^2}$)	P_{IJ} (10^{-1} m)	d_j (10^{-2} m)	d_i (10^{-3} m)	L_{IJ} (10^{-2} m)	N
Min	3.10	3.24	1.09	0.590	1.93	6.49	2.26	0
Max	5.72	4.08	5.76	3.52	2.91	8.80	12.5	3

(b) Calculated non-dimensional properties

	Ca (10^{-1})	Re (10^3)	We (10^3)	Bo	$\hat{\mathrm{Fr}}$
Min	2.86	2.28	0.654	2.14	17.3
Max	5.27	5.27	2.78	3.40	29.7

(c) Coefficients of variation (in percentages)

Height	u_0	d_0	A_{IJ}	d_j	d_i	L_{IJ}	N
0.5 m	1.24	1.19	29.81	11.93	2.70	37.57	0.00
1.0 m	1.30	5.08	44.76	13.38	8.53	43.59	70.71
1.5 m	0.76	1.85	38.52	6.37	6.39	44.92	0.00
2.0 m	1.63	4.51	11.72	6.70	5.72	23.28	53.63

Table E.23: Statistical properties of the experimental data from droplets impacting smooth steel at 18°.

(a) Measured droplet and stain properties

	u_0 ($\mathrm{m\,s^{-1}}$)	d_0 (10^{-3} m)	A_{IJ} (10^{-4} $\mathrm{m^2}$)	P_{IJ} (10^{-1} m)	d_j (10^{-2} m)	d_i (10^{-3} m)	L_{IJ} (10^{-2} m)	N
Min	3.11	3.12	1.12	0.952	2.28	6.43	2.55	1
Max	5.47	3.80	5.14	2.53	3.00	9.67	9.52	2

(b) Calculated non-dimensional properties

	Ca (10^{-1})	Re (10^3)	We (10^3)	Bo	$\hat{\mathrm{Fr}}$
Min	2.87	2.22	0.641	1.99	17.3
Max	5.04	4.53	2.27	2.95	30.7

(c) Coefficients of variation (in percentages)

Height	u_0	d_0	A_{IJ}	d_j	d_i	L_{IJ}	N
0.5 m	0.58	2.90	25.60	6.52	4.26	20.95	0.00
1.0 m	15.43	6.15	38.47	9.76	14.00	28.65	22.91
1.5 m	11.68	4.49	33.11	8.24	9.96	28.02	34.95
2.0 m	8.85	3.69	31.56	6.20	7.32	35.33	35.90

Table E.24: Statistical properties of the experimental data from droplets impacting roughened steel ($R_a = 1.6 \times 10^{-6}$ m) at 18°.

(a) Measured droplet and stain properties

	u_0 ($\mathrm{m\,s^{-1}}$)	d_0 (10^{-3} m)	A_{IJ} (10^{-4} $\mathrm{m^2}$)	P_{IJ} (10^{-1} m)	d_j (10^{-2} m)	d_i (10^{-3} m)	L_{IJ} (10^{-2} m)	N
Min	3.13	3.05	1.70	0.972	2.27	6.66	3.03	1
Max	5.46	3.76	5.89	5.87	3.13	9.54	11.8	3

(b) Calculated non-dimensional properties

	Ca (10^{-1})	Re (10^3)	We (10^3)	Bo	$\hat{\mathrm{Fr}}$
Min	2.88	2.16	0.622	1.90	17.3
Max	5.03	4.31	2.17	2.89	29.6

(c) Coefficients of variation (in percentages)

Height	u_0	d_0	A_{IJ}	d_j	d_i	L_{IJ}	N
0.5 m	0.80	2.93	12.99	5.35	3.00	12.05	0.00
1.0 m	0.68	3.72	24.27	4.23	4.98	26.26	0.00
1.5 m	3.59	1.91	27.66	2.19	2.22	29.87	28.75
2.0 m	1.19	2.19	39.33	3.71	3.76	42.17	55.80

Table E.25: Statistical properties of the experimental data from droplets impacting roughened steel ($R_a = 3.2 \times 10^{-6}$ m) at 18°.

(a) Measured droplet and stain properties

	u_0 ($\mathrm{m\,s^{-1}}$)	d_0 (10^{-3} m)	A_{IJ} (10^{-4} $\mathrm{m^2}$)	P_{IJ} (10^{-1} m)	d_j (10^{-2} m)	d_i (10^{-3} m)	L_{IJ} (10^{-2} m)	N
Min	3.10	3.28	0.816	1.65	6.45	0.913	3.52	1
Max	5.69	4.20	3.81	3.43	9.96	3.61	7.95	4

(b) Calculated non-dimensional properties

	Ca (10^{-1})	Re (10^3)	We (10^3)	Bo	$\hat{\mathrm{Fr}}$
Min	2.86	2.30	0.656	2.20	16.9
Max	5.24	5.35	2.78	3.60	29.9

(c) Coefficients of variation (in percentages)

Height	u_0	d_0	A_{IJ}	d_j	d_i	L_{IJ}	N
0.5 m	0.65	1.79	14.58	10.83	4.82	15.92	0.00
1.0 m	0.61	2.75	17.78	4.18	4.98	22.74	0.00
1.5 m	4.60	3.29	11.81	2.94	5.62	15.69	36.89
2.0 m	1.32	5.10	27.65	7.98	4.43	22.57	30.69

Table E.26: Statistical properties of the experimental data from droplets impacting roughened steel ($R_a = 6.3 \times 10^{-6}$ m) at 18°.

Appendix F

Comparing the ASC to manual determination of spines

F.1 Motivation

In order to validate the use of the ASC on horse bloodstains and pig bloodstains, the ASC was compared to the number of spines found manually by different participants.

F.2 Using horse blood

To validate the ASC model, it needed to be compared with the number of spines determined manually. The properties of horse blood (all measured at a temperature of 37 °C) used in the following calculations are: $\rho = 1058.05\,\mathrm{kg\,m^{-3}}$ for density (Doom [2012]), $\mu = 5.5 \times 10^{-3}\,\mathrm{Pa\,s}$ for dynamic viscosity (Doom [2012]; Attinger et al. [2013]), and $\sigma = 4.55 \times 10^{-2}\,\mathrm{N\,m^{-1}}$ for surface tension (Doom [2012]). Five people participated in a study to determine the number of spines on bloodstains from the horse blood experiments. Each person was given a digital photograph for each of the 40 stains and recorded the number of spines they counted manually. The experience of the participants included: two people who have supervised many MSc projects in the field of BPA (one of which has published), two students working on doctorates in the field of BPA (one of whom participated twice to see if their results would change, this is labeled N_{1a} and N_{1b} in Table F.1), and one doctoral student with zero experience in the field of BPA. Using the models described in Subsection 3.1.3, the predicted values for number of spines (based on the Weber number) was also included in this analysis.

First, the Levene's statistical test (Section C.2) was used to ensure the data comes from a normal distribution with the same variance. The ANOVA test (Section C.4) will compare the

means of each of the first seven columns in Table F.1. In this instance, only the manual counts and the ASC are being compared.

The Levene's test yields a p-value of 0.3877 which is greater than 0.05. This indicates that the data set is from a normal distribution with the same variance.

The results of a two-way ANOVA test showed that:

- the method of counting spines (whether manually or using the ASC) had no effect on the number of spines ($F_{5,216} = 1.36$, $p = 0.2393$);
- the height from which the droplet has fallen from does effect the number of spines on the resulting stain ($F_{3,216} = 177.76$, $p = 0$); and
- the method of counting and the height are independent of each other ($F_{15,216} = 1.1$, $p = 0.3594$).

Further, a Tukey test (a post-hoc statistical test to check if there is any statistical difference in the means of each column in the data set, Section C.5), confirms that there is no statistical difference in the means (shown in Figure F.1). These statistical tests confirm that number of spines on the bloodstains automatically counted by the ASC is not statistically different from the results of the manual counts. The need for a standardised algorithm is shown by the difference in results from the participants (shown in Figure F.1), as no single participant is achieving the same mean number of spines as another participant. While the two-way ANOVA test indicates that the height does effect the number of spines on a stain, it is still acceptable to compare the means (using a Tukey test, Figure F.1) because the height variable is independent of the method variable. Therefore the Tukey test is still useful for giving a general overview of how participants count spines as compared to each other and the ASC.

The next set of statistical tests included models by Knock and Davison [2007], Hulse-Smith et al. [2005] and Mehdizadeh et al. [2004]. These models predict the number of spines based on the Weber number of the droplet. The number of spines predicted by these models is shown in the last three columns of Table F.1. Adding these models into the Levene's test pushes the p-value of the test to 0, which fails the Levene's test and indicates this data cannot be used in

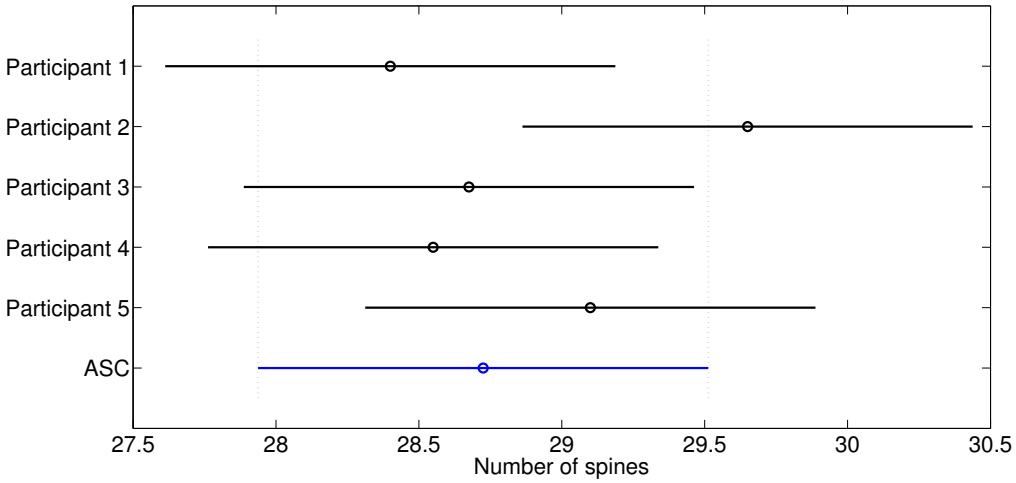

Figure F.1: A comparison of the means of the number of spines on horse bloodstains as counted manually by five participants and counted automatically by the ASC. The circles are the means of each group and the lines are the comparison intervals around each mean.

an ANOVA test. This also indicates the models by Knock and Davison [2007], Hulse-Smith et al. [2005] and Mehdizadeh et al. [2004] have statistically different means compared to the number of spines manually counted and counted by the ASC. This is shown by the Tukey test in Figure F.2.

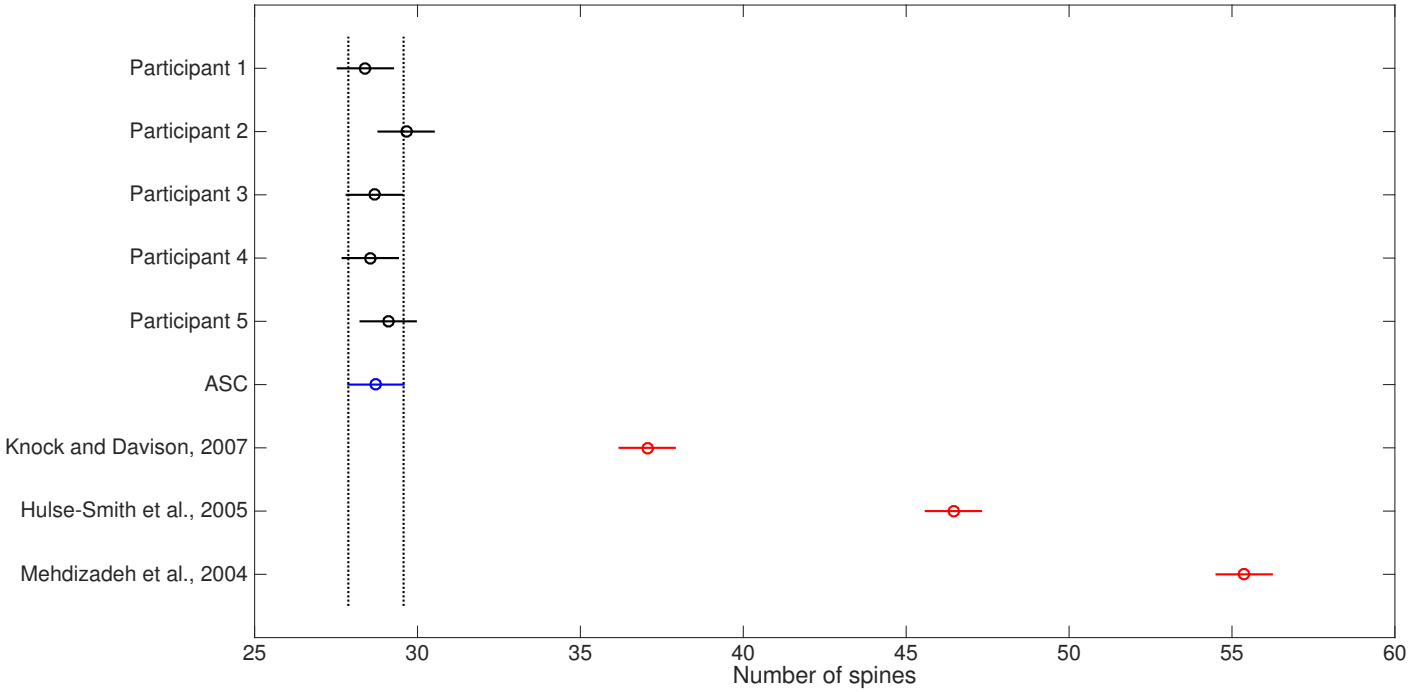

Figure F.2: A comparison of the means of the number of spines on horse bloodstains as counted manually by five participants, counted automatically by the ASC, and as predicted by the models: Knock and Davison [2007], Hulse-Smith et al. [2005], and Mehdizadeh et al. [2004]. The circles are the means of each group and the lines are the comparison intervals around each mean.

Table F.1: Number of spines on horse bloodstains as counted by participants, calculated by the ASC, and predicted by various models.

Height (m)	N_{1a}	N_2	N_3	N_4	N_{1b}	N_5	N_{ASC}	Eqn 3.5	Eqn 3.4	Eqn 3.3
0.5	21	36	24	18	18	18	20	26	33	39
	22	22	24	21	21	20	22	26	33	39
	22	23	26	24	22	23	24	23	29	35
	24	24	26	24	24	25	25	23	29	35
	18	21	22	18	19	22	23	23	29	35
	24	24	29	24	24	24	24	23	29	35
	20	21	21	20	19	21	20	23	29	35
	22	24	25	23	22	23	21	23	29	35
	20	21	21	21	19	21	21	26	33	39
	22	26	23	24	22	23	23	23	29	35
1.0	30	33	30	31	30	31	31	33	41	49
	32	32	30	31	30	31	30	33	41	49
	27	27	29	27	26	30	27	33	41	49
	30	31	30	31	30	30	30	36	45	53
	31	33	33	32	31	32	32	31	39	46
	31	31	31	31	29	31	31	35	44	52
	27	28	33	29	27	29	29	36	45	54
	28	28	29	28	27	31	30	36	45	53
	29	30	32	30	28	30	30	32	40	48
	28	28	28	28	28	27	28	35	44	52
1.5	34	36	32	34	32	34	34	42	52	63
	27	28	26	28	25	26	29	42	52	63
	29	31	28	29	26	30	29	39	49	58
	32	32	32	31	26	33	30	42	52	62
	33	33	30	33	31	33	31	42	52	63
	29	28	29	30	27	31	28	42	53	63
	29	31	29	29	28	33	30	42	52	62
	29	29	28	30	28	32	31	39	49	58
	30	33	29	32	30	32	33	42	52	62
	31	31	29	31	31	31	31	43	54	65
2.0	33	34	35	33	30	34	33	52	65	77
	34	35	34	30	30	32	33	45	56	67
	35	35	33	34	33	36	34	48	60	71
	34	33	29	32	31	33	32	47	60	71
	37	37	34	35	34	36	35	52	65	77
	32	33	35	34	32	33	33	49	62	74
	32	32	29	32	28	33	31	47	59	70
	36	36	28	35	30	34	31	48	60	71
	26	28	23	29	21	27	32	47	60	71
	26	28	29	26	26	29	28	53	67	80

F.3 Using pig blood

The performance of the ASC was also tested against pig blood experiments Knock and Davison [2007]. The properties of the pig blood used (all at a temperature of 37 °C) for these calculations were: $\rho = 1062\,\mathrm{kg\,m^{-3}}$ for density Raymond et al. [1996b], $\mu = 4.8 \times 10^{-3}\,\mathrm{Pa\,s}$ for dynamic viscosity (Raymond et al. [1996b]), and $\sigma = 5.6 \times 10^{-2}\,\mathrm{Nm^{-1}}$ for surface tension (Raymond et al. [1996b]). The original data from the pig blood experiments included manual determination of the number of spines on the bloodstains. The manual determination of spines was compared to the results from the ASC and the three models discussed in Section 3.1.3.

The Levene's test was used to check if the manual counting of spines on the pig bloodstains (Davison [2005]) and the results from the ASC are from a normal distribution with the same variance. Included in this test is the model by Knock and Davison [2007] which was developed using the pig blood experiments from the work by Davison [2005]. It is expected that the spine counts from all three should be statistically the same because the ASC has been shown to count the number of spines on horse bloodstains accurately (Subsection F.2) and the model by Knock and Davison [2007] is based on the work by Davison [2005].

The Levene's test using the first three columns of Tables F.2, F.3, and F.4 yields a p-value of 0.1959, which is greater than 0.05 indicating the manual spine count, the ASC spine count, and the model by Knock and Davison [2007] come from a normal distribution with the same variance. This result also allows the use of a two-way ANOVA test which yields the following results:

- the method of counting spines (either the manual count by Davison [2005], the ASC, or the model by Knock and Davison [2007]) does not affect the number of spines ($F_{2,207} = 1.48$, $p = 0.2305$);
- the height from which the droplet has fallen does affect the number of spines on a bloodstain ($F_{7,207} = 180.12$, $p = 0$);
- the variables height and method of counting are dependent on each other ($F_{14,207} = 5.29$,

Table F.2: Number of spines on horse bloodstains as counted by participants, calculated by the ASC, and predicted by various models. Heights of 0.2 m, 0.4 m, 0.6 m, and 0.8 m.

Height (m)	Davison [2005]	N_{ASC}	Eqn 3.5	Eqn 3.4	Eqn 3.3
0.2	6	10	11	14	17
	10	13	11	14	17
	9	11	12	15	18
0.4	15	16	17	21	25
	17	19	18	22	26
	20	18	18	23	27
	17	14	18	22	27
	18	17	17	22	26
	15	16	18	22	27
0.5	24	24	19	24	29
	24	24	19	24	29
	21	22	20	25	30
	23	24	19	24	29
	23	21	20	25	29
	24	25	19	24	29
	27	27	21	26	31
	22	25	21	26	31
	23	23	21	26	31
	26	26	20	25	30
	23	24	21	26	31
	25	26	20	26	31
0.6	20	18	21	26	31
	18	19	21	26	31
	21	20	21	27	32
	20	20	22	27	32
	25	22	21	27	32
0.8	20	22	24	30	36
	20	19	24	30	36
	19	19	23	30	35
	23	20	21	27	32
	23	22	23	30	35
	17	18	24	30	36

$p = 0$);

It is unclear why these variables are interacting but the F-statistic indicates that the interaction has more weight than the effect of the method of counting, which means while the variables

Table F.3: Number of spines on horse bloodstains as counted by participants, calculated by the ASC, and predicted by various models. Heights of 1.0 m and 1.5 m.

Height (m)	Davison [2005]	N_{ASC}	Eqn 3.5	Eqn 3.4	Eqn 3.3
1.0	31	32	27	34	40
	33	33	28	35	42
	29	29	26	32	39
	29	28	26	32	39
	26	27	27	34	40
	30	32	27	35	41
	29	31	28	35	42
	29	30	28	35	41
	31	32	27	34	41
	29	29	27	33	40
1.5	25	27	32	40	48
	24	24	32	40	47
	26	27	32	40	48
	26	27	33	41	49
	27	28	32	40	48
	18	23	32	40	48
	35	33	31	39	46
	30	29	31	39	46
	30	34	32	40	48
	33	33	31	39	47
	32	33	31	39	46
	35	36	33	41	49
	34	34	33	42	50
	35	34	33	42	50
	33	34	27	34	41
	32	34	34	43	51
	35	38	33	41	50

(height and method of counting) are interacting, the method of counting still does not have a comparable effect on the number of spines on the bloodstain. The post-hoc Tukey test was used to confirm this result, shown in the Figure F.3. The result shows that the ASC can not only be used to count spines on horse bloodstains (Subsection F.2) but also pig bloodstains.

The same statistical tests were carried out with the models Hulse-Smith et al. [2005] and Mehdizadeh et al. [2004] included. This was completed to investigate if the models could predict the number of spines on the horse bloodstains, since the Weber numbers of these stains

Table F.4: Number of spines on horse bloodstains as counted by participants, calculated by the ASC, and predicted by various models. Heights of 2.0 m.

Height (m)	Davison [2005]	N_{ASC}	Eqn 3.5	Eqn 3.4	Eqn 3.3
2.0	25	26	37	46	55
	26	25	36	45	54
	28	27	37	47	56
	28	28	37	47	56
	28	26	37	47	56
	29	28	37	47	56
	34	34	37	47	56
	36	33	36	46	55
	34	32	35	44	52
	35	33	37	47	56
	35	35	35	44	52
	35	33	35	44	53
	33	33	38	47	56
	32	33	37	46	55
	39	38	37	47	55
	34	29	38	48	57
	34	35	37	47	56
	34	34	37	47	55

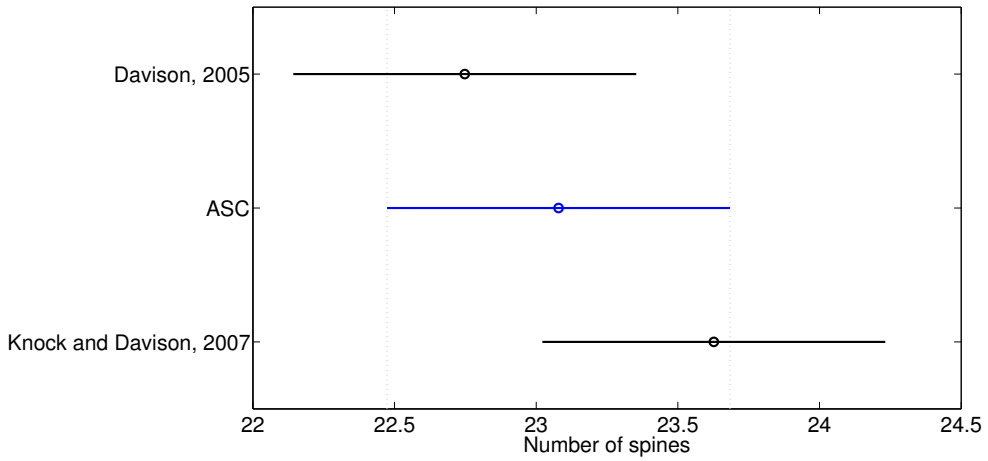

Figure F.3: A comparison of the means of the number of spines on pig bloodstains as counted manually by Davison [2005], counted automatically by the ASC, and predicted by the model by Knock and Davison [2007]. The circles are the means of each group and the lines are the comparison intervals around each mean.

are known. The Levene's test on all columns in Tables F.2, F.3, and F.4 yields a p-value of 0 indicating that the data does not come from a normal distribution with the same variance. Simply adding in two columns of data from models that predict the number of spines causes this change in the Levene's test (*i.e.* the models by Hulse-Smith et al. [2005] and Mehdizadeh et al. [2004] are skewing the distributions causing a the Levene's test to fail). Failure to pass the Levene's test indicates the data cannot be used in an ANOVA test and further the Tukey test (which is normally used as post-hoc test). However, for the purposes of visualising the differences in mean number of spines from each of the different methods of counting spines. Figure F.4 shows that the models by Hulse-Smith et al. [2005] and Mehdizadeh et al. [2004] have significantly different means than the manual spine counts and ASC spine counts. This indicates that these models are not suited for horse bloodstains.

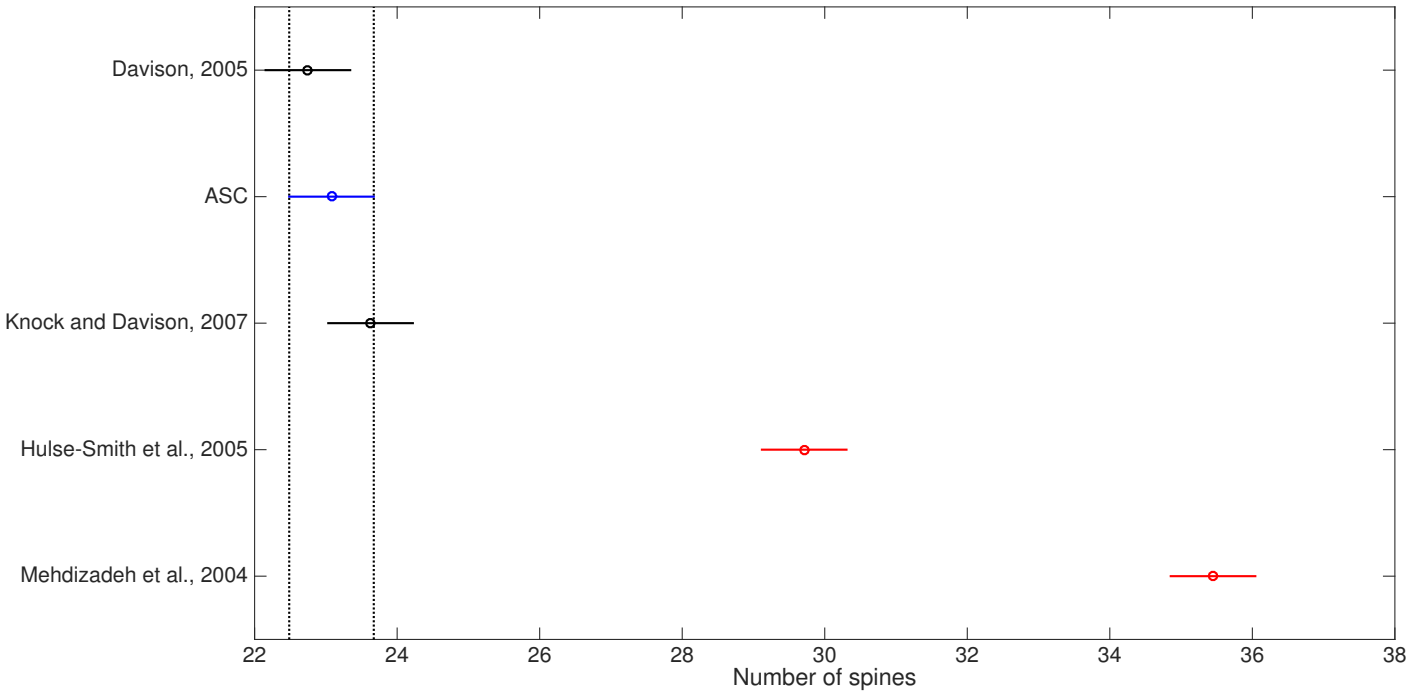

Figure F.4: A comparison of the means of the number of spines on pig bloodstains as counted manually by Davison [2005], counted automatically by the ASC, and as predicted by the models: Knock and Davison [2007], Hulse-Smith et al. [2005], and Mehdizadeh et al. [2004]. The circles are the means of each group and the lines are the comparison intervals around each mean.

F.4 Conclusions

This appendix has presented an automated method for retrieving the area of a bloodstain from a digital photograph and determining the number of spines on the bloodstain. The ASC was tested against experiments using horse blood and pig blood. The horse bloodstains were analysed manually by five participants of varying experience in BPA. The five participants manually determined the number of spines on 40 bloodstains. It should be noted that it is acceptable to test all of the data together regardless of height fallen (*i.e.* impact velocity) because the two-way ANOVA test accounts for the height being a variable in the test. Their results did not show any statistically significant difference from each other but there is some variation in the average number of spines found by the participants. This variation indicates the need for a standardised method for counting spines. The ASC determined the number of spines with good agreement to all the participants.

Next, the ASC was tested against pig blood experiments. These experiments have been published (Knock and Davison [2007]). The ASC proved to determine the number of spines with good agreement the manual determination of spines on pig bloodstains (Davison [2005]). This result shows that the ASC can be used with horse blood or pig blood. While all the results of the ASC counting spines are statistically similar to the manual counts, the ASC presents a method that is consistent and saves time, as opposed to inviting inconsistencies and human error.

A major difference between the ASC and the other models (in Section 3.1.3) for determining the number of spines on a bloodstain is that it is not reliant on the Weber number. Instead, it makes use of image analysis tools in MATLAB, and a consistent procedure to determine the number of spines. Manual counting also does not rely on knowing the Weber number of the droplet, however, manual counts can vary between each person. The ASC removes the human variability by using a consistent method for automatic determination of the number of spines.

Appendix G

A comparison between conditioned or unconditioned paper as a substrate in BPA experiments

G.1 Introduction and motivation

Paper is often used as a substrate in bloodstain pattern analysis experiments (Pizzola et al. [1986a,b]; Hulse-Smith et al. [2005]; Knock and Davison [2007]) because it is easily acquired and is simple to use. Since paper is an absorbent material, experimentation requires that the paper is conditioned according to the British Standard EN 20187:1993 (British Standard [1993], see Appendix A). This conditioning process can take at least 4 hours in an environmental chamber, which has good air circulation. Once conditioned, the paper must be stored correctly (to retain its conditioning properties) until it is used in experiment. This process is not time efficient, so statistical tests were carried out to investigate if the conditioning of paper to British Standard EN 20187:1993 would change the number of spines or stain area of horse bloodstains.

G.2 Strategy

The aim of this set of experiments is to investigate if the conditioning of paper to British Standard EN 20187:1993 (British Standard [1993]) would change the number of spines or stain area of horse bloodstains. To achieve this aim the following steps were carried out:

- 40 paper samples were conditioned to British Standard EN 20187:1993 (British Standard [1993]), which can be found in Appendix A. 20 paper samples were not conditioned.
- Horse bloodstains were collected from horse blood droplets that have been dripped from

known heights onto both conditioned paper and unconditioned paper.

- The number of spines on each bloodstain were counted and the inner and outer diameter of the stains were measured. The area of the stain and the perimeter of the stain were also measured. All of these properties were measured using the Automated Spine Counter (ASC), see Chapter 3.
- A Levene's statistical test was used to check if all the horse bloodstain data come from normal distributions of the same variance. These conditions must be met in order to use a two-way analysis of variance test (see Appendix C.2 and C.4).
- A two-way ANOVA test was used to check if the height the droplet has fallen from, the conditioning of the paper, or both variables have an effect on the number of spines and/or the stain area of the bloodstains.
- A post-hoc Tukey test (Appendix C.5) was used to check if the means of either group (bloodstains on conditioned paper or unconditioned paper) were statistically different.

G.3 Experimental technique

The purpose of the horse blood experiments is to produce data of horse bloodstains on conditioned and unconditioned paper. The details of the experimental method are found in Chapter 4. The details of how to condition paper can be found in Appendix A.

G.4 Statistical tests

G.4.1 Comparing number of spines

Table G.1 shows the number of spines on each horse bloodstain as counted by the ASC. This table is used in the Levene's test and the two-way ANOVA test.

The Levene's test yielded a p-value of 0.32408 which indicates that the data in Table G.1 is from a normal distribution with the same variance. The results of the two-way ANOVA test are

Table G.1: Number of spines on horse bloodstains as counted by the ASC.

Height (m)	Conditioned paper	Unconditioned paper
0.5	20	25
	22	23
	24	25
	25	26
	23	22
1.0	31	32
	30	29
	27	22
	30	28
	32	34
1.5	34	31
	29	28
	29	31
	30	28
	31	31
2.0	35	31
	34	33
	36	32
	33	29
	35	30

as follows:

- Height: $F_{3,32} = 29.6595$, p-value = 2.2981×10^{-9}
- Interaction: $F_{3,32} = 2.008$, p-value $= 0.1326$
- Conditioning: $F_{1,32} = 1.9185$, p-value $= 0.1756$

This two-way ANOVA test indicates that the height from which the droplet has fallen has an effect on the number of spines on the bloodstain. The conditioning of the paper does not have an effect on the number of spines on the bloodstain and there is no interaction between the variables height and conditioning of paper. Finally, a Tukey test indicates that the means of the two groups, conditioned and unconditioned, are statistically the same.

G.4.2 Comparing inner diameter

Table G.2 shows the inner diameters of each horse bloodstain as measured by the ASC. This table is used in the Levene's test and the two-way ANOVA test.

Table G.2: Inner diameter (in m) of horse bloodstains as measured by the ASC.

Height (m)	Conditioned paper	Unconditioned paper
0.5	0.01116	0.01219
	0.01141	0.01290
	0.01171	0.01205
	0.01250	0.01279
	0.01169	0.01299
1.0	0.01338	0.01384
	0.01320	0.01359
	0.01356	0.01128
	0.01352	0.01337
	0.01278	0.01389
1.5	0.01354	0.01492
	0.01402	0.01473
	0.01335	0.01518
	0.01336	0.01460
	0.01358	0.01510
2.0	0.01354	0.01341
	0.01412	0.01375
	0.01315	0.01297
	0.01389	0.01438
	0.01384	0.01370

The Levene's test yielded a p-value of 0.53478 which indicates that the data in Table G.2 is from a normal distribution with the same variance. The results of the two-way ANOVA test are as follows:

- Height: $F_{3,32} = 27.8480$, p-value = 4.7568×10^{-9}
- Conditioning: $F_{1,32} = 9.4051$, p-value $= 0.0044$
- Interaction: $F_{3,32} = 4.4747$, p-value $= 0.0098$

The results of this two-way ANOVA test indicates that the height and the conditioning of the paper both have an effect on the inner diameter of the bloodstains. However, the F-statistics

show that the height variable has more significance than the conditioning variable. Since both variables have an effect on the inner diameter it is reasonable for the variables to be interacting, as shown by its p-value. The post-hoc Tukey test indicates that the means of the two groups, conditioned and unconditioned paper, have statistically different means.

G.4.3 Comparing outer diameters

Table G.3 shows the outer diameters of each horse bloodstain as measured by the ASC. This table is used in the Levene's test and the two-way ANOVA test.

Table G.3: Outer diameter (in m) of horse bloodstains as measured by the ASC.

Height (m)	Conditioned paper	Unconditioned paper
0.5	0.01253	0.01321
	0.01301	0.01429
	0.01346	0.01305
	0.01514	0.01393
	0.01299	0.01457
1.0	0.01598	0.01542
	0.01580	0.01506
	0.01602	0.02729
	0.01548	0.01688
	0.01457	0.01493
1.5	0.01528	0.01677
	0.01575	0.01668
	0.01543	0.01755
	0.01638	0.01704
	0.01561	0.01736
2.0	0.01645	0.01516
	0.01729	0.01542
	0.01538	0.01434
	0.01705	0.01628
	0.01614	0.01702

The Levene's test yielded a p-value of 0.16731 which indicates that the data in Table G.2 is from a normal distribution with the same variance. The results of the two-way ANOVA test are as follows:

- Height: $F_{3,32} = 5.0368$, p-value $= 0.0057$

- Conditioning: $F_{1,32} = 1.7115$, p-value $= 0.2001$
- Interaction: $F_{3,32} = 1.1567$, p-value $= 0.3414$

The results of this ANOVA test indicates that the height variable has an effect on the outer diameter of the stain. The conditioning of the paper does not have an effect on the outer diameter and there is no interaction between the height and conditioning of the paper. A Tukey test indicates that there is no statistical difference in the means of the outer diameters on conditioned paper and unconditioned paper.

G.4.4 Comparing stain area

Table G.4 shows the stain areas of each horse bloodstain as measured by the ASC. This table is used in the Levene's test and the two-way ANOVA test.

Table G.4: Stain area (in 10^{-4} m^2) of horse bloodstains as measured by the ASC.

Height (m)	Conditioned paper	Unconditioned paper
0.5	1.107	1.284
	1.146	1.429
	1.204	1.250
	1.343	1.420
	1.178	1.475
1.0	1.542	1.641
	1.508	1.564
	1.620	1.540
	1.585	1.589
	1.414	1.635
1.5	1.597	1.937
	1.716	1.872
	1.550	1.964
	1.571	1.834
	1.633	1.969
2.0	1.638	1.520
	1.737	1.584
	1.495	1.399
	1.652	1.734
	1.681	1.621

The Levene's test yielded a p-value of 0.78217 which indicates that the data in Table G.4 is

from a normal distribution with the same variance. The results of the two-way ANOVA test are as follows:

- Height: $F_{3,32} = 55.9746$, p-value = 7.8993×10^{-13}
- Conditioning: $F_{1,32} = 19.1972$, p-value = 1.1863×10^{-4}
- Interaction: $F_{3,32} = 8.7905$, p-value = 2.1375×10^{-4}

The results of this ANOVA test indicate that both the height and the condition of the paper have an effect on the stain area of the bloodstains. This test also indicates that there is interaction between the two variables. However, the F-statistics show that the height variable has a more significant effect on the stain area as compared to the condition of the paper and the interaction of the variables. Finally, a Tukey test indicates that the means of the stain areas on conditioned and unconditioned paper are statistically different.

G.4.5 Comparing stain perimeter

Table G.5 shows the stain perimeters of each horse bloodstain as measured by the ASC. This table is used in the Levene's test and the two-way ANOVA test.

The Levene's test yielded a p-value of 0.22506 which indicates that the data in Table G.5 is from a normal distribution with the same variance. The results of the two-way ANOVA test are as follows:

- Height: $F_{3,32} = 23.6611$, p-value = 2.9341×10^{-8}
- Interaction: $F_{3,32} = 10.9156$, p-value = 4.2794×10^{-5}
- Conditioning: $F_{1,32} = 2.2531$, p-value $= 0.1432$

The height variable has an effect on the perimeter of the bloodstains but the conditioning of the paper does not. There is an interaction between the variables but this interaction does not hold as much significance as the effect of the height on the perimeter of the bloodstains. The Tukey test showed that the mean perimeter of bloodstains on conditioned paper and unconditioned paper are not statistically different.

Table G.5: Stain perimeter (in m) of horse bloodstains as measured by the ASC.

Height (m)	Conditioned paper	Unconditioned paper
0.5	0.03987	0.04243
	0.04300	0.04452
	0.04582	0.04183
	0.04824	0.04528
	0.04197	0.04641
1.0	0.05679	0.04930
	0.06355	0.04802
	0.05917	0.06802
	0.05511	0.06216
	0.05357	0.04842
1.5	0.05557	0.06216
	0.05543	0.05958
	0.05294	0.06692
	0.05854	0.06775
	0.05855	0.06755
2.0	0.06743	0.04786
	0.06907	0.04878
	0.05882	0.04471
	0.06933	0.05056
	0.06398	0.05900

G.5 Conclusion

Five properties of bloodstains on conditioned paper and unconditioned paper have been compared statistically. The properties investigated were all measured by the ASC. These properties are the number of spines on the stain, the inner and outer diameter of the stain, the area of the stain, and the perimeter of the stain. These bloodstains have been formed from horse blood droplets falling from four different heights. The statistical tests used are the Levene's test, the two-way ANOVA test, and the Tukey test.

All five data sets passed the Levene's test, indicating that the are all from normal distributions with the same variance. This allowed for the used of the two-way ANOVA test to be carried out on all five data sets. For each property of the bloodstain, the two-way ANOVA test indicated that the height from which the blood droplet has fallen always has an effect on that property. Further,

the height variable always had the greatest effect on any given property of the bloodstain.

The conditioning of the paper was shown to have an effect on the inner diameter of the bloodstains and the area of the bloodstains. In both those statistical investigations, there was an interaction between the height variable and the conditioning variable. While the F-statistics of the these interactions did not outweigh the F-statistics of the conditioning, in both cases the height variable still carried the most significance.

It is reasonable to interpret from these results that the height of the droplet has a greater effect on the the properties of the bloodstain. It is also reasonable to conclude that even though the conditioning of the paper effects two of the five properties, its effect was never more significant than the effect of the height of the droplet, and thus its effect can be ignored (since the F-statistic showed the effect of height to always outweigh the effect of the paper's conditioning or even the interaction between variables). With each stain property, the influence of the height is always at least three times bigger (comparing the F-statistics) than the conditioning of the paper. The results of this appendix show that the lengthy process of conditioning paper is unnecessary. This is a helpful contribution to experimentation in bloodstain pattern analysis as it will make testing more time efficient.

Appendix H

A comparison between horse blood and pig blood – properties and bloodstains

H.1 Introduction and motivation

In bloodstain pattern analysis (BPA), horse blood and pig blood are used as biological substitutes to human blood in experimentation (Raymond et al. [1996b]; Knock and Davison [2007]; Kendall [2008]; McKechnie [2009]). The purpose of this appendix is to investigate if there is a difference between the horse bloodstains and pig bloodstains when looking at the number of spines on a bloodstain, the inner and outer diameter of a bloodstain, the stain area and the perimeter of the bloodstain. The number of spines on a stain and the size of the stain are key variables in calculating the impact velocity of a droplet and the initial droplet size, which are then used to find the source of bloodletting.

H.1.1 Strategy

The physical properties, *i.e.*, the density, dynamic viscosity, and surface tension are compared. The properties of the bloodstains, dependant on the height the droplet has fallen, are investigated for both horse and pig bloodstains. To carry out this investigation the following steps are carried out:

- 20 pig bloodstains and 20 horse bloodstains on unconditioned paper are analysed by the Automated Spine Counter (ASC).
- The ASC outputs the number of spines on each bloodstain, and the inner and outer diameters of each stain, the stain area, and the perimeter of the stain. These are the five

data sets to be used for statistical analysis.

- A Levene's test is used to check if the five data sets are from normal distributions with the same variance.
- A two-way ANOVA test is used to check if the type of blood affects the properties of the bloodstain.
- A Tukey test is used to compare the means of the data sets.

H.1.2 Survey

The purpose of this appendix is to investigate the differences between using horse blood and pig blood in vertical droplet impact experiments. The literature values for the physical properties of horse blood, pig blood, and human blood are in the tables below:

Table H.1: Physical properties of water at different temperatures from literature

Citation	Temperature (°C)	Dynamic Viscosity (10^{-3} Nsm^{-2})	Density (kgm^{-3})	Surface Tension (10^{-2} Nm^{-1})
Knock [2011]	25	1.00	1000	6.6-7.25 Raymond et al. [1996b]
Attinger et al. [2013]	37	0.7	993	7.0

Table H.2: Physical properties of human blood at different temperatures from literature

Citation	Temperature (°C)	Dynamic Viscosity (10^{-3} Nsm^{-2})	Density (kgm^{-3})	Surface Tension (10^{-2} Nm^{-1})
Attinger et al. [2013]	20	6.3	1052-1063	6.1
MacDonell [1993]	25	N/A	N/A	4.9-5.8
Raymond et al. [1996b]	37	3.2-4.4	1056-1061	5.1-6.1
MacDonell [1993]	37	N/A	N/A	2.7-3.4
Hulse-Smith et al. [2005]	37	3.8-5.1	1052-1063	5.1-5.7
Attinger et al. [2013]	37	1.6-5.1	1052-1063	2.7-5.8

Table H.3: Physical properties of pig blood at different temperatures from literature

Citation	Temperature (°C)	Dynamic Viscosity (10^{-3} Nsm^{-2})	Density (kgm^{-3})	Surface Tension (10^{-2} Nm^{-1})
Raymond et al. [1996b]	37	3.9-5.4	1062	5.1-5.8
Knock and Davison [2007]	37	4.8	1062	5.6
Hulse-Smith et al. [2005]	37	3.4-6.1	1062	5.3-5.8
Attinger et al. [2013]	20	8.6	1062	6.5
Attinger et al. [2013]	37	3-20	1062	5.1

Table H.4: Physical properties of horse blood at different temperatures from literature

Citation	Temperature (°C)	Dynamic Viscosity (10^{-3} Nsm^{-2})	Density (kgm^{-3})	Surface Tension (10^{-2} Nm^{-1})
Attinger et al. [2013]	20	8.6	1062	6.5
Attinger et al. [2013]	37	3-20	1062	5.1
Doom [2012]	37	4-49	1045.7-1070.4	4.5-4.6

H.2 Experimental technique

The data from two different experiments are being compared. The first experiment used pig blood from Davison [2005] and the second used horse blood (as described in Chapter 4). Both experiments consisted of a single droplet of blood falling from a known height onto a paper surface at an angle perpendicular to the paper. The paper substrate in the pig blood experiments was not conditioned. However, the paper used in the horse blood experiments was conditioned to British Standard EN 20187:1993 (British Standard [1993]).

H.3 Statistical tests

There are five trials randomly selected from each of the four heights for each fluid. The impact velocities and diameters are in Table H.5. The measurements of impact velocity and droplet diameter of the pig blood droplets were carried out by Davison [2005]. The measurements of impact velocity and droplet diameters of the horse blood droplets were carried out using the *Phantom Camera Control* software using the high-speed videos collected in this work.

H.3.1 Comparing the number of spines

The first property compared between horse and pig blood is the number of spines on the bloodstains. Table H.6 shows the raw data used in the statistical tests.

The Levene's test yields a p-value of 0.0617 which indicates that this data set comes from a normal distribution with the same variance. A two-way ANOVA test (investigating the variables of height and type of blood) yields the following results:

- Height: $F_{3,32} = 11.364$, p-value = 3.1067×10^{-5}
- Blood: $F_{1,32} = 9.3753$, p-value = 0.0044
- Interaction: $F_{3,32} = 0.904$, p-value = 0.45

The height from which the blood droplets are falling and the type of blood both have an

effect on the number of spines on the bloodstains. The height variable has a larger F-statistic which indicates it has a more significant effect on the number of spines. There is no interaction between these two variables. Finally, a Tukey test indicates that the mean number of spines on horse bloodstains is statistically different from the mean number of spines on pig bloodstains.

H.3.2 Comparing the inner diameter

Table H.7 shows the inner diameter of the horse bloodstains and pig bloodstains as measured by the ASC.

The Levene's test on Table H.7 yields a p-value of 0.02354 which is less than 0.05 and indicates that the data set does not come from a normal distribution with the same variance. A two-way ANOVA cannot be performed on this data set.

H.3.3 Comparing the outer diameter

Table H.8 shows the outer diameter of the horse bloodstains and pig bloodstains as measured by the ASC.

The Levene's test in this instance yields a p-value of 0.34562. A two-way ANOVA can be performed on this data set and yields the following results:

- Blood: $F_{1,32} = 7.2158$, p-value = 0.0114
- Height: $F_{3,32} = 1.8466$, p-value = 0.1586
- Interaction: $F_{3,32} = 1.0052$, p-value = 0.4032

These results show that the type of blood has an effect on the outer diameter of the bloodstains. The height variable does not have an effect on the outer diameter in this case (which is peculiar since physically the height should always effect the outer diameter). There is also no interaction between the variables. Lastly, a Tukey test shows that the mean outer diameter of the horse bloodstains is statistically different from the mean outer diameter of pig bloodstains.

H.3.4 Comparing the stain area

Table H.9 shows the raw data of stain areas as measured by the ASC.

The Levene's test on Table H.7 yields a p-value of 3.1355×10^{-4} which is less than 0.05 and indicates that the data set does not come from a normal distribution with the same variance. A two-way ANOVA cannot be performed on this data set.

H.3.5 Comparing the stain perimeter

The Levene's test on Table H.7 yields a p-value of 0.031 56 which is less than 0.05 and indicates that the data set does not come from a normal distribution with the same variance. A two-way ANOVA cannot be performed on this data set.

Table H.5: Impact velocity and diameter of horse blood and pig blood droplets.

Fluid	Height (m)	Impact velocity ($m\,s^{-1}$)	Diameter (10^{-3} m)
horse blood	0.5	3.03	4.000
		3.03	4.000
		3.03	3.800
		3.03	3.800
		3.03	4.000
	1.0	4.38	4.200
		4.04	4.000
		4.71	4.000
		4.04	4.000
		4.38	4.000
	1.5	4.86	4.400
		4.71	4.000
		5.05	4.000
		5.05	3.800
		4.71	4.000
	2.0	5.72	3.900
		5.72	3.900
		5.33	3.900
		5.72	4.100
		5.32	4.100
pig blood	0.5	2.951	3.953
		3.006	3.807
		3.033	4.300
		3.020	4.300
		2.967	4.305
	1.0	4.140	3.535
		4.146	3.527
		4.048	4.210
		4.051	4.215
		4.028	4.210
	1.5	4.926	3.788
		4.908	3.821
		4.967	4.000
		5.002	4.006
		4.986	4.000
	2.0	5.683	3.961
		5.679	3.961
		5.693	3.455
		5.562	4.166
		5.592	3.964

Table H.6: Number of spines on pig and horse bloodstains as counted by the ASC.

Height (m)	Horse blood	Pig blood
0.5	25	23
	23	23
	25	23
	26	22
	22	26
1	32	26
	29	25
	22	30
	28	29
	34	27
1.5	31	28
	28	26
	31	29
	28	28
	31	26
2	31	28
	33	28
	32	24
	29	26
	30	29

Table H.7: Inner diameter (in 10^{-2} m) of pig and horse bloodstains as measured by the ASC.

Height (m)	Horse blood	Pig blood
0.5	1.219	1.369
	1.290	1.330
	1.205	1.487
	1.279	1.484
	1.299	1.521
1	1.384	1.447
	1.359	1.483
	1.128	1.689
	1.337	1.390
	1.389	1.568
1.5	1.492	1.326
	1.473	1.262
	1.518	1.683
	1.460	1.697
	1.510	1.782
2	1.341	1.399
	1.375	1.347
	1.297	1.590
	1.438	1.744
	1.370	1.761

Table H.8: Outer diameter (in 10^{-2} m) of pig and horse bloodstains as measured by the ASC.

Height (m)	Horse blood	Pig blood
0.5	1.321	1.694
	1.429	1.546
	1.305	1.746
	1.393	1.863
	1.457	1.777
1	1.542	1.734
	1.506	1.869
	2.729	2.023
	1.688	1.607
	1.493	2.070
1.5	1.677	1.420
	1.668	1.364
	1.755	1.956
	1.704	2.235
	1.736	2.117
2	1.516	1.715
	1.542	1.536
	1.434	2.320
	1.628	2.357
	1.702	2.097

Table H.9: Stain area (in 10^{-4} m^2) of pig and horse bloodstains as measured by the ASC.

Height (m)	Horse blood	Pig blood
0.5	1.284	1.663
	1.429	1.542
	1.250	1.952
	1.420	1.991
	1.475	2.040
1	1.641	1.827
	1.564	1.901
	1.540	2.514
	1.589	1.681
	1.635	2.321
1.5	1.937	1.469
	1.872	1.349
	1.964	2.452
	1.834	2.585
	1.969	2.836
2	1.520	1.666
	1.584	1.548
	1.399	2.246
	1.734	2.722
	1.621	2.750

Table H.10: Stain perimeter (in 10^{-2} m) of pig and horse bloodstains as counted by the ASC.

Height (m)	Horse blood	Pig blood
0.5	4.243	6.186
	4.452	5.486
	4.183	6.525
	4.528	7.831
	4.641	6.935
1	4.930	7.234
	4.802	7.307
	6.802	8.077
	6.216	6.820
	4.842	9.350
1.5	6.216	4.989
	5.958	4.747
	6.692	7.921
	6.775	9.468
	6.755	8.396
2	4.786	6.185
	4.878	5.630
	4.471	10.637
	5.056	10.830
	5.900	8.176

H.4 Conclusion

This appendix investigated five different properties of horse bloodstain and pig bloodstains: number of spines, inner and outer diameter, stain area, and stain perimeter. The purpose of comparing the stains of these two fluids is to confirm if using horse blood in vertical impact experiments is statistically the same as using pig blood.

Three of five data sets failed the Levene's test and thus the two-way ANOVA could not be performed on those data sets (inner diameter, stain area, and stain perimeter). The two properties that did pass the Levene's test (number of spines and outer diameter) were used in two-way ANOVA tests. These tests showed that the type of blood used has an effect on those properties and in both data sets, the means were statistically different.

These results indicate that pig blood and horse blood do yield different stain properties when impacting unconditioned paper. These statistical tests do not give any information about how the stains are physically formed, only if the stain properties are statistically different or not.

Appendix I

Analysis of bloodstains: Automated Spine Counter versus *ImageJ*

I.1 Introduction and motivation

Two methods have been used to analyse the resulting bloodstain patterns from the experimental work. The first method is using the program *ImageJ* and the second is a program developed in this work called the Automated Spine Counter (ASC, Chapter 3). These two methods have been compared to see which is best for use in investigating **drip stains**.

I.1.1 Strategy

The properties of **drip stains** are measured by different methods are compared. The properties measured by the ASC are: number of spines, inner and outer diameter, stain area, and stain perimeter. The properties measured by *ImageJ* are: stain area and stain perimeter. To carry out this investigation the following steps are carried out:

- Horse blood drip stains onto conditioned paper (British Standard [1993]), unconditioned paper, and steel substrates of different roughness parameters are analysed by the Automated Spine Counter (ASC) and *ImageJ*.
- A Levene's test is used to check if the measurements yielded from the different methods (ASC or *ImageJ*) are from a normal distribution.
- A two-way ANOVA test is used to check if the substrate affects the properties measured (it is expected that it will) or if the method used affects the measured values.
- A Tukey test is used to compare the means of the data sets.

I.2 Experimental technique

The measurements on bloodstains from the setup described in Chapter 4 are investigated. Experiments consisted of a single droplet of blood falling from a known height onto different substrates vertically.

I.3 Statistical tests

There are five trials for each substrate at four heights.

I.3.1 Comparing the stain areas

The areas (as measured by the ASC and *ImageJ*) of the drip stains onto different substrates falling from a height of 0.5 m are compared. The Levene's test yields a p-value of 0.97755 which indicates that this data set comes from a normal distribution with the same variance. A two-way ANOVA test (investigating the variables of substrate and method) yields the following results:

- Substrate: $F_{5,48} = 15.5582$, p-value = 4.3731×10^{-9}
- Interaction: $F_{5,48} = 0.0400$, p-value = 0.9991
- Method: $F_{1,48} = 7.2257 \times 10^{-5}$, p-value = 0.9933

These results show that the substrate affects the stain area measured (at 0.5 m) but the method used to measure the stain area does not have an effect on the measured result. There is also no interaction between the variables.

Comparing the stain area, of droplets falling from a height of 1.0 m, as measured by the ASC and *ImageJ*. The Levene's test yields a p-value of 0.95 which indicates that this data set comes from a normal distribution with the same variance. A two-way ANOVA test (investigating the variables of substrate and method) yields the following results:

- Substrate: $F_{5,36} = 27.5385$, p-value = 2.2799×10^{-11}

- Method: $F_{1,36} = 0.0804$, p-value = 0.7784
- Interaction: $F_{5,36} = 0.0042$, p-value = 1.0

These results show that the substrate affects the stain area measured (at 1.0 m) but the method used to measure the stain area does not have an effect on the measured result. There is also no interaction between the variables.

Comparing the stain area, of droplets falling from a height of 1.5 m, as measured by the ASC and *ImageJ*. The Levene's test yields a p-value of 0.70497 which indicates that this data set comes from a normal distribution with the same variance. A two-way ANOVA test (investigating the variables of substrate and method) yields the following results:

- Substrate: $F_{5,48} = 9.7180$, p-value = 1.8578×10^{-6}
- Interaction: $F_{5,48} = 0.0553$, p-value = 0.9979
- Method: $F_{1,48} = 0.0399$, p-value = 0.8425

These results show that the substrate affects the stain area measured (at 1.5 m) but the method used to measure the stain area does not have an effect on the measured result. There is also no interaction between the variables.

Comparing the stain area, of droplets falling from a height of 2.0 m, as measured by the ASC and *ImageJ*. The Levene's test yields a p-value of 0.96777 which indicates that this data set comes from a normal distribution with the same variance. A two-way ANOVA test (investigating the variables of substrate and method) yields the following results:

- Substrate: $F_{5,48} = 30.0523$, p-value = 1.0556×10^{-13}
- Interaction: $F_{5,48} = 0.0049$, p-value = 1.000
- Method: $F_{1,48} = 0.0038$, p-value = 0.9513

These results show that the substrate affects the stain area measured (at 2.0 m) but the method used to measure the stain area does not have an effect on the measured result. There is also no interaction between the variables.

I.3.2 Comparing the stain perimeters

Comparing the stain perimeter, of droplets falling from a height of 0.5 m, as measured by the ASC and *ImageJ*. The Levene's test yields a p-value of 0 which indicates that this data set does not come from a normal distribution with the same variance. A two-way ANOVA test cannot be performed.

Comparing the stain perimeter, of droplets falling from a height of 1.0 m, as measured by the ASC and *ImageJ*. The Levene's test yields a p-value of 0.0901 which indicates that this data set comes from a normal distribution with the same variance. A two-way ANOVA test (investigating the variables of substrate and method) yields the following results:

- Substrate: $F_{5,36} = 24.0828$, p-value = 1.4428×10^{-10}
- Method: $F_{1,36} = 6.2016$, p-value = 0.0175
- Interaction: $F_{5,36} = 2.7692$, p-value = 0.0324

This ANOVA test shows that the substrate used has an effect on the measured stain perimeter. It also shows that the methods are measuring the stain perimeter to be different values. The variables are also interacting but the reason for this is unknown.

Comparing the stain perimeter, of droplets falling from a height of 1.5 m, as measured by the ASC and *ImageJ*. The Levene's test yields a p-value of 0.86994 which indicates that this data set comes from a normal distribution with the same variance. A two-way ANOVA test (investigating the variables of substrate and method) yields the following results:

- Substrate: $F_{3,32} = 30.8644$, p-value = 6.5481×10^{-14}
- Interaction: $F_{5,48} = 3.6430$, p-value = 0.0071
- Method: $F_{1,48} = 0.0327$, p-value = 0.8572

A two-way ANOVA shows that the substrate used has an effect on the measured stain perimeter. It also indicates that the methods are not different as the methods do not effect the measured value of the perimeter. The substrate and method variables are interacting but the reason for this is unknown.

Comparing the stain perimeter, of droplets falling from a height of 2.0 m, as measured by the ASC and *ImageJ*. The Levene's test yields a p-value of 0.40645 which indicates that this data set comes from a normal distribution with the same variance. A two-way ANOVA test (investigating the variables of substrate and method) yields the following results:

- Substrate: $F_{5,48} = 42.7105$, p-value = 1.5200×10^{-16}
- Method: $F_{1,48} = 4.0813$, p-value = 0.0490
- Interaction: $F_{5,48} = 1.2652$, p-value = 0.2943

This ANOVA test shows that the substrate and the method used has an effect on the measured value of the stain perimeter. There is no interaction between the variables.

I.4 Conclusion

When comparing the stain area measured by the ASC compared to *ImageJ*, the two-way ANOVA tests indicate (at each height) that the method of measurement does not effect the result. This means that the ASC and *ImageJ* are achieving the same measurements for the stain area of the bloodstains.

When comparing the stain perimeter, the ASC and *ImageJ* yield different values (at heights 1.0 m and 2.0 m). This is probably caused by the way the perimeter is measured by the ASC. In the ASC, the edges of the stain are smoothed using a filter (see Chapter 3). For example, Figure I.1 shows the measurements of a stain (Figure I.1a) in both *ImageJ* (Figure I.1b) and the ASC (Figure I.1c). The perimeter of the stain as measured by *ImageJ* is 11.056×10^{-2} m and the perimeter of the stain as measured by the ASC is 7.254×10^{-2} m. The perimeters are different because the image of the bloodstain in *ImageJ* is very pixelated. This causes the line used to trace the outside of the bloodstain to move in and out between pixels. The ASC smooths the edges of the bloodstain and then traces the edge of the bloodstain which eliminates the error of tracing between pixels, making the perimeter of the stain longer than it is in reality.

Along with the stain area and perimeter, the ASC is also capable of measuring the inner

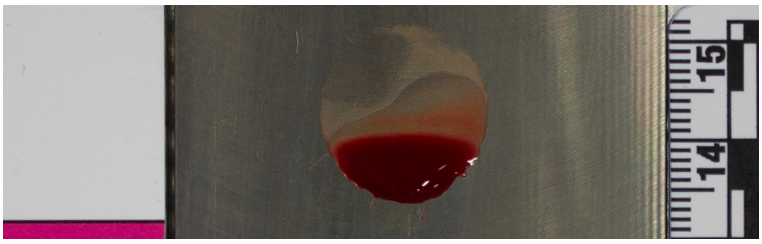

(a)

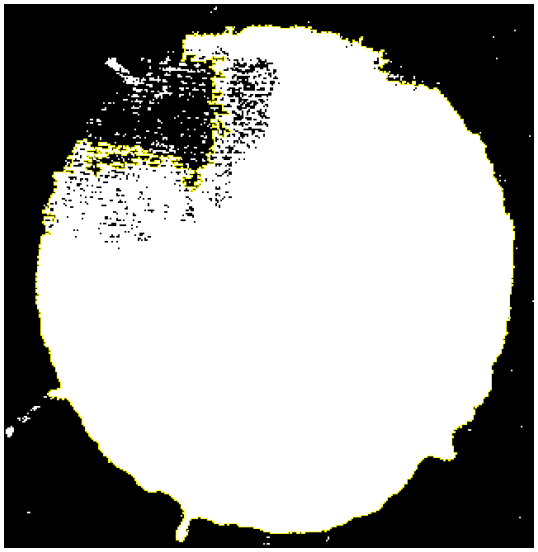

(b)

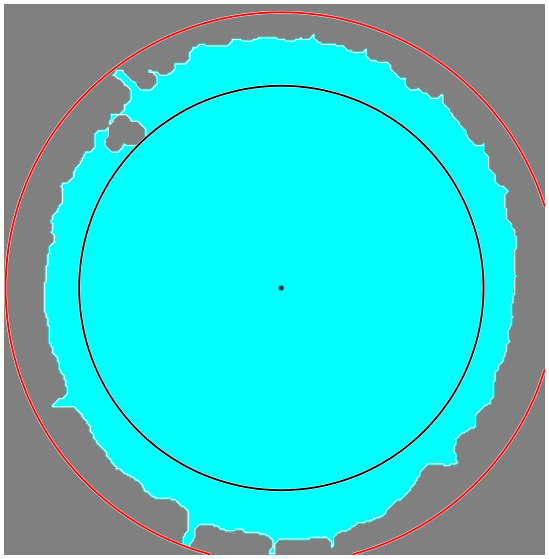

(c)

Figure I.1: Bloodstain from a droplet impacting a steel substrate of roughness $R_a = 1.6 \times 10^{-6}$ m at 18°. The droplet's diameter before impact was 4.11×10^{-3} m and its impact velocity was $5.62\,\mathrm{m\,s^{-1}}$.

and outer diameters of the bloodstain. This is done automatically by finding the centroid of the stain then drawing a circle using the smallest radius from the centroid to the edge (for the inner diameter) and the largest radius from the centroid to the edge of the stain (for the outer diameter). This can be seen in Figure I.1c. In *ImageJ*, a circle can be drawn manually in order to approximate the inner and outer diameter of the stain but this may be time consuming (to get the circle to fit correctly). The ASC does not have an issue with human error when finding the inner and outer diameters. For this reason, the diameters were not compared because the ASC will logically be more accurate.

In conclusion, the ASC has more capabilities than *ImageJ* and has shown to be just as or more accurate in measuring properties of bloodstains.

Appendix J

Derivation of the dissipation function

The basics of fluid flow are governed by the conversation of mass and the conservation of momentum. The conservation of momentum, is given by the Cauchy equation (**?**):

$$\rho \frac{D\mathbf{u}}{Dt} = \rho \mathbf{g} + \nabla \cdot \Pi. \tag{J.1}$$

All the stresses on an incompressible fluid ($\nabla \cdot \mathbf{u} = 0$) can be written as a total stress tensor, Π_{ij} (**?**):

$$\Pi_{ij} = -p\delta_{ij} + \tau_{ij} \tag{J.2}$$

where p is the pressure, δ_{ij} is the Kronecker delta function, and τ_{ij} is the viscous stress tensor.

The Kronecker delta function is defined as:

$$\delta_{ij} = \begin{cases} 0 & \text{if } i \neq j \\ 1 & \text{if } i = j \end{cases} \tag{J.3}$$

The viscous stress tensor, τ, is written as (White [1991]):

$$\tau_{ij} = \mu \left[\left(\frac{\partial u_i}{\partial x_j} + \frac{\partial u_j}{\partial x_i} \right) - \frac{2}{3} \delta_{ij} \frac{\partial u_k}{\partial x_k} \right] \tag{J.4}$$

where $\mathbf{u}$ is the velocity vector and $\mathbf{x}$ is a position vector.

The viscous term in the Navier-Stokes equation (Equation 2.18, see Batchelor [2000]) is described by τ. The work done by these viscous stresses is described as the dissipation function:

$$\Phi = \tau : \nabla \mathbf{u} \,. \tag{J.5}$$

When a droplet impacts a surface it will release energy as heat as the droplet deforms due viscosity. The dissipation function, Φ is often written in the following form (Chandra and Avedisian [1991]; Pasandideh-Fard et al. [1996]):

$$\Phi = \tau_{ij} \frac{\partial u_i}{\partial x_j} \,. \tag{J.6}$$

This function becomes important when looking into the energy lost during droplet deformation.

Appendix K

The kinetic energy of a droplet before impact according to Chandra and Avedisian [1991], Pasandideh-Fard et al. [1996], Roisman et al. [2002], and Adam [2012]

This calculation of the kinetic energy of a droplet (Equation K.6) assumes that the droplet is a sphere before impact, thus its volume, V_{sphere}, is:

$$V_{\text{sphere}} = \frac{4}{3}\pi r_0^3, \tag{K.1}$$

where the r_0 is the radius of the spherical droplet before impact. The kinetic energy before impact, E_K, is:

$$E_K = \frac{1}{2}mu_0^2 \tag{K.2}$$

$$= \frac{1}{2}\rho V_{\text{sphere}} u_0^2 \tag{K.3}$$

$$= \frac{1}{2}\rho \left(\frac{4}{3}\pi r_0^3\right) u_0^2 \tag{K.4}$$

$$= \frac{2}{3}\rho\pi \left(\frac{d_0}{2}\right)^3 u_0^2 \tag{K.5}$$

$$= \frac{1}{12}\rho\pi d_0^3 u_0^2 \tag{K.6}$$

where m is the mass of the droplet, ρ is the density of the droplet, u_0 is the impact velocity of the droplet, and d_0 is the diameter of the droplet before impact.

Appendix L

The kinetic energy of a droplet before impact according to Engel [1955]

Engel [1955] states that the kinetic energy of a droplet that has impacted a solid surface can be written as a function of, r_s, the observed radius of the droplet's spread. Figure L.1 shows an adaptation of the illustration by Worthington [1876] of the cross-sectional of a droplet spreading along a substrate. This figure is then simplified by Engel [1955] which is shown in Figure L.2.

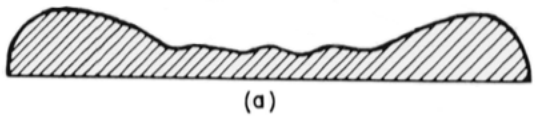

Figure L.1: Edited illustrations (from Engel [1955]) of the cross-sectional area of a droplet spreading along a solid surface after impact, the cross sectional area of a droplet spreading as observed by Worthington [1876].

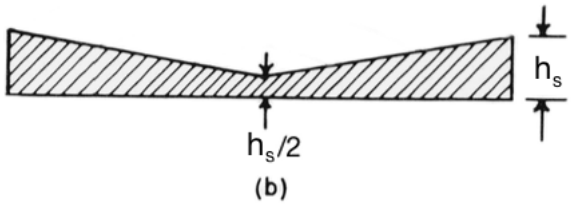

Figure L.2: Edited illustrations (from Engel [1955]) of the cross-sectional area of a droplet spreading along a solid surface after impact, an assumed shape of the cross section of the spreading of a droplet during impact stated by Engel [1955].

The volume of the shape shown in Figure L.2 is calculated by taking the volume of a cylinder of radius, r_s, and height, h_s and subtracting the volume of a triangle of revolution with a length of, r_s and height, $\frac{h_s}{2}$. The observed height of the droplet spread is h_s. The volume of the disc is:

$$V_{\text{disc}} = \pi r_s^2 h_s \,. \tag{L.1}$$

The volume of the rotated triangle has a hypotenuse:

$$y = \frac{h_s x}{2r_s}\,, \tag{L.2}$$

and the volume of the rotated triangle is:

$$V_{\text{triangle}} = \pi \int_0^{\frac{h_s}{2}} \left(\frac{2r_s y}{h_s}\right)^2 dy \tag{L.3}$$

$$= \frac{4r_s^2}{h_s^2} \int_0^{\frac{h_s}{2}} y^2 dy \tag{L.4}$$

$$= \frac{4r_s^2}{h_s^2} \left(\frac{1}{3}\right) \left(\frac{h_s}{2}\right)^3 \tag{L.5}$$

$$= \frac{1}{6}\pi r_s^2 h_s \,. \tag{L.6}$$

Therefore the volume of the spreading droplet can be written as:

$$V_{\text{spread}} = V_{\text{disc}} - V_{\text{triangle}} \tag{L.7}$$

$$= \pi r_s^2 h_s - \frac{1}{6}\pi r_s^2 h_s \tag{L.8}$$

$$= \frac{5}{6}\pi r_s^2 h_s \,, \tag{L.9}$$

which is the volume of the shape in Figure L.2. This derivation (to find the volume of the shape in Figure L.2) is not shown by **?**. It has been derived here for clarity.

The equation for kinetic energy in general is:

$$E_K = \frac{1}{2} m \mathbf{u}^2 \,, \tag{L.10}$$

where m is the mass of an object and $\mathbf{u}$ is the velocity of the object. Engel [1955] substituted $m = \rho V$, where V is the volume of an object and ρ is its density. The volume Engel [1955] uses in this case is an integration of the lateral area of the spreading droplet (*i.e.* $2\pi rh$, which is the area of the outside, excluding the top and bottom, of a cylinder) over the range of radii 0 to r_s.

Engel [1955] then writes the kinetic energy of the spreading droplet as:

$$E_K = \frac{\rho}{2} \int_0^{r_s} 2\pi r_s h_s u_{\text{rad}}^2 dr \tag{L.11}$$

where u_{rad} is the velocity of the radial flow outwards, h_s is the thickness of the droplet as it spreads, and r_s is the observed radius of the spread. Engel [1955] assumes the velocity of the radial flow is 0 at the centre of the droplet and is u_{edge} at the edge of the spreading droplet. Engel [1955] also assumes the thickness of the spreading is $\frac{h_s}{2}$ at the centre and h_s at the edge (as shown by Figure L.2). The expression for u_{rad} is the radial distance over time:

$$u_{\text{rad}} = \frac{r}{t}, \tag{L.12}$$

where t is the time during impact ($t = 0$ is when the droplet first makes contact with the solid) and r is the radius of the spread over time. The expression for the thickness of the spread in general is derived by finding the equation of a line between points $(0, \frac{h_s}{2})$ and (r_s, h_s) (see Figure L.2):

$$h = \left(\frac{h_s - \frac{h_s}{2}}{r_s - 0} \right) r + \frac{h_s}{2} \tag{L.13}$$

$$h = \frac{r}{r_s} \frac{h_s}{2} + \frac{h_s}{2}, \tag{L.14}$$

where r_s is the radius of the spread at it's final point. Since the volume of the spreading droplet is known (Equation L.9), h_s is:

$$h_s = \frac{6V_{\text{spread}}}{5\pi r_s^2} \tag{L.15}$$

Substituting Equations L.12, L.14, and L.15 into Equation L.11 (the following is not shown in the publication by Engel [1955]):

$$E_K = \frac{\rho}{2}\int_0^{r_s} 2\pi r h u_{\text{rad}}^2 dr \tag{L.16}$$

$$= \pi\rho\int_0^{r_s} r\left(\frac{r}{r_s}\frac{h_s}{2}+\frac{h_s}{2}\right)\left(\frac{r}{t}\right)^2 dr \tag{L.17}$$

$$= \pi\rho\int_0^{r_s}\left(\frac{r^4}{r_s}\frac{1}{2t^2}\frac{6V_{spread}}{5\pi r_s^2}+\frac{r^3}{2t^2}\frac{6V_{spread}}{5\pi r_s^2}\right)dr \tag{L.18}$$

$$= \pi\rho\int_0^{r_s}\left(\frac{r^4}{r_s}\frac{1}{2t^2}\frac{6m}{5\pi\rho r_s^2}+\frac{r^3}{2t^2}\frac{6m}{5\pi\rho r_s^2}\right)dr \tag{L.19}$$

$$= \pi\rho\left(\frac{r_s^5}{5r_s}\frac{1}{2t^2}\frac{6m}{5\pi\rho r_s^2}+\frac{r_s^4}{8t^2}\frac{6m}{5\pi\rho r_s^2}\right) \tag{L.20}$$

$$= \frac{3mr_s^2}{25t^2}+\frac{3mr_s^2}{20t^2} \tag{L.21}$$

$$= \frac{27mr_s^2}{100t^2}. \tag{L.22}$$

Finally Engel [1955] approximates the kinetic energy of a droplet (of mass, m) spreading after impact as:

$$E_K \approx \frac{m}{4}\left(\frac{r_{\max}}{t}\right)^2 \tag{L.23}$$

where $r_{\max}$ is the radius of the spread once it is at its maximum stretch. The derivation of Equation L.23 is not shown by Engel [1955], it has been shown in this appendix for clarity. The reason for the approximation is not made clear by Engel [1955] but the approximation is simply rounding $\frac{27}{100}$ (which is 0.27) down to 0.25 or $\frac{1}{4}$. For the purposes of this thesis, this equation will be cited with respect to the maximum diameter:

$$E_K \approx \frac{m}{16}\left(\frac{d_{\max}}{t}\right)^2 . \tag{L.24}$$

Appendix M

The surface energy of a droplet before impact according to Engel [1955], Chandra and Avedisian [1991], Pasandideh-Fard et al. [1996], Roisman et al. [2002], and Adam [2012]

The surface energy before droplet impact, E_S, is described as energy per unit area. Dimensional analysis shows that surface energy and surface tension have the same dimensional quantity:

$$\text{Surface Energy} = [J] \tag{M.1}$$

$$= [N]\,[m] \tag{M.2}$$

$$= \frac{[N]}{[m]}\left[m^2\right], \tag{M.3}$$

which is the dimensional quantity of surface tension multiplied by area. Therefore, surface energy, can be written as surface tension, σ, multiplied by surface area of a droplet, A (Engel [1955]; Chandra and Avedisian [1991]; Pasandideh-Fard et al. [1996]; Roisman et al. [2002]; Adam [2012]):

$$E_S = 4\sigma_{lg}\pi r_0^2 \tag{M.4}$$

$$= \sigma_{lg}\pi d_0^2\,. \tag{M.5}$$

Appendix N

The deformation of a droplet during impact according to Engel [1955]

The deformation of a droplet during impact is described by Engel [1955] to be the dissipation of energy integrated over the volume of the droplet, over time. Thus the energy lost to deformation is (stated by Engel [1955]):

$$E_D = 2\pi \int_0^{t_{\max}} \int_0^{\Omega} \Phi d\Omega \mathrm{d}t \tag{N.1}$$

$$= 2\pi \int_0^{t_{\max}} \Phi\Omega \mathrm{d}t\,, \tag{N.2}$$

where $t_{\max}$ is the time taken for the droplet to reach the shape of a flattened disc, Ω is the volume of the boundary of the droplet while it is collapsing (which is approximated by a cylinder), and Φ is the dissipation function. This is very similar to the definition by Chandra and Avedisian [1991] (see Equation O.1) but it is unclear why Engel [1955] multiplies the expression by 2π. Chandra and Avedisian [1991] used the same approximation of the dissipation function as Engel [1955] (see Appendix Q, Equation P.1).

The boundary layer Ω is approximated by the volume of a disc:

$$\Omega = \pi r_{max}^2 \delta\,, \tag{N.3}$$

where δ is the thickness of the boundary layer and r_{max} is the radius of the droplet's spread.

The dissipation function (see Appendix J) is written by Engel [1955] to be the radial flow of the droplet spreading outwards with respect to the thickness of the spread, all multiplied by the dynamic viscosity. Engel [1955] only states this in words, but the assumption made here is:

$$\Phi = \mu \left(\frac{u_{\text{edge}}}{\delta} \right)^2 , \tag{N.4}$$

where u_{edge} is the velocity of the fluid at the edge of spreading.

Substituting Equation N.3 and Equation N.4 into Equation N.1, the deformation is then:

$$E_D = 2\pi \int_0^{t_{\max}} \mu \left(\frac{u_{\text{edge}}}{\delta} \right)^2 \pi r_{max}^2 \delta \, \mathrm{d}t \tag{N.5}$$

$$= 2\pi^2 \mu \int_0^{t_{\max}} \left(\frac{u_{\text{edge}}^2}{\delta} \right) r_{max}^2 \mathrm{d}t \, . \tag{N.6}$$

Next, Engel [1955] states that $u_{\text{edge}} = r_{max}/t$:

$$E_D = 2\pi^2 \mu \int_0^{t_{\max}} \left(\frac{r_{max}}{t} \right)^2 \frac{r_{max}^2}{\delta} \mathrm{d}t \tag{N.7}$$

$$= 2\pi^2 \mu \int_0^{t_{\max}} \frac{r_{max}^4}{t^2 \delta} \mathrm{d}t \, . \tag{N.8}$$

Engel [1955] then states that the boundary layer varies linearly with time but does not state the relationship explicitly. This appendix will use $\delta = \xi t$, where ξ is a constant with the units of velocity, in order to satisfy dimensional analysis:

$$E_D = 2\pi^2 \mu \int_0^{t_{\max}} \frac{r_{max}^4}{t^2 (\xi t)} \mathrm{d}t \tag{N.9}$$

$$= \frac{2\pi^2 \mu}{\xi} \int_0^{t_{\max}} \frac{r_{max}^4}{t^3} \mathrm{d}t \, . \tag{N.10}$$

Putting the deformation in terms of diameter instead of radius (as that is easier to measure in experiment):

$$E_D = \frac{2\pi^2\mu}{\xi}\int_0^{t_{\max}} \frac{d_{max}^4}{16t^3}\mathrm{d}t \tag{N.11}$$

$$= \frac{\pi^2\mu}{8\xi}\int_0^{t_{\max}} \frac{d_{max}^4}{t^3}\mathrm{d}t\,. \tag{N.12}$$

Combining all of the terms in front of the integral, into ϖ:

$$\varpi = \frac{\pi^2\mu}{8\xi}\,, \tag{N.13}$$

the deformation energy is:

$$E_D = \varpi\int_0^{t_{\max}} \frac{d_{max}^4}{t^3}\mathrm{d}t\,. \tag{N.14}$$

Appendix O

The deformation of a droplet during impact according to Chandra and Avedisian [1991]

When a droplet impacts a non-yielding surface, it deforms, and energy is lost. The energy lost can be calculated by integrating the dissipation of energy (Φ) first over the volume of the deforming droplet, V_{disc}, then over the time it takes for the droplet to reach maximum spread, t_{max}. The energy lost to deformation, E_D, is:

$$E_D = \int_0^{t_{\text{max}}} \int_V \Phi dV dt \tag{O.1}$$

$$\approx \Phi V_{\text{disc}} t_{\text{max}}\,, \tag{O.2}$$

where the volume, V_{disc} is taken by Chandra and Avedisian [1991] to be the volume of a flattened out disc at maximum extension (splat thickness, z):

$$V_{\text{disc}} \approx \frac{\pi}{4} d_{\text{max}}^2 z\,, \tag{O.3}$$

where d_{max} is the diameter of the flattened disc and the time taken for the droplet to reach the shape of a flattened disc, t_{max}, is calculated using:

$$t_{\text{max}} \approx \frac{d_0}{u_0}\,, \tag{O.4}$$

where d_0 is the initial diameter of the droplet and u_0 is the impact velocity of the droplet (which is assumed to be constant). It is assumed that the droplet is in the shape of a disc during the

entirety of spreading. Therefore,

$$E_D \approx \Phi \left(\frac{\pi}{4} d_{\max}^2 z \right) \left(\frac{d_0}{u_0} \right). \tag{O.5}$$

The dissipation function is written as (see Appendix J):

$$\Phi = \tau_{ij} \frac{\partial u_i}{\partial x_j} \tag{O.6}$$

$$= \mu \left(\frac{\partial u_i}{\partial x_j} + \frac{\partial u_j}{\partial x_i} - \frac{2}{3} \delta_{ij} \frac{\partial u_k}{\partial x_k} \right) \frac{\partial u_i}{\partial x_j}. \tag{O.7}$$

It is taken that the components i and j are not the same so the Kronecker delta function will go to 0 (see Equation J.3). Chandra and Avedisian [1991] do not explain the next step of their approximation of the dissipation function. The easiest explanation is that the flow of the droplet spreading is symmetrical in all directions (being approximated by a disc). The coordinate system that Chandra and Avedisian [1991] seem to be using is i for the outwards direction and j for the upwards direction. Further, it is assumed (but not mentioned) that there is no change in velocity in the upwards direction (*i.e.* the droplet isn't jumping off the surface or that the flow in the horizontal direction is constant with depth of the droplet). Therefore, the dissipation function can be simplified to:

$$\Phi \approx \mu \left(\frac{\partial u_i}{\partial x_j} \right)^2. \tag{O.8}$$

This can be read as a change in velocity outwards (droplet spreading outwards) with respect to a change in height (droplet compressing towards the surface), using a normal coordinate system, let $i = x$ and $j = y$, thus:

$$\Phi \approx \mu \left(\frac{\partial u_x}{\partial y} \right)^2. \tag{O.9}$$

This is written (without derivation) by Moita et al. [2014] as:

$$\Phi \approx \mu \left(\frac{u_0}{z}\right)^2, \tag{O.10}$$

where μ is the dynamic viscosity of the droplet, u_0 is the impact velocity of the droplet, and z is the height of the droplet as it is compressing or splat thickness. Therefore, the energy lost due to deformation, according to Chandra and Avedisian [1991], is:

$$E_D \approx \mu \left(\frac{u_0}{z}\right)^2 \left(\frac{\pi}{4} d_{\max}^2 z\right) \frac{d_0}{u_0} \tag{O.11}$$

$$\approx \mu \left(\frac{u_0}{z}\right) \left(\frac{\pi}{4} d_{\max}^2\right) d_0 \tag{O.12}$$

$$\approx \frac{\pi \mu u_0 d_0 d_{\max}^2}{4z} .. \tag{O.13}$$

Appendix P

Deformation of a droplet according to Pasandideh-Fard et al. [1996]

Pasandideh-Fard et al. [1996] starts from Chandra and Avedisian [1991]'s Equation O.1 but makes a different approximation for the dissipation function. Recall, Chandra and Avedisian [1991] writes the dissipation function, Φ, as:

$$\Phi \approx \mu \left(\frac{u_0}{z} \right)^2 , \tag{P.1}$$

where μ is the dynamic viscosity of the droplet, u_0 is the impact velocity of the droplet, and z is the height of the flattened out disc shape that the droplet has become during impact or splat thickness.

Therefore, instead of using the thickness of the spread as the scale for the compression of the droplet, Pasandideh-Fard et al. [1996] suggests to use the boundary layer thickness of the spread instead. Recall that the boundary layer is a layer of fluid in contact with a surface and is a section of fluid that has not yet reached full velocity (during spreading). Pasandideh-Fard et al. [1996] writes the dissipation function as:

$$\Phi \approx \mu \left(\frac{u_0}{\delta} \right)^2 , \tag{P.2}$$

where u_0 is the impact velocity of the droplet and δ is the boundary layer thickness. This is similar to the approximation used by Engel [1955]. The boundary layer Pasandideh-Fard et al. [1996] used is cited from White [1991]:

$$\delta = \frac{2d_0}{\sqrt{\mathrm{Re}}} , \tag{P.3}$$

where the Reynolds numbers in droplet impacts tend to be laminar in flow (see Chapter 5). Pasandideh-Fard et al. [1996] goes on to explain the other assumptions used to approximate the dissipation function. Pasandideh-Fard et al. [1996] describes the impact of the spherical droplet onto the surface to be sphere of diameter d_0 (with impacting velocity u_0) turning into a cylinder of diameter d_s (with outer edge velocity of u_{edge}). These variables are shown in Figure P.1. In order for the sphere to expand into the cylinder, the sphere must first impact the surface, becoming a truncated sphere. The base of this truncated sphere, or spherical cap, has a diameter of d_{cap} (thus an area of $\frac{\pi}{4}d_{cap}$). The fluid will flow from it's spherical form, through this circle of diameter d_{cap}, and into the cylinder with diameter d_s (with a lateral surface area of $\pi d_s z$). Using the conservation of momentum, Pasandideh-Fard et al. [1996] finds the following relationship between the ratio of the velocity at the edge of the spread and the impact velocity (the following steps are not shown by Pasandideh-Fard et al. [1996]):

$$A_{cap}u_0 = A_{cyl}u_{edge} \tag{P.4}$$

$$\frac{1}{4}\pi d_{cap}^2 u_0 = \pi d_s h u_{edge} \tag{P.5}$$

$$\frac{d_{cap}^2}{4d_s z} = \frac{u_{edge}}{u_0}. \tag{P.6}$$

Recall that d_s is changing over time as the droplet is spreading.

By setting the volume of the droplet before impact (diameter of d_0) equal to the volume of the droplet at maximum extension (diameter of d_{max}), the thickness of the spread, z, can be written as (the following steps are not shown by Pasandideh-Fard et al. [1996]):

$$\frac{\pi}{6}d_0^3 = \frac{\pi}{4}d_{max}^2 z \tag{P.7}$$

$$z = \frac{2}{3}\frac{d_0^3}{d_{max}^2}. \tag{P.8}$$

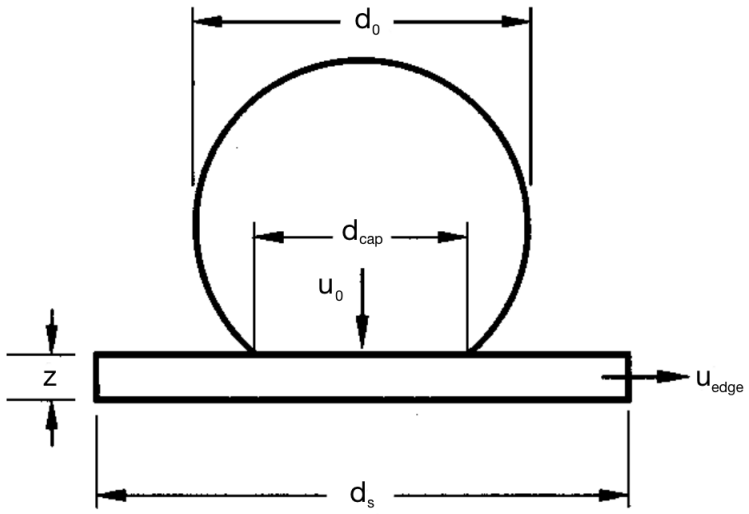

Figure P.1: Droplet spreading with dimensions labeled.

Using Equation P.7, Equation P.6, and assuming that on average d will be $\frac{d_0}{2}$ (because d_{cap} ranges from 0 to d_0, assuming constant impact velocity), an expression for the growing diameter of the droplet spreading, d_{s}, can be written (the following steps are not shown by Pasandideh-Fard et al. [1996]):

$$\frac{u_{\text{edge}}}{u_0} = \frac{d_{\text{cap}}^2}{4d_{\text{s}}} \frac{3d_{\text{max}}^2}{2d_0^3} \tag{P.9}$$

$$u_{\text{edge}} = \frac{3}{8} \frac{d_{\text{cap}}^2}{d_{\text{s}}} \frac{d_{\text{max}}^2}{d_0^3} u_0 \tag{P.10}$$

$$u_{\text{edge}} = \frac{3}{8} \left(\frac{d_0}{2}\right)^2 \frac{1}{d_{\text{s}}} \frac{d_{\text{max}}^2}{d_0^3} u_0 \tag{P.11}$$

$$u_{\text{edge}} = \frac{3}{8} \left(\frac{1}{4}\right) \frac{1}{d_{\text{s}}} \frac{d_{\text{max}}^2}{d_0} u_0 \tag{P.12}$$

$$u_{\text{edge}} = \frac{3}{32} \frac{u_0}{d_{\text{s}}} \frac{d_{\text{max}}^2}{d_0}. \tag{P.13}$$

Pasandideh-Fard et al. [1996] brings a factor of 2 over to the left hand side of Equation P.13 but it is unclear why. Pasandideh-Fard et al. [1996] then writes the the velocity in terms of the derivative of the growing diameter of the droplet:

$$2u_{\text{edge}} = \frac{3}{16}\frac{u_0}{d_\text{s}}\frac{d_\text{max}^2}{d_0} \tag{P.14}$$

$$\frac{dd_\text{s}}{dt} = \frac{3}{16}\frac{u_0}{d_\text{s}}\frac{d_\text{max}^2}{d_0}\,. \tag{P.15}$$

It is not stated by Pasandideh-Fard et al. [1996] why $2u_{\text{edge}} = \frac{dd_\text{s}}{dt}$. Next, Pasandideh-Fard et al. [1996] integrates both sides (Moita and Moreira [2002] performed this operation as well but neither publication shows the following steps):

$$\frac{\mathrm{d}d_\text{s}}{\mathrm{d}t} = \frac{3}{16}\frac{u_0}{d_\text{s}}\frac{d_\text{max}^2}{d_0} \tag{P.16}$$

$$d_\text{s}\mathrm{d}d_\text{s} = \frac{3}{16}u_0\frac{d_\text{max}^2}{d_0}\mathrm{d}t \tag{P.17}$$

$$\int d_\text{s}\mathrm{d}d_\text{s} = \int \frac{3}{16}u_0\frac{d_\text{max}^2}{d_0}\mathrm{d}t \tag{P.18}$$

$$\frac{d_\text{s}^2}{2} = \frac{3}{16}u_0\frac{d_\text{max}^2}{d_0}t\,. \tag{P.19}$$

Pasandideh-Fard et al. [1996] defines a dimensionless time term to be:

$$t^* = \frac{u_0 t}{d_0}\,. \tag{P.20}$$

Substituting Equation P.20, into Equation P.19:

$$\frac{d_\text{s}^2}{2} = \frac{3}{16}u_0\frac{d_\text{max}^2}{d_0}\frac{t^* d_0}{u_0} \tag{P.21}$$

$$d_\text{s}^2 = \frac{3}{8}d_\text{max}^2 t^* \tag{P.22}$$

$$\frac{d_\text{s}}{d_\text{max}} = \sqrt{\frac{3}{8}t^*}\,. \tag{P.23}$$

Therefore, when $d_\text{s} = d_\text{max}$, *i.e.*, when the droplet has reached its maximum spread, $t^* = \frac{8}{3}$

which can be substituted into Equation P.20 to find the time at which the droplet has reached its maximum spread:

$$t^* = \frac{u_0 t}{d_0} \tag{P.24}$$

$$\frac{8}{3} = \frac{u_0 t_{\max}}{d_0} \tag{P.25}$$

$$t_{\max} = \frac{8 d_0}{3 u_0}\,. \tag{P.26}$$

The volume of the droplet at maximum spread (*i.e.*, at $t_{\max}$) is taken to be the volume of a disc:

$$V = \frac{\pi}{4} d_{\max}^2 \delta\,. \tag{P.27}$$

Now, substituting Equation P.33, Equation P.3, Equation P.26, and Equation P.27 into Equation O.1:

$$E_D \approx \Phi V t_{\max} \tag{P.28}$$

$$\approx \mu \left(\frac{u_0}{\delta}\right)^2 \left(\frac{\pi}{4} d_{\max}^2 \delta\right) \frac{8 d_0}{3 u_0} \tag{P.29}$$

$$\approx \mu \frac{u_0}{\delta} \left(\frac{\pi}{4} d_{\max}^2\right) \frac{8 d_0}{3} \tag{P.30}$$

$$\approx \frac{2}{3} \mu \pi \frac{u_0}{\delta} d_{\max}^2 d_0 \tag{P.31}$$

$$\approx \frac{2}{3} \mu \pi u_0 d_{\max}^2 d_0 \frac{\sqrt{\mathrm{Re}}}{2 d_0} \tag{P.32}$$

$$\approx \frac{\pi}{3} \mu u_0 d_{\max}^2 \sqrt{\mathrm{Re}}\,. \tag{P.33}$$

In order to write Equation P.33 like Pasandideh-Fard et al. [1996], the Reynolds number needs to be substituted in:

$$E_D \approx \frac{\pi}{3}\mu u_0 d_{\max}^2 \sqrt{\frac{\rho u_0 d_0}{\mu}} \tag{P.34}$$

$$\approx \frac{\pi}{3}\mu^{\frac{1}{2}} u_0^{\frac{3}{2}} d_{\max}^2 \rho^{\frac{1}{2}} d_0^{\frac{1}{2}} \tag{P.35}$$

$$\approx \frac{\pi}{3} d_{\max}^2 \left(\frac{\rho}{\rho^{\frac{1}{2}}}\right)\left(\frac{d_0}{d_0^{\frac{1}{2}}}\right)\left(\frac{u_0^2}{u_0^{\frac{1}{2}}}\right)\mu^{\frac{1}{2}} \tag{P.36}$$

$$\approx \frac{\pi}{3} d_{\max}^2 \rho d_0 u_0^2 \frac{1}{\sqrt{\mathrm{Re}}}\,. \tag{P.37}$$

Appendix Q

Deriving the spread factor according to Chandra and Avedisian [1991]

When a droplet impacts a surface it will have kinetic energy before impact, E_K, surface energy before impact, E_S, surface energy after impact, E'_S, and energy lost due to the deformation of the droplet, E_D, also known as the work done to the droplet by viscosity. The conservation of energy of a droplet impact, assuming there is no energy lost to the surface, dictates that:

$$E_K + E_S = E'_S + E_D \,. \tag{Q.1}$$

The kinetic energy of the droplet is (Appendix K):

$$E_K = \frac{\pi}{12}\rho d_0^3 u_0^2 \,, \tag{Q.2}$$

where d_0 is the diameter of the droplet before impact and u_0 is the impact velocity of the droplet. Also, using the surface area of a sphere (πd_0^2), the surface energy of the droplet before impact is (Appendix M):

$$E_S = \sigma_{lg}\pi d_0^2 \tag{Q.3}$$

where σ_{lg}, is the surface tension between the air and the fluid. Once the droplet impacts the surface its surface energy is written as:

$$E'_S = \frac{\sigma_{lg}\pi}{4} d_{\max}^2 \left(1 - \cos\theta_a\right) , \tag{Q.4}$$

where $d_{\max}$ is the maximum spread (diameter) of the droplet and θ_a is the advancing contact

angle. Chandra and Avedisian [1991] simply cites from Ford and Furmidge [1967c] without a derivation. Strangely, Ford and Furmidge [1967c] do not write the surface energy during impact as shown in Equation R.4. Instead, Ford and Furmidge [1967c] writes the surface energy during impact (again, without derivation) as:

$$E_S' = \frac{\pi}{4} d_{\max}^2 \sigma_{lg} \left(1 - \cos\theta_a\right) + \frac{2\pi}{3} \frac{d_0^3}{d_{\max}} \sigma_{lg}\,, \tag{Q.5}$$

where σ_{lg} is the surface tension between the air and the fluid. The deformation of a droplet at impact is written by Chandra and Avedisian [1991] as (Appendix O):

$$E_D = \mu \left(\frac{u_0}{z}\right) \left(\frac{\pi}{4} d_{\max}^2\right) d_0\,, \tag{Q.6}$$

where z is the thickness of the impacting droplet, which is approximated as a thin disc. The spread factor is written as (Chandra and Avedisian [1991]):

$$\beta_{\max} = \frac{d_{\max}}{d_0}\,, \tag{Q.7}$$

which is a dimensionless ratio of the diameter of the spread at its maximum extension, $d_{\max}$, to the diameter of the droplet before impact, d_0. Equations K.6, M.5, R.4, and O.13 are substituted into Equation Q.1 in order to find an expression for conservation of energy (the following derivation is not shown by Chandra and Avedisian [1991]):

$$E_K + E_S = E_S' + E_D \tag{Q.8}$$

$$\frac{\pi}{12}\rho d_0^3 u_0^2 + \sigma_{lg}\pi d_0^2 = \frac{\pi}{4}\sigma_{lg} d_{\max}^2 \left(1 - \cos\theta_a\right) + \mu \left(\frac{u_0}{z}\right)^2 \left(\frac{\pi}{4} d_{\max}^2 z\right) \left(\frac{d_0}{u_0}\right). \tag{Q.9}$$

Multiply all terms by $\frac{4}{\pi\sigma}$:

$$\frac{1}{3}\frac{\rho d_0^3 u_0^2}{\sigma_{lg}} + 4d_0^2 = d_{\max}^2 (1-\cos\theta_a) + \frac{\mu}{\sigma_{lg}}\left(\frac{u_0}{z}\right) d_{\max}^2 d_0 \tag{Q.10}$$

$$\frac{\mathrm{We}}{3} d_0^2 + 4d_0^2 = d_{\max}^2 (1-\cos\theta_a) + \frac{\rho d_0 u_0}{\rho d_0 u_0}\left(\frac{\mu}{\sigma_{lg}}\right)\left(\frac{u_0}{z}\right) d_{\max}^2 d_0 \tag{Q.11}$$

$$\frac{\mathrm{We}}{3} d_0^2 + 4d_0^2 = d_{\max}^2 (1-\cos\theta_a) + \frac{\mathrm{We}}{\mathrm{Re}}\left(\frac{1}{z}\right) d_{\max}^2 d_0 \,. \tag{Q.12}$$

Next, divide all terms by d_0^2:

$$\frac{\mathrm{We}}{3} + 4 = \frac{d_{\max}^2}{d_0^2}(1-\cos\theta_a) + \frac{\mathrm{We}}{\mathrm{Re}}\left(\frac{d_0}{z}\right)\frac{d_{\max}^2}{d_0^2} \,. \tag{Q.13}$$

Using Equation Q.7:

$$\frac{\mathrm{We}}{3} + 4 = \beta_{\max}^2 (1-\cos\theta_a) + \frac{\mathrm{We}}{\mathrm{Re}}\left(\frac{d_0}{z}\right)\beta_{\max}^2 \,. \tag{Q.14}$$

Equating the volume of the droplet before impact and the volume of a thin disc during impact:

$$V_{sph} = V_{disc} \tag{Q.15}$$

$$\frac{\pi}{6} d_0^3 = \frac{\pi}{4} d_{\max}^2 z \tag{Q.16}$$

$$\frac{d_0}{z} = \frac{3}{2}\frac{d_{\max}^2}{d_0^2} \tag{Q.17}$$

$$\frac{d_0}{z} = \frac{3}{2}\beta_{\max}^2 \,. \tag{Q.18}$$

Substituting Equation Q.18 into Equation Q.14:

$$\frac{\mathrm{We}}{3}+4=\beta_{\max}^2\left(1-\cos\theta_a\right)+\frac{\mathrm{We}}{\mathrm{Re}}\left(\frac{3}{2}\beta_{\max}^2\right)\beta_{\max}^2 \tag{Q.19}$$

$$0=\beta_{\max}^2\left(1-\cos\theta_a\right)+\frac{3}{2}\frac{\mathrm{We}}{\mathrm{Re}}\beta_{\max}^4-\left(\frac{\mathrm{We}}{3}+4\right). \tag{Q.20}$$

$$\beta_{\max}\approx\sqrt{\frac{\frac{\mathrm{We}}{3}+4}{1-\cos\theta_a}}. \tag{Q.21}$$

When the Reynolds number approaches infinity, a fluid's inertial forces are much larger than its viscous forces, which promotes turbulent flow. Therefore, during impact, when the flow is turbulent, Equation Q.21 can be used to describe the spread factor.

Appendix R

Deriving the spread factor according to Pasandideh-Fard et al. [1996]

Similar to Appendix Q, the derivation of the spread factor starts with the conservation of energy. When a droplet impacts a surface it will have kinetic energy before impact, E_K, surface energy before impact, E_S, surface energy after impact, E'_S, and energy lost due to the deformation of the droplet, E_D, also known as the work done to the droplet by viscosity. The conservation of energy of a droplet impact dictates that:

$$E_K + E_S = E'_S + E_D \,. \tag{R.1}$$

The kinetic energy of the droplet is (Appendix K):

$$E_K = \frac{\pi}{12}\rho d_0^3 u_0^2 \,, \tag{R.2}$$

where d_0 is the diameter of the droplet before impact and u_0 is the impact velocity of the droplet. Also, using the surface area of a sphere (πd_0^2), the surface energy of the droplet before impact is (see Appendix M):

$$E_S = \sigma_{lg}\pi d_0^2 \tag{R.3}$$

where σ_{lg}, is the surface tension between the air and the fluid. Once the droplet impacts the surface its surface energy is written as:

$$E'_S = \frac{\sigma_{lg}\pi}{4} d_{\max}^2 \left(1 - \cos\theta_a\right) , \tag{R.4}$$

where $d_{\max}$ is the maximum spread (diameter) of the droplet. The deformation of the droplet E_D is written by Pasandideh-Fard et al. [1996] as (see Appendix P):

$$E_D = \frac{\pi}{3} d_{\max}^2 \rho d_0 u_0^2 \frac{1}{\sqrt{\mathrm{Re}}}. \tag{R.5}$$

This is the major difference between the spread factor by Chandra and Avedisian [1991] (Appendix Q) and the spread factor by Pasandideh-Fard et al. [1996]. Using Equations K.6, M.5, R.4, and R.5 in Equation R.1 (the following work is not shown in the publications by Pasandideh-Fard et al. [1996]; Adam [2012, 2013]):

$$E_K + E_S = E_S' + E_D \tag{R.6}$$

$$\frac{\pi\rho}{12} d_0^3 u_0^2 + \sigma_{lg} \pi d_0^2 = \frac{\sigma_{lg}\pi}{4} d_{\max}^2 (1 - \cos\theta_a) + \frac{\pi}{3} d_{\max}^2 \rho d_0 u_0^2 \frac{1}{\sqrt{\mathrm{Re}}} \tag{R.7}$$

$$\frac{\rho}{12} d_0^3 u_0^2 + \sigma_{lg} d_0^2 = \frac{\sigma_{lg}}{4} d_{\max}^2 (1 - \cos\theta_a) + \frac{1}{3} d_{\max}^2 \rho d_0 u_0^2 \frac{1}{\sqrt{\mathrm{Re}}}. \tag{R.8}$$

Multiply all terms by $\frac{12}{\sigma_{lg}}$:

$$\frac{\rho}{12} d_0^3 u_0^2 \frac{12}{\sigma_{lg}} + \sigma_{lg} d_0^2 \frac{12}{\sigma_{lg}} = \frac{\sigma_{lg}}{4} d_{\max}^2 (1 - \cos\theta_a) \frac{12}{\sigma_{lg}} + \frac{1}{3} d_{\max}^2 \rho d_0 u_0^2 \frac{1}{\sqrt{\mathrm{Re}}} \frac{12}{\sigma_{lg}} \tag{R.9}$$

$$\rho d_0^3 u_0^2 \frac{1}{\sigma_{lg}} + 12 d_0^2 = 3 d_{\max}^2 (1 - \cos\theta_a) + 4 d_{\max}^2 \rho d_0 u_0^2 \frac{1}{\sqrt{\mathrm{Re}}} \frac{1}{\sigma_{lg}}. \tag{R.10}$$

Using Equation 2.11 for the Weber number:

$$d_0^2 \mathrm{We} + 12 d_0^2 = 3 d_{\max}^2 (1 - \cos\theta_a) + 4 d_{\max}^2 \mathrm{We} \frac{1}{\sqrt{\mathrm{Re}}} \tag{R.11}$$

$$d_0^2 (\mathrm{We} + 12) = d_{\max}^2 \left[3 (1 - \cos\theta_a) + \frac{4\mathrm{We}}{\sqrt{\mathrm{Re}}} \right] \tag{R.12}$$

$$\frac{\mathrm{We} + 12}{3 (1 - \cos\theta_a) + \frac{4\mathrm{We}}{\sqrt{\mathrm{Re}}}} = \frac{d_{\max}^2}{d_0^2} . \tag{R.13}$$

Finally, the spread factor, β, is expressed as:

$$\beta = \frac{d_{\max}}{d_0} = \sqrt{\frac{\mathrm{We} + 12}{3 (1 - \cos\theta_a) + \frac{4\mathrm{We}}{\sqrt{\mathrm{Re}}}}} . \tag{R.14}$$

Appendix S

The Del Operator

The del operator, ∇, is a mathematical operation used mostly in vector calculus (Spiegel et al. [2009]). It is used to perform the gradient or laplacian (on scalar functions), divergence, and curl of functions (on vector functions).

The gradient in general is (Spiegel et al. [2009]):

$$\nabla f = \frac{\partial f}{\partial x}\hat{\mathbf{x}} + \frac{\partial f}{\partial y}\hat{\mathbf{y}} + \frac{\partial f}{\partial z}\hat{\mathbf{z}}. \tag{S.1}$$

The divergence of a vector function in general is (Spiegel et al. [2009]):

$$\nabla \cdot \mathbf{F} = \frac{\partial F_x}{\partial x} + \frac{\partial F_y}{\partial y} + \frac{\partial F_z}{\partial z}. \tag{S.2}$$

The curl of a vector function in general is (Spiegel et al. [2009]):

$$\nabla \times \mathbf{F} = \left(\frac{\partial F_z}{\partial y} - \frac{\partial F_y}{\partial z}\right)\hat{\mathbf{x}} + \left(\frac{\partial F_x}{\partial z} - \frac{\partial F_z}{\partial x}\right)\hat{\mathbf{y}} + \left(\frac{\partial F_y}{\partial x} - \frac{\partial F_x}{\partial y}\right)\hat{\mathbf{z}}. \tag{S.3}$$

The laplacian of a scalar function in general is (Spiegel et al. [2009]):

$$\nabla^2 f = \frac{\partial F_x}{\partial x} + \frac{\partial F_y}{\partial y} + \frac{\partial F_z}{\partial z}. \tag{S.4}$$

APPENDIX S. THE DEL OPERATOR

Appendix T

Unit Analysis

In the literature, there are some unit systems used that are not strictly SI units. Below are conversions from other units to SI units which is used in this thesis.

- Dynamic viscosity: $1\,\mathrm{cP} = 0.01\,\mathrm{poise} = 1 \times 10^{-3}\,\mathrm{N\,s\,m^{-2}}$
- Kinematic viscosity: $1\,\mathrm{cSt} = 1 \times 10^{-6}\,\mathrm{m^2\,s^{-1}}$
- Surface tension: $1\,\mathrm{Dynes\,cm^{-1}} = 1 \times 10^{-3}\,\mathrm{N\,m^{-1}}$
- Density: $1\mathrm{g\,cm^{-3}} = 1000\,\mathrm{kg\,m^{-3}}$

Appendix U

Derivation of d_0 and u_0 based on Knock and Davison [2007]'s work

Starting with Knock and Davison [2007]'s expression for stain area:

$$d_i d_j = 111.74 \left(\mathrm{Re}\sqrt{\mathrm{We}}\right)^{\frac{3}{8}} d_0^2 + 0.00084\,, \tag{U.1}$$

where d_i is the stain width, d_j is the stain length, Re is the Reynolds number (Equation 2.9, We is the Weber number (Equation 2.11), and d_0 is the initial droplet diameter. Let the fitting constants be $q_1 = 111.74$, $q_2 = 0.00084$, thus:

$$d_i d_j = q_1 \left(\mathrm{Re}\sqrt{\mathrm{We}}\right)^{\frac{3}{8}} d_0^2 + q_2\,. \tag{U.2}$$

Also the expression for number of spines (N) by Knock and Davison [2007] was rearranged in this thesis to isolate impact velocity, u_0:

$$u_0 = \sqrt{\frac{\sigma_{lg}}{\rho_l d_0}} \left(\frac{N}{0.76 \sin^3 \theta_f}\right), \tag{U.3}$$

where σ_{lg} is the surface tension, ρ_l is the density of the fluid, θ_f is the impact angle. Let the fitting constants be $q_3 = 0.76$, thus:

$$u_0 = \sqrt{\frac{\sigma_{lg}}{\rho_l d_0}} \left(\frac{N}{q_3 \sin^3 \theta_f}\right). \tag{U.4}$$

Expand Equation U.2 using known expressions for Reynolds number and Weber number (see Section 2.1):

$$d_i d_j = q_1 \left(\frac{\rho_l u_0 d_0}{\mu_l} \sqrt{\frac{\rho_l u_0^2 d_0}{\sigma_{lg}}} \right)^{\frac{3}{8}} d_0^2 + q_2$$

$$d_i d_j = q_1 \left(\frac{\rho_l^{3/2} u_0^2 d_0^{3/2}}{\mu_l \sigma_{lg}^{1/2}} \right)^{\frac{3}{8}} d_0^2 + q_2$$

$$d_i d_j = q_1 \left(\frac{\rho_l^{3/2}}{\mu_l \sigma_{lg}^{1/2}} \right)^{\frac{3}{8}} d_0^{41/16} u_0^{3/4} + q_2 \,. \tag{U.5}$$

Now substitute in Equation U.4:

$$d_i d_j = q_1 \left(\frac{\rho_l^{3/2}}{\mu_l \sigma_{lg}^{1/2}} \right)^{\frac{3}{8}} d_0^{41/16} \left[\sqrt{\frac{\sigma_{lg}}{\rho_l d_0}} \left(\frac{N}{q_3 \sin^3 \theta_f} \right) \right]^{3/4} + q_2$$

$$d_i d_j = q_1 \left(\frac{\rho_l^{9/16}}{\mu_l^{3/8} \sigma_{lg}^{3/16}} \right) d_0^{35/16} \left(\frac{\sigma_{lg}^{3/8}}{\rho_l^{3/8}} \right) \left(\frac{N}{q_3 \sin^3 \theta_f} \right)^{3/4} + q_2$$

$$d_i d_j = q_1 \left(\frac{\rho_l^{3/16} \sigma_{lg}^{3/16}}{\mu_l^{3/8}} \right) d_0^{35/16} \left(\frac{N}{q_3 \sin^3 \theta_f} \right)^{3/4} + q_2$$

$$\frac{d_i d_j - q_2}{q_1} = \left(\frac{\rho_l^{1/2} \sigma_{lg}^{1/2}}{\mu_l} \right)^{3/8} d_0^{35/16} \left(\frac{N}{q_3 \sin^3 \theta_f} \right)^{3/4}$$

$$\left(\frac{d_i d_j - q_2}{q_1} \right) \left(\frac{q_3 \sin^3 \theta_f}{N} \right)^{3/4} \left(\frac{\mu_l}{\rho_l^{1/2} \sigma_{lg}^{1/2}} \right)^{3/8} = d_0^{35/16}$$

$$\left(\frac{d_i d_j - q_2}{q_1} \right)^{16/35} \left(\frac{q_3 \sin^3 \theta_f}{N} \right)^{12/35} \left(\frac{\mu_l}{\sqrt{\rho_l \sigma_{lg}}} \right)^{6/35} = d_0$$

$$\left[\left(\frac{d_i d_j - q_2}{q_1} \right)^8 \left(\frac{q_3 \sin^3 \theta_f}{N} \right)^6 \left(\frac{\mu_l}{\sqrt{\rho_l \sigma_{lg}}} \right)^3 \right]^{2/35} = d_0 \,. \tag{U.6}$$

Substituting this back into Equation U.4 to find an expression for impact velocity (that depends solely on parameters of the stain):

$$u_0 = d_0^{-1/2}\sqrt{\frac{\sigma_{lg}}{\rho_l}}\left(\frac{N}{q_3\sin^3\theta_f}\right)$$

$$u_0 = \left(\left[\left(\frac{d_i d_j - q_2}{q_1}\right)^8\left(\frac{q_3\sin^3\theta_f}{N}\right)^6\left(\frac{\mu_l}{\sqrt{\rho_l\sigma_{lg}}}\right)^3\right]^{2/35}\right)^{-1/2}\sqrt{\frac{\sigma_{lg}}{\rho_l}}\left(\frac{N}{q_3\sin^3\theta_f}\right)$$

$$u_0 = \left[\left(\frac{d_i d_j - q_2}{q_1}\right)^8\left(\frac{q_3\sin^3\theta_f}{N}\right)^6\left(\frac{\mu_l}{\sqrt{\rho_l\sigma_{lg}}}\right)^3\right]^{-1/35}\sqrt{\frac{\sigma_{lg}}{\rho_l}}\left(\frac{N}{q_3\sin^3\theta_f}\right)$$

$$u_0 = \left(\frac{d_i d_j - q_2}{q_1}\right)^{-8/35}\left(\frac{q_3\sin^3\theta_f}{N}\right)^{-6/35}\left(\frac{\mu_l}{\sqrt{\rho_l\sigma_{lg}}}\right)^{-3/35}\sqrt{\frac{\sigma_{lg}}{\rho_l}}\left(\frac{N}{q_3\sin^3\theta_f}\right)$$

$$u_0 = \left(\frac{d_i d_j - q_2}{q_1}\right)^{-8/35}\left(\frac{\sigma_{lg}^{22}}{\rho_l^{16}\mu_l^3}\right)^{1/35}\left(\frac{N}{q_3\sin^3\theta_f}\right)^{41/35}$$

$$u_0 = \left(\frac{q_1}{d_i d_j - q_2}\right)^{8/35}\left(\frac{\sigma_{lg}^{22}}{\rho_l^{16}\mu_l^3}\right)^{1/35}\left(\frac{N}{q_3\sin^3\theta_f}\right)^{41/35}$$

$$u_0 = \left[\left(\frac{q_1}{d_i d_j - q_2}\right)^8\left(\frac{\sigma_{lg}^{22}}{\rho_l^{16}\mu_l^3}\right)\left(\frac{N}{q_3\sin^3\theta_f}\right)^{41}\right]^{1/35}. \tag{U.7}$$

If the fitting constants are set to reasonable approximations, the expressions for d_0 and u_0 can be more general. Let $q_1 = 100$, $q_2 = 0$, and $q_3 = 1$. Then, the equations for impact velocity and droplet diameter would be:

$$d_0 = \left[\left(\frac{d_i d_j}{100}\right)^8\left(\frac{\sin^3\theta_f}{N}\right)^6\left(\frac{\mu_l}{\sqrt{\rho_l\sigma_{lg}}}\right)^3\right]^{2/35} \tag{U.8}$$

and

$$u_0 = \left[\left(\frac{100}{d_i d_j}\right)^8\left(\frac{\sigma_{lg}^{22}}{\rho_l^{16}\mu_l^3}\right)\left(\frac{N}{\sin^3\theta_f}\right)^{41}\right]^{1/35}. \tag{U.9}$$

Appendix V

Testing other non-dimensional numbers for better correlations to stain properties

Table V.1: R^2 values for alternative correlations of impact properties to stain properties

Stain Property	u_0	Re	We	Ca	Bo	Fr
A	0.40	0.44	0.36	0.40	0.47	0.38
P	0.53	0.52	0.38	0.53	0.59	0.52
N or T	0.42	0.38	0.32	0.42	0.33	0.43
d_j	0.79	0.80	0.73	0.79	0.80	0.78
d_i	0.65	0.67	0.61	0.65	0.63	0.64
L	0.70	0.68	0.56	0.70	0.76	0.71